Aarhus University

Department of Physics and Astronomy

PhD thesis

Aspects of Sideband Unresolved Photon Recoil Spectroscopy of Atomic and Molecular Ions

Emilie Hindbo Clausen

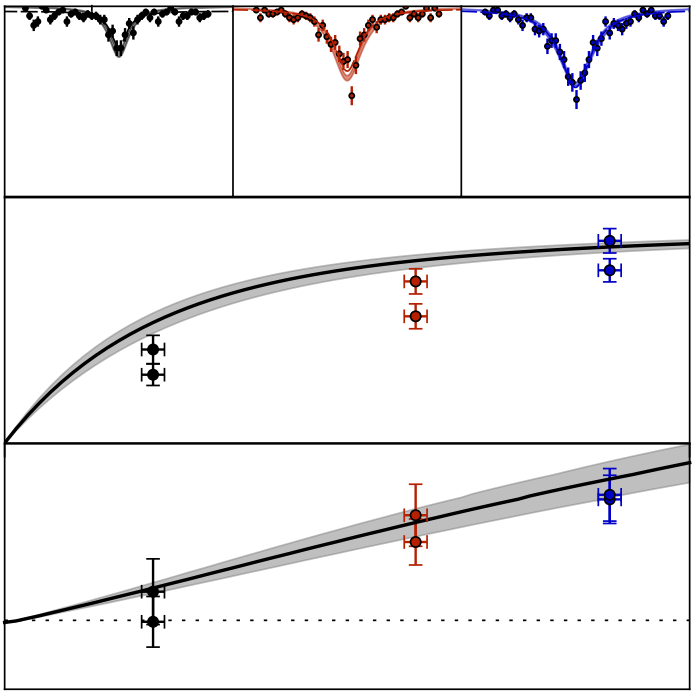

August 2021

This thesis is submitted to the Faculty of Natural Sciences at Aarhus University, Denmark, in order to fulfill the requirements for obtaining the PhD degree in Physics.

The studies have been carried out under the supervision of Prof. Michael Drewsen in the Ion Trap Group at the Department of Physics and Astronomy at Aarhus University from August 2018 to July 2021.

Pictures from the Ion Trap Lab, Department of Physics and Astronomy, Aarhus University, November 24 2020.

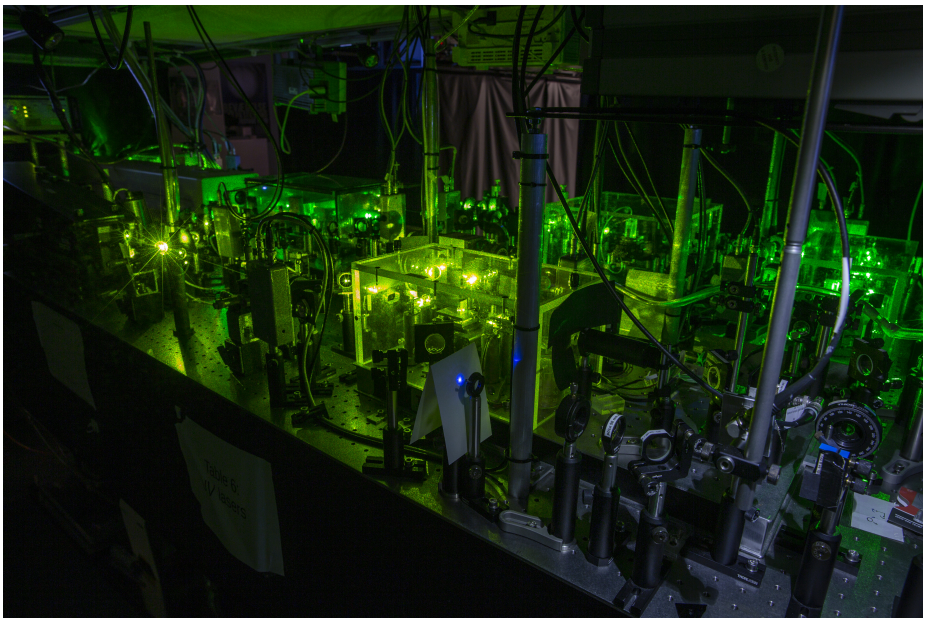

The UV laser table.

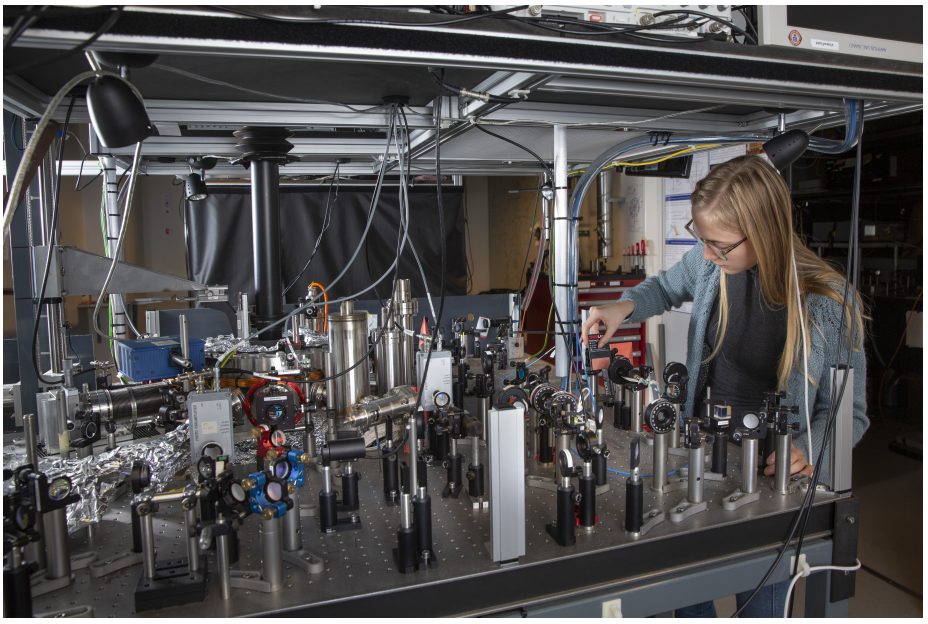

The Molecule Trap table.

Abstract

This thesis presents a model that can describe the expected spectroscopic signals when applying photon recoil spectroscopy (PRS) in the unresolved sideband limit where the linewidth of either the addressed transitions or the exciting light sources is broader than the frequencies of the involved motional modes.

The model is compared to experimental results with respect to the former case by carrying out unresolved sideband PRS on the 3s $^2S_{1/2}$ - 3p $^2P_{3/2}$ electronic transition of a single $^{24}Mg^+$ ion. Very good agreement between the experimental and simulation results strongly suggests that the model will be useful for other spectroscopic investigations as well.

A search for the closed rovibrational $^1\Sigma^+$ $|v = 0, J = 1\rangle$ - $|v' = 1, J' = 0\rangle$ transition in $^{24}MgH^+$ is also presented. The largest limitation of this experiment, are found to be the population distribution among the rotational states in $^{24}MgH^+$ due to coupling to room temeperature black-body radiation (BBR), not only decreasing the expected signal depth by 8.5% but also necessitating very long measurement times to average out the relatively slow rotational dynamics. Here we cannot rule out that the lack of signal is due to statistical fluctuations

An important feature of unresolved sideband PRS is that the spectroscopic signal does essentially not depend on which of the two transition states are occupied by the target ion when applying the spectroscopic light pulses.

Additionally, it was found that the scenario of unresolved PRS, due to motional ground state depletion, gives rise to a broadening of the spectroscopic signals that can be much larger than the natural linewidth of the transition or the spectral width of the applied light source. In situations where the aim is to localize undetermined spectroscopic lines, this technique together with rather imprecise theoretical predictions of the line positions can turn out to be a very powerful tool to search for the transitions.

Hence the technique should be well suited to localize still vastly unknown narrow lines in various target ions, such as rovibrational and electronic transitions in molecular ions, and electronic and (hyper)fine structure transitions in highly charged ions.

Dansk resumé

I denne afhandling præsenteres en model til at beskrive det forventede signal for photon-rekyl-spektroskopi (PRS) i det tilfælde hvor sidebåndene ikke er opløst. Enten fordi den spektrale linjebredde af overgangen, eller lyskilden der driver den, er større end frekvensforskellen mellem de ydre bevægelsestilstande.

Modellen sammenlignes med eksperimentelle resultater for det første af tilfældene, opnået ved at udføre ikke-opløst sidebånds PRS på den elektroniske 3s $^2S_{1/2}$ - 3p $^2P_{3/2}$ overgang i $^{24}Mg^+$. God overensstemmelse mellem eksperimentelle og simulerede resultater tyder kraftigt på, at modellen også vil være brugbar til andre spektroskopiske undersøgelser.

Et forsøg på at lokalisere den lukkede rovibrationelle $^1\Sigma^+$ $|v = 0, J = 1\rangle$ - $|v' = 1, J' = 0\rangle$ overgang i $^{24}MgH^+$ præsenteres også. Den største begrænsning i dette eksperiment er populationsfordelingen mellem de rotationalle tilstande i $^{24}MgH^+$ forårsaget af koblingen til sortlegemestråling ved stuetemperatur. Dette reducerer ikke kun signaldybden til 8.5% af den forventede, men gør også meget lange måletider nødvendige for at kunne midle over den forholdsvis langsomme rotationelle dynamik. For disse målinger kan det ikke udelukkes, at det manglende signal skyldes statistiske fluktuationer.

En vigtig egenskab ved ikke-opløst sidebånds PRS er, at det spektroskopiske signal essentielt ikke afhænger af, hvilken af de to overgangstilstande den addresserede ion befinder sig i, når den spektroskopiske lyspuls anvendes.

Ydermere ses det, at PRS-scenariet hvor sidebåndenene ikke er opløst, pga. udtømning af bevægelsesgrundtilstanden, giver anledning til en forbredning af det spektroskopiske signal, som kan være meget større end den naturlige linjebredde af overgangen eller spektralbredden af den anvendte lyskilde. I situationer hvor målet er at lokalisere en ikke tidligere bestemt linje, kan denne teknik, sammen med en forholdsvis upræcis teoretisk forudsigelse af linjens position, vise sig at være et fortræffeligt værktøj til at lede efter overgangen med.

Dermed burde teknikken være meget anvendelig til at lede efter endnu dårligt bestemte smalle linjer i mange forskellige ioner, så som rovibrationelle og elektriske overgange i molekylære ioner og elektriske og (hyper)finstrukturlinjer i ioner med høj ladning.

Acknowledgements

First and foremost I would like to thank my supervisor Prof. Michael Drewsen for trusting me with this project. A special thanks goes to the former postdoc in our group, Cyrille Solaro, whom I have worked with on The Molecule Trap during my master studies and for more than two years during my PhD studies. Your enthusiasm about physics and strong determination to obtain results have been very inspiring. I also want to thank the former postdocs Karin Fisher and Vincent Jarlaud for nice physics discussions. Thanks to Steffen Meyer, who is both a former and current postdoc in our group, for always being able to fix technical issues. Also thanks to my fellow PhD student Frederik Tribler, whom I share an office with, for always listening to details about my newest plot. Thanks to my partner Thomas for understanding what it is like to do a PhD in physics, not many I know have. And also thanks to my sister Mathilde for regularly asking me fun and hard questions about physics with great enthusiasm.

Contents

Chapter 1

Introduction

The field of ion trapping goes more than 65 years back and originates with Wolfgang Paul inventing the Paul trap in 1954 [1] and Hans Dehmelt inventing the Penning trap in 1959 [2]. Ion traps offer an ideal setting for studying charged particles due to their long storage times of up to years facilitating long interrogation and coherence times, and a very high degree of isolation from the environment especially under ultra-high vacuum (UHV). The long-ranging Coulomb trapping force mostly leaves the ion's internal levels undisturbed, and at the trap center the trapping fields vanish completely resembling a particle in free-space scenario. For these reasons they shared the Nobel prize in 1989.

Due to the deep trapping potential of a few eV equivalent to temperatures of thousands of kelvin it is easy to load ions into the trap, however these will generally follow large trajectories far from the field free trap center. Thus, in order to restrict the ion motion to the trap center and minimize Doppler broadening, the ions have to be cooled down. This was made possible with the Doppler cooling technique proposed in 1975 [3, 4] and demonstrated in 1978 [5], which at the same time facilitated imaging of ions through fluorescence detection where photons continuously scattered from the closed short-lived cooling transition are being recorded. The first single ion to be imaged was Ba^+ in 1979 in the group of Peter Toschek [6].

Fluorescence detection of ions also made it possible to do spectroscopy of long-lived states via the so-called shelving technique already proposed by Wineland and Dehmelt in 1975 [3]. Here the ion is purposely excited to a long-lived state (i.e. 'shelved') by a resonant light field, from where it cannot fluoresce. The probability to shelve the ion is greatest when the exciting light field is resonant with the shelving transition, and hence by varying the frequency of the exciting light field, the shelving technique can be used to measure the transition frequency. This unprecedented opportunity to detect the state of a single atom in real-time also lead to the first ever observations of so-called quantum jumps in 1986 [7–9], which is the spontaneous change of the eigenstate of a system. Since quantum jumps are the hallmark of a

single quantum system these observations definitively answered the question asked by Erwin Schrödinger in 1952 [10] and still debated as late as 1985 [11] on whether experiments with single quantum systems could ever be realized.

With high-precision measurements of atomic states also comes the possibility to perform extremely precise time measurements, since transitions in trapped atoms constitutes some of the most stable and reproducible measurable oscillators in the world. In fact since 1967 the second has been defined by spectroscopy in ^{133}Cs. The prospect of using single trapped ions to improve on atomic clock and frequency standards was the driving force behind the invention of the resolved sideband cooling technique already proposed by Wineland and Dehmelt in 1975 and first demonstrated by Diedrich, et al. in 1989 [12]. With this technique ions can be cooled to their ground state of motion paving the way for full coherent control of the internal and motional states of single and few-ion systems. For his contributions to this achievement Wineland later received the Nobel prize in 2012. The first clock in the optical regime [13] was a single trapped $^{199}Hg^{+}$ ion in 2001 reaching a stability of 7×10^{-15} in 1 s [14]. Nowadays, the best clocks in the world, reach stabilities of 10^{-18} [13, 15–20] outperforming the Cs clock by two orders of magnitude. This level of uncertainty corresponds to a misreading of 1 second in 30 billion years or around 2.3 times the age of the universe!

The high level of coherent control of both the internal and motional states of single and few-ion systems achievable with sideband cooling also makes trapped ions good candidates for quantum information. In fact trapped sideband cooled ions is one of the few known systems, which fulfill all of DiVincenzo's now famous criteria for the physical implementation of quantum computation from 2000 [21]. In an ion quantum computer the internal state of each co-trapped ion constitutes a quantum bit (qubit), and coupling between qubits necessary for multi-qubit gate operations is facilitated through the ions' common outer motional excitation [22–24].

All these ground-breaking experiments could however initially only be conducted for a small subset of atomic ions, which possess broad closed transitions suitable for Doppler cooling and fluorescence detection. However that obviously does not mean that all so-called inaccessible atoms and molecules are not interesting to study, far from it!

For both atoms and molecules there are many examples of inaccessible species possessing narrow lines insensitive to B-field fluctuations and therefore suitable for clock and qubit applications. Other lines, especially in molecules, might at the same

time be sensitive to the size of natural constants such as the electron mass, the proton-electron mass ratio and the fine structure constant making it possible to measure them more precisely [25–29]. This would also make it possible to measure a possible time variation of these natural 'constants' leading to the discovery of new physics [30]!

Especially the study of molecules offers insight into a whole new realm of physics. Molecules have a richer level structure compared to atoms stemming from their additional vibrational and rotational degrees of freedom. Consequently the level structure is also harder to predict making high-resolution spectroscopy of molecules a key tool for improving theoretical models [31] and gain more fundamental knowledge on the structure of molecules. Further, due to their densely spaced level structure leading to low-energy transitions, molecules possess many long-lived states interesting for atomic clock and qubit applications since the linewidth of dipole transitions scales as ν^3 and the transition dipoles are typically lower for rovibrational transitions compared to electronic ones. Furthermore, controlled reaction experiments with ground-state-cooled molecules can be used to study the role of quantum mechanics in reactions dynamics, which below 1 K starts to play a major role [32, 33]. Additionally, the study of reactions with and spectroscopy of cold molecular ions can help to make models of molecule formation is space, which is currently believed to take place almost exclusively between ion-neutral reactants due to the long ranging interaction potential compared to neutral-neutral reactants [34, 35].

Unfortunately, the same thing that makes molecules so interesting, namely the rich level structure, is also the reason why they are so difficult to laser cool. Since an excited electronic state can decay to many different rovibrational levels of the electronic ground state many different lasers are required to obtain an effectively closed transition. Some molecules however, for which the exciting electron does not take part in the molecular bond, have a good Franck-Condon overlap between the vibrational wavefunctions of the ground and excited electronic states. This results in decay only to the same vibrational state and thus reduces the number of lasers needed [36]. Direct laser cooling schemes of such ideal molecules have gained ground over the recent years [37–41], as well as the creation of ultracold molecules by binding together laser cooled (especially alkali) atoms [42, 43]. However these techniques are limited to very few species.

A much more wide-ranging solution for cooling the external motion of molecules (and inaccessible atoms) is to ionize them and sympathetically cool them by co-trapping them with atomic ions suitable for laser cooling. Due to their strong coupling via the Coulomb interaction the two species will eventually reach the same

temperature. Since the cooling lasers are tailored for the atomic cooling ions only, the molecular ion can be replaced by another species with relative ease making sympathetic cooling extremely versatile. This is in stark contrast to laser cooling of neutral molecules which is highly species dependent.

The first sympathetically cooled ensembles of molecular ions where reported in 1995 [44], and in 2000 the first larger Coulomb crystals containing sympathetically cooled molecular ions where reported by Mølhave and Drewsen [45].

Internal cooling of molecular ions, the population of which at room temperature is distributed among the rotational and for large molecules also among the vibrational levels, have also been demonstrated trough buffer gas cooling [46] and laser-induced rotational cooling [47], however, not leaving the molecular ion in a single internal quamtum state. Internal state preparation via projection measurements of molecular ions have also been proposed [48].

The spectroscopic precision achievable in large mix-species Coulomb crystal experiments is limited for two reasons. One is that the trapping fields are felt more strongly by the outer ions, resulting in higher temperatures than achievable with single ions. Secondly, in these experiments, measurements often take place destructively, e.g. by reactions [45], ion ejection [49] or photo-dissociation [50, 51] which fundamentally alters the system under investigation, and hence requires reloading of the ions of interest.

More recently, single molecular ions have been sympathetically cooled to microkelvin temperatures by single atomic ions, where the common modes of the strongly coupled two-ion system are close to their quantum mechanical ground states [52–54]. The latter scenario constitutes a novel setting for conducting molecular spectroscopy with potentially very high resolution for fundamental studies of the structure of molecular ions [28, 55–59], tests of fundamental physics theories [60, 61], and quantum technology oriented applications [62].

However, since it is practically impossible to count a single absorbed photon from a light beam, or to detect with high probability a single photon emitted by a single molecular ion, standard absorption and emission spectroscopy cannot be applied efficiently.

This problem can be circumvented with the technique of quantum logic spectroscopy (QLS) first devised by Wineland in 2002 [63, 64] with the prospect of developing optical atomic clocks using inaccessible species.

In QLS, spectroscopy is carried out by trapping a single spectroscopic target ion together with a single atomic logic ion that can be sideband cooled and cooling them

to their quantum mechanical ground state with respect to one or more motional modes. The technique exploits that the momentum recoil associated with absorption and emission of individual photons by the target ion excites the common motion of the two-ion system, which can then be read out on the logic ion.

Unlike large ion Coulomb crystal experiments, and many other types of so-called 'action spectroscopy', where absorption is detected by other means than emitted photons, QLS does not depend on destroying the investigated system. In QLS the same target ion can be reused, and the spectroscopic resolution will only be limited by the linewidth of the laser exciting the target transition or the natural linewidth of the transition itself. As opposed to original fluorescence spectroscopy, QLS is not limited by detecting photons from spontaneous emission, since the decisive recoil kick can just as well be associated with absorption or stimulated emission. In extension of this, the target ion neither has to initially be in the lower of the two states constituting the target transition.

Thus far, QLS for spectroscopy of atomic ions has proven very successful [64–68]. In fact the current best clock in the world, a $^{27}Al^+$ clock with a stability of 0.94×10^{-18}, is based on QLS using $^{25}Mg^+$ as the logic ion [19]! Also QLS of the highly charged ion $^{40}Ar^{+13}$ has been demonstrated [69], the transitions of which are especially insensitive to external perturbations due to the high binding energies of the outer electrons.

The technique has also gained ground within molecular ions the last few years with results for electronic transitions in $^{24}MgH^+$ [55], Zeeman levels [56] and rotational transitions in $^{40}CaH^+$ [57], and a spin ro-vibronic transition in N_2^+ [59].

In the original QLS paper [64], the authors consider a so-called resolved sideband scenario where the two motional mode angular frequencies corresponding to the in-phase mode (ω_{ip}) and out-of-phase mode (ω_{op}) along the trap-axis are significantly larger than both the spectroscopic transition linewidth and the spectral width of the spectroscopy laser. In this scenario, it is possible to selectively address both target ion and logic ion with lasers tuned resonantly to either carrier or specific motional sideband transitions. By in addition using very weak light fields in order to not off-resonantly drive other than the addressed sideband it is possible to only absorb a single photon exciting a single quanta.

A version of QLS where more than one photon is absorbed is referred to as photon recoil spectroscopy (PRS). This will typically be the case in the so-called unresolved sideband regime where several sidebands are driven simultaneously because the motional sideband angular frequencies ($\omega_{ip/op}$) of the two-ion system are either smaller

than or similar to: 1) the natural linewidth of the spectroscopic transition, or 2) the linewidth of the applied spectroscopic light source.

Although QLS was originally developed for ultra-precise spectroscopy in the resolved sideband regime, PRS in unresolved sideband scenarios, which is the subject of this thesis, can be equally interesting for a range of investigations of molecules in the gas phase. This includes internal state preparation, broad line absorption spectroscopy under diverse but well-controlled conditions, and single photon absorption studies of non- or weakly-fluorescing molecules.

Scenario 1) is ideal for searching for broad electronic transitions in large bio-relevant molecules, in wavelength regimes where other types of action spectroscopy would normally fail. This is because spontaneously emitted photons of weak transitions are hard to detect, especially in the mid-IR.

Scenario 2) provides a unique opportunity for searching for spectroscopic lines previously only localized to within a frequency interval much larger than the expected linewidth. This is highly relevant since generally molecular structure models cannot be expected to estimate line frequencies better than on the 5% level, and traditional absorption spectroscopy methods have an accuracy of a few GHz [70]. The very few absorbed photons needed for PRS detection makes it possible to apply a laser with a broad spectral linewidth and correspondingly low spectral energy density to cover a large frequency span faster. Once a signal has been obtained the laser linewidth can be gradually narrowed to localize the transition even better in a binary search fashion.

The goal set out for my thesis work was to investigate PRS on a rovibrational transition in $^{24}MgH^+$. $^{24}MgH^+$ is primarily chosen for its relatively simple structure compared to larger molecules, making it an ideal test bed for studying PRS of molecules, and because previous spectroscopic measurements exist [70]. Due to the large abundance of Mg in space compared to most other metals, spectroscopy of $^{24}MgH^+$ is also interesting for astrochemistry. Moreover, from a photon recoil point of view PRS of small molecules in the IR regime is equivalent to PRS of large molecules in the optical regime, since the probability to excite a motional quanta is determined by the square of the so-called Lamb-Dicke parameter approximately given as

$$\eta_{ip/op}^2 \propto \left(\frac{2\pi}{\lambda_t}\right)^2 \frac{\hbar}{2m_t\omega_{ip/op}} \tag{1.1}$$

where m_t is the mass of the target ion, and λ_t is the wavelength of the target transition. This measure expresses the ratio between the recoil energy of the trapped ion

over the energy difference between the motional states. By increasing the trapping voltage the trap frequency can be kept constant for a target ion of higher mass giving $\eta^2 \propto 1/(m\lambda^2)$, such that if we go from $m_t = 25$ a.m.u and $\lambda_t = 6\,\mu\text{m}$ to $m_t = 2500$ a.m.u and $\lambda_t = 600$ nm, η^2 would be the same. This fact makes the $^{24}MgH^+$ case highly relevant for future experiments with large molecular ions.

The chosen target transition in $^{24}MgH^+$ is the very narrow mid-infrared $|v = 0, J = 1\rangle$ - $|v' = 1, J' = 0\rangle$ transition ($\Gamma_t/2\pi = 2.50$ Hz [71, 72]) at $\lambda = 6.17\,\mu\text{m}$ in the $^1\Sigma^+$ electronic ground state for two reasons. First of all it is a closed transition allowing for repeated photon scattering and secondly the transition frequency has previously been determined to within a frequency interval of $\pm$ 1.5 GHz [70]. Since this is still a large interval compared to the expected transition linewidth we want to use a broadband laser source ($\Gamma_L/2\pi \gtrsim 50$ MHz) to search for the transition resembling PRS scenario 2) above.

Before pursuing PRS of $^{24}MgH^+$ a test of both the theoretical model and the experimental procedure was needed. The system of choice was the broad 3s $^2S_{1/2}$ - 3p $^2P_{3/2}$ electronic transition ($\Gamma_t/2\pi = 41.8\,\text{MHz}$) at $\lambda = 279.6$ nm in $^{24}Mg^+$ for two reasons. Firstly the trapping of $^{24}Mg^+$ and excitation of the transition is already an important experimental step in the $^{24}MgH^+$ trapping procedure. Secondly the two ions have almost the same mass meaning that the optimum parameters for sideband cooling by $^{40}Ca^+$ are practically the same for $^{24}Mg^+$ and $^{24}MgH^+$. The transition in $^{24}Mg^+$ is excited by a narrow laser source ($\Gamma_L/2\pi \lesssim 1$ MHz) such that this PRS experiment resembles scenario 1) above. Knowledge about PRS in this broad transition and narrow laser linewidth scenario is also useful for doing PRS of electronic transitions in large molecules, since they are generally expected to be much broader than the sideband level spacing.

Outline of the thesis

This thesis is divided into four main parts. Part I, **Theory of trapping and cooling of ions**, consists of three chapters. First Chapter 2 covers the theory of 3D ion confinement, focusing on the linear Paul trap. The part continues with Chapter 3 on light-matter interactions before moving on to Chapter 4 where the principles of the Doppler and sideband cooling techniques are explained. The chapter ends with a discussion of trap-induced heating, and a presentation of how the ion temperature after cooling can be evaluated.

Part II **Photon recoil spectroscopy theory and simulations** consists of five chapters. It starts with Chapter 5 giving an introduction to the nomenclature and basic principle of PRS. The chapter also provides a detailed Hamiltonian model of the original case of sideband resolved PRS. This sets the scene for moving on to the sideband unresolved scenario, which is modeled with rate equations. In Chapter 6 simulations of PRS, based on the rate equation model, for the two specific test systems of $^{24}Mg^+$ and $^{24}MgH^+$, are performed. The systems represent unresolved scenarios due to a broad transition and a broad laser linewidth, respectively. After this very specific treatment, in Chapter 7 a simple qualitative model of PRS is presented which underlines the important parameters and essence of the technique. In Chapter 8 the specific issues related to doing PRS of $^{24}MgH^+$ when its rotational transitions couple to blackbody radiation is treated. The part ends with Chapter 9 on how to best use PRS to search for narrow lines in a broad frequency interval.

Part III, **Experimental setup and procedure**, consists of three chapters. In Chapter 10 the experimental trap setup and procedure for ion trapping is presented along with a brief introduction to experiment automation. In Chapter 11 the experimental procedure for ion cooling and evaluation is presented, before giving experimental details on the PRS experiments with $^{24}Mg^+$ and $^{24}MgH^+$ in Chapter 12

The last part IV **Experimental results** consists of two chapters. In Chapter 13 the results obtained for sideband cooling and PRS of $^{24}Mg^+$ are presented and compared to the simulated results, and in Chapter 14 the sideband cooling results for $^{24}MgH^+$ are presented along with the conducted search for PRS signals in $^{24}MgH^+$.

The thesis ends with a conclusion and outlook in Chapter 15.

Chapter 3, 5, 6, and 13 are based on our arXiv article [73]. Only minor adjustments have been made to make the content fit into the context of the thesis. Explicitly Chapter 3 corresponds to Sec. 2.1 of the article, Sec. 5.1 to Sec. 2 until 2.1, Sec.

5.2 to Sec. 2.2, Sec. 6.1 to Sec. 3.1 not including 3.1.7, Sec. 6.2 to Sec. 3.2, and Chapter 13 corresponds to Sec. 3.1.7.

Part I

Theory of trapping and cooling of ions

Chapter 2

Ion trapping

For neutral particles the trapping force relies on magnetic and/or optical interactions with the internal states of the atoms or molecules. Hence, the depth of neutral particle traps are fundamentally limited by the particle's structure and internal state. In comparison, ions are much easier to confine since their charge interacts strongly with electromagnetic fields independent of their internal state.

An intuitive way to trap a charged particle would be to create an electrostatic potential minimum in all three dimensions using a harmonic potential of the form

$$\phi(x, y, z) = \alpha x^2 + \beta y^2 + \gamma z^2. \tag{2.1}$$

However, by Gauss's law any electric potential in free space must satisfy Laplace's equation

$$\nabla^2 \phi(x, y, z) = \frac{\partial^2 \phi(x, y, z)}{\partial x^2} + \frac{\partial^2 \phi(x, y, z)}{\partial y^2} + \frac{\partial^2 \phi(x, y, z)}{\partial z^2} = 0. \tag{2.2}$$

In order to have a confining potential in all three dimensions all three derivatives must be positive. This would give $\alpha, \beta, \gamma > 0$ which contradicts Eq. 2.2 demanding $\alpha + \beta + \gamma = 0$. Thus it is impossible to confine a charged particle by a static electric potential alone. This rule, central for ion trapping, is named Earnshaw's theorem [74].

There exist several clever ways to circumvent this problem, two of the most popular ones are the Paul and the Penning trap. The Penning trap [2] combines a static quadropolar electric field with a homogeneous magnetic field, such that the untrapped direction of the electrostatic potential is counteracted by cyclotron motion around the magnetic field lines. In a Paul trap [1] a combination of static and oscillating electric fields are used, which leads to an effective dynamic confinement along directions of repulsive electrostatic forces. The trap used for this work is a so-called linear Paul trap, which will be presented in more detail in the next section.

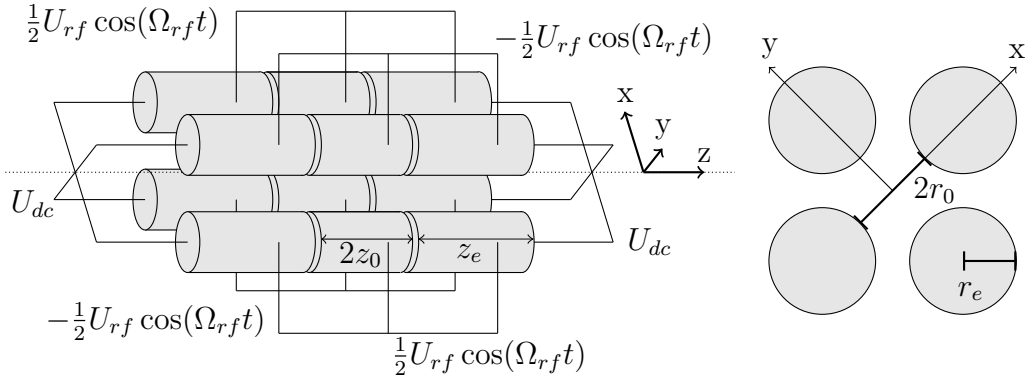

FIGURE 2.1: *Drawing of the 12 electrodes constituting a linear Paul trap: 4 center electrodes with oscillating voltages and 8 endcap electrodes with additional stationary voltages U_{dc} as indicated.*

Geometric trap parameters	
z_0	2.70 mm
r_0	3.50 mm
r_e	4.00 mm
z_e	20.00 mm
κ	0.248

TABLE 2.1: *Trap geometries for the trap used for this thesis with reference to Fig. 2.1 and Eq. 2.4.*

2.1 The linear Paul trap

The original Paul trap from 1954 was shaped like a hyperbolic ring with two hyperbolic endcap electrodes creating an oscillating and static electric field, respectively [75]. The trap used for this thesis is called a linear Paul trap, first proposed and demonstrated by Prestage et. al in 1989 [76]. The linear version allows for much better optical access to the trap center and a higher level of control over the electric potential due to a higher number of electrodes. Actually, the linear Paul trap is only a slight modification of the quadropolar mass spectrometer proposed by Paul and Steinwedel already in 1953 [1], but more than three decades should pass before the connection was made.[1]

The linear Paul trap consists of four cylindrical rods, each divided into three electrodes placed in a geometry as seen in Fig. 2.1. The axis of symmetry, the z-axis, is called the trap axis. For future reference the geometric trap parameters, as indicated in Fig. 2.1, are given for the specific trap used for this thesis in Table 2.1.

[1]Instead of endcap electrodes the filter has an extra static potential on top of the oscillating potiential on the center rods, making it unable to confine particles along the z-axis.

All 12 electrodes are applied voltages

$$\pm \frac{U_{rf}}{2} \cos(\Omega_{rf} t) \tag{2.3}$$

oscillating with radio frequency (RF) Ω_{rf}, where U_{rf} is the peak-to-peak amplitude. In the trap used for this thesis $\Omega_{rf} = 2\pi \times 4.692$ MHz. Diagonally opposite rods are applied voltages of the same sign, as indicated in Fig. 2.1, such that neighboring rods will always have the exact opposite RF voltages because the oscillations are π out of phase.

To the eight outer electrodes, called the endcap electrodes, are applied static voltages U_{dc}, in addition to the RF voltage. The resulting potential along the z-axis close to $z = 0$ is

$$\phi_z = \frac{\kappa}{z_0^2} U_{dc} z^2, \tag{2.4}$$

where z_0 is half the length of the center electrodes, and the factor κ depends on the trap geometry.

The potential in the xy-plane close to the trap center results from both the endcap and center electrodes and is approximately quadropolar and given by

$$\phi_{xy} = -\frac{\kappa U_{dc}}{z_0^2}(x^2 + y^2) - \frac{U_{rf}}{r_0^2} \cos(\Omega_{rf} t)(x^2 - y^2), \tag{2.5}$$

where r_0 is the shortest distance between the z-axis and the electrodes. We see that the signs differ from the intuitively proposed potential of Eq. 2.1 such that the total potential $\phi_{xyz} = \phi_{xy} + \phi_z$ fulfills Laplace's equation at all times (α, β, γ not all > 0).

In order for the potential to be truly quadropolar the electrode rods must have hyperbolic curvatures towards the center and not be cylindrical. However, by choosing the right dimensions the deviation from quadropolar is very small [77] and thus cylindrical electrodes are very popular due to the relative ease of construction.

2.1.1 Single ion motion

The force exerted on a single ion with charge Q and mass m along the z-direction in the ϕ_z potential of Eq. 2.4 is

$$\vec{F}_z = m \frac{d^2 \vec{z}}{dt^2} = -Q \vec{\nabla} \phi_z, \tag{2.6}$$

leading to the following equation of motion

$$\frac{d^2z}{dt^2} = \frac{2\kappa}{z_0^2}U_{dc}z, \tag{2.7}$$

resulting in a harmonic oscillator movement with frequency

$$\omega_z = \sqrt{\frac{u_0}{m}}, \quad u_0 = \frac{2Q\kappa U_{dc}}{z_0^2} \tag{2.8}$$

From the ϕ_{xy} potential of Eq. 2.5 the equations of motion in the xy-plane take the form of the Mathieu equations

$$\frac{d^2u}{d\zeta^2} + [a + q_u\cos(2\zeta)]u = 0, \quad u = x, y \tag{2.9}$$

with

$$\zeta = \frac{\Omega_{rf}t}{2}, \quad a = -\frac{4Q\kappa}{mz_0^2\Omega_{rf}^2}U_{dc}, \quad q_x = -q_y = \frac{2Q}{mr_0^2\Omega_{rf}^2}U_{rf}. \tag{2.10}$$

From this point we will refer to $q_x = q$ and since the modes along the x- and y-axis are degenerate, we will collectively refer to them as the radial modes.

Only certain combinations of the a- and q-parameters of Eq. 2.10 give non-diverging solutions to the Mathieu equations and thereby stable ion trajectories in the radial plane. These can be plotted in a so-called stability diagram as seen in Fig. 2.2a). To have confinement in the z-direction we must additionally require $U_{dc} > 0$ for positively charged ions, which reduces the stability region to negative a-values as seen in figure 2.2b). Stability regions in terms of U_{dc} and U_{rf} is shown in Fig. 2.3 for the masses of the $^{40}Ca^+$, $^{24}Mg^+$ and $^{24}MgH^+$ ions of 40, 24 and 25 u, respectively. During the experiments presented in this thesis we normally applied $U_{dc} = 5$ V and $U_{rf} = 526$ Vpp corresponding to $a = -0.00199$ and $q = 0.239$ for mass 40 u. The difference in stability region for different masses can be exploited to remove unwanted ions from the trap by changing the electric potential.

When $|a|, |q| \ll 1$ the solution of the Mathieu equations can be approximated as [78]

$$u(t) = u_0\left[1 - \frac{q_u}{2}\cos(\Omega_{rf}t)\right]\cos(\omega_r t) \tag{2.11}$$

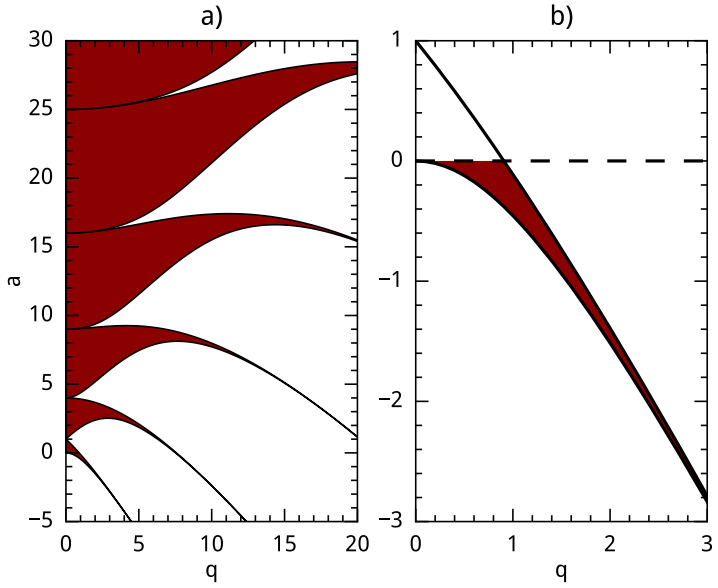

FIGURE 2.2: *a) Stable charged particle trajectories in the radial plane in terms of the a and q parameters. For additional confinement along the trap axis the a parameter becomes negative for positively charged ions, and the stability region is reduced to the one shown in figure b).*

where

$$\omega_r = \frac{\Omega_{rf}}{2}\sqrt{\frac{q^2}{2} + a}. \tag{2.12}$$

This is a harmonic motion with frequency ω_r, amplitude modulated by the RF frequency Ω_{rf}. The motion with frequency ω_r, called the *secular motion*, will be slower and have a larger amplitude than the motion with frequency Ω_{rf}, the *micromotion*, for appropriately chosen trap parameters. Along the z-axis there is no micromotion because the RF electric fields cancel and the radial potential simplifies to

$$\phi_r = \frac{1}{2}m\omega_r^2 r^2, \quad r^2 = x^2 + y^2. \tag{2.13}$$

The micromotion amplitude grows with the distance from the z-axis as illustrated in Fig. 2.4. Since the ion always oscillates to some extent around $r = 0$ due to the non-zero minimum energy of a quantum mechanical oscillator, its movement will always contain some amount of micromotion.

The absence of micromotion along the z-axis constitutes a big advantage of the linear Paul trap compared to other ion traps where the motion is typically only truly harmonic at the single point of symmetry [80]. This allows for trapping several ions in the trap without forcing them to areas of higher micromotion, as long as they sit

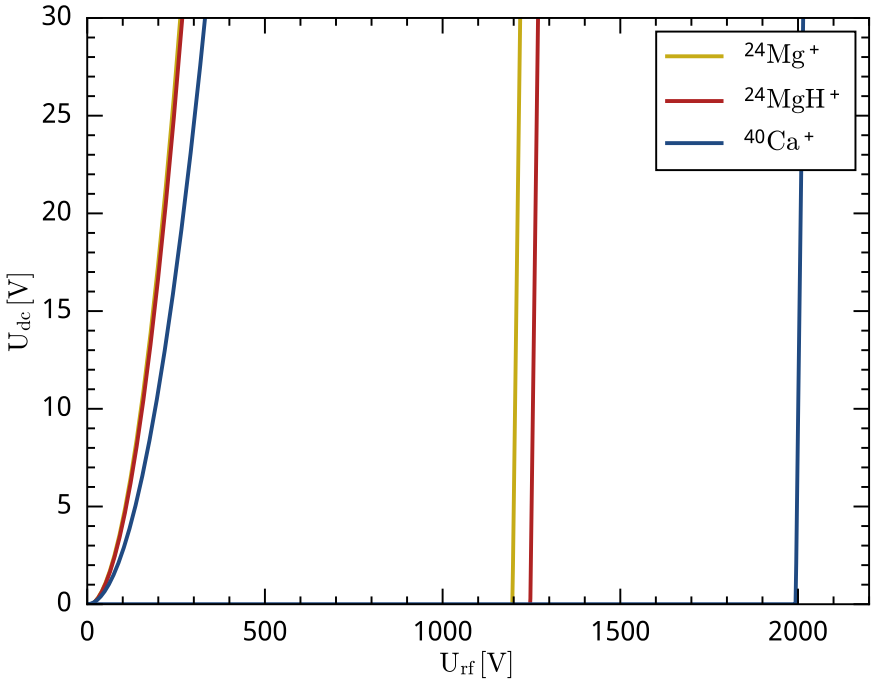

FIGURE 2.3: *Stability regions in terms of U_{dc} and U_{rf} for the masses of the $^{40}Ca^{+}$, $^{24}Mg^{+}$ and $^{24}MgH^{+}$ ions of 40, 24 and 25 u, respectively.*

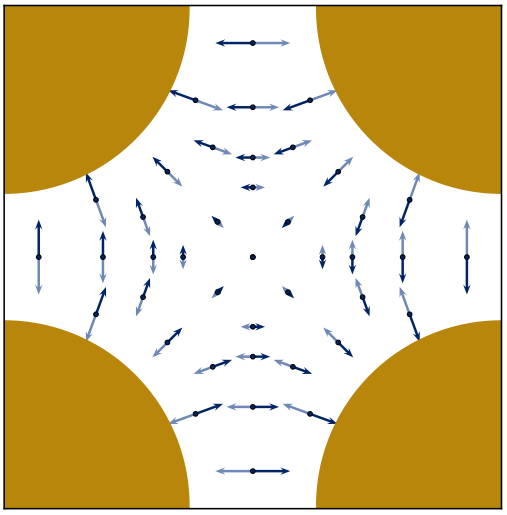

FIGURE 2.4: *Illustration of the micromotion amplitude in the radial trapping plane. This is a side view along the trap axis, with the 4 electrode rods in each corner. The color (light/dark blue) indicates the phase. Courtesy of Hans Harhoff [79].*

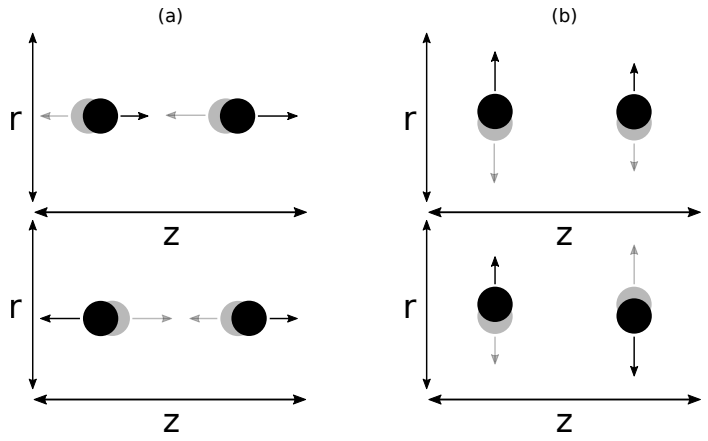

FIGURE 2.5: *Motional modes of two ions trapped along the z-axis, showing the axial modes in a) and the radial modes in b). In both figures the top panel shows the IP mode, and the bottom panel the OP mode. Courtesy of Karin Fisher [82].*

on a string along the z-axis. This is generally obtained when $\omega_r \gg \omega_z$. In this thesis, and in general, the two ions used for PRS are therefore kept in this configuration.

2.1.2 Two-ion motion

Two ions in a trap will be subject to both the trapping potential and the Coulomb interaction with the each other. Two cold co-trapped ions along the z-axis of equal charge will find an equilibrium position with a symmetric displacement around the potential center. Along the z-axis the potential for two ions of the same charge Q at positions z_1 and z_2 can be written as [81]

$$V = \frac{1}{2}u_0(z_1^2 + z_2^2) + \frac{Q^2}{4\pi\epsilon_0|z_2 - z_1|}. \tag{2.14}$$

If we only consider small displacements the potential can be considered to be harmonic, and one finds that there exist two axial modes called the in-phase (IP) mode where the ions will oscillate in phase with respect to each other, and the out-of-phase (OP) mode where the ions will oscillate out of phase as shown in Fig. 2.5.

To use this description as a reference for the PRS section we will already now name the two ions the *readout ion* and the *target ion* indicated by the suffixes r and t, respectively.

Each ion has an eigenvector component (in a mass-weighted space) for each mode denoted $b_{ip,j}$ and $b_{op,j}$, where $j \in \{r, t\}$. They can be written for the readout and

target ions as

$$\begin{aligned} b_{ip/op,r} &= \frac{r_{ip/op}}{\sqrt{1+r_{ip/op}^2}} \\ b_{ip/op,t} &= \frac{1}{\sqrt{1+r_{ip/op}^2}} \end{aligned} \tag{2.15}$$

with

$$\begin{aligned} r_{ip} &= \frac{-\mu+1+\sqrt{\mu^2-\mu+1}}{\sqrt{\mu}} \\ r_{op} &= \frac{-\mu+1-\sqrt{\mu^2-\mu+1}}{\sqrt{\mu}} \end{aligned} \tag{2.16}$$

and $\mu = m_t/m_r$ being the ion mass ratio. For the IP mode the eigenvectors for the two ions have the same sign, whereas they have opposite signs for the OP mode, in accordance with the in-phase/out-of-phase movements.

Even though two ions of different masses do not oscillate with the same absolute amplitudes, they still share common angular oscillation frequencies, which for singly charged ions are given by [81, 83]

$$\begin{aligned} \omega_{ip} &= \omega_z\left(1+\frac{1}{\mu}-\sqrt{1-\frac{1}{\mu}+\frac{1}{\mu^2}}\right)^{1/2} \\ \omega_{op} &= \omega_z\left(1+\frac{1}{\mu}+\sqrt{1-\frac{1}{\mu}+\frac{1}{\mu^2}}\right)^{1/2} \end{aligned} \tag{2.17}$$

where ω_z is the motional angular frequency of the readout ion if it were alone in the trap, all trapping parameters being the same.

For completion the radial angular frequencies are given as [84]

$$\begin{aligned} \omega_{ip}^R &= \omega_{z,1}\sqrt{-\frac{\mu+\mu^2-\epsilon^2(1+\mu^2)-s}{2\mu^2}} \\ \omega_{op}^R &= \omega_{z,1}\sqrt{-\frac{\mu+\mu^2-\epsilon^2(1+\mu^2)+s}{2\mu^2}} \end{aligned} \tag{2.18}$$

where $\epsilon = \sqrt{-\frac{q_r^2}{4a_r}}$ and $s = \sqrt{\epsilon^4(\mu^2-1)^2 - 2\epsilon^2(1-\mu)^2\mu(1+\mu) + \mu^2(1+(\mu-1)\mu)}$.

So in conclusion the two ion system has a total of six modes; two axial and four radial, where the radial modes are pairwise degenerate for a perfect trap construction.

Chapter 3

Light-matter interactions

In the experiments presented in this thesis, laser light is used to address internal transitions in the trapped ions, atomic and/or molecular, and to couple their internal levels to the outer motional modes. By describing the basics of light-matter interactions this section lays the foundation for explaining ion cooling, motional state readout and PRS in later sections.

3.1 Two-level atom in free space

The simplest way to describe how light interacts with an atom, is to assume that the atom has only two electronic states, namely the ground state $|g\rangle = (1\ 0)^T$ and an excited state $|e\rangle = (0\ 1)^T$ with energy difference $\hbar\omega_t$. The state of the atom at a time t can be written as a linear superposition of these two atomic states

$$|\psi(t)\rangle = c_g(t)\,|g\rangle + c_e(t)\,|e\rangle\,, \tag{3.1}$$

where normalization requires $|c_g|^2 + |c_e|^2 = 1$ at all times. The Hamiltonian of the two-level system is given by

$$\hat{H}_t = \frac{\hbar\omega_t}{2}(|e\rangle\langle e| - |g\rangle\langle g|) \tag{3.2}$$

$$= -\frac{\hbar\omega_t}{2}\hat{\sigma}_z. \tag{3.3}$$

For simplicity we consider the interacting light field to be a monochromatic plane wave traveling in the z-direction the electric field of which is expressed as

$$\vec{E}(z,t) = \frac{E_0}{2}\hat{\epsilon}[e^{i(k_L z - \omega_L t + \phi)} + e^{-i(k_L z - \omega_L t + \phi)}], \tag{3.4}$$

with E_0 being the amplitude, $\hat{\epsilon}$ the polarization direction, $k_L = \omega_L/c$ the wavenumber of the light, and ϕ the phase. This is a classical, and not a quantum mechanical, description of the light field making the model semi-classical. The dipole interaction

Hamiltonian between the two-level atom and the light field can be written as

$$\hat{H}_{int}(z,t) = e\hat{z} \cdot \vec{E}(z,t), \tag{3.5}$$

where $\hat{z}$ is the position operator of the ion. By doing so we have made the dipole approximation and assumed that the electric field is constant over the distance between the nucleus and the electron defining the electric dipole interacting with the light.[1]

The total Hamiltonian of the system is then given by

$$\hat{H} = \hat{H}_t + \hat{H}_{int}. \tag{3.6}$$

$\hat{H}_{int}$ can be expressed by means of the atomic basis vectors as

$$\hat{H}_{int} = \frac{\hbar}{2}\Omega_0(|g\rangle\langle e| + |e\rangle\langle g|)[e^{i(k_L z - \omega_L t + \phi)} + e^{-i(k_L z - \omega_L t + \phi)}] \tag{3.7}$$

$$= \frac{\hbar}{2}\Omega_0(\hat{\sigma}_+ + \hat{\sigma}_-)[e^{i(k_L z - \omega_L t + \phi)} + e^{-i(k_L z - \omega_L t + \phi)}], \tag{3.8}$$

where Ω_0 is the vacuum Rabi frequency for dipole allowed transitions given as

$$\Omega_0 = \frac{eE_0}{\hbar}\langle g|\,\hat{\epsilon}\cdot\hat{z}\,|e\rangle\,. \tag{3.9}$$

By substituting $\hat{H}$ into the time-dependent Scrodinger equation

$$i\hbar\frac{\partial}{\partial t}|\psi(t)\rangle = \hat{H}\,|\psi(t)\rangle \tag{3.10}$$

we obtain a second order differential equation. By assuming that all the population starts out in the ground state (by putting $c_g(0) = 1$ and $c_e(0) = 0$) the solution is

$$c_g(t) = 1 \tag{3.11}$$

$$c_e(t) = \frac{\Omega_0^*}{2}\left(\frac{1 - e^{i(\omega_t + \omega_L)t}}{\omega_t + \omega_L} + \frac{1 - e^{i(\omega_t - \omega_L)t}}{\omega_t - \omega_L}\right) \tag{3.12}$$

to first order. This is thus only a good approximate solution as long as $c_e(t)$ remains small i.e. the light field is weak. If the detuning $\delta = \omega_L - \omega_t$ is small compared to the sum of the two angular frequencies, we can make the rotating wave approximation and neglect all terms oscillating with $e^{i(\omega_L + \omega_t)}$. The probability to find the atom in

[1] This is a good approximation since the wavelength of optical transitions are typically hundreds of nm while the electron-nucleus separation in atoms is typically 0.1-1 nm.

the excited state $|e\rangle$ becomes

$$\begin{aligned}\rho_{ee}(t) = |c_e(t)|^2 &= \left|\frac{\Omega_0 \sin(\delta t/2)}{\delta}\right|^2 \\ &= \frac{1}{4}|\Omega_0|^2 t^2 \mathrm{sinc}^2(x),\end{aligned} \tag{3.13}$$

where $x = \delta t/2$. The width of the $\rho_{ee}(t)$ peak in terms of detuning decreases as the interaction time t increases.

We now wish to solve the Schrödinger equation to more than first order, to obtain a solution that also holds for strong fields. This is most easily done by transforming into the interaction picture, in which the interaction Hamiltonia can be written as

$$\hat{H}_{int,I} = \frac{\hbar}{2}\Omega_0(\hat{\sigma}_+ e^{i\omega_t t} + \hat{\sigma}_- e^{-i\omega_t t})[e^{i(k_L z - \omega_L t + \phi)} + e^{-i(k_L z - \omega_L t + \phi)}]. \tag{3.14}$$

Performing the above multiplication results in terms of $e^{i(\omega_L - \omega_t)}$ and $e^{i(\omega_L + \omega_t)}$ and we can again make the rotating wave approximation. If the atom is at rest, $e^{k_L z}$ does not vary over time, so these terms are also neglected since they just add a complex phase. $\hat{H}_{int,I}$ then simplifies to

$$\hat{H}_{int,I} = \frac{\hbar}{2}\Omega_0(\hat{\sigma}_+ e^{-i\delta t + \phi} + \hat{\sigma}_- e^{i\delta t + \phi}). \tag{3.15}$$

From here we can make the unitary transformation $\hat{H}' = \hat{\mathcal{U}}\hat{H}_{int,I}\hat{\mathcal{U}}^\dagger - \hat{A}$ with $\hat{\mathcal{U}} = e^{\frac{i\hat{A}t}{\hbar}}$ and $\hat{A} = -\frac{\hbar}{2}\delta\hat{\sigma}_z$. This results in the Hamiltonian

$$\hat{H} = \frac{\hbar}{2}\begin{pmatrix} \delta & \Omega \\ \Omega^* & -\delta \end{pmatrix}, \tag{3.16}$$

where $\Omega = \Omega_0 e^{i\phi}$. Solving the time-dependent Schrödinger equation gives the expression

$$\rho_{ee}(t) = \frac{\Omega_0^2}{\Omega_0^2 + \delta^2}\sin^2\left(\sqrt{\Omega_0^2 + \delta^2}\frac{t}{2}\right) \tag{3.17}$$

for the time evolution of the probability to find the atom in the excited state. This probability undergoes so-called Rabi oscillations with the generalized Rabi frequency $\sqrt{\Omega_0^2 + \delta^2}$ as seen in Fig. 3.1(a). If the atom is initially in the ground state and the light field is resonant with the transition such that $\delta = 0$, a laser pulse with duration $t_\pi = \pi/\Omega_0$ will transfer it to the excited state with 100% probability. Such a perfect

transfer pulse is called a π-pulse. Inserting this into Eq. 3.17 we get

$$\rho_{ee}(t_\pi) = \frac{\Omega_0^2}{\Omega_0^2 + \delta^2} \sin^2\left(\sqrt{\Omega_0^2 + \delta^2}\frac{\pi}{2\Omega_0}\right) \tag{3.18}$$

$$= \left(\frac{2}{\pi}\right)^2 \mathrm{sinc}^2(C), \tag{3.19}$$

where $C = \frac{2}{\pi}\frac{\sqrt{\Omega_0^2+\delta^2}}{\Omega_0}$, as plotted as a function of δ/Ω_0 in Fig. 3.1(b) (blue line). We see that the probability to transfer the population to the excited state with a 100% efficiency decreases significantly when moving away from resonance. Also note that the width of the central peak as a function of detuning is proportional to Ω_0.

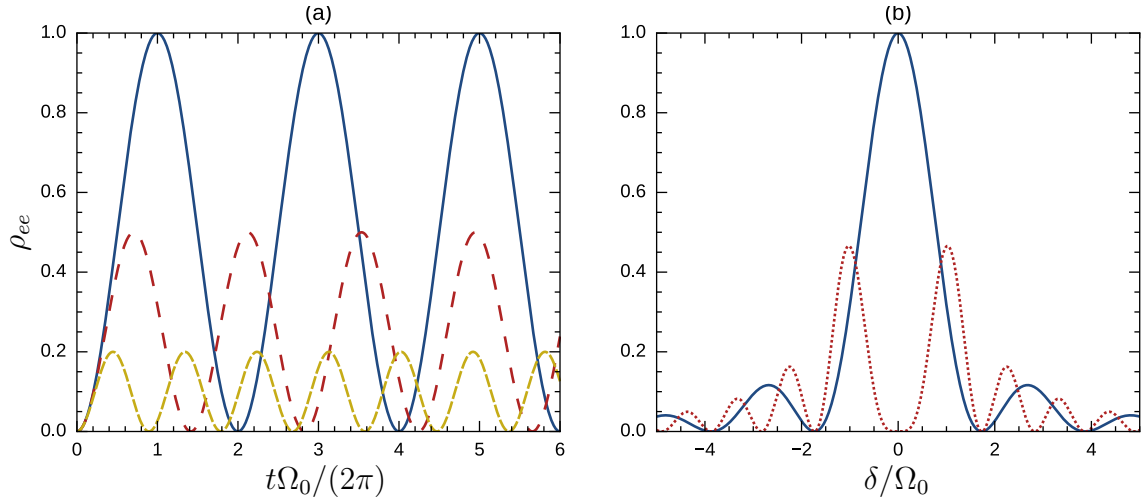

FIGURE 3.1: *Excited state population probability as a function of (a) time and (b) detuning. In (a) rabi oscillations are shown for different detunings. Blue: $\Delta = 0$, red: $\Delta = \Omega_0$, yellow: $\Delta = 2\Omega_0$. (b) shows the excited state population after a π-pulse (blue) and a 2π-pulse (red) when starting in the ground state at $t = 0$. Figure from [82].*

3.1.1 Optical Bloch equations

An essential feature of light-matter interactions is missing in the description given so far, namely spontaneous emission. This feature is not present when considering a classical electromagnetic field as above, but appears naturally in a description where the field is also quantized. Thus the above description is only valid for times much smaller than the lifetime of the excited state $t \ll 1/\Gamma_t$, Γ_t being the transition linewidth, where spontaneous emission can be neglected. However, spontaneous emission can easily be added heuristically to the semi-classical model already presented by means of the density matrix formalism.

The density operator of a given state is written as

$$\hat{\rho} = |\psi\rangle \langle\psi| = \begin{pmatrix} c_g c_g^* & c_g c_e^* \\ c_e c_g^* & c_e c_e^* \end{pmatrix} = \begin{pmatrix} \rho_{gg} & \rho_{ge} \\ \rho_{eg} & \rho_{ee} \end{pmatrix}, \tag{3.20}$$

where ρ_{gg} (ρ_{ee}) is the probability of the state $|\psi\rangle$ collapsing into the ground state $|g\rangle$ (the excited state $|e\rangle$) upon a measurement of it. The off-diagonal matrix elements ρ_{ge} and ρ_{eg}, the so-called coherences, are a measure of the relative phase between $|g\rangle$ and $|e\rangle$. The time evolution of the density operator, and thereby the state, is governed by the Hamiltonian of the system and is given by the Liouville von Neuman equation

$$\frac{d\rho}{dt} = \frac{i}{\hbar}[\hat{\rho}, \hat{H}], \tag{3.21}$$

which is equivalent to the time-dependent Schrödinger equation. By inserting $\hat{H}$ from Eq. 3.16 and applying the dipole and rotating wave approximations as earlier we obtain coupled rate equations for the population probabilities and coherences written as

$$\begin{aligned} \dot{\rho}_{gg} &= -\frac{i}{2}(\Omega_0 \rho_{ge} - \Omega_0^* \rho_{e,g}) \\ \dot{\rho}_{ee} &= \frac{i}{2}(\Omega_0 \rho_{ge} - \Omega_0^* \rho_{eg}) \\ \dot{\rho}_{ge} &= i\Delta\rho_{ge} - \frac{i\Omega_0^*}{2}(\rho_{gg} - \rho_{ee}) \\ \dot{\rho}_{eg} &= -i\Delta\rho_{eg} + \frac{i\Omega_0}{2}(\rho_{gg} - \rho_{ee}). \end{aligned} \tag{3.22}$$

Now for ρ_{gg} (ρ_{ee}) the spontaneous emission from $|e\rangle$ to $|g\rangle$ with the rate Γ_t can simply be added to the rate equations as an extra gain (loss) term given by

$$(\dot{\rho}_{gg})_{\text{spon}} = -(\dot{\rho}_{ee})_{\text{spon}} = \Gamma_t \rho_{ee}. \tag{3.23}$$

The effect on the coherences is less intuitive and given by

$$(\dot{\rho}_{ge})_{\text{spon}} = -(\gamma_c + \frac{\Gamma_t}{2})\rho_{ge} \quad \text{and} \quad (\dot{\rho}_{eg})_{\text{spon}} = (\gamma_c + \frac{\Gamma_t}{2})\rho_{eg}, \tag{3.24}$$

where γ_c is the loss rate due to other coherent events (where the population stays within the two levels considered) like soft collisions or fluctuations in ω_L. Eq.s 3.22 with the extra terms of Eq.s 3.23 and 3.24 are called the optical Bloch equations. For zero detuning the optical Bloch equations can be solved exactly. For initial conditions

$\rho_{ee} = 0$ and $\rho_{ge} = 0$ and $\gamma_c = 0$ this gives ([85] p. 66)

$$\rho_{ee}(t, \delta = 0) = \frac{|\Omega_0|^2}{\Gamma_t^2 + 2|\Omega_0|^2} \left[1 - \left(\cos(C't) + \frac{3\Gamma_t}{4C'} \sin(C't) \right) e^{-3\Gamma_t t/4} \right], \tag{3.25}$$

where $C' = \sqrt{|\Omega_0|^2 - (\Gamma_t/4)^2}$. For arbitrary detunings they must instead be solved numerically.

Without spontaneous emission the excited state population probability will oscillate back and forth between zero and one forever as plotted in Fig. 3.1(a). The effect of spontaneous emission is that the system after interaction times much longer than $1/\Gamma_t$ will settle into a steady state, where the level populations are constant. The steady state solution for arbitrary light intensities and detunings and $\gamma_c = 0$ is given by

$$\rho_{ee,ss} = \frac{\frac{\Omega_0^2}{4}}{\delta^2 + \frac{\Gamma_t^2}{4} + \frac{\Omega_0^2}{2}}. \tag{3.26}$$

When the detuning is zero we get

$$\begin{aligned} \rho_{ee,ss}(\delta = 0) &= \frac{1/2}{\Gamma_t^2/(2\Omega_0^2) + 1} \\ &= \frac{1/2}{I_{sat}/I_L + 1}. \end{aligned} \tag{3.27}$$

From this we see that the excited state steady state value on resonance is determined by the ratio

$$s = \frac{I_L}{I_{sat}} = \frac{2\Omega_0^2}{\Gamma_t^2}. \tag{3.28}$$

where I_L is the intensity of the light field at the atom and I_{sat} is the so-called saturation intensity defined as ([86] p. 142)

$$I_{sat} = \frac{\hbar \omega_t^3 \Gamma_t}{12\pi c^2}. \tag{3.29}$$

For this definition, when the light intensity equals the saturation intensity, $I = I_{sat}$, we see from Eq. 3.27 that the excited state population probability $\rho_{ee,ss}(\delta = 0) = 1/4$. Other definitions of I_{sat} exist. At very high intensities, $\rho_{ee,ss}$ saturates to 1/2 for any detuning. This results in a broadening of the observed transition peak, a phenomenon called power broadening.

3.1.2 Einstein rate equations

Before the invention of lasers the idea of a coherent and effectively monochromatic light source with a spectral linewidth much smaller than the transition linewidth, was unheard of. Hence Einstein originally imagined an atom with levels $|g\rangle$ and $|e\rangle$, with degeneracies g_g and g_e, respectively, interacting with black-body radiation with energy spectral density described by Planck's distribution law

$$\rho(\omega) = \frac{\hbar\omega^3}{\pi^2 c^3} \frac{1}{e^{\hbar\omega/k_B T} - 1}. \tag{3.30}$$

It is assumed that the atom will only interact strongly with the part of the distribution close to resonance with the transition, namely $\rho(\omega_t)$. The interaction causes a symmetric change in the level populations through absorption and stimulated emission proportional to $\rho(\omega_t)$ with proportionality constants B_{ge} and B_{eg}, respectively. I.e. the rates of absorption and stimulated emission are

$$\begin{aligned} R_{abs}(\omega_t) &= B_{ge}\rho(\omega_t) \\ R_{stim}(\omega_t) &= B_{eg}\rho(\omega_t) \end{aligned}. \tag{3.31}$$

Additionally, the atom decays from the excited state to the ground state via spontaneous emission with a rate A_{eg} independent of the external light source

$$R_{spon}(\omega_t) = A_{eg}. \tag{3.32}$$

B_{ge}, B_{eg} and A_{eg} are called the Einstein coefficients.

In this model we denote the population probability of the two levels as $P_{|g\rangle}$ and $P_{|e\rangle}$ instead of ρ_{gg} and ρ_{ee} as in the optical Bloch equations, to underline the fact that Einstein's rate equations do not contain coherence terms ρ_{ge} and ρ_{eg}.

The time development for the populations of the two levels can be described by the rate equations ([86] p. 12)

$$\begin{aligned} \frac{dP_{|e\rangle}}{dt} &= P_{|e\rangle}B_{ge}\rho(\omega_t) - P_{|e\rangle}B_{eg}\rho(\omega_t) - P_{|e\rangle}A_{eg} \\ \frac{dP_{|g\rangle}}{dt} &= -\frac{dP_{|e\rangle}}{dt}. \end{aligned} \tag{3.33}$$

The solution for $g_e = g_g$ with initial conditions $P_{|g\rangle} = 1$ and $P_{|e\rangle} = 0$ is ([85] p. 22)

$$P_{|e\rangle}(t) = \frac{B_{ge}\rho(\omega_t)}{A_{eg} + (B_{ge} + B_{eg})\rho(\omega_t)} \left(1 - e^{-(A_{eg}+(B_{ge}+B_{eg})\rho(\omega_t))t}\right). \tag{3.34}$$

For long times the excited state population reaches its steady state value of

$$P_{|e\rangle,ss} = \frac{B_{ge}\rho(\omega_t)}{A_{eg} + (B_{ge} + B_{eg})\rho(\omega_t)}. \tag{3.35}$$

If we assume the states to be non-degenerate, $B_{ge} = B_{eg} = B$, and this reduces to

$$P_{|e\rangle,ss} = \frac{1}{\frac{A_{eg}}{B\rho(\omega_t)} + 2}. \tag{3.36}$$

We see that when $B \gg A_{eg}$, i.e. for strong interaction, we obtain the same optimum steady state value of $1/2$ as for the optical Bloch equations.

At steady state we also have $\frac{dP_{|e\rangle}}{dt} = \frac{dP_{|g\rangle}}{dt} = 0$ and from Eq. 3.33 we obtain

$$\rho(\omega_t) = \frac{A_{eg}}{B_{ge}} \frac{1}{(P_{|g\rangle}/P_{|e\rangle})(B_{ge}/B_{eg}) - 1}. \tag{3.37}$$

At thermal equilibrium the level populations are related by Boltzmann's law ([87] p. 249)

$$P_{|g\rangle}/P_{|e\rangle} = (g_g/g_e)e^{\hbar\omega/k_BT}. \tag{3.38}$$

Combining Eq.s 3.30, 3.37 and 3.38 and equating the parts that contain $e^{\hbar\omega/k_BT}$ and the ones that do not separately, since the equation holds for all T, gives

$$A_{eg} = \frac{\hbar\omega_t^3}{\pi^2 c^3} B_{eg} \tag{3.39}$$

$$B_{ge} = \frac{g_e}{g_g} B_{eg} \tag{3.40}$$

These relations between the Einstein coefficients hold for all types of radiation, also narrow bandwidth radiation from a laser ([86] p. 13).

3.1.3 Expressions for the Einstein coefficients

From the semi-classical treatment of light interacting with a two-level atom, we can find expressions for the Einstein coefficients. In the semi-classical case we considered

monochromatic radiation, but to relate to the Einstein theory we now consider a slice with frequency $\omega + \mathrm{d}\omega$ of a broadband field with energy density $\rho(\omega)$. The amplitude of the field at ω is $E_0(\omega)$ and the energy per unit volume is $\rho(\omega)\,\mathrm{d}\omega = I(\omega)/c = \epsilon_0 E_0^2(\omega)/2$. For this field interval the Rabi frequency defined in Eq. 3.9 can be written as ([86] p. 126)

$$|\Omega_0|^2 = \left|\frac{eE_0}{\hbar}\langle g|\, z\,|e\rangle\cos(\theta)\right|^2 = \frac{e^2|\,\langle g|\, z\,|e\rangle\cos(\theta)|^2}{\hbar^2}\frac{2\rho(\omega)\mathrm{d}\omega}{\epsilon_0}, \tag{3.41}$$

where $\cos(\theta) = \hat{\epsilon}\cdot\hat{z}$ expresses the angle between the electric field polarization and the dipole, and z is the length of the dipole. This form of the Rabi frequency is inserted into the semi-classical expression for ρ_{ee} for a weak field from of Eq. 3.13. To calculate the effect of a broadband field we must now integrate this expression over a broad range of ω. If we assume long interaction times the sinc peak becomes narrow and we can take the smooth function $\rho(\omega_t)$ outside the integral and find the steady state absorption rate as

$$R_{ge,ss} = \frac{\rho_{ee}}{t} \approx \frac{e^2|\,\langle g|\, z\,|e\rangle\cos(\theta)|^2}{\hbar^2}\frac{2\rho(\omega_t)}{\epsilon_0}\frac{\pi}{2}. \tag{3.42}$$

In Einstein's rate equations the absorption rate is given as $B_{ge}\rho(\omega_t)$. Comparing this expression to the above gives

$$B_{ge} = \frac{e^2\pi|\,\langle g|\, z\,|e\rangle\cos(\theta)|^2}{\hbar^2\epsilon_0} \tag{3.43}$$

from which we also obtain the relation

$$B_{ge} = \frac{\pi|\Omega_0|^2}{\epsilon_0 E_0^2} = \frac{\pi c|\Omega_0|^2}{2I_L}. \tag{3.44}$$

Since the Einstein coefficients are related through Eq.s 3.39 we also obtain

$$A_{eg} = \frac{g_1}{g_2}\frac{\omega_t^3 e^2}{\hbar\pi\epsilon_0 c^3}|\,\langle g|\, z\,|e\rangle\cos(\theta)|^2. \tag{3.45}$$

Typically the A_{eg} value describes the spontaneous decay rate to all lower sublevels (m_J or m_F) such that the resulting decay pattern is spherically symmetric. The decay rate is the same from each individual upper sublevel. Hence an average over

all angles must always be made for A_{eg}, such that

$$\cos^2(\theta) \rightarrow \overline{\cos^2(\theta)} = \frac{1}{4\pi}\int_0^{2\pi}\int_0^{\pi}\cos^2(\theta)\sin(\theta)\,d\theta\,d\phi = 1/3. \tag{3.46}$$

giving

$$\Gamma_t = A_{eg} \equiv \frac{1}{3}\frac{g_1}{g_2}\frac{\omega_t^3 e^2}{\hbar\pi\epsilon_0 c^3}|\langle g|\,z\,|e\rangle\,|^2. \tag{3.47}$$

This definition always holds and is completely independent of any applied light field. The same expression is found from a fully quantum mechanical treatment, where spontaneous decay is found to be a result of the atom's interaction with the vacuum modes of the electromagnetic field [88].

However, for the B-coefficients an average over all angles should only be made if the applied light field is unpolarized and randomly propagating, which is not the case in most modern laser experiments. Generally, when the transition can be considered as two-level (without substates) and the light has the right polarization to drive the transition we have $\theta = 0$ resulting in $\cos^2(\theta) = 1$ in the expression for B_{ge} in Eq. 5.5 ([85] p. 51, [86] p. 140). This gives a B-coefficient 3 times higher than what one would obtain for unpolarized and randomly propagating light. Thus only A_{eg} is a fundamental property of the atom whereas B_{ge} and B_{eg} depend on the applied light field.

3.1.4 Einstein rate vs. optical Bloch equations

The coherence terms in the optical Bloch equations express the phase coherence between the two level populations, which, without other decoherence effects, is only interrupted by spontaneous emission. In the Einstein rate equations such terms are not present. However we saw in Eq. 3.27 (for zero detuning) and Eq. 3.36 that the two models give the same maximal steady state excited state population probability of 1/2, as expected.

In order to compare the results of the Einstein rate equations and the optical Bloch equations in more detail, we must calculate $\rho(\omega_t, \omega_L)$ which is the effective spectral energy density at the transition frequency ω_t due to a laser line centered around ω_L, and not due to a black-body field as originally considered by Einstein.

Generally, we can write $\rho(\omega_t, \omega_L)$ as

$$\rho(\omega_t, \omega_L) = \frac{I_L}{c} \int_{-\infty}^{\infty} L_t(\omega', \omega_t) L_L(\omega', \omega_L)\, d\omega', \tag{3.48}$$

where $L_t(\omega, \omega_t)$ and $L_L(\omega, \omega_L)$ represent the lineshape functions for the two-level transition and the laser field, respectively. Without other broadening mechanisms than spontaneous emission the transition has a Lorentzian lineshape governed by the natural decay rate Γ_t written as

$$L_t(\omega, \omega_t) = \frac{1}{\pi} \frac{\Gamma_t/2}{(\omega - \omega_t)^2 + \Gamma_t^2/4}. \tag{3.49}$$

For a laser linewidth much smaller than the transition linewidth, $\Gamma_L \ll \Gamma_t$, $\rho(\omega_t, \omega_L)$ reduces to

$$\rho^t(\omega_t, \omega_L) = \frac{I_L}{c} L_t(\omega_L, \omega_t) \tag{3.50}$$

and for a laser linewidth much larger than the transition linewidth , $\Gamma_L \gg \Gamma_t$, it reduces to

$$\rho^L(\omega_t, \omega_L) = \frac{I_L}{c} L_L(\omega_t, \omega_L). \tag{3.51}$$

In the optical Bloch equations we assumed the light field to be monochromatic, corresponding to Eq. 3.50. On resonance this gives

$$\rho^t(\omega_t, \omega_t) = \frac{I_L}{c} \frac{2}{\pi \Gamma_t} \tag{3.52}$$

Inserting this into the steady state Einstein rate equation solution Eq. 3.36 and using Eq. 3.44, we retrieve the steady state solution on resonance to the optical Bloch equations Eq. 3.27. So the steady state solutions are the same for the two models for arbitrary light intensities.

But how much do the solutions differ before the populations reach steady state? This is best illustrated by plotting the solutions together, which is done in Fig. 3.2. Here we see the excited state population as a function of $\Omega_0 t/(2\pi)$ for different Ω_0/Γ_t. For the same atom this corresponds to different light intensities. The solid curves represent the optical Bloch equations, and the dashed curves represent the Einstein rate equations. For $\Gamma_t = 0$ the optical Bloch equations give the former mentioned Rabi flopping behavior, while larger Γ_t (or smaller Ω_0) results in less flopping and

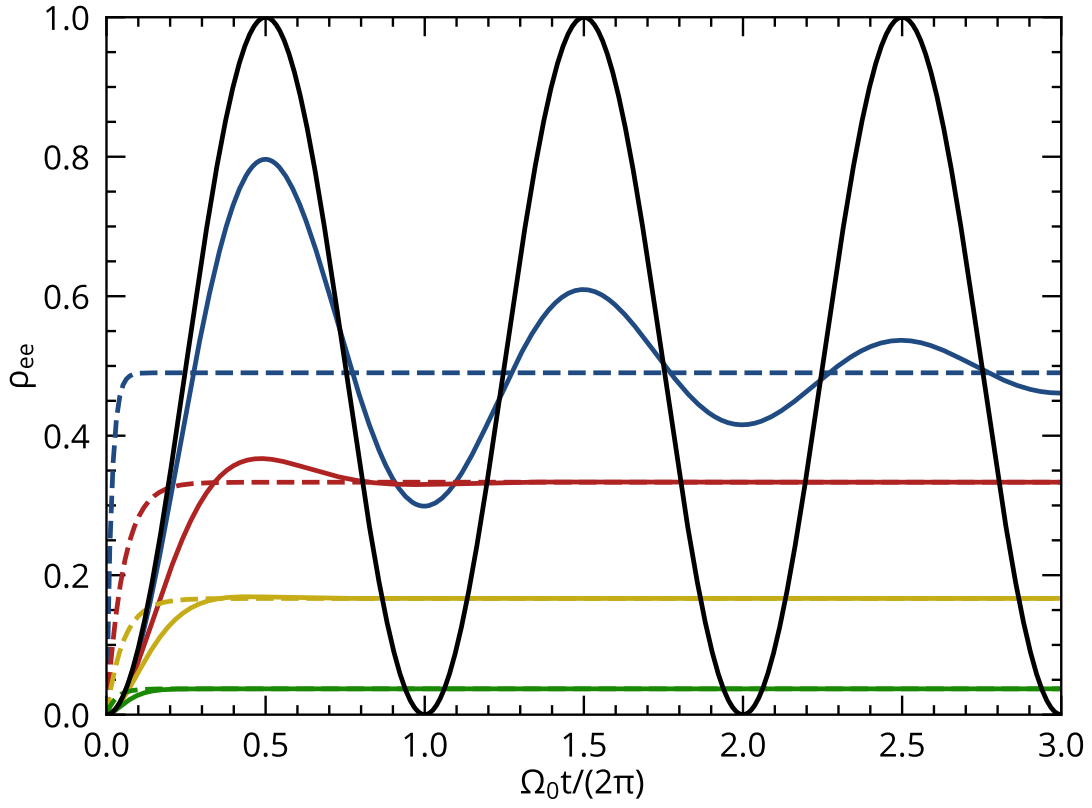

FIGURE 3.2: *Solutions to the optical Bloch equations (solid lines) and the the Einstein rate equations (dashed lines) for monochromatic radiation on resonance for* $\Omega_t/\Gamma_t = 5$ *(blue), 1 (red), 1/2 (yellow) and 1/5 (green). The black curve is the solutions to the optical Bloch equations for* $\Gamma_t = 0$.

a lower steady state value. The Einstein rate equation solutions reach the same steady state values as expected, but faster than the optical Bloch equation solutions and without any flopping. We also see that for $\Omega_0 t \ll 1$ all the solid curves have a quadratic behavior, which is also easily seen from Eq. 3.13, in contrast to the linear behavior for the Einstein rate equations.

The time to reach steady state is similar for all Ω_0/Γ_t for the Einstein solutions, while the optical Bloch solutions reach steady state faster the more spontaneous emission dominates. Thus for small Ω_0/Γ_t and $t \gg 1/\Omega_0$ the two models agree.

3.2 Two trapped ions

Since the main subject of this thesis is PRS, it is not sufficient to understand the interaction between light and a single atom in free space. In this section we thus consider the coherent interaction between a light field and two ions co-trapped in

a harmonic potential. We consider the situation where two ions, for later reference called the target and the readout ion, are both confined along the z-axis thanks to suitably high trapping frequencies in the perpendicular plane. We assume that both ions have an internal two level structure, with states $\{|g_j\rangle, |e_j\rangle\}$ where $j \in \{r, t\}$ referring to the readout and target ion, respectively, leading to the internal state Hamiltonians

$$\hat{H}_j = \frac{\hbar\omega_j}{2}\left(|e_j\rangle\langle e_j| - |g_j\rangle\langle g_j|\right) \tag{3.53}$$

with $\hbar\omega_j = E_{e,j} - E_{g,j}$, where $E_{g,j}$ and $E_{e,j}$ are the energies of the two states. In addition to the two ions' internal states, the external motional states of the two-ion system along the z-axis can be described by the following Hamiltonian

$$\hat{H}_z = \hbar\omega_{ip}\left(\hat{a}_{ip}^\dagger\hat{a}_{ip} + \frac{1}{2}\right) + \hbar\omega_{op}\left(\hat{a}_{op}^\dagger\hat{a}_{op} + \frac{1}{2}\right) \tag{3.54}$$

where we have introduced the standard harmonic oscillator ladder operators $\hat{a}_{ip}^\dagger$, $\hat{a}_{ip}$ and $\hat{a}_{op}^\dagger$, $\hat{a}_{op}$ for the IP and OP modes, respectively. Here $\omega_{ip/op}$ are the associated mode angular frequencies, for singly charged ions given in Eq. 2.17.

Essential for both PRS and resolved sideband cooling is the Hamiltonian describing the light induced interaction between the internal and external degrees of freedom of the ions. We assume here that the light field can be approximated by a monochromatic plane wave with angular frequency ω_L travelling along the z-axis. Furthermore, we assume that the difference between the two transition angular frequencies ω_t and ω_r is large enough that a light field close to resonance with one of the ions will not perturb the other. In this case, one can write up the Hamiltonian for the light interaction as

$$\hat{H}_{int,j} = \hbar\Omega_{0,j}\cos(k_L\hat{z}_j - \omega_L t)\left(|e_j\rangle\langle g_j| + |g_j\rangle\langle e_j|\right) \tag{3.55}$$

where $\Omega_{0,j}$ is the vacuum Rabi angular frequency associated with the particular light field and oscillator strength and $\vec{k}_L$ is the wave vector of the laser field. The coupling of the ions' internal and external degrees of freedom appears through the position operator $\hat{z}_j$ of the interaction Hamiltonian. This operator can be written for each ion in terms of the ladder operators as [84, 89, 90]

$$\hat{z}_j = |b_{ip,j}|\sqrt{\frac{\hbar}{2m_j\omega_{ip}}}(\hat{a}_{ip}^\dagger + \hat{a}_{ip}) + |b_{op,j}|\sqrt{\frac{\hbar}{2m_j\omega_{op}}}(\hat{a}_{op}^\dagger + \hat{a}_{op}) \tag{3.56}$$

where $b_{ip,j}$ and $b_{op,j}$ are the components of the eigenvectors (in a mass-weighted space) for the IP and OP modes, respectively, given in Eq.s 2.15 and 2.16.

Now we introduce the Lamb-Dicke parameters (LDPs) [81]

$$\begin{aligned}\eta_{ip,j} &= \vec{k}_L \cdot \vec{e}_z |b_{ip,j}| \sqrt{\frac{\hbar}{2m_j\omega_{ip}}} \\ \eta_{op,j} &= \vec{k}_L \cdot \vec{e}_z |b_{op,j}| \sqrt{\frac{\hbar}{2m_j\omega_{op}}},\end{aligned} \tag{3.57}$$

where $\vec{e}_z$ is a unit vector along z. They express the ratio of the extent of the ground state wavefunction of the ion in each mode over the wavelength of the interacting light, but also the ratio of the recoil energy imposed on the ion to the trap level spacing. In simple words the LPDs are a measure of how easily the motional state can be changed upon absorption and emission of a photon.

Using the LPDs we can rewrite the interaction Hamiltonian as

$$\begin{aligned}\hat{H}_{int,j} = \hbar\Omega_{0,j} \cos\big(\eta_{ip,j}(\hat{a}^\dagger_{ip} + \hat{a}_{ip}) + \eta_{op,j}(\hat{a}^\dagger_{op} + \hat{a}_{op}) - \omega_L t\big) \\ \times \big(|e_j\rangle\langle g_j| + |g_j\rangle\langle e_j| \big).\end{aligned} \tag{3.58}$$

The full Hamiltonian is given by

$$\hat{H}_{tot} = \hat{H}_r + \hat{H}_t + \hat{H}_z + \hat{H}_{int,j} \equiv \hat{H}_0 + \hat{H}_{int,j}. \tag{3.59}$$

Here $\hat{H}_{int,j}$ only refers to the ion interacting directly with the light field.

In order to investigate the dynamics of the interaction between the internal and external degrees of freedom, it is convenient to work in the interaction picture through the transformation

$$\hat{H}_I = e^{i\hat{H}_0 t/\hbar} \hat{H}_{int,j} e^{-i\hat{H}_0 t/\hbar} \tag{3.60}$$

which, due to the commutativity between the internal and external state operators, leads to

$$\begin{aligned}\hat{H}_I = \hbar\Omega_{0,j}\Big(e^{i\omega_j t}|e_j\rangle\langle g_j| + e^{-i\omega_j t}|g_j\rangle\langle e_j|\Big) e^{i\hat{H}_z t/\hbar} \\ \times \cos\big(\eta_{ip,j}(\hat{a}^\dagger_{ip} + \hat{a}_{ip}) + \eta_{op,j}(\hat{a}^\dagger_{op} + \hat{a}_{op}) - \omega_L t\big) e^{-i\hat{H}_z t/\hbar}.\end{aligned} \tag{3.61}$$

Performing the rotating wave approximation, i.e. keeping time dependent terms containing $\omega_j - \omega_L$ and not the ones containing $\omega_j + \omega_L$, one arrives at

$$\hat{H}_I = \frac{\hbar}{2}\Omega_{0,j} \left|e_j\right\rangle \left\langle g_j\right| e^{i\hat{H}_z t/\hbar} e^{i(\eta_{ip,j}(\hat{a}_{ip}+\hat{a}_{ip}^\dagger)+\eta_{op,j}(\hat{a}_{op}+\hat{a}_{op}^\dagger)-\delta_j t)} e^{-i\hat{H}_z t/\hbar} + h.c., \tag{3.62}$$

where we have introduced the laser detuning $\delta_j = \omega_L - \omega_j$ from the addressed ion's internal transition. By introducing the time scaled ladder operators

$$\begin{aligned} \tilde{\hat{a}}_{ip} &= \hat{a}_{ip} e^{-i\omega_{ip}t} \quad , \quad \tilde{\hat{a}}_{ip}^\dagger = \hat{a}_{ip}^\dagger e^{i\omega_{ip}t} \\ \tilde{\hat{a}}_{op} &= \hat{a}_{op} e^{-i\omega_{op}t} \quad , \quad \tilde{\hat{a}}_{op}^\dagger = \hat{a}_{op}^\dagger e^{i\omega_{op}t} \end{aligned} \tag{3.63}$$

and using the Baker-Campbell-Haussdorff formula for decomposing the exponential term [91], one can re-express the interaction Hamiltonian as

$$\hat{H}_I = \frac{\hbar\Omega_{0_j}}{2} \left|e_j\right\rangle \left\langle g_j\right| e^{-i\delta_j t} e^{-\eta_{ip,j}^2/2} e^{-\eta_{op,j}^2/2} e^{i\eta_{ip,j}\tilde{\hat{a}}_{ip}^\dagger} e^{i\eta_{ip,j}\tilde{\hat{a}}_{ip}} e^{i\eta_{op,j}\tilde{\hat{a}}_{op}^\dagger} e^{i\eta_{op,j}\tilde{\hat{a}}_{op}} + h.c. \tag{3.64}$$

The specific quantum dynamics now depends on which ion we address with the light field, and can be found by solving the Schrödinger equation of motion Eq. 3.10 in the state-basis of $|i_r, i_t, n_{ip}, n_{op}\rangle$, where $|i_j\rangle$ indicates the internal state $i \in \{g, e\}$ of the ion $j \in \{r, t\}$. In the case where the readout ion is addressed by the light field, we obtain the following interaction matrix elements [92]

$$\begin{aligned} \left\langle e_r, i_t, n'_{ip}, n'_{op}\right| \hat{H}_I \left|g_r, i_t, n_{ip}, n_{op}\right\rangle = \frac{\hbar\Omega_{0,r}}{2} e^{i(s_{ip}\omega_{ip}+s_{op}\omega_{op}-\delta_r)t} e^{-\eta_{ip,r}^2/2} e^{-\eta_{op,r}^2/2} \\ \times \sum_{m_{ip}=0}^{n_{ip}^<} \sum_{m_{op}=0}^{n_{op}^<} \frac{(i\eta_{ip,r})^{2m_{ip}+|s_{ip}|} \sqrt{n_{ip}^<! n_{ip}^>!}}{m_{ip}!(m_{ip}+|s_{ip}|)!(n_{ip}^< - m_{ip})!} \\ \times \frac{(i\eta_{op,r})^{2m_{op}+|s_{op}|} \sqrt{n_{op}^<! n_{op}^>!}}{m_{op}!(m_{op}+|s_{op}|)!(n_{op}^< - m_{op})!} \end{aligned} \tag{3.65}$$

where $s_{ip/op} = n'_{ip/op} - n_{ip/op}$ is the so-called sideband order, and $n_{ip/op}^< = \min\{n_{ip/op}, n'_{ip/op}\}$ and $n_{ip/op}^> = \max\{n_{ip/op}, n'_{ip/op}\}$. In a slightly more compact form, we can rewrite this expression as

$$\begin{aligned} \left\langle e_r, i_t, n'_{ip}, n'_{op}\right| \hat{H}_I \left|g_r, i_t, n_{ip}, n_{op}\right\rangle = \frac{\hbar\Omega_{0,r}}{2} e^{i(s_{ip}\omega_{ip}+s_{op}\omega_{op}-\delta_r)t} \\ \times \xi(\eta_{ip,r}, \eta_{op,r}, n_{ip}, n_{op}, s_{ip}, s_{op}) \end{aligned} \tag{3.66}$$

with

$$\xi(\eta_{ip,r},\eta_{op,r},n_{ip},n_{op},s_{ip},s_{op}) = \left(e^{-\eta_{ip,r}^2/2}(i\eta_{ip,r})^{|s_{ip}|}\sqrt{\frac{n_{ip}^{<}!}{n_{ip}^{>}!}}L_{n_{ip}^{<}}^{|s_{ip}|}(\eta_{ip,r}^2)\right) \times \left(e^{-\eta_{op,r}^2/2}(i\eta_{op,r})^{|s_{op}|}\sqrt{\frac{n_{op}^{<}!}{n_{op}^{>}!}}L_{n_{op}^{<}}^{|s_{op}|}(\eta_{op,r}^2)\right) \tag{3.67}$$

where $L_{n_{ip}^{<}}^{|s_{ip}|}(\eta_{ip,r}^2)$ and $L_{n_{op}^{<}}^{|s_{op}|}(\eta_{op,r}^2)$ are the generalized Laguerre polynomials. One can see from Eq. (3.66) that, for the monochromatic situation considered now, dynamics involving transitions with specific changes in motional quantum numbers can be efficient by tuning the laser field to be resonant with a specific sideband such that

$$s_{ip}\omega_{ip} + s_{op}\omega_{op} - \delta_r = 0. \tag{3.68}$$

In this case the explicit time dependence in the coupling matrix elements vanishes for the particular type of transitions, while the off-resonant coupling terms to other transitions will generally average to zero. In the case where $\delta_r = 0$ meaning $s_{ip} = s_{op} = 0$ we say that we drive the **carrier** transition and the motional state is unchanged after excitation ($n'_{ip} = n_{ip}$, $n'_{op} = n_{op}$). If s_{ip} or s_{op} is different from zero, we drive a sideband transition and couple to a different motional state than the initial such that $n'_{ip} = n_{ip} + s_{ip}$, $n'_{op} = n_{op} + s_{op}$. For this we must tune the light to $\omega_L = \omega_r + s_{ip}\omega_{ip} + s_{op}\omega_{op}$. If s_{ip} or s_{op} is positive we couple to a higher motional state and drive a **blue sideband** transition, and oppositely if s_{ip} or s_{op} is negative, we couple to a lower motional state and drive a **red sideband** transition. Hence the sideband order refers to the number of motional quanta we can change with a complete transfer to the coupling state. It is possible to drive mixed sidebands, also where one is blue and one is red for two modes, respectively.

The strength of the different sideband transitions is given by the Rabi angular frequency, which for a specific sideband and initial motional state is given by [89]

$$\Omega_{n_{ip},n_{op},s_{ip},s_{op}} = \Omega_{0,r}\xi(\eta_{ip,r},\eta_{op,r},n_{ip},n_{op},s_{ip},s_{op}). \tag{3.69}$$

The situation becomes particularly simple in the so-called Lamb-Dicke regime where $\eta_{ip/op,r}\sqrt{2\langle n_{ip/op}\rangle + 1} \ll 1$. In this regime transitions changing the motional state by more than a single quanta are strongly suppressed. In this case, we can simplify Eq.

(3.67) to [89]

$$\xi(\eta_{ip,r},\eta_{op,r},n_{ip},n_{op},s_{ip},s_{op}) = \left(\frac{\eta_{ip,r}^{|s_{ip}|}}{|s_{ip}|!}\sqrt{\frac{n_{ip}^{>}!}{n_{ip}^{<}!}}\right)\left(\frac{\eta_{op,r}^{|s_{op}|}}{|s_{op}|!}\sqrt{\frac{n_{op}^{>}!}{n_{op}^{<}!}}\right) \tag{3.70}$$

for $s_{ip/op} = 0, \pm 1$, and zero otherwise. Thus in this case the coupling to all other sidebands is negligible, which is always true for small $n_{ip/op}$ i.e. when the system is prepared close to the motional ground state. In this regime the first order sideband angular Rabi frequencies are approximately $\Omega_{n_{ip},n_{op},s_{ip}=1,s_{op}=0} = \eta_{ip,r}\sqrt{n_{ip}+1}\Omega_0$ and $\Omega_{n_{ip},n_{op},s_{ip}=-1,s_{op}=0} = \eta_{ip,r}\sqrt{n_{ip}}\Omega_0$, and likewise for the OP mode.

To resolve the sidebands, both the natural linewidth of the addressed transition Γ_j and the spectral linewidth of the light field Γ_L must be much smaller than the motional mode angular frequencies $\omega_{ip/op}$ which correspond to the spacing between sidebands. Another requirement is that $\Omega_0 \ll \omega_{ip/op}$ such that the transition is not broadened to a width similar to the sideband spacing. In the resolved case it is possible to only address a single sideband or the carrier and coherently change the internal state of the addressed ion and the motional state of the two-ion system. If we assume the readout ion is prepared in the internal ground state and in a single motional state $|g_r, i_t, n_{ip}, n_{op}\rangle$, the excited state as a function of light exposure time τ_r when tuned near a resonance (carrier or sideband) will evolve as

$$P_{|e_r\rangle}(\tau_r,\Delta_r) = \frac{\Omega_{n_{ip},n_{op},s_{ip},s_{op}}^2}{\Delta_r^2+\Omega_{n_{ip},n_{op},s_{ip},s_{op}}^2}\sin^2\left(\sqrt{\Delta_r^2+\Omega_{n_{ip},n_{op},s_{ip},s_{op}}^2}\frac{\tau_r}{2}\right) \tag{3.71}$$

if no other sideband is driven. Here $\Delta_r = \omega_L - (\omega_r + s_{ip}\omega_{ip} + s_{op}\omega_{op}) = \delta_r - (s_{ip}\omega_{ip} + s_{op}\omega_{op})$ is the detuning from the sideband in question. This is the same Rabi flopping behavior as we saw for a single atom in free space in Eq. 3.17. Recall from Sec. 3.1.1 that this fully coherent behavior arises because spontaneous emission is not included in the model, i.e. we have neglected that the transition has a linewidth Γ_r. For this to be a good approximation we must have $\Gamma_r \ll \Omega_0$.

Only the readout ion's interaction with the light field is coherent during unresolved sideband PRS, which is why we chose this ion as the exmaple case.

Chapter 4

Ion cooling

The basic idea of laser cooling, is to exploit the fact that photons carry momentum, which they transfer to atoms upon absorption. If the momentum kicks from many absorption and emission events on average is slowing down the motion of the atom, the atom will effectively be cooled.

In the experiments presented in this thesis, two types of laser cooling are used to cool down trapped ions: Doppler cooling and resolved sideband cooling. The main difference between the techniques is the linewidth of the addressed electronic transition, Γ, relative to the motional level spacings ω_{ip} and ω_{op}.

For Doppler cooling the sidebands are unresolved since $\Gamma \gg \omega_{ip/op}$ and the process is well-described by a semi-classical model. For sideband cooling the sidebands are resolved $\Gamma \ll \omega_{ip/op}$ and the quantum mechanical nature of the ion's motion must be taken into account.

Prior to laser cooling the ion temperature equals that of the hot ovens corresponding to kinetic energies of about 0.05 eV. From this energy the ions are first cooled to the mK Doppler cooling limit, and subsequently close to the motional ground state by means of sideband cooling.

The linewidth of a transition expresses its decay rate from the upper level to the ground state, and hence how often it can absorb a new photon. Many photons can thus be scattered in a short time from broad transitions. This is exploited in Doppler cooling, which cools the ions fast relative to sideband cooling. This is why sideband cooling is only applied after the Doppler cooling limit has been reached.

The theory of light-matter interactions presented in the former Chapter 3 form the basis for the following description of laser cooling.

4.1 Doppler cooling

Doppler cooling was first proposed by Hänsch and Schawlow in 1975 [4] and was first experimentally realized in ions traps by Wineland et. al. [5] and Neuhasuer et. al.

[93] in 1978. Before Doppler cooling all other cooling techniques were limited by the temperature of liquid helium (temperatures of a few kelvin).

4.1.1 Unconfined species

Since $\Gamma \gg \omega_{ip/op}$ for Doppler cooling, a scattering event can be considered to happen instantaneously in the atom's frame. Hence we can assume the velocity of the atom to be constant during photon absorption. For now we assume the wave vector of the photon to be parallel with the atom velocity $\vec{k_L} \| \vec{v}$ and only consider cooling in one dimension.

The average force exerted on the atom from many scattered photons can thus be written as a momentum change $\Delta p = \hbar k$ times the scattering rate

$$\frac{dp}{dt} \approx F = \hbar k_L \Gamma \rho_{ee}, \tag{4.1}$$

where ρ_{ee} is the population probability of the excited state, which is dependent on the detuning between the transition and photon wavelength. The detuning is dependent on the ion velocity $\vec{v}$ through the Doppler effect. As seen in the atom frame, the effective detuning is

$$\delta_{\text{eff}} \simeq \delta - \vec{k_L} \cdot \vec{v}, \tag{4.2}$$

where $\delta = \omega_L - \omega$ is the detuning for a stationary atom.

To take the Doppler effect into account, δ must be replaced by δ_{eff} in the expression for $\rho_{ee,ss}$ (Eq. 3.26) leading to an average force

$$F = \hbar k \Gamma \rho_{ee,ss} = \frac{\frac{s}{2}}{1 + s + \left(\frac{2(\delta - kv)}{\Gamma}\right)^2}. \tag{4.3}$$

This expression can be expanded to first order in v giving $F \simeq F_0 + \beta v$, where F_0 is a constant force and β is a frictional coefficient. This is a good approximation close to the Doppler cooling limit where v is small. The coefficient β is proportional to δ, so for $\delta < 0$ (i.e. red detuning) $\beta < 0$ and the atom motion is dampened by the light force. Hence for Doppler cooling the light must be red detuned relative to the addressed electronic transition to work.

To also slow down the atom motion in the opposite direction, on must apply another anti-propagating laser beam. If the atom is untrapped, two more pairs of

anti-propagating laser beams perpendicular to the first one and to each other must be applied to target the two other dimensions.

4.1.2 Trapped ions

If the atom is trapped in a spherically symmetric potential only three perpendicular laser beams are necessary. Because the trapping potential of a linear Paul trap is cylindrically symmetric all three dimensions can be cooled with only two laser beams. The circular symmetry of the radial plane, however, will never be perfect simply due to minor construction defects, but the asymmetry can be enhanced by applying an offset DC voltage to a pair of diagonal electrode rods. Then the twofold degeneracy of the radial modes, which are usually considered as one single mode, becomes visible. In this case it is possible to cool all degrees of freedom with a single laser beam, as long as it has an angle to the trap axis, since the radial modes will be coupled.

The average kinetic energy of the ion after Doppler cooling is minimized for isotropic radiation with a 45° projection onto all three axes and a detuning of $\delta_{\min} = -\frac{\Gamma\sqrt{1+s}}{2}$. This leads to a minimum temperature obtainable with Doppler cooling of [94]

$$T_D = \frac{\hbar\Gamma}{2k_B}. \tag{4.4}$$

This minimum temperature is above zero since there is a lower limit to how well-determined the atom's momentum can be due to the randomness of the emission process. T_D is typically on the order of $\sim 0.1 - 1$ mK for atomic ions.

4.1.3 Using $^{40}Ca^{+}$ as the cooling ion

The Doppler cooling scheme for $^{40}Ca^{+}$ is shown in Fig. 4.1. The transition used is the dipole-allowed $^2S_{1/2} \rightarrow {}^2P_{1/2}$ of 397 nm with linewidth $\Gamma_{397} = 2\pi \times 21.57(15)$ MHz [96], which is much larger than the trap level frequencies (see Table 6.1), as required for Doppler cooling. The scattered light from this transition is used to detect a fluorescence signal on the CCD camera above the trap. However, the $^2S_{1/2} \rightarrow {}^2P_{1/2}$ transition is not closed, since decay to the $^2D_{3/2}$ level happens with a branching ratio of 0.06. This is problematic since $^2D_{3/2}$ has a very long lifetime of 1.2 s compared to the short lifetime of the $^2P_{1/2}$ of only 6.9 ns [97]. While the ion is shelved in the $^2D_{3/2}$ state it can be neither cooled nor detected. Therefore it is necessary to apply a laser light of 866 nm to pump the population in $^2D_{3/2}$ back into $^2P_{1/2}$ from where

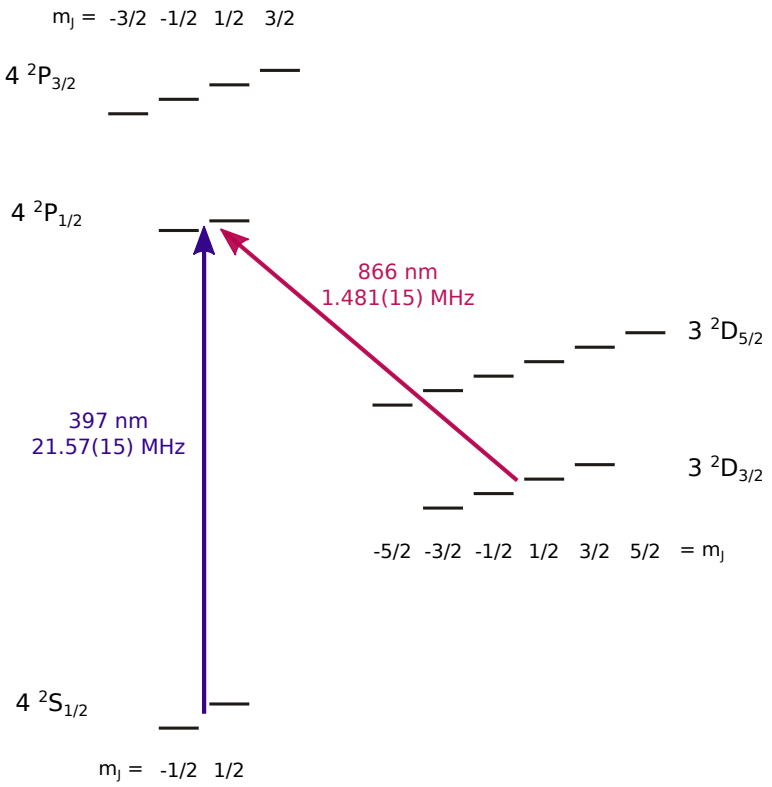

FIGURE 4.1: *Doppler cooling sceme for* $^{40}Ca^{+}$. *Two beams of 397 nm and 866 nm are required to close the cooling cycle. The frequencies give the linewidths* $\Gamma/2\pi$ *of the transitions. Fig. from [95].*

it can decay to the ground state. The 866 nm laser polarization makes a 45° angle with the B-field in order to address all m_J-levels of the $^2D_{3/2}$ state.

Due to the applied magnetic field the $^2S_{1/2}$ and $^2P_{1/2}$ levels both split into two sublevels with $m_J = \pm\frac{1}{2}$ which are separated by 18.2 MHz and 6.1 MHz, respectively. With σ-polarized (mixture of σ^+ and σ^-) 397 nm light we can drive transitions such that $\Delta m_j = \pm 1$. That is, the transition of highest frequency and the transition of lowest frequency out of the four possible. The difference between them is 24.4 MHz which is broader than the transition linewidth. The two transitions where $\Delta m_j = 0$, which can be driven by π-polarized light[1] only have a difference of 12 MHz. To keep the transition as narrow as possible we hence use π-polarized 397 nm light.

In our setup the 397 nm Doppler cooling beam propagates with a 45° degree angle to all trap axes in order to cool in all 3 dimensions. The resulting theoretical Doppler limit temperature of a single ion when using a detuning of $\delta_{\min}$ is $T_D = 0.75$ mK when considering the Zeeman broadened width of the 397 nm transition [94]. This value also matches the Doppler cooling temperature obtained in everyday experiments [82].

[1]Light traveling perpendicularly to the B-field axis is σ-polarized (π-polarized) if the polarization is perpendicular (parallel) to the B-field.

4.2 Sideband cooling

In order to cool the two-ion motion below the Doppler cooling limit the sideband cooling (SBC) technique [3, 98] is used. Here, the motional sidebands must be resolved, which requires $\Gamma_L, \Gamma_r, \Omega_0 \ll \omega_{ip}, \omega_{op}$.[2] The principle of sideband cooling is to drive a red sideband (RSB) transition, which is then followed by spontaneous decay, most likely via the carrier transition if in the Lamb-Dicke regime. This is illustrated in Fig. 4.2 for a single mode. In this way the motional state can be changed from e.g. $|n_{ip}, n_{op}\rangle$ to $|n_{ip}, n_{op} - 1\rangle$, and likewise for the IP mode, from where the procedure can be repeated until the motional ground state is reached.

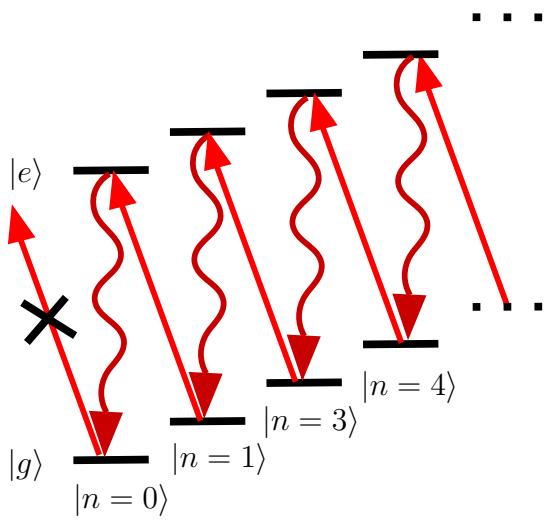

FIGURE 4.2: *Graphical representation of the principle of sideband cooling. When driving a RSB, population is moved from $|g, n\rangle$ to $|e, n - 1\rangle$. After spontanous decay to $|g, n - 1\rangle$ the process can be repeated until the motional ground state is reached. Here the RSB no longer exist as indicated by the black cross. Figure from [95].*

The probability of transfer to $|e\rangle$ is a maximum when the duration and intensity of the laser pulse corresponds to a π-pulse. However, the coupling strength depends on the specific motional state of the ion, which is unknown. We only know that after Doppler cooling the population of each mode is thermally distributed with average motional numbers $\bar{n}_{ip}$ and $\bar{n}_{op}$. For each realization of the experiment, the system can only be in one particular motional state. This means, that what is a multiple of a π-pulse in one experiment, resulting in perfect transfer, can potentially be a multiple of a 2π-pulse for the next experiment, resulting in no transfer.

This is also the reason why one has to wait for a spontaneous decay to happen, instead of using a blue sideband (BSB) to drive population down from $|e, n\rangle$ to

[2] We now call the linewidth of the transition Γ_r to match later notation.

$|g, n-1\rangle$, since there is a risk to instead drive the transition $|g, n\rangle$ to $|e, n+1\rangle$, which results in heating.

On the contrary, if one only addresses the RSB, it will be impossible to accidentally drive population out of $n = 0$, because no RSB exists for the motional ground state. Also, due to spontaneous emission, the probability to find the ion in the electronic ground state is higher than finding it in the excited state. Thus, if one drives a RSB from the electronic ground state one either cools or stays in the same n-state. If one drives a BSB from the electronic ground state one either heats or cools. Thus only by driving a RSB, can we have cooling on average.

In order to cool the ion from every possible n of the thermal distribution, it is necessary in addition to the 1st RSB, to drive RSBs of higher orders. This is due to the fact that the coupling strength for some combinations of motional state and sideband order is zero. To help the reader this is illustrated for a singly trapped $^{40}Ca^{+}$ ion in Fig. 4.3. A similar figure for the more relevant, but also more complex,

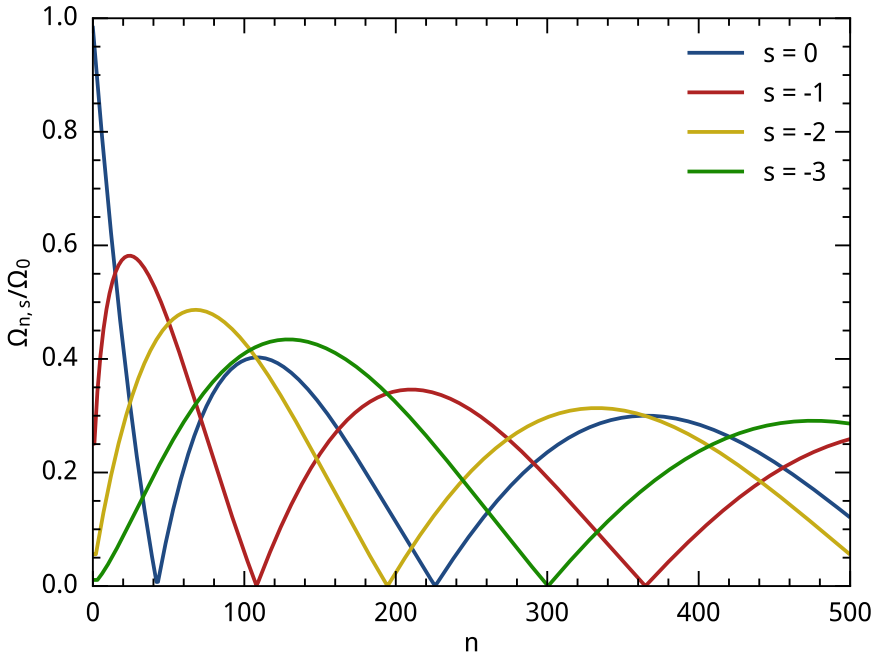

FIGURE 4.3: *Plot of Rabi frequencies divided by the vacuum Rabi frequency for the carrier and first 3 red sidebands as a function of the motional quantum number n for $\eta = 0.1834$ corresponding to light of 729 nm at $\omega_z = 279.1$ kHz. Fig. from [95].*

case of a $^{40}Ca^{+}$-$^{24}Mg^{+}$ ion pair is given in Fig. E.1 of the appendix. In such a case it is impossible to transfer population on this sideband, independent of the pulse length and intensity. Fortunately the coupling strength is never zero for all sideband orders

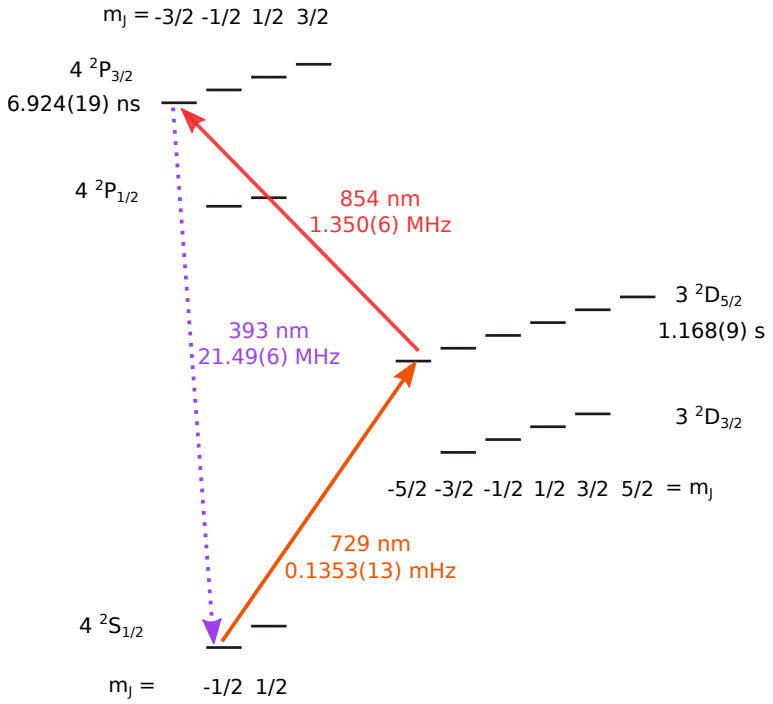

FIGURE 4.4: *Lasers and specific electronic levels in $^{40}Ca^{+}$ used for sideband cooling. The sidebands are driven with the 729 nm laser, and the population is pumped back to the ground state with the 854 nm laser, from where the process can be repeated. Fig. from [95].*

at the same time, such that it always will be possible to choose a RSB order that is not zero for the given n.

The theoretical SBC limit along the z-axis without any external heating can be expressed as the remaining harmonic oscillator energy

$$E(\bar{n}_{ip/op}) = \hbar\omega_{ip/op}\left(\left(\frac{\Gamma_r/2}{\omega_{ip/op}}\right)^2\left(1+\frac{\gamma}{4}\right)+\frac{1}{2}\right), \tag{4.5}$$

where γ is a constant describing the spontaneous emission probability along the z-axis [94, 99]. Since usually $\omega_{ip/op} \gg \Gamma_r$ the ground state energy dominates. The ion is thus very often in the absolute motional ground state after sideband cooling, if it is optimized.

4.2.1 Using $^{40}Ca^{+}$ as the cooling ion

The electronic levels of $^{40}Ca^{+}$ used for SBC are depicted in Fig. 4.4. The transition used for coherent population transfer is the dipole-forbidden quadropole transition $^2S_{1/2}$, $m_J = -1/2 \leftrightarrow {}^2D_{5/2}$ $m_J = -5/2$ of 729 nm. The condition of $\Gamma_r \ll \omega_{ip}, \omega_{op}$ is easily satisfied since $\Gamma_r = 0.1353(13)$ mHz due to the long 1.168(9) s lifetime of the

$^2D_{5/2}$ level. Thus to speed up the cooling the $^2D_{5/2}$ state is coupled to the $^2P_{3/2}$ state (with a lifetime of 6.924(19) ns [97]) by the 854 nm laser, from where it immediately decays to the ground state.

4.2.1.1 Internal state initialization of $^{40}Ca^+$

After Doppler cooling $^{40}Ca^+$ is in a mixture of $^2S_{1/2}$, $m_J = \pm 1/2$, so to prepare the ion for sideband cooling we pump all the population from $m_J = +1/2$ to $m_J = -1/2$ by pumping population out of the $^2S_{1/2}$, $m_J = +1/2$ state to the $^2D_{5/2}$, $m_J = -3/2$ state. From here it can go to $^2P_{3/2}$, $m_J = -1/2$ or $-3/2$. From $^2P_{3/2}$, $m_J = -3/2$ it can only go back to $^2S_{1/2}$, $m_J = -1/2$ where we want it. It can also go back to $^2S_{1/2}$, $m_J = +1/2$ by different decay channels, but since we keep pumping population out of this state, all the population will eventually end up in $m_J = -1/2$.

From $^2D_{5/2}$, $m_J = -5/2$ the only dipole allowed ($\Delta m_J = 1$) transition to $^2P_{3/2}$ is to $m_J = -3/2$. From here the only dipole allowed transition back to $^2S_{1/2}$ is to $m_J = -1/2$. However, the ion can also decay from $^2P_{3/2}$ to $^2D_{3/2}$ and $^2D_{5/2}$ with branching ratios of 0.0587(2) and 0.00661(4), respectively. During SBC the 866 nm and 854 nm lasers repump this population to the $^2S_{1/2}$, but this detour results in population going to both $^2S_{1/2}$, $m_J = -1/2$ and $m_J = +1/2$, giving an unclosed scheme. Hence to have efficient sideband cooling we perform state initialization, called qinit, regularly during the SBC sequence.

4.2.1.2 Pulsed scheme

In the pulsed scheme the 729 nm and 854 nm lasers are not on simultaneously. The 729 nm laser is applied first for a time τ_r in order to coherently drive a RSB, and then the population is pumped back to the electronic ground state with the 854 nm laser, from where the process can be repeated. If we use 729 nm ligth resonat with a given sideband, $\Delta_r = 0$, the probability to end up in the excited state, $^2D_{5/2}$, after a pulse of length τ_r, is from Eq. 4.6 given by

$$P_{|e\rangle}(\tau_r) = \sin^2\left(\Omega_{n_{ip},n_{op},s_{ip},s_{op}}\frac{\tau_r}{2}\right) \tag{4.6}$$

if we neglect off-resonant coupling to other sidebands or the carrier. For a given LDP, if we choose a certain pulse time and intensity (Ω_0) this probability can be plotted as a function of n_{ip}, n_{op}. This plot then provides a picture of how efficiently we can move population from $|n_{ip}, n_{op}\rangle$ to $|n_{ip} + s_{ip}, n_{op} + s_{op}\rangle$ for the given parameters.

Good transfer is not possible for all $|n_{ip}, n_{op}\rangle$ for the same set of parameters, and is even zero for some. These points of zero transfer stems from two different effects.

The first reason is the Rabi flopping behavior of the transfer expressed by $\sin^2$. If the used pulse is an integer times 2π-pulse for the given $|n_{ip}, n_{op}\rangle$, there can be no transfer from this motional state. These zero-crossings can be moved to different $|n_{ip}, n_{op}\rangle$ by changing τ_r or Ω_0 if $\Omega_{n_{ip},n_{op},s_{ip},s_{op}} > 0$.

The second reason for zero transfer is more constant. For some combinations of $|n_{ip}, n_{op}\rangle$ and s_{ip}, s_{op}, $\Omega_{n_{ip},n_{op},s_{ip},s_{op}}$ is simply zero as we saw in Fig. E.1. If $\Omega_{n_{ip},n_{op},s_{ip},s_{op}}$ is zero you can tune τ_r or Ω_0 all you want, the argument of $\sin^2$, and hence the transfer efficiency, will always be zero. This problem can be solved by driving different sidebands, since as also seen in Fig. E.1 the zero points occur for different $|n_{ip}, n_{op}\rangle$ for different sidebands.

After Doppler cooling the ions have an average motional state in each mode of $\bar{n}_{ip/op} \simeq \frac{\Gamma_{397}}{2\omega_{ip/op}}$ given by the Boltzmann distribution.[3] This makes it favorable to operate at a high DC voltage in order to increase $\omega_{ip/op}$, however to have good conditions for PRS $\omega_{ip/op}$ cannot be too large, so in our experiment we must compromise.

For specific initial $\bar{n}_{ip}, \bar{n}_{op}$, it can be calculated how much of the population lies before the first zero-crossing of the 1st RSBs. If this is 100%, we principally only need to use the 1st RSB of each mode to drive all the population to $|n_{ip} = 0, n_{op} = 0\rangle$. Though, if a significant amount lies in higher motional states, application of 2nd order RSB pulses prior to the 1st order pulses are necessary. Once the population has been transferred to lower $|n_{ip}, n_{op}\rangle$ where the 1st order pulses are more efficient, we can switch to this, in order to reach the motional ground state faster. In case the initial $\bar{n}_{ip}, \bar{n}_{op}$ are very large, one needs to apply many sideband orders in succession to address the entire population.

The different sidebands are always driven one at a time starting from the highest applied sideband order. By doing this we 'push the population in front of us' as we gradually go from cooling most efficiently at the highest n's to the lowest n's. In this way the population in the high n-states will be moved to a lower n for every applied sideband. Hence, a high initial temperature after Doppler cooling complicates the SBC process, both because we have to move more quanta to end up near the motional ground state, but also because we have to apply more sideband orders such that the tail of the distribution is not left in the high n-states.

[3]The lower the trap level spacing, the higher the average n's for the same temperature.

As mentioned, the pulses cannot be perfect π-pulses for every $|n_{ip}, n_{op}\rangle$ simultaneously, which is remedied by targeting different n-states for each sideband order (again from high to low) by varying the pulse length and light intensity.

Near the end of sideband cooling almost all the population will be distributed among the lowest couple of motional states. Because the coupling to the carrier is larger than to the 1st RSB for small n, there is a risk that the carrier transition will be driven off-resonantly for too high intensities, since the transfer peak width is proportional to Ω_0 as discussed in relation to Fig. 3.1. This will result in a higher than optimum average steady state, and thus the last steps of SBC must be done at very low intensities to fine-tune the ground state preparation. The pulse time naturally has to be increased accordingly, such that it still corresponds to a π-pulse.

4.2.1.3 Continuous scheme

Instead of applying the 729 nm and 854 nm lasers one at a time, they can also be applied simultaneously. In this case the coupling to the ground state through the 854 nm transition will effectively broaden the 729 nm transition. The effective linewidth is given by

$$\Gamma_{\text{eff}} = \frac{\Omega_{854}^2}{(\Gamma_{393} + \Gamma_{854})^2 + 4\delta_{729}^2}\Gamma_{393}. \tag{4.7}$$

The 854 nm light field also results in an AC Stark shift of the 729 nm transition given by $\delta_{854}\frac{\Gamma_{\text{eff}}}{\Gamma_{397}}$ [100]. Therefore the 729 nm laser must be tuned to the new resonance for optimum transfer efficiency.

The coherent nature of the procedure is no longer important when both lasers are continuously on, and we no longer have to worry about the zero-crossings stemming from $\sin^2$, but still the ones stemming from $\Omega_{n_{ip},n_{op},s_{ip},s_{op}}$. Since we do not have to repump, but can cool continuously, cooling is generally faster when using a continuous scheme.

Thus we start with continuous SBC and follow up with low-intensity pulsed sideband cooling to reach the motional ground state as fast and flawlessly as possible.

4.3 Trap-induced heating

When talking about cooling, one also has to consider uncontrolled heating of the motional modes that will inevitably happen due to a non-perfect lab environment.

These so-called trap-induced heating rates, different for each mode, puts a limit to how cold we can get, and also how long the ions will stay cold after SBC.

As the name suggest trap-induced heating stems from a non-ideal trapping potential resulting in unwanted oscillating electric fields driving the ion motion. The electric field noise will interact differently with the modes of a two-ion system, both due to their different trap level spacings and different eigenvectors.

When the two ions have equal masses, the IP mode has a pure center-of-mass motion (COM), and the OP mode has the same but opposite amplitudes, and is called the breathing mode. If the electric noise is spatially correlated over the two ions (same phase and amplitude), only the COM mode will be excited. To excite the breathing mode, the noise would have to be perfectly anti-correlated (π out of phase on each ion). Because the ion-electrode distance is much larger than the distance between the ions, the noise will most likely be spatially correlated.

When the mass ratio μ changes from 1, the IP and OP modes will become superpositions of the COM and breathing modes, such that both modes can be excited by correlated noise.

If we assume that the electric field noise is spatially correlated and has a white noise spectral density the trap induced heating rate can be written as [101]

$$\frac{R_{H,ip/op}}{R_{H,r}} = \frac{1}{\zeta^{ip/op,r}} \left(b^{ip/op,r} + \frac{b^{ip/op,t}}{\sqrt{\mu}} \right)^2, \tag{4.8}$$

where $\zeta^{ip/op,r} = \omega_{ip/op}/\omega_z$ and ω_z refers to the axial trap frequency if the readout ion were alone in the trap for the same trapping conditions. The eigenvectors $b^{ip/op,i}$ are given in Eq. 2.15. Here $R_{H,r}$ is the trap-induced heating rate of the axial mode, if the readout ion was alone in the trap.

The heating rate of the two axial modes normalized to $R_{H,r}$ are shown in Fig. 4.5a). When the mass ratio is close to one, the heating rate of the IP mode is much larger than for the OP mode, as we expect. As we move away from $\mu = 1$ the hating rate of the OP mode increases. The asymmetry is a result of normalization to the axial frequency of one ion, i.e. the readout ion in this case. The ratio of the IP and OP heating rates is given in Fig. 4.5b). For the $^{40}Ca^+$-$^{24}Mg^+$ system we thus expect a ratio of 12.6, from this model, and 14.6 for the $^{40}Ca^+$-$^{24}MgH^+$ system.

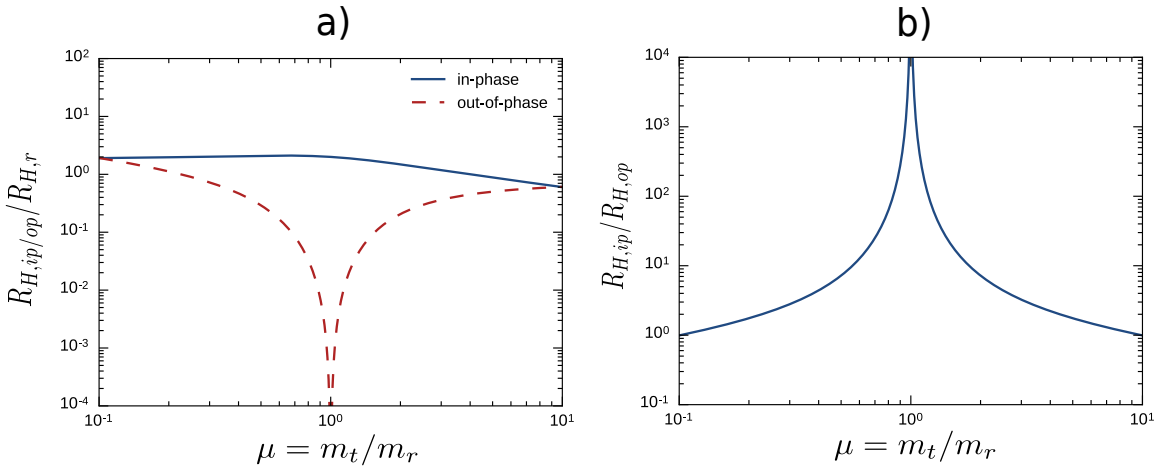

FIGURE 4.5: ***a)*** *Trap-induced heating rates of the IP and OP modes of a two-ion crystal normalized to the heating rate of a single readout ion $R_{H,r}$ as a function of ion mass ratio.* ***b)*** *The ratio between the IP and OP heating rates. A spatially correlated white electric field noise spectral density is assumed. Figures from [82].*

4.4 Temperature evaluation

In connection with ion cooling it is relevant to define what is meant by the temperature of an ion or an ion pair. This concept is quite different from the temperature in the vacuum chamber surrounding the trap, which is at room temperature.

When giving a certain ion temperature, I refer to the population distribution of a specific outer motional mode. Most often I talk about the axial modes with level spacing ω_{ip} and ω_{op}, since these are the ones we are cooling actively in the experiments. After Doppler cooling and at the very end of SBC the population can be assumed to be Boltzmann distributed. An example where this not holds, is if some population is left at some high motional state after SBC due to a $\Omega_{n_{ip},n_{op},s_{ip},s_{op}}$ zero point.

For a Boltzmann distribution the probability of finding the ion in a specific motional state n is given by

$$P_n = \frac{e^{-\frac{E_n}{k_B T}}}{\sum_{i=0}^{\infty} e^{-\frac{E_i}{k_B T}}} \tag{4.9}$$

with $E_n = \left(\frac{1}{2} + n\right)\hbar\omega_z$ being the energy of a harmonic oscillator level. Putting $n = 0$ and solving for T gives

$$T = \frac{-\hbar\omega_z}{k_B \ln(1 - P_0)}. \tag{4.10}$$

In terms of the average motional state $\bar{n}$ the probability to be in a certain motional state can also be written as

$$P_n = \frac{\bar{n}^n}{(\bar{n}+1)^{n+1}}. \tag{4.11}$$

By inserting P_0 in Eq. 4.10 one obtains the ion temperature as a function of $\bar{n}$. A way to approximate $\bar{n}$ is to measure the height of different sidebands, that is, the maximum probability to transfer the ion to the excited electronic state when driving a sideband transition for a fixed Ω_0, and pulse time τ_r. This works because the height will depend on the motional distribution through $\Omega_{n_{ip},n_{op},s_{ip},s_{op}}$.

Considering only one mode, the probability to transfer the ion from $|g_r, n\rangle$ to $|e_r, n+s\rangle$ for zero detuning from the sideband in question is given by (assuming transfer on no other modes nor the carrier)

$$P_{|e_r,n+s\rangle}(\tau_r) = \sum_n \sin^2\left(\Omega_{n,s} \times \frac{\tau_r}{2}\right) P_{|g_r,n\rangle} \tag{4.12}$$

where in this case we assume the probability $P_{|g_r,n\rangle}$ to be in $|g_r, n\rangle$, is given from the Boltzmann distribution. This is a sum over the transfer efficiency from n times the probability to be in n.

When the ion is in the motional ground state, it is not possible to drive a RSB, and the height of the sideband can thus be expressed as

$$\rho_{\text{rsb}} \simeq \sum_{n=1}^{\infty} P_n \sin^2\left(\frac{1}{2}\sqrt{n}\eta\Omega_0 t\right) = \sum_{n=0}^{\infty} \frac{\bar{n}}{\bar{n}+1} P_n \sin^2\left(\frac{1}{2}\sqrt{n+1}\eta\Omega_0 t\right). \tag{4.13}$$

The 1st blue sideband height is

$$\rho_{\text{bsb}} \simeq \sum_{n=0}^{\infty} P_n \sin^2\left(\frac{1}{2}\sqrt{n+1}\eta\Omega_0 t\right). \tag{4.14}$$

Where approximate expressions for $\Omega_{n,s=-1}$ and $\Omega_{n,s=1}$ valid in the Lamb-Dicke regime have been inserted in the two expressions above. Dividing the two sideband heights gives

$$\frac{\rho_{\text{rsb}}}{\rho_{\text{bsb}}} = \frac{\bar{n}}{\bar{n}+1} \tag{4.15}$$

which finally gives [90]

$$\bar{n} = \frac{\rho_{\mathrm{rsb}}}{\rho_{\mathrm{bsb}} - \rho_{\mathrm{rsb}}}. \tag{4.16}$$

Hence by measuring the 1st red and blue sidebands, we can estimate the ions motional population. It is therefore denoted the sideband strength comparison method. Note that this method only is valid after SBC, since we have assume that we are in the Lamb-Dicke regime.

For hotter distributions a more correct method is to fit $P_{|e_r,n+s\rangle}(\tau_r, \Delta_r)$ to Eq. 5.18 and use the average motional state as a fitting parameter. This is e.g. done in Fig. 13.1.

Part II

Photon recoil spectroscopy theory and simulations

Chapter 5

Working principle and mathematical description of PRS

The idea of exploiting the photon recoil associated with absorption and emission in connection with spectroscopy was first devised by the Nobel laureate Prof. Wineland in 2002 [63] and first demonstrated in 2005 [64]. It was invented with the prospect of developing optical atomic clocks based on single atomic ions with suitably narrow optical transitions, but lacking transitions for direct laser cooling.

In this case, spectroscopy is carried out by trapping a single spectroscopic target ion together with a single atomic ion that can be sideband cooled. Via the Coulomb interaction between the ions, the two-ion system can be brought to the quantum mechanical ground state with respect to one or more motional modes as explained in Sec. 4.2. From here the common motion is excited by addressing the target ion with a light field on a red sideband. The fact that the system is no longer in the motional ground state can then be detected on the readout ion, indirectly indicating that the target ion interacted with the light field.

In this way the PRS technique allows for spectroscopic measurements of target ions, which would have been difficult or impossible to perform by other means.

5.1 Resolved sideband PRS

In the original paper, the authors consider a so-called resolved sideband scenario where the two motional mode angular frequencies along the trap axis corresponding to the IP mode (ω_{ip}) and OP mode (ω_{op}) are significantly larger than both the transition linewidth (Γ_t) and the spectral width of the spectroscopy laser (Γ_L) and additionally $\Omega_0 \ll \omega_{ip/op}$. In this scenario, it is possible to selectively address both the spectroscopy ion (target ion) and the sideband-cooling ion (readout ion) with lasers tuned resonantly to either carrier or specific motional sideband transitions.

Fig. 5.1 illustrates one of the simplest specific implementations of PRS capturing the elements important to this thesis.

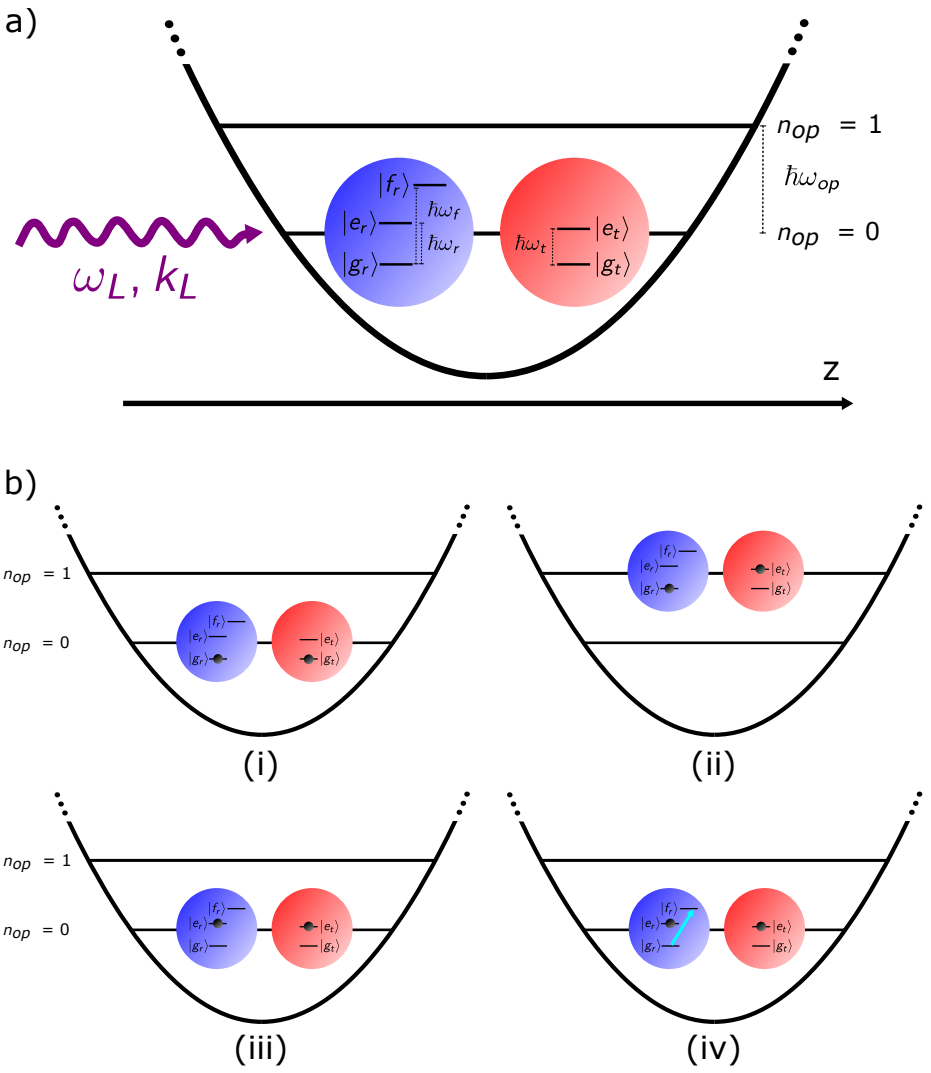

FIGURE 5.1: *a) A single spectroscopic target ion (red) is trapped together with one readout atomic ion (blue) in a linear Paul trap. Doppler cooling followed by sideband cooling on the readout ion ensures that the two-ion Coulomb crystal is in the motional ground state along z. The simplified internal structure of each ion is also shown: the target ion has a simple two-level structure and the readout ion has a three-level structure with two excited states, one long-lived ($|e_r\rangle$) used for sideband cooling and RSB shelving and one short-lived ($|f_r\rangle$) used for fluorescence detection. A light field of frequency ω_L propagating along z interacts with one of the two ions only. b) Schematic of PRS. (i) The two-ion system is initialized in its motional ground state along z with respect to e.g. the out-of-phase mode of motion. The readout ion is prepared in its electronic ground state and the molecular ion in its internal target state. (ii) After a resonant BSB spectroscopy pulse on the target ion, the two-ion system is transferred to the first excited state $n_{op} = 1$. (iii) After a resonant RSB pulse on the readout ion, the two-ion system is transferred back to the motional ground state, and the readout ion is in the $|e_r\rangle$ state. (iv) When exposed to light resonant with the $|g_r\rangle \leftrightarrow |f_r\rangle$ transition, the readout ion does not fluoresce, reflecting a successful excitation of the target ion by the BSB pulse before step (ii).*

This procedure starts by **(i)** initializing the two-ion system in the quantum mechanical ground state of at least one of the two motional modes along the axis defined by the two ions (e.g. the OP mode), the readout atomic ion in its electronic ground state, and the molecular ion in its internal target state for the spectroscopy.

Next, the target molecular ion is exposed to a light pulse expected to be resonant with the BSB of the spectroscopy transition (i.e. $\omega_L = \omega_t + \omega_{op}$, where ω_L, ω_t are the angular frequencies of the light and of the target transition respectively). If the correct interaction time τ_{spec} is chosen, the resonant BSB pulse leads to a full excitation of the target ion to $|e_t\rangle$ (a perfect π-pulse as explained in Sec. 3.1), and the two-ion system is transferred to the state depicted in **(ii)**, where the OP mode is now excited by one quanta ($n_{op} = 1$).

This motional excitation can be monitored by addressing the readout atomic ion with a light pulse resonant with the RSB of the narrow sideband cooling transition ($\omega_L = \omega_r - \omega_{op}$, where ω_r is the transition frequency) for a time τ_r corresponding to a full excitation to the $|e_r\rangle$ state at the expense of the motional excitation **(iii)**.

In the final step **(iv)**, the readout ion is exposed to light resonant with a closed fast fluorescing transition $|g_r\rangle \leftrightarrow |f_r\rangle$. This leads to the emission of many photons at the frequency ω_f if the readout ion is in the $|g_r\rangle$ state, versus no photon emission if it is in the $|e_r\rangle$ state. Since we assumed in step (iii) to have brought the readout ion to the $|e_r\rangle$ state, we expect no fluorescence in the last step (iv) if the pulse applied to the target molecular ion was indeed excited by the first BSB pulse. Conversely, if the target ion was not excited on the BSB, the readout ion would stay in the $|g_r\rangle$ state after step (iii), and fluorescence light would be emitted during the final step (iv).

Hence, through repetition of the PRS sequence (i)-(iv) for different values of ω_L when addressing the target ion, the total fluorescence signal from the readout atomic ion will reflect the excitation probability of the target molecular ion and thus produce a spectroscopy signal.

5.1.1 Hamiltonian dynamics relevant to resolved sideband PRS

If we assume $\Gamma_t, \Gamma_L \ll \Omega_0$, the relevant Hamiltonian dynamics for sideband resolved PRS are the ones already presented in Sec. 3.2 for the interaction between two co-trapped ions and a classical monochromatic light field, where spontaneous decay can be neglected. The only difference to Sec. 3.2 is that for PRS the readout ion must have a three-level structure $\{|g_r\rangle, |e_r\rangle, |f_r\rangle\}$ in order to perform fluorescence readout

on the $|g_r\rangle \leftrightarrow |f_r\rangle$ transition as depicted in Fig. 5.1. However this reduces to the two levels $|g_r\rangle$ and $|e_r\rangle$, which were assumed in Sec. 3.2, when considering only the Hamiltonian evolution of the PRS sequence before readout (steps (i) to (iii), Fig. 5.1).

For resolved sideband PRS, the typical starting point is to have both motional modes cooled to the quantum mechanical ground state. Eq. 3.70 is then typically a good approximation for simulating the internal and external quantum dynamics before the final unresolved sideband detection addressing the $|g_r\rangle \leftrightarrow |f_r\rangle$ transition of the readout ion (step (iv), Fig. 5.1). This readout signal corresponds to a projection measurement of the readout ion to its ground state $|g_r, i_t, n_{ip}, n_{op}\rangle$. Formally, it is proportional to

$$P_{|g_r\rangle} = \sum_{n_{ip},n_{op},i_t} |\langle \psi_{\mathrm{Ham}} | g_r, i_t, n_{ip}, n_{op}\rangle|^2, \tag{5.1}$$

with ψ_{Ham} being the wavefunction after the Hamiltonian evolution of steps i) to iii) of the PRS sequence. Thus the fluorescence level corresponds directly to how much population was left in $|g_r, i_t, n_{ip}, n_{op}\rangle$ before step (iv).

5.2 Model for PRS in the unresolved sideband regime

Although PRS was originally developed for ultra-precise spectroscopy in the resolved sideband regime, PRS in unresolved sideband scenarios can be equally interesting for a range of investigations of molecules in the gas phase. This includes internal state preparation, broad line absorption spectroscopy under diverse but well-controlled conditions, and single photon absorption studies of non- or weakly-fluorescing molecules.

The unresolved sideband PRS scenario appears naturally in two generic cases, when the motional sideband frequencies of the two-ion system, $\omega_{ip/op}$, are either smaller than or similar to: 1) the natural linewidth of the spectroscopic transition Γ_t, or 2) the linewidth of the applied light source Γ_L.

In general, to simulate the photon recoil spectrum under such circumstances, one has to include the laser linewidth and/or the natural linewidth of the addressed transition in the theory presented in Sec. 3.2 and 5.1.1. In the broad transition linewidth case this is similar to what was done for a single ion in free space in Sec. 3.1.1, where spontaneous emission was included in the model. However due to the large state space for two trapped ions the resulting density matrix would be of

dimension $M \times M$ where $M = 2 \cdot 2 \cdot N_{ip} \cdot N_{op}$ is the total number of eigenstates $|i_r, i_t, n_{ip}, n_{op}\rangle$ and $N_{ip/op}$ are how many motional modes are considered in the model. This means that already for few motional states the master equations [94] will be very time-consuming to solve.

However, in the limit of no remaining coherence in the interaction with the light field, the description can be simplified by instead using the Einstein rate equation formalism presented in Sec.s 3.1.2 to 3.1.4.

5.2.1 Rate equation description

Before using the Einstein rate equation formalism to describe sideband unresolved PRS, we must argue why the more detailed semi-classical model reduces to the rate equation description in each of the two generic cases 1) $\Gamma_t \gg \omega_{ip/op}$, and 2) $\Gamma_L \gg \omega_{ip/op}$.

In order for the first case to be well-described by rate equations we must assume $\Gamma_t \gg \Omega_0$ such that spontaneous emission dominates. In this case the time to reach steady state is much shorter than $\Omega_0 t/(2\pi)$ as depicted in Fig. 3.2, and the steady state value is very low. In this case the Einstein rate and the optical Bloch solutions are so similar, especially for interaction times $\tau_{spec} \gg \Omega_0 t/(2\pi)$ that we choose to neglect the difference when describing the system with rate equations.

The second case inherently resembles the scenario originally considered by Einstein of broadband black-body radiation, and the dynamics are therefore considered to be incoherent. In this case the different sideband transitons can be seen as degenerate levels compared to the broad light field.

Hence in both cases, the internal state evolution can be described by excitation and de-excitation rates in accordance with Einstein's theory for light absorbers interacting with broadband (black-body) fields [102]. We will further assume that the wave vectors of the absorbed and emitted photons can all be represented by the one corresponding to that of the transition center (i.e. assuming the transition linewidth to be much narrower than the transition frequency). We can then apply Eq. 3.67 using a single value of $\|\vec{k}_L\|$ (or $\|\vec{k}_{spon}\|$ for spontaneous emission) to evaluate the relative coupling between motional states. Based on these approximations, we can formally write up rate equations governing the dynamics of the internal and external

state populations during the spectroscopy pulse as

$$\begin{aligned}\frac{\mathrm{d}}{\mathrm{d}t}P_{|i_r,g_t,n_{ip},n_{op}\rangle} = \sum_{s_{ip},s_{op}} & - R_{\mathrm{abs}}(n_{ip},n_{op},s_{ip},s_{op})P_{|i_r,g_t,n_{ip},n_{op}\rangle} \\ & + [R_{\mathrm{stim}}(n_{ip},n_{op},s_{ip},s_{op}) \\ & + R_{\mathrm{spon}}(n_{ip},n_{ip},s_{ip},s_{op})]P_{|i_r,e_t,(n_{ip}+s_{ip}),(n_{op}+s_{op})\rangle} \\ & - (R_{H,ip}+R_{H,op})P_{|i_r,g_t,n_{ip},n_{op}\rangle} \\ & + R_{H,ip}P_{|i_r,g_t,(n_{ip}-1),n_{op}\rangle} \\ & + R_{H,op}P_{|i_r,g_t,n_{ip},(n_{op}-1)\rangle}\end{aligned} \tag{5.2}$$

$$\begin{aligned}\frac{\mathrm{d}}{\mathrm{d}t}P_{|i_r,e_t,n_{ip},n_{op}\rangle} = \sum_{s_{ip},s_{op}} & - [R_{\mathrm{stim}}(n_{ip}-s_{ip},n_{op}-s_{op},s_{ip},s_{op}) \\ & + R_{\mathrm{spon}}(n_{ip}-s_{ip},n_{op}-s_{op},s_{ip},s_{op})]P_{|i_r,e_t,n_{ip},n_{op}\rangle} \\ & + R_{\mathrm{abs}}(n_{ip}-s_{ip},n_{op}-s_{op},s_{ip},s_{op})P_{|i_r,g_t,(n_{ip}-s_{ip}),(n_{op}-s_{op})\rangle} \\ & - (R_{H,ip}+R_{H,op})P_{|i_r,e_t,n_{ip},n_{op}\rangle} \\ & + R_{H,ip}P_{|i_r,e_t,(n_{ip}-1),n_{op}\rangle} \\ & + R_{H,op}P_{|i_r,e_t,n_{ip},(n_{op}-1)\rangle}\end{aligned} \tag{5.3}$$

for the target ion being in the internal ground or excited state, respectively. Here, $R_{\mathrm{abs/stim}}(n_{ip},n_{op},s_{ip},s_{op})$ describe the rates of photon absorption and stimulated emission, and can be expressed as

$$\begin{aligned}R_{\mathrm{abs/stim}}(n_{ip},n_{op},s_{ip},s_{op}) =& B_{\mathrm{abs/stim}} \times \rho_{\mathrm{eff}}(\omega_t,\omega_L) \times |\xi(\eta_{ip,t},\eta_{op,t},n_{ip},n_{op},s_{ip},s_{op})|^2 \\ =& R_{\mathrm{abs/stim},0}(\omega_t,\omega_L) \times |\xi(\eta_{ip,t},\eta_{op,t},n_{ip},n_{op},s_{ip},s_{op})|^2\end{aligned} \tag{5.4}$$

with the Einstein B-coefficients given as

$$B_{\mathrm{stim}} = \frac{\pi^2 c^3}{\hbar\omega_t^3}\Gamma_t, \quad B_{\mathrm{abs}} = B_{\mathrm{stim}}, \tag{5.5}$$

in accordance with Eq. 3.39, however here we omit the degeneracy of the levels and consider a true two-level system. $\rho_{\mathrm{eff}}(\omega_t,\omega_L)$ denotes the effective spectral energy

density at the carrier transition frequency ω_t due to a laser line centered around ω_L.[1] Generally, we can write $\rho_{\text{eff}}(\omega_t, \omega_L)$ as

$$\rho_{\text{eff}}(\omega_t, \omega_L) = \frac{3I_L}{c} \int_{-\infty}^{\infty} L_t(\omega', \omega_t) L_L(\omega', \omega_L)\, d\omega', \tag{5.6}$$

similarly to Eq. 3.48 but here we introduce a factor of 3 because we consider, in contrast to the original scenario considered by Einstein of classical electric dipoles interacting with unpolarized and randomly propagating electromagnetic fields, a laser field with a well-defined polarization and an aligned induced electric dipole by construction. We assume the laser field to have a Gaussian[2] frequency distribution with a full width at half maximum (FWHM) $\Gamma_L \equiv \sqrt{8\ln(2)}\sigma_L$ (where $2\sigma_L$ is the full width at $1/\sqrt{e}$), and the target transition to be Lorentzian[3] and governed by the natural decay rate Γ_t. The two line shapes can be written as

$$L_L(\omega, \omega_L) = \frac{1}{\sqrt{2\pi}\sigma_L} e^{\frac{-(\omega-\omega_L)^2}{2\sigma_L^2}} \tag{5.7}$$

and

$$L_t(\omega, \omega_t) = \frac{1}{\pi} \frac{\Gamma_t/2}{(\omega-\omega_t)^2 + \Gamma_t^2/4}. \tag{5.8}$$

For the two cases where either $\Gamma_L \ll \Gamma_t$ or $\Gamma_L \gg \Gamma_t$, $\rho_{\text{eff}}(\omega_t, \omega_L)$ reduces to

$$\rho_{\text{eff}}^t(\omega_t, \omega_L) = \frac{3I_L}{c} L_t(\omega_L, \omega_t) \tag{5.9}$$

and

$$\rho_{\text{eff}}^L(\omega_t, \omega_L) = \frac{3I_L}{c} L_L(\omega_t, \omega_L), \tag{5.10}$$

respectively. It is obvious from Eq. 5.4 that we have the largest absorption and stimulated emission rates when $\omega_L = \omega_t$, which leads to, for the two cases of $\Gamma_L \ll \Gamma_t$

[1] In principle we should write $\omega_t \to \omega_L - \Delta_t$ where $\Delta_t = \omega_L - (\omega_t + s_{ip}\omega_{ip} + s_{op}\omega_{op})$ is the detuning from the specific sideband. However, for smooth spectral shapes simply using ω_t will be a good approximation, since Γ_L or Γ_t is assumed to be much larger than $\omega_{ip/op}$.

[2] This laser lineshape is chosen as an example since it is common, but any lineshape can be considered.

[3] Typical for the natural lineshape of a transition, but it could have a different shape if other processes than spontaneous emission play a significant role.

and $\Gamma_L \gg \Gamma_t$, the following values for $R_{\mathrm{abs/stim},0}(\omega_t, \omega_L)$

$$\begin{aligned} R^t_{\mathrm{abs/stim},0}(\omega_t, \omega_t) \equiv R^{\mathrm{res},t}_{\mathrm{abs},0} &= \frac{6\pi c^2}{\hbar\omega_t^3} I_L \\ &\equiv \Gamma_t \frac{I_L}{I^t_{\mathrm{sat}}}, \end{aligned} \tag{5.11}$$

where

$$I^t_{\mathrm{sat}} \equiv \frac{\hbar\omega_t^3 \Gamma_t}{6\pi c^2}, \tag{5.12}$$

and

$$\begin{aligned} R^L_{\mathrm{abs/stim},0}(\omega_t, \omega_t) \equiv R^{\mathrm{res},L}_{\mathrm{abs},0} &= \frac{3\pi^{3/2} c^2}{\sqrt{2}\hbar\omega_t^3} \frac{\Gamma_t}{\sigma_L} I_L \\ &\equiv \Gamma_t \frac{I_L}{I^L_{\mathrm{sat}}}, \end{aligned} \tag{5.13}$$

where

$$I^L_{\mathrm{sat}} \equiv \frac{\sqrt{2}\hbar\omega_t^3 \sigma_L}{3\pi^{3/2} c^2}, \tag{5.14}$$

respectively. Here, the intensity I_{sat} is defined in both cases as the laser intensity which leads to an excitation rate $R^{\mathrm{res}}_{\mathrm{abs},0}$ equal to Γ_t.[4]

Furthermore the absorption and stimulated emission rates are scaled by the factor $|\xi(\eta_{ip,t}, \eta_{op,t}, n_{ip}, n_{op}, s_{ip}, s_{op})|^2$ given in Eq. 3.67 which represents the relative strength of the coupling to different sidebands. This factor is norm squared because $B_{abs/stim}(n_{ip}, n_{op}, s_{ip}, s_{op})$ is proportional to $|\Omega_{n_{ip},n_{op},s_{ip},s_{op}}|^2$ through Eq. 3.44, which is connected to the scaling factor by Eq. 3.69.

Regarding the contribution of spontaneous emission to Eq.s 5.2-5.3, one has to scale the rate Γ_t with a factor accounting for the average probability to emit on a certain sideband. This factor depends on the spatial emission pattern of the specific transition. If we define $\theta \in [0, \pi]$ as the angle between the spontaneously emitted photon wave vector $\vec{k}_{spon}$ and the z-axis, and $\phi \in [0, 2\pi]$ as the angle between the y-axis and the projection of $\vec{k}_{spon}$ on the xy-plane, we can write

$$\frac{\vec{k}_{spon}}{\|\vec{k}_{spon}\|} = \begin{pmatrix} \sin\theta\cos\phi \\ \sin\theta\sin\phi \\ \cos\theta \end{pmatrix}. \tag{5.15}$$

[4]This leads to a steady state value of 1/3 when $I_L = I^{t/L}_{\mathrm{sat}}$, which differs from the definition of I_{sat} given in Eq. 3.29.

In spherical coordinates, we can then write the spontaneous emission rate as

$$R_{\text{spon}}(n_{ip}, n_{op}, s_{ip}, s_{op}) = \Gamma_t D(n_{ip}, n_{op}, s_{ip}, s_{op}) \tag{5.16}$$

with

$$D(n_{ip}, n_{op}, s_{ip}, s_{op}) = \int d\Omega |\xi(\eta_{ip,t}(\theta), \eta_{op,t}(\theta), n_{ip}, n_{op}, s_{ip}, s_{op})|^2 W(\theta, \phi), \tag{5.17}$$

where $\vec{k}_L$ must be replaced by $\vec{k}_{spon}$ in Eq. 3.57 for $\eta_{ip/op,t}$. The emission pattern $W(\theta, \phi)$ is the probability that the spontaneously emitted photon propagates along the (θ, ϕ) direction.

Finally, for realistic simulation of the PRS spectra, one has to take into account heating of the motional modes due to imperfect trapping conditions. As we saw in Sec. 4.3 the associated heating rates can be very mode-dependent but are typically independent of the internal state of the two ions as well as on the specific mode excitation [81]. They are introduced in Eq. (5.2)-(5.3) by the terms containing the rates $R_{H,ip/op}$.

Although the spectroscopy laser does not exclusively address the first BSB as in the case of resolved sideband PRS (it actually addresses many sidebands simultaneously), light-ion interaction still leads to excitation of both motional modes according to Eq.s 5.2-5.3. The resulting motional state populations depend on the transition line profile, the laser parameters (intensity, central frequency, lineshape and linewidth) as well as the time τ_{spec} the laser light is applied.

A signal reflecting the motional mode distribution after the spectroscopy pulse can be obtained by applying to the readout ion a sideband resolved shelving pulse of length τ_r with respect to one of the two modes (step (iii) Fig. 5.1). If assuming no other sidebands nor the carrier transition are driven the probability for the readout ion to be shelved in the $|e_r\rangle$ state is given by

$$P_{|e_r\rangle}(\tau_r, \Delta_r) = \sum_{n_{ip}, n_{op}} \frac{\Omega^2_{n_{ip}, n_{op}, s_{ip}, s_{op}}}{\Delta_r^2 + \Omega^2_{n_{ip}, n_{op}, s_{ip}, s_{op}}} \sin^2\left(\sqrt{\Delta_r^2 + \Omega^2_{n_{ip}, n_{op}, s_{ip}, s_{op}}} \frac{\tau_r}{2}\right) P_{|g_r, i_t, n_{ip}, n_{op}\rangle} \tag{5.18}$$

similarly to Eq. 4.6. The difference is that now we have a sum of contributions from the different motional states with population probability $P_{|g_r, i_t, n_{ip}, n_{op}\rangle}$. The probability to stay in the ground state $|g_r\rangle$ when addressing the 1st RSB of the OP

mode for $\Delta_r = 0$ (i.e. $\omega_L = \omega_r - \omega_{op}$) is then

$$P_{|g_r\rangle}(\tau_r) = 1 - \sum_{n_{ip},n_{op}} \sin^2\left(\Omega_{n_{ip},n_{op},s_{ip}=0,s_{op}=-1} \times \frac{\tau_r}{2}\right) P_{|g_r,i_t,n_{ip},n_{op}\rangle} \tag{5.19}$$

where $\Omega_{n_{ip},n_{op},s_{ip}=0,s_{op}=-1}$ indicates the Rabi angular frequency of the 1st RSB transition for a given motional state. As mentioned previously for resolved PRS (see Eq. 5.1), the readout fluorescence signal during step (iv) is directly proportional to $P_{|g_r\rangle}$. Clearly, if there is no motional excitation by the spectroscopy laser, there is also no excitation by the resolved RSB laser pulse since $P_{|e_r\rangle} = 0$ for $n_{ip} = n_{op} = 0$ (assuming no heating from other sources), and the readout ion fluoresces when finally driving the $|g_r\rangle \leftrightarrow |f_r\rangle$ transition. Conversely, any excitation by the spectroscopy laser pulse leads to a reduced fluorescence signal. As is evident from Eq. 5.19, the fluorescence reduction also depends on the duration of the resolved RSB pulse. If $\Delta_r = 0$ and $\tau_r = \pi/\Omega_{n_{ip},n_{op},s_{ip},s_{op}}$, we drive a π-pulse from this specific motional state and on this specific sideband, meaning all population in $|g_r, i_t, n_{ip}, n_{op}\rangle$ will be transferred to $|e_r\rangle$. In the following chapter we will present simulated PRS spectra obtained by applying the model presented here to two specific unresolved sideband scenarios.

Chapter 6

Simulations of unresolved photon recoil spectra

In this Chapter, we present simulated unresolved PRS spectra based on the model presented in Sec. 5.2, where either the natural linewidth of the transition or the linewidth of the laser dominates the dynamics. More specifically, in Sec. 6.1, we consider PRS of the rather broad 3s $^2S_{1/2}$ - 3p $^2P_{3/2}$ electronic transition ($\Gamma_t/2\pi = 41.8(4)$ MHz) of a single $^{24}Mg^+$ ion at $\lambda = 279.6$ nm by a narrow laser source ($\Gamma_L/2\pi \lesssim 1\,\text{MHz} \ll \Gamma_t/2\pi$). Section 6.2 is devoted to simulation of mid-infrared rovibrational PRS spectra of the very narrow $|\nu = 0, J = 1\rangle \leftrightarrow |\nu' = 1, J' = 0\rangle$ closed transition ($\Gamma_t/2\pi = 2.50$ Hz) at $\lambda = 6.17\,\mu$m in the $^1\Sigma^+$ electronic ground state of $^{24}MgH^+$ by a laser source with a linewidth varying from $\Gamma_L/2\pi \sim 50$ MHz to 1 GHz. In both cases we use a single $^{40}Ca^+$ ion as the readout/cooling ion and the 4s $^2S_{1/2}$ - 3d $^2D_{5/2}$ quadrupole transition at $\lambda = 729$ nm of this ion as the readout transition $|g_r\rangle \rightarrow |e_r\rangle$. An overview of the trap frequencies, transition wavelengths, and Lamb-Dicke parameters used in the simulations are given in Table 6.1.

	Broad transition $^{40}Ca^+$ and $^{24}Mg^+$	Broad laser $^{40}Ca^+$ and $^{24}MgH^+$
$\omega_{ip}/2\pi$	162.9 kHz	162.0 kHz
$\omega_{op}/2\pi$	300.2 kHz	295.7 kHz
λ_t	279.6 nm	6.17 μm
λ_r	729 nm	729 nm
$\eta_{ip,t}$ [0°(45°)]	0.419 (0.296)	0.0192 (0.0136)
$\eta_{op,t}$ [0°(45°)]	0.507 (0.358)	0.0224 (0.0159)
$\eta_{ip,r}$[0°]	0.204	0.203
$\eta_{op,r}$[0°]	0.0917	0.0949

TABLE 6.1: *Trap frequencies, transition wavelengths and Lamb-Dicke parameters for the two different two-ion systems considered. The LPDs depend on which ion is addressed (target or readout) and on the angle between the laser beam and the z-axis.*

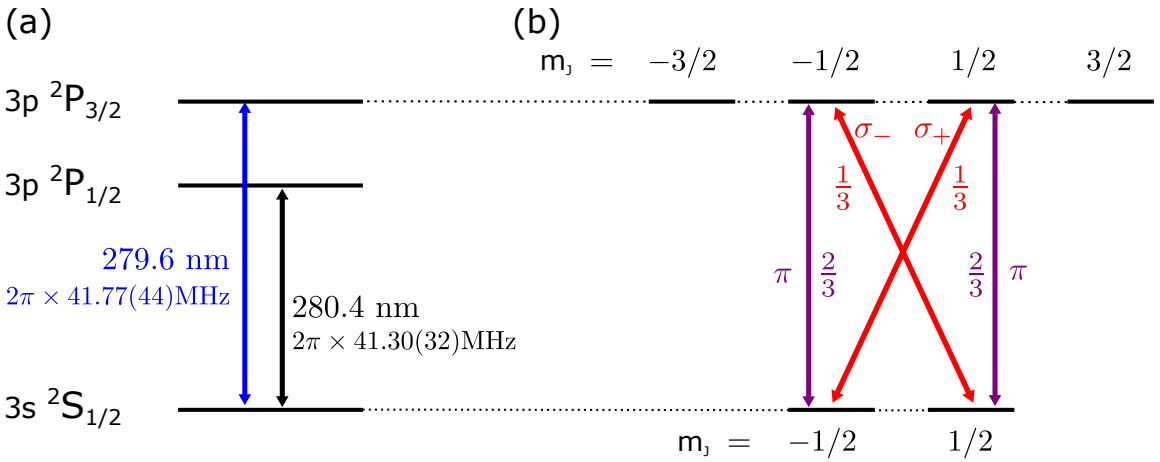

FIGURE 6.1: *(a) Energy levels of $^{24}Mg^+$. The 3s $^2S_{1/2}$ - 3p $^2P_{3/2}$ transition is the spectroscopic target transition ($|g_t\rangle \leftrightarrow |e_t\rangle$) in our simulations and experiments. (b) The energy levels of $^{24}Mg^+$ have sub-levels which are degenerate in the presence of a magnetic field. π-transitions do not change the secondary total angular momentum m_J whereas $\sigma_\pm$ transitions change it by ± 1. The norm squared values of the Clebsch-Gordan coefficients associated with these transitions are shown.*

6.1 Transition linewidth dominating case ($^{24}Mg^+$)

In this section we simulate photon recoil spectra of the rather broad 3s $^2S_{1/2}$ - 3p $^2P_{3/2}$ electronic transition ($\Gamma_t/2\pi = 41.8(4)$ MHz) of a single $^{24}Mg^+$ ion at $\lambda = 279.6$ nm (See Fig. 6.1(a)) by a laser source with such a narrow linewidth ($\Gamma_L \ll \Gamma_t$) that we disregard it. The two levels have sub-levels as seen in Fig. 6.1(b), which are non-degenerate in the presence of a magnetic field, and they therefore do not constitute a perfect two-level system. However, when applying linearly polarized spectroscopic laser light along a bias magnetic field axis (y-axis), only two sub-level transitions $^2S_{1/2}$ ($m_J = \pm 1/2$) - $^2P_{3/2}$ ($m_J = \pm 1/2$) can be excited. The strength of these two transitions are equal (see Fig. 6.1.(b)). Furthermore, since the spontaneous emission pattern from the $^2P_{3/2}$ ($m_J = \pm 1/2$) sub-states have identical effects on the motional mode excitations, the two transitions are identical from an excitation and spontaneous emission point of view, and the dynamics are equivalent to the ones of a two-level system. The effective saturation intensity is, however, 1.5 times larger than in the two-level theory presented in Sec. 5.2.1 due to the norm squared of the Clebsch-Gordan coefficient being 2/3. In the simulations this has been implemented by multiplying $R^{\text{res}}_{\text{abs},0}$ from Eq. 5.11 by 2/3. We furthermore assume that the $^{24}Mg^+$ target ion is initially sympathetically cooled to the motional ground state of both modes by a directly sideband-cooled readout $^{40}Ca^+$ ion.

6.1.1 Absorption and stimulated emission

Assuming $\omega_z = 2\pi \times 147.9\,\text{kHz}$ for a single $^{40}Ca^+$ ion, we get from Eq. 2.17 $\omega_{ip} = 2\pi \times 162.9\,\text{kHz}$ and $\omega_{op} = 2\pi \times 300.2\,\text{kHz}$. Both mode angular frequencies are more than two orders of magnitude smaller than Γ_t. Hence, we are clearly in the regime where we can apply Eqs. 5.2-5.3 with Eq. 5.9. In the simulations presented in this chapter we use $\omega_t \rightarrow \omega_L - \Delta_t$ in Eq. 5.9 for ρ^t_{eff}. With $\lambda_t = 279.6\,\text{nm}$ for the target ion and the mode angular frequencies above, the LDPs for absorption and spontaneous emission are $\eta_{ip,t} = 0.42$ and $\eta_{op,t} = 0.51$ for the spectroscopy laser beam propagating along the z-axis. In the simulations to be presented below, we will, however, use the values $\eta_{ip,t} = 0.30$ and $\eta_{op,t} = 0.36$ in order to compare the results with experiments where the $^{24}Mg^+$ spectroscopy laser beam propagates at a 45° angle to the z-axis, reducing the LDPs by a factor $\sqrt{2}$. While this approach gives the correct effect of the momentum recoil along the z-axis with respect to absorption and stimulated emission, it neglects the effect of motional excitations in the plane perpendicular to the z-axis. In the present unresolved sideband PRS situation, it is merely expected to lead to slightly reduced induced transition rates and a minor Doppler broadening of the target line (see details in Sec. 13.2).

6.1.2 Spontaneous emission

To simulate the effect of spontaneously emitted photons following Eq. (5.16-5.17), we must know the emission pattern of the specific transition. To determine that, we have to take into account the particular Zeeman sub-level structure of the 3s $^2S_{1/2}$ - 3p $^2P_{3/2}$ electronic transition in the $^{24}Mg^+$ ion and the relative branching ratios between sub-level transitions given by the norm squared of the Clebsch-Gordan coefficients (See Fig. 6.1.(b)). With respect to the chosen spherical coordinate system described in connection with Eq. (5.15), the spontaneous emission pattern is given by

$$W(\theta,\phi) = \frac{2}{3}W_\pi(\theta,\phi) + \frac{1}{3}W_\sigma(\theta,\phi), \tag{6.1}$$

where

$$\begin{aligned} W_\pi(\theta,\phi) &= \frac{3}{8\pi}\sin^2(\arccos(\sin\theta\sin\phi)) \quad \text{and} \\ W_\sigma(\theta,\phi) &= \frac{3}{16\pi}(1+\sin^2\theta\sin^2\phi) \end{aligned} \tag{6.2}$$

are the individual emission patterns of the two possible types of sub-level transitions, π ($\Delta m_J = 0$) and σ ($\Delta m_J = \pm 1$) respectively (see Ref. [103] p. 437-439).

6.1.3 Basis for the numerical simulation

In the following simulations, we will assume the target and readout ions to initially be in the $|g_t\rangle$ and $|g_r\rangle$ states, respectively, and both the motional modes cooled to their ground state (i.e. $n_{ip} = 0$ and $n_{op} = 0$). In order to perform the simulations in a reasonable time on a standard personal computer, we have limited the motional state basis to a grid corresponding to $n_{ip} = 0 - 19$ and $n_{op} = 0 - 19$. This gives $20 \times 20 = 400$ motional states. Consequently, the population will eventually be moved outside the state space for long spectroscopy pulse times τ_{spec}. For the present calculations the amount of population outside the state space has been limited to 1%, effectively limiting the duration of the dynamics evolution we can simulate. Based on Eq. (3.67), which represents the relative coupling strengths of the various sidebands, we have found that it suffices to take into account sidebands up to $s_{ip,max} = \pm 5$ and $s_{op,max} = \pm 6$. (See Appendix D for details.) Based on trap-induced heating rate measurements presented in Sec. 13.1, we use $R_{H,ip} = 14(1)\,\text{s}^{-1}$ and $R_{H,op} = 1.7(3)\,\text{s}^{-1}$.

6.1.4 Dynamics of motional state population

In the present case, we consider the limit where $\Gamma_L \ll \Gamma_t$. From Eq. 5.11, the saturation intensity is $I^t_{sat} = 0.749\,\text{W cm}^{-2}$. For laser intensities $I_L \ll I^t_{sat}$, we cannot ignore the spontaneous emission terms of Eqs. 5.2-5.3, while in the case of $I_L \gg I^t_{sat}$, the spontaneous emission terms can effectively be neglected. In the latter case, when the trap-induced heating rates can also be ignored, all terms on the right hand side of Eqs. 5.2-5.3 are proportional to $R^{\text{res,t}}_{\text{abs},0}$ and the dynamics should have exactly the same behavior when τ_{spec} is scaled by this factor. To express this we define $\tau^t_{\text{scaled}} \equiv \tau_{\text{spec}} \times R^{\text{res},t}_{\text{abs},0}$, which is roughly proportional to the number of absorbed photons from the laser beam.

In Fig. 6.2, we show the temporal evolution of the population of the various motional states (n_{ip}, n_{op}) from solving Eqs. 5.2-5.3 assuming $\omega_L = \omega_t$ and for $I_L = 6.54 \times 10^{-6} I^t_{sat}$. This intensity is chosen to compare with experimental results presented in Sec. 13.2. For this intensity we have $I_L \ll I^t_{sat}$ and the spontaneous emission is dominating. More specifically, Fig. 6.2 shows the populations versus

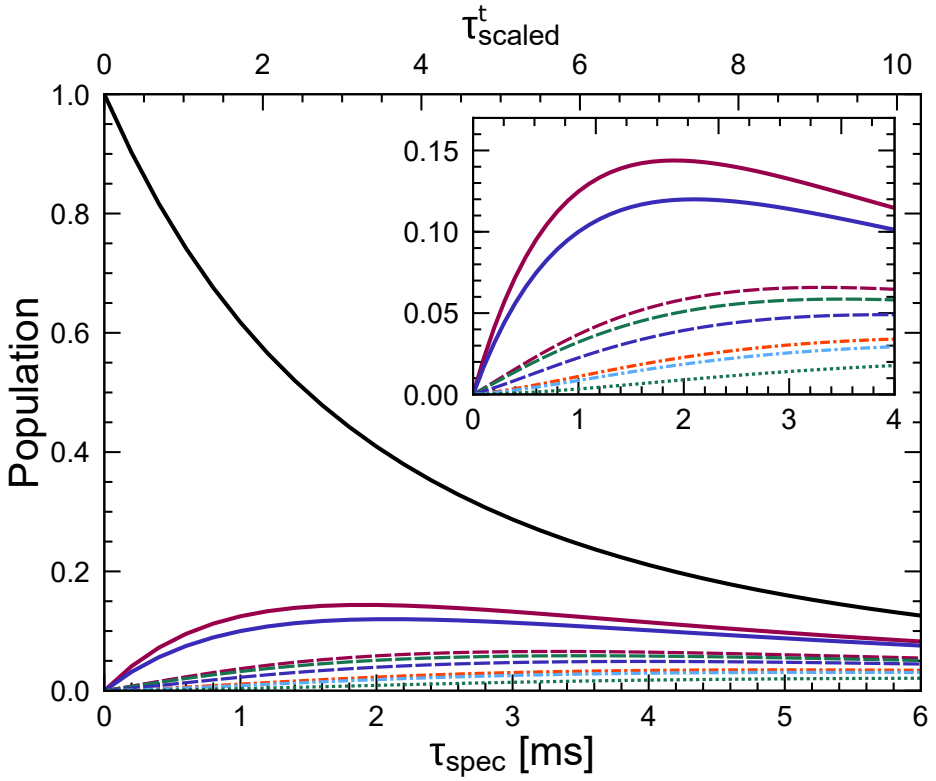

FIGURE 6.2: *Simulated evolution of the population in different motional states as a function of spectroscopy pulse time τ_{spec} (bottom axis) and scaled time τ^t_{scaled} (top axis) for a laser on resonance ($\omega_L = \omega_t$) and with $I_L = 4.9\,\mu\mathrm{W\,cm^{-2}} = 6.54 \times 10^{-6} I^t_{sat}$. The following notation refers to motional states (n_{ip}, n_{op}): (0,0) —, (0,1) —, (1,0) —, (0,2) - - -, (1,1) - - -, (2,0) - - -, (1,2) -·-·-, (2,1) -·-·-, (2,2) ·····.*

real time τ_{spec} (bottom x-axis) as well as the scaled time τ^t_{scaled} (top x-axis). As evident from this figure, the motional ground state population (0,0) is a monotonically decreasing function of time. For short times, the populations of all other motional states $(n_{ip}, n_{op}) \neq (0,0)$ increase linearly with time as expected for rate equations. For longer times, the populations of the individual motional states saturate and eventually decrease as a broader range of motional states is reached.

6.1.5 Motional population spectra

Scanning the laser frequency ω_L across the resonance of the target ion transition for a fixed τ_{spec} leads to what we name the motional population spectra. They show the population of a specific motional state as a function of detuning after a given interaction time with the spectroscopy light. In Fig. 6.3, we present such spectra for $I_L = 6.54 \times 10^{-6} I^t_{sat}$ and for spectroscopy times $\tau_{\mathrm{spec}} = 1.3\,\mathrm{ms}$ and $5.3\,\mathrm{ms}$ ($\tau^t_{\mathrm{scaled}} = 2.23$ and 9.10). For these parameters, one clearly sees the effect of population depletion of the lower excited motional states around the resonance due to the effective motional

state spreading. A normal spectral response with a width reflecting the natural linewidth of the transition is observed only for the weakly populated states. For PRS one has, however, to be aware that the motional spectra presented in Fig. 6.3 will not be read out individually by the readout procedure (steps (iii) and (iv) in Fig. 5.1) reported previously. The final fluorescence signal is instead an intricate combination of contributions from each of the motional population spectra, as will be discussed in the following sub-section.

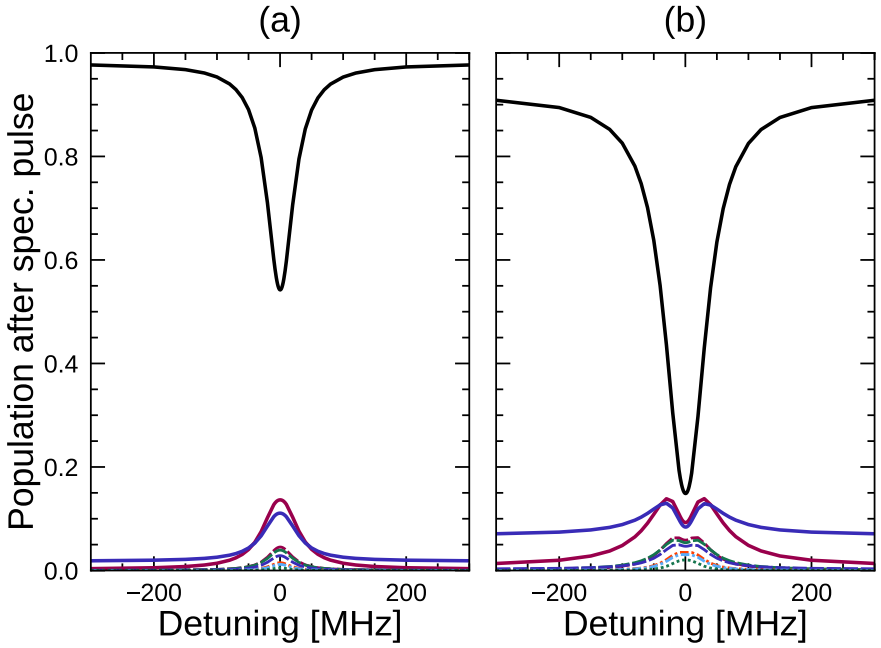

FIGURE 6.3: *Simulated population in different motional states after a spectroscopy pulse of length τ_{spec} = 1.3 ms ($\tau^t_{scaled} = 2.23$) **(a)** and 5.3 ms ($\tau^t_{scaled} = 9.10$) **(b)** as a function of spectroscopy laser detuning for a spectroscopy laser intensity of $I_L = 4.9\,\mu\mathrm{W\,cm^{-2}} = 6.54 \times 10^{-6} I^t_{sat}$. The following notation refers to motional states (n_{ip}, n_{op}): (0,0) ——, (0,1) ——, (1,0) ——, (0,2) - - -, (1,1) - - -, (2,0) - - -, (1,2) -·-·-, (2,1) -·-·-, (2,2) ·····.*

6.1.6 Readout spectra

To simulate the PRS spectrum one would obtain in an experiment, we now need to calculate how much population will be left in $|g_r\rangle$ after addressing the readout ion on a specific RSB transition (step (iii) Fig. 5.1), since this corresponds exactly to the fluorescence signal one will obtain when subsequently addressing $|g_r\rangle \leftrightarrow |f_r\rangle$ (step (iv)). The initial state before the RSB shelving pulse of duration τ_r is the mixed state resulting from the rate equation dynamics during the spectroscopy pulse presented in the previous sub-section. To calculate $P_{|g_r\rangle}(t_r)$ we use Eq. 5.19 with the

populations of all the states $P_{|g_r,i_t,n_{ip},n_{op}\rangle}(\tau_{spec})$ found from the rate equations. In fact $P_{|g_r,i_t,n_{ip},n_{op}\rangle}(\tau_{spec})$ is exactly what is plotted in Fig. 6.3, just for different detunings. In Fig. 6.4, we show the result of applying Eq. 5.19 to the two population spectra

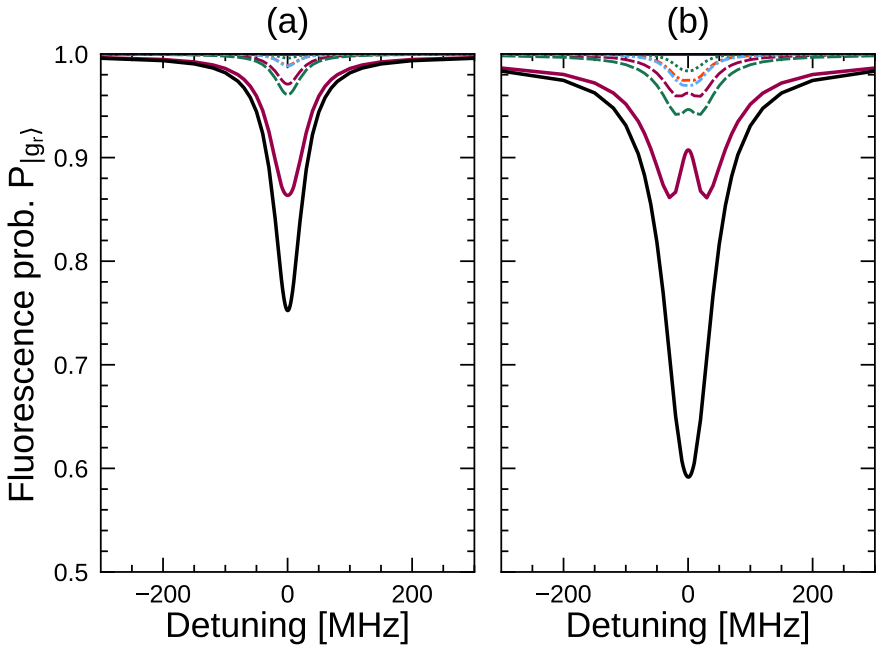

FIGURE 6.4: *Simulated fluorescence probability* $P_{|g_r\rangle}$, —, *corresponding to the detected signal for readout on the OP mode, for spectroscopy pulse lengths of* $\tau_{spec} = 1.3$ *ms* ($\tau^t_{scaled} = 2.23$) ***(a)*** *and 5.3 ms* ($\tau^t_{scaled} = 9.10$) ***(b)*** *as a function of spectroscopy laser detuning for a spectroscopy laser intensity of* $I_L = 4.9\,\mu\mathrm{W\,cm^{-2}} = 6.54 \times 10^{-6} I^t_{sat}$. *The other curves are the contributions from different motional states, corresponding to the terms in the sum of Eq. (5.19). The following notation refers to motional states* (n_{ip}, n_{op})*: (0,1)* —, *(1,1)* - - -, *(2,1)* -·-·-, *(0,2)* - - -, *(1,2)* -·-·-, *(2,2)* ·····.

in Fig. 6.3 i.e. the result of applying a RSB pulse to the readout transition in $^{40}Ca^+$ with this initial motional population. More specifically, this pulse corresponds to a π-pulse on the 1st RSB of the OP mode with respect to the $|n_{ip} = 0, n_{op} = 1\rangle$ state, i.e. $\tau_r = \pi/\Omega_{n_{ip}=0,n_{op}=1,s_{ip}=0,s_{op}=-1}$ and $\omega_L = \omega_r - \omega_{op}$. With a readout transition wavelength of 729 nm and the mode frequencies given above, we get $\eta_{ip,r} = 0.204$ and $\eta_{op,r} = 0.0917$ (the 729 nm beam propagates along the z-axis so $\hat{k}_L \cdot \hat{z} = 1$). The black curve corresponds to the expected fluorescence signal $P_{|g_r\rangle}(\tau_r)$, whereas the other colored curves are the contributions from different motional states, corresponding to the terms in the sum of Eq. (5.19). The sum of the colored curves thus gives the black curve. It is evident that the population in the different motional states seen in Fig. 6.3 are not all transferred to $|e_r\rangle$ to the same extent by the RSB pulse. Only the population in $|n_{ip} = 0, n_{op} = 1\rangle$ is fully transferred, since we specifically target this state. A bit surprisingly, the fluorescence spectrum (black curve) in Fig. 6.4.(b)

shows no sign of the depletion around resonance seen in the corresponding population spectrum presented in Fig 6.3(b). This is because the many small contributions from non-depleted higher motional states 'fill out the dip'. For very long τ^t_{scaled}, however, a depletion dip will be visible in the fluorescence signal as well.

It is clear from Fig. 6.4 that there is a spectral broadening and an increase in signal depth with τ_{spec} for a fixed $R^{\text{res},t}_{\text{abs},0}$. However, the spectroscopic signal does not significantly change as long as τ^t_{scaled} is constant. This can be seen in Fig. 6.5 (solid lines) showing the simulated signal FWHM and depth as a function of τ^t_{scaled} for various laser intensities. The slight discrepancies between the different lines are due to trap-induced heating, which I will elaborate on in Sec. 6.3.

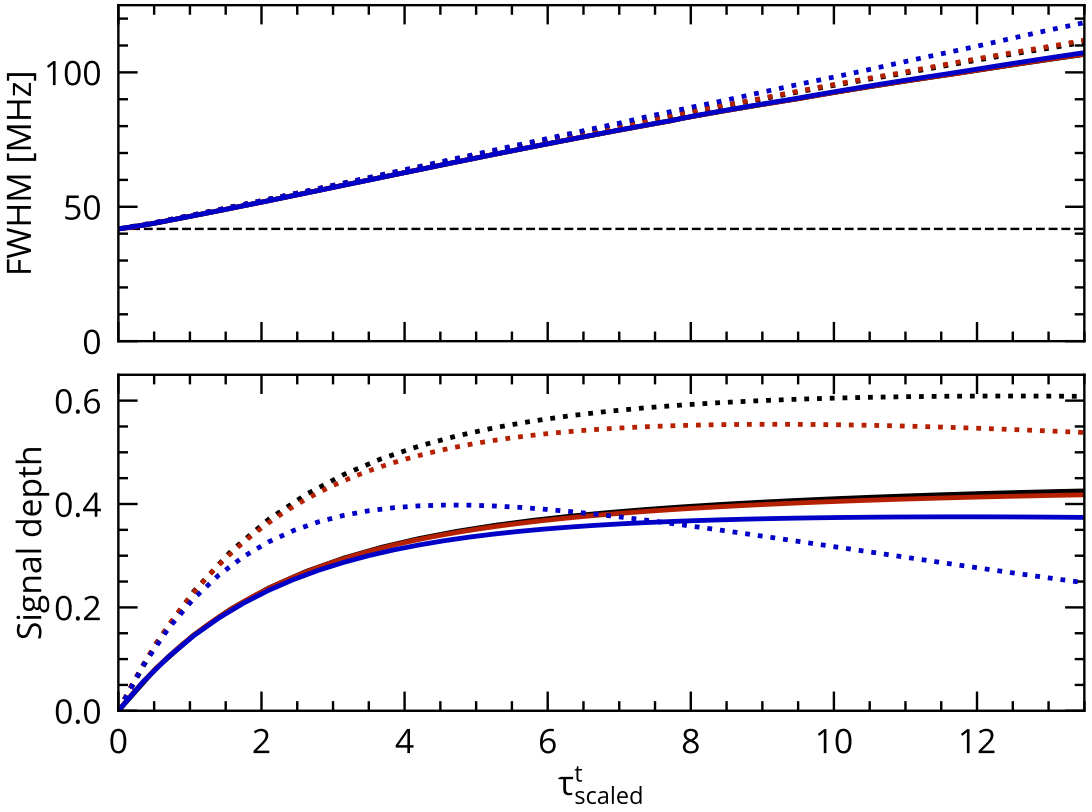

FIGURE 6.5: *FWHM (top) and signal depth (bottom) of simulated PRS spectra for readout on the OP mode (solid lines only) as a function of scaled time for three different spectroscopy laser intensities* $I_L = 1\,\mu\text{W}\,\text{cm}^{-2} = 1.34\times10^{-6} I^t_{sat}$ (—), $I_L = 5\,\mu\text{W}\,\text{cm}^{-2} = 6.68\times10^{-6} I^t_{sat}$ (—), *and* $I_L = 15\,\mu\text{W}\,\text{cm}^{-2} = 2.00\times10^{-5} I^t_{sat}$ (—). *The deviation between the lines is caused by trap-induced heating, which influences low intensities more, due to lower* $R^{res,t}_{abs,0}$ *values. The dashed line (top) represents the natural linewidth of the target transition. The dotted lines are the results for readout on both the OP and IP modes (see Sec. 6.5.3).*

The FWHM at scaled times $\tau^t_{\text{scaled}} \to 0$ has the expected value of the target transition linewidth and increases almost linearly with τ^t_{scaled}. This is because the

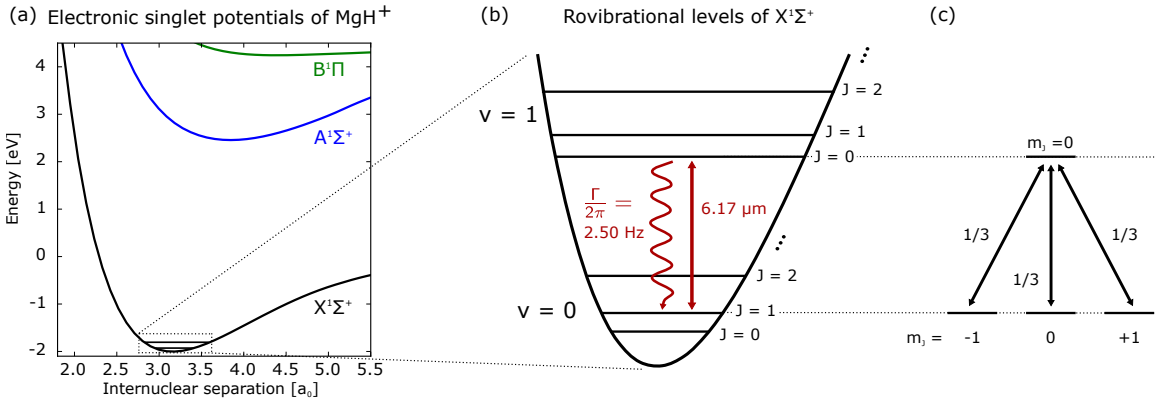

FIGURE 6.6: *(a) The electronic singlet potentials of MgH^+. Only the electronic ground state $X^1\Sigma^+$ is considered in the simulation. (b) Rovibrational structure of the electronic ground state $X^1\Sigma^+$ showing the closed transition of interest $|v = 0, J = 1\rangle - |v' = 1, J' = 0\rangle$. The decay rate of $\Gamma_t = 2\pi \times 2.50$ Hz is the slowest timescale of our experiment and spontaneous emission is negligible. (c) Sub-levels of the $|v = 0, J = 1\rangle$ and $|v' = 1, J' = 0\rangle$ states showing the norm squared of the Clebsch-Gordan coefficients.*

signal relies on the depletion of the motional ground state. Even at large detunings, there is still a small probability to excite the transition and to move population out of the motional ground state. The probability for each detuning increases with τ^t_{scaled}, but eventually saturates when all the population is moved out. As τ^t_{scaled} keeps increasing, depletion of the motional ground state happens for a broader and broader frequency span around the resonance, and thus the signal width increases indefinitely. This depletion effect also causes the observed signal depth saturation for high τ^t_{scaled}. However, if the RSB shelving pulse were efficient for all motional states, the motional state spreading beyond $|n_{ip} = 0, n_{op} = 1\rangle$ would not cause the signal to converge to values below 1. More about this in Sec. 6.5.

6.2 Laser linewidth dominating case ($^{24}MgH^+$)

In this section we present simulation results of mid-infrared rovibrational PRS of the very narrow $|v = 0, J = 1\rangle \leftrightarrow |v' = 1, J' = 0\rangle$ transition ($\Gamma_t/2\pi = 2.50$ Hz) at 6.17 µm in the $^1\Sigma^+$ electronic ground state of $^{24}MgH^+$ (see Fig. 6.6) by laser sources with varying linewidths from $\Gamma_L \sim 2\pi \times 50$ MHz to 1 GHz. The considered state is shown in Fig. 6.6. The transition is closed due to the selection rule $\Delta m_J = \pm 1$, which is why it was chosen for spectroscopy. As for the $^{24}Mg^+$ ion, the considered internal state structure does not really constitute a two-level system but a four-level one as shown in Fig. 6.6(c). However, in the basis of the light field, and choosing a linear polarization, absorption can only happen from a single rotational sub-state, the

$m_J = 0$ state. Similarly, stimulated emission can only happen back to the same sub-state and an effective two-level scheme is established with respect to interactions with the light field. However, as in the case of the $^{24}Mg^+$ ion, the saturation intensity has to be scaled by the norm squared of the relevant Clebsch-Gordan coefficient. This is implemented by scaling $R^L_{\text{abs/stim}}$ by 1/3 for both absorption and stimulated emission. The present level scheme has the further complication that population in the $m_J = \pm 1$ sub-states does not interact with the light field. Hence, if the molecular ion was originally in one of these sub-states (or if one of these sub-states were populated through spontaneous emission), it would not contribute (anymore) to the PRS signal. To avoid this effect, one can apply a magnetic field not aligned with the polarization axis of the light source, which would lead to Larmor precession of populations between the three sub-states of the $|v = 0, J = 1\rangle$ level. The situation becomes particularly simple when the Larmor frequency $\omega_{Larmor} \gg R^L_{\text{abs}}$. In this case, one can assume the total lower state population at any instance to be equally distributed between the three $m_J = 0, \pm 1$ sub-states, i.e. one third in each. Therefore we can reestablish an effective two-level scenario, but with the absorption rate (and not the stimulated emission rate) scaled by another factor of 1/3. This leads to a saturation intensity 9 times larger than the one presented in Eq. (5.13). In the following simulations, we assume this picture to be true and also disregard the hyperfine splitting of the involved rotational levels. Indeed, the splitting is typically $\sim 10\,\text{kHz}$, which is much smaller than the linewidth of the light source. All hyperfine components are thus addressed and are hence of no importance for the PRS signal.

In the basis of the B-field the rotational m_J-sublevels are split due to the interaction between the rotational angular momentum and the B-field. Linearly polarized light parallel to $\vec{B}$ is π-light, resulting in transitions of $\Delta m_J = 0$, and circularly polarized light in each direction is σ^+ and σ^- light resulting in transitions of $\Delta m_J = \pm 1$, respectively. Linearly polarized light perpendicular to $\vec{B}$ is an equal superposition of σ^+ and σ^- light. In this basis, since our B-field is vertical, horizontal linear light polarization would result in a dark state, since we cannot drive the central sub-level. To avoid dark states, we instead need a mixture of π and $\sigma^\pm$ light. We define $\vec{B} \cdot \vec{\epsilon} = B\epsilon \cos(\alpha)$, where $\vec{\epsilon}$ is the linear polarization vector. From the Clebsch-Gordan coefficients we know that the three transitions are equally strong. To repump the 3 sublevels equally efficient, the light must contain equal amounts of π, σ^+ and σ^- light. Thus, we want the horizontal component of the linearly polarized light to be twice as long as the vertical one, since the two σ-types share the strength equally. In

this way, we have the same amount of all three light types and thereby all three transitions are addressed with the same strength. The angle satisfying this requirement is $\alpha = \arctan(2) = 63.4°$.

6.2.1 Absorption and stimulated emission

We assume again $\omega_z = 2\pi \times 147.9\,\text{kHz}$ for a single $^{40}Ca^+$ ion, which leads to $\omega_{ip} = 2\pi \times 162.0\,\text{kHz}$ and $\omega_{op} = 2\pi \times 295.7\,\text{kHz}$ (only slightly different than for $^{24}Mg^+$as the target ion due to the similar mass). Both mode angular frequencies are at least about two orders of magnitude smaller than Γ_L. We are thus clearly in the regime where we can apply Eqs. 5.2-5.3 with Eq. 5.10. In the simulations presented in this chapter we use $\omega_t \to \omega_L - \Delta_t$ in Eq. 5.10 for ρ^L_{eff}. With $\lambda_t = 6.17\,\mu\text{m}$ for the target ion and the above mode angular frequencies, the LDPs are $\eta_{ip,t} = 0.0192$ and $\eta_{op,t} = 0.0224$ for the spectroscopy laser beam propagating along the z-axis. In the simulations to be presented below, we use the values $\eta_{ip,t} = 0.0136$ and $\eta_{op,t} = 0.0159$ in order to eventually compare these results with experiments. Here, the laser beam makes a 45° angle with the z-axis, and hence the LDPs are reduced by a factor $\sqrt{2}$. For the same reasons as stated in Sec. 6.1.1, the simulation results presented here should still be representative of the expected experimental signals.

6.2.2 Spontaneous emission

To simulate the effect of spontaneously emitted photons, according to Eq. 5.17 we have to take into account the particular emission pattern of the $|\nu = 0, J = 1\rangle \leftrightarrow |\nu' = 1, J' = 0\rangle$ transition (See Fig. 6.6(c)). From the upper level, the spontaneous emission pattern is completely isotropic (i.e. angle independent), since it can decay to all lower sub-levels. The general form is thus

$$W(\theta, \phi) = \frac{1}{4\pi}. \tag{6.3}$$

6.2.3 Basis for the numerical simulation

The basis for the simulations is essentially the same as in Sec. 6.1.3. However, based on Eq. 3.67, which represents the relative coupling strengths of the various sidebands, we have found that, in this case, it suffices to only take into account sidebands up to $s_{ip,max} = \pm 1$ and $s_{op,max} = \pm 1$. Because the mass ratios of the $^{40}Ca^+$ - $^{24}Mg^+$ and $^{40}Ca^+$ - $^{24}MgH^+$ systems are almost the same, we do not expect the mode coupling

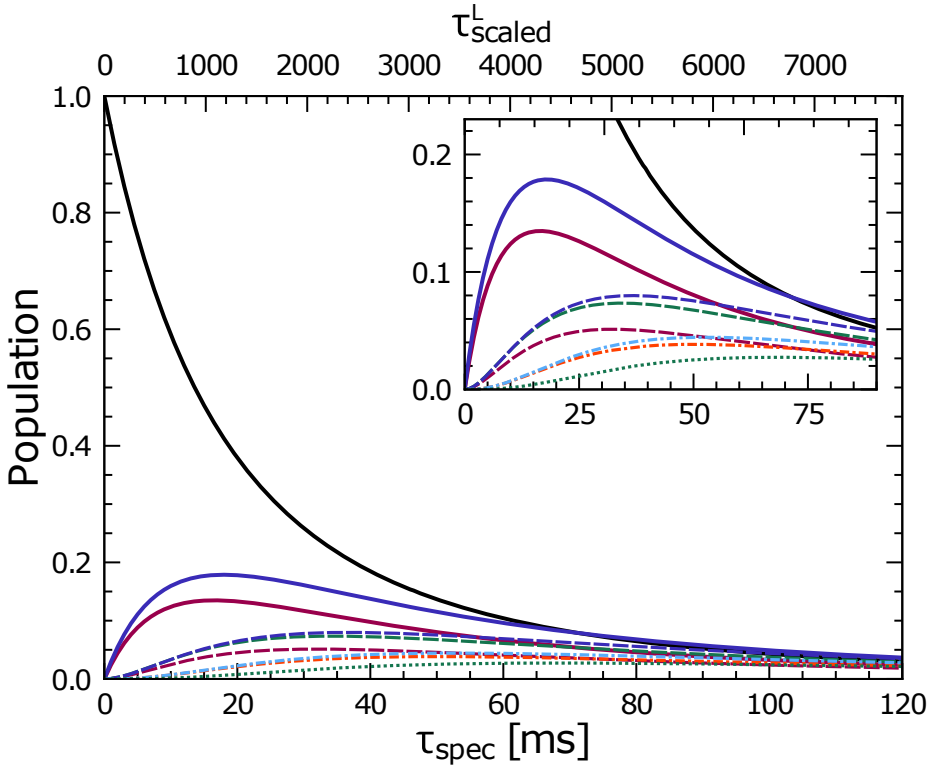

FIGURE 6.7: *Simulated evolution of the population in different motional states as a function of spectroscopy time τ_{spec} (bottom axis) and scaled time τ^L_{scaled} (top axis) on resonance. The spectroscopy laser FWHM is $\Gamma_L = 2\pi \times 250$ MHz and intensity $I_L = 7.07\,\mathrm{W\,cm^{-2}} = 4.16 \times 10^3 I^L_{sat}$. The following notation refers to motional states (n_{ip}, n_{op}): (0,0) ━, (1,0) ━, (0,1) ━, (2,0) ╍, (0,2) ╍, (1,1) ╍, (2,1) ┅, (1,2) ┅, (2,2) ┅.*

and thereby the trap-induced heating rates to be significantly different [81]. We thus use the same values of $R_{H,ip} = 14(1)\,\mathrm{s^{-1}}$ and $R_{H,op} = 1.7(3)\,\mathrm{s^{-1}}$, when modeling the $^{40}Ca^+$ - $^{24}MgH^+$ system.

6.2.4 Dynamics of motional state population

In contrast to the simulations discussed in Sec. 6.1, here $\Gamma_L \gg \Gamma_t$ and according to Eq. (5.13) the saturation intensity I^L_{sat} depends on the laser linewidth. As for the $^{24}Mg^+$ case, for laser intensities $I_L \ll I^L_{sat}$, we can ignore the stimulated emission terms in Eqs. (5.2-5.3), while in the case of $I_L \gg I^L_{sat}$, the spontaneous emission terms can be neglected. Equivalently to the $^{24}Mg^+$ case, we introduce the scaled time $\tau^L_{\mathrm{scaled}} \equiv \tau_{\mathrm{spec}} \times R^{\mathrm{res},L}_{\mathrm{abs},0}$. In Fig. 6.7, we show the evolution of the populations of the various motional states (n_{ip}, n_{op}) on resonance $(\omega_L = \omega_t)$ as a function of real time τ_{spec} (bottom x-axis) and scaled time τ^L_{scaled} (top x-axis). Here, we take $\Gamma_L/2\pi = 250$ MHz and $I_L = 7.07$ W cm^{-2} $= 4.16 \times 10^3 I^L_{sat}$ with $I^L_{sat} = 1.7$ mW cm^{-2}. Thus for this example stimulated emission dominates. As in Fig. 6.2 for $^{24}Mg^+$, the motional

ground state population (0,0) is a monotonically decreasing function of time. For short times the populations of all other motional states $(n_{ip}, n_{op}) \neq (0,0)$ increase linearly with time, while for longer times, the rate of increasing population saturates and eventually decreases as a broader range of motional states is reached. The main reason for the difference in the evolution of the excited motional state populations at a given scaled time, as compared to the $^{24}Mg^+$ case, is the difference in motional excitations per absorbed photon due to the difference in LPDs (see detailed discussion in Chapter 7).

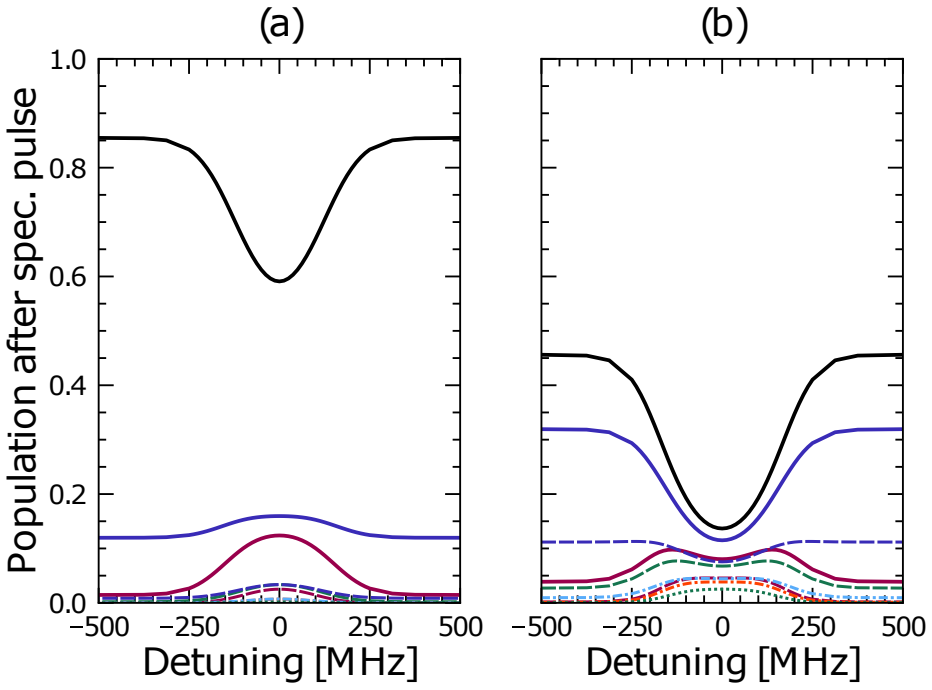

FIGURE 6.8: *Simulated population in different motional states as a function of spectroscopy laser detuning, after spectroscopy times τ_{spec} of 10 ms (τ^L_{scaled} = 655)* ***(a)*** *and 50 ms (τ^L_{scaled} = 3277)* ***(b)****. The FWHM of the spectroscopy laser is $\Gamma_L = 2\pi \times 250$ MHz and the intensity is $I_L = 7.07\,\mathrm{W\,cm^{-2}} = 4.16 \times 10^3 I^L_{sat}$. The following notation refers to motional states (n_{ip}, n_{op}): (0,0) —, (1,0) —, (0,1) —, (2,0) - - -, (0,2) - - -, (1,1) - - -, (2,1) -·-·-, (1,2) -·-·-, (2,2) ·····.*

6.2.5 Motional population spectra

By scanning the laser frequency ω_L across the resonance of the $|v = 0, J = 1\rangle \leftrightarrow |v' = 1, J' = 0\rangle$ transition, we obtain the motional population spectra. In Fig. 6.8, we present two such spectra for $\Gamma_L/2\pi = 250$ MHz, $I_L = 7.07$ Wcm$^{-2} = 4.16 \times 10^3 I^L_{sat}$ and for spectroscopy times $\tau_{\mathrm{spec}} = 10\,\mathrm{ms}$ and $50\,\mathrm{ms}$ ($\tau^L_{\mathrm{scaled}} = 655$ and 3277). For these parameters one clearly sees the effect of motional state depletion, but the higher weakly populated states now have a spectral response reflecting the Gaussian

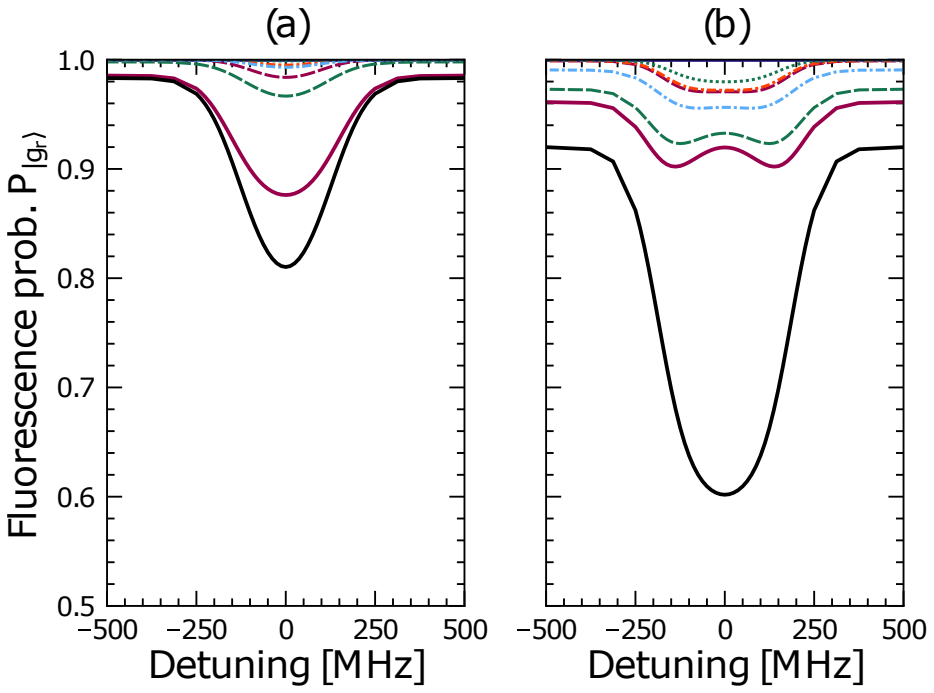

FIGURE 6.9: *Simulated fluorescence probability* $P_{|g_r\rangle}$, —, *corresponding to the expected signal for readout on the OP mode, for spectroscopy pulse lengths* τ_{spec} *of 10 ms* (τ^L_{scaled} *= 655)* ***(a)*** *and 50 ms* (τ^L_{scaled} *= 3277)* ***(b)*** *as a function of spectroscopy laser detuning, for a FWHM of* $\Gamma_L = 2\pi \times 250$ *MHz and intensity of* $I_L = 7.07\,\mathrm{W\,cm^{-2}} = 4.16 \times 10^3 I^L_{sat}$ *on resonance. The remaining curves are the contributions from various motional states, corresponding to the terms in the sum of Eq. (5.19). The following notation refers to motional states* (n_{ip}, n_{op})*: (0,1)* —*, (1,1)* - - -*, (2,1)* -·-·-*, (0,2)* - - -*, (1,2)* -·-·-*, (2,2)* ·····.

line shape of the laser. Another difference from the $^{24}Mg^+$ case is the increased background stemming from trap-induced heating. We will come back to the effect of trap induced heating on the PRS spectra in Sec. 6.3.

6.2.6 Readout spectra

To simulate the PRS spectrum, we follow the same recipe as in Sec. 6.1.6. In Fig. 6.9, we show readout spectra corresponding to the two population spectra in Fig. 6.8 after first having applied the readout pulse. The latter corresponds to a π-pulse with respect to the $|n_{ip} = 0, n_{op} = 1\rangle \rightarrow |n_{ip} = 0, n_{op} = 0\rangle$ 1st RSB of the $^{40}Ca^+$ quadrupole transition. With a transition wavelength of 729 nm, and the mode frequencies given above, we get $\eta_{ip,r} = 0.203$ and $\eta_{op,r} = 0.0949$. As for the $^{24}Mg^+$ case the fluorescence spectrum in Fig. 6.9(b) shows no sign of the depletion around resonance that could be seen in the corresponding population spectra presented in Fig 6.8(b).

It is clear from Fig. 6.9 that there is a spectral broadening and an increase in signal depth with τ_{spec} for a fixed $R^{\mathrm{res},L}_{\mathrm{abs},0}$. However, the spectroscopic signal does not

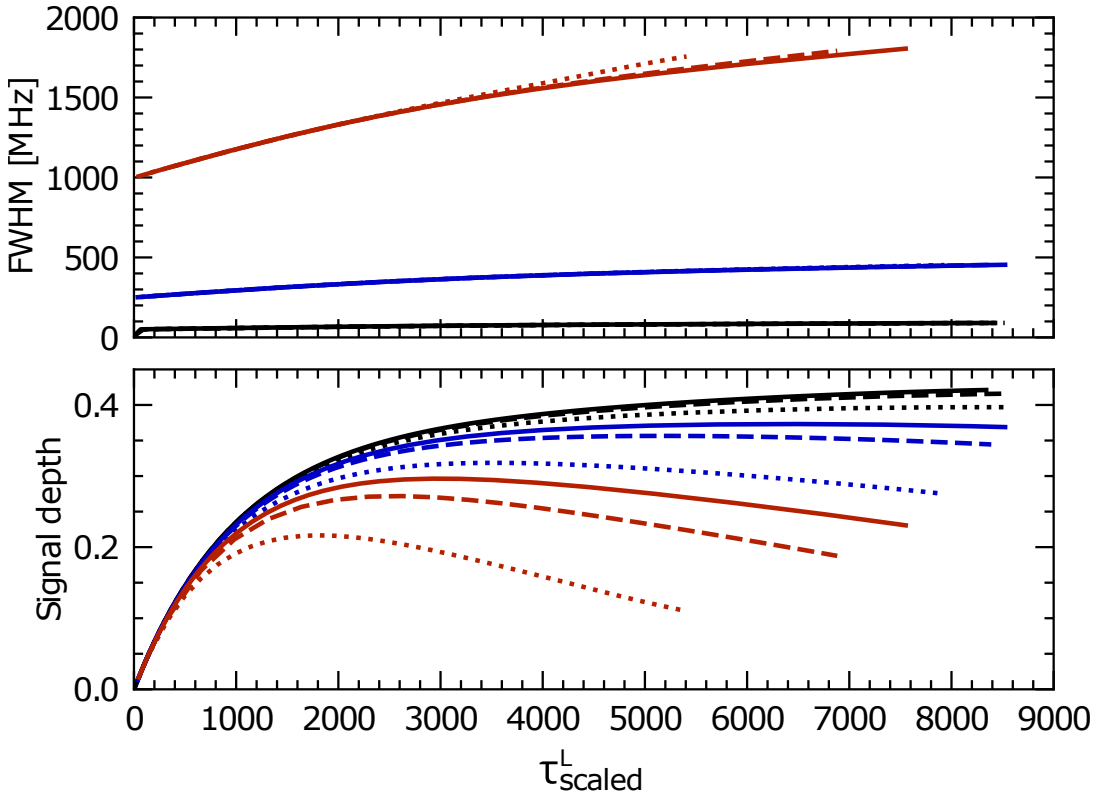

FIGURE 6.10: *FWHM (top) and signal depth (bottom) of simulated fluorescence probability spectra for readout on the OP mode as a function of scaled time for three different spectroscopy laser FWHM $\Gamma_L/2\pi$ of 50 MHz (—), 250 MHz (—), and 1 GHz (—) and 3 different intensities: $I_L = 20.0\,\mathrm{W\,cm^{-2}}$ (solid), $I_L = 14.15\,\mathrm{W\,cm^{-2}}$ (dashed), and $I_L = 7.07\,\mathrm{W\,cm^{-2}}$ (dotted). The deviation in signal depth for the different intensities is caused by trap-induced heating, which influences low intensities and broad spectroscopy laser linewidths more due to slower spectroscopy laser heating.*

significantly change as long as τ^L_{scaled} is a constant. This can be seen in Fig. 6.10 showing the simulated signal FWHM and depth as a function of τ^L_{scaled} for various laser intensities and linewidths Γ_L. The discrepancies between the different lines are due to trap-induced heating. The FWHM at scaled times $\tau^L_{\mathrm{scaled}} \to 0$ has the expected value of the laser linewidth, and then increases almost linearly with τ^L_{scaled}.

6.3 Effect of trap-induced heating

As already mentioned in relation to Fig. 6.5 and 6.10 showing the PRS signal depth as a function of scaled time for the $^{24}Mg^+$ and $^{24}MgH^+$ example cases, respectively, trap-induced heating effectively reduces the PRS signal. In these figures, we use the scaled times $\tau^{t/L}_{\mathrm{scaled}}$ for the respective systems, such that the evolution should be completely independent of laser energy spectral density, i.e. I_L and also Γ_L in the laser linewidth

dominating case. However, especially for low laser spectral densities the signal depths are reduced. We see this effect much more strongly for the $^{24}MgH^+$ example in Fig. 6.10 compared to the $^{24}Mg^+$ case in Fig. 6.5. This is because the PRS signal depth is a measure of how much population is moved out of the motional ground state by the laser alone. Ideally this population depletion would only be caused by the spectroscopy laser, however, simultaneously the population is moved out of the ground state via trap-induced heating, i.e. with the rates $R_{H,ip}$ and $R_{H,op}$ independent of the laser. Thus if the rate of ground state depletion by the laser is not fast compared to the trap-induced heating rates, we cannot obtain a considerable signal depth. To understand this better we define P_{off} as the probability for fluorescence when the spectroscopy laser is far from resonance or even completely off during τ_{spec}. If $P_{off} < 1$ we have trap-induced heating. Remember that in the case of no trap-induced heating, normally a fluorescence probability smaller than 1 corresponds to a positive PRS signal. In comparison, when the laser is on and close enough to resonance to excite the target transition the fluorescence probability is denoted P_{on}. However P_{on} is a result of the combined motional excitation caused by both the laser and the trap-induced heating. So if $P_{on} < 1$ it can stem from both effects. Therefore we always have $P_{off} \geq P_{on}$. With this notation the signal depth is given by $P_{off} - P_{on}$.

In Fig. 6.11 we show an example for the $^{24}MgH^+$ case with laser parameters $\Gamma_L/(2\pi)$ and $I_L = 20\ \text{W/cm}^2$. In the top panel we compare the evolution of the PRS signal depth $P_{off} - P_{on}$ with and without trap-induced heating with rates $R_{H,ip} = 14(1)\,\text{s}^{-1}$ and $R_{H,op} = 1.7(3)\,\text{s}^{-1}$ during the spectroscopy pulse of duration τ_{spec}. This is the same as plotted in the bottom panel of Fig. 6.10 with the same trap-induced heating for all lines. In the bottom panel of Fig. 6.11 the individual P_{off} (black) and P_{on} (light blue) values are plotted without (solid lines) and with (dashed lines) trap-induced heating. We see that P_{on} saturates almost interdependently of the trap-induced heating, whereas P_{off} is linear in time. Hence P_{off} effectively cuts into the signal depth.

The rate by which population is moved out of the motional ground state by the spectroscopy laser at resonance is approximately given by $R_{abs}^{motional} = R_{abs,0}^{res,t/L} \times 2(\eta_{ip,t}^2 + \eta_{op,t}^2)$. This extra factor depending on the Lamb-Dicke parameters will be accounted for in detail in Chapter 7. However, it makes good physical sense that the motional excitation rate depends on the LDPs, since they describe the ratio between the recoil energy and the energy difference between the motional mode levels.

If we consider the $^{24}MgH^+$ case, using $I_L = 20\ \text{W/cm}^2$ and $\Gamma_L/(2\pi) = 1$ GHz as in Fig. 6.11 (also red solid line in Fig. 6.10) we obtain $R_{abs}^{motional} \sim 40\ \text{s}^{-1}$. This is similar

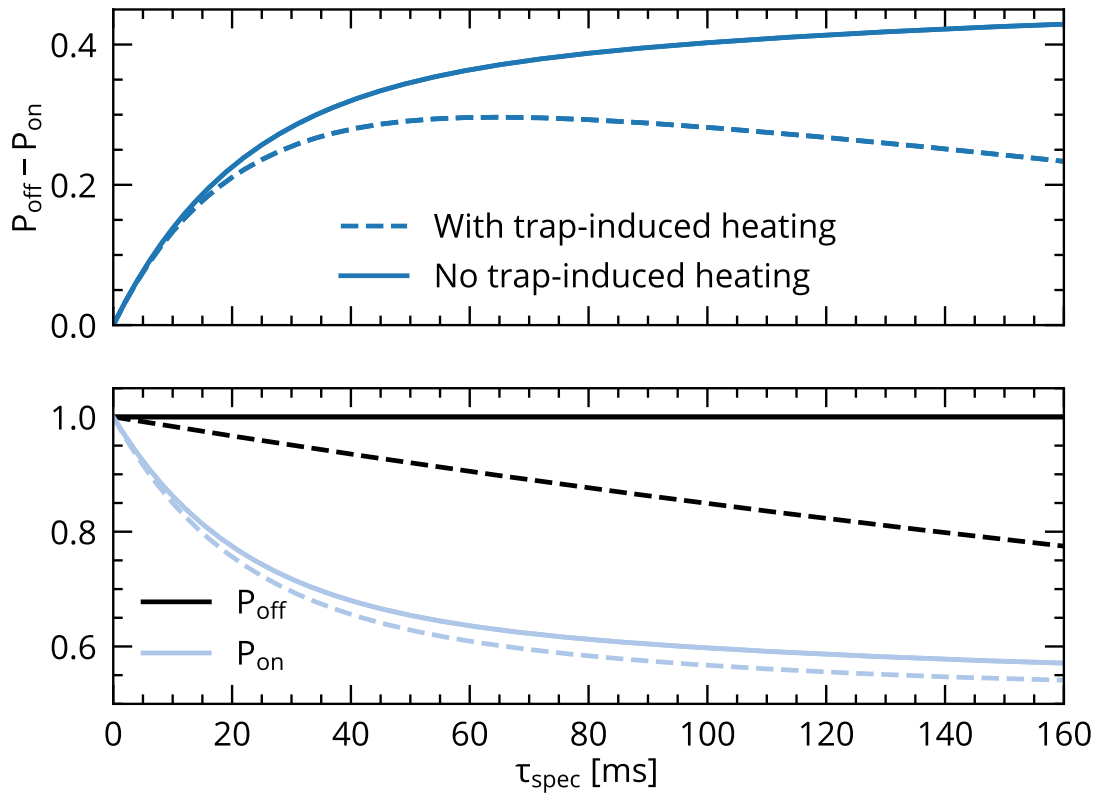

FIGURE 6.11: ***Top:*** *Comparison of the evolution of the PRS signal depth $P_{off} - P_{on}$ with and without trap-induced heating with rates $R_{H,ip} = 14(1)\,\mathrm{s}^{-1}$ and $R_{H,op} = 1.7(3)\,\mathrm{s}^{-1}$ during the spectroscopy pulse of duration τ_{spec}.* ***Bottom:*** *The expected P_{off} (black) and P_{on} (light blue) fluorescence signals without (solid lines) and with (dashed lines) trap-induced heating. The example case is $^{24}MgH^+$ with laser parameters $\Gamma_L/(2\pi)$ and $I_L = 20\ W/cm^2$.*

to the considered heating rates of $R_{H,ip} = 14(1)\,\mathrm{s}^{-1}$ and $R_{H,op} = 1.7(3)\,\mathrm{s}^{-1}$. For a 20 times smaller laser FWHM of $\Gamma_L/(2\pi) = 50$ MHz (black solid line in Fig. 6.10) $R_{abs}^{motional}$ is 20 times larger i.e. around 2000 s^{-1}, which is much larger than the trap induced heating rates, and hence we do not see any decrease in signal depth compared to the no trap-induced heating example in Fig. 6.11. To compare to the $^{24}\mathrm{Mg}^+$ case we consider $I_L = 4.9\,\mu\mathrm{W\,cm}^{-2}$ (red solid line in Fig. 6.5) and get $R_{abs}^{motional} \sim 742\ \mathrm{s}^{-1}$, which is also much larger than the trap-induced heating rates, as expected.

Hence, by calculating $R_{abs}^{motional}$ and comparing it to measured trap-induced heating rates, one can get a quick feeling for whether PRS experiment for the given system and parameters, including the spectroscopy light field, are feasible. So even though excitation of the target line does not happen coherently in unresolved sideband PRS, trap induced heating rates can still be a limiting factor.

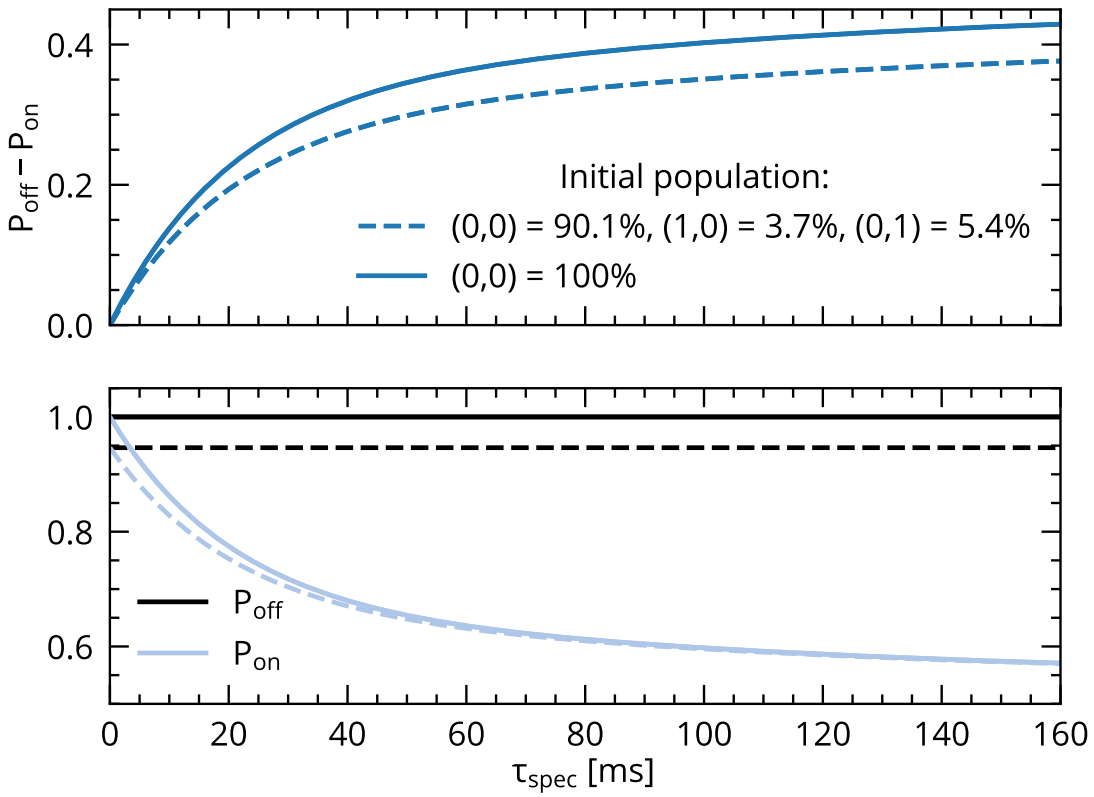

FIGURE 6.12: ***Top:*** *Comparison of the evolution of the PRS signal depth* $P_{off} - P_{on}$ *for different initial populations* (n_{ip}, n_{op}) *before the spectroscopy pulse of duration* τ_{spec}. ***Bottom:*** *The expected* P_{off} *(black) and* P_{on} *(light blue) fluorescence signals for perfect ground state cooling (solid lines) and imperfect ground state cooling (dashed lines) as given in the top panel. The example case is* $^{24}MgH^+$ *with laser parameters* $\Gamma_L/(2\pi)$ *and* $I_L = 20$ W/cm^2.

6.4 Effect of imperfect ground state cooling

In the top panel of Fig. 6.12 the PRS signal depth $P_{off} - P_{on}$ for perfect and imperfect ground state cooling before the spectroscopy pulse of duration τ_{spec} is shown. The example case is as in Fig. 6.11 $^{24}\text{MgH}^+$ with laser parameters $\Gamma_L/(2\pi)$ and I_L = 20 W/cm^2. In this example imperfect ground state cooling corresponds to average motional populations of $\bar{n}_{ip} = 0.04$, $\bar{n}_{op} = 0.06$ corresponding to $P_{|0,0\rangle} = 0.901$, $P_{|1,0\rangle}$ = 0.037, $P_{|0,1\rangle}$ = 0.054. In this case the population in higher states is so low, that we choose to normalize to the two first states of each mode. We see that an initial population different from zero reduces the signal depth.

In the bottom panel of Fig. 6.12 the expected P_{off} (black) and P_{on} (light blue) fluorescence signals for perfect ground state cooling (solid lines) and the same imperfect ground state cooling (dashed lines) are given. We see that P_{on} goes towards

the same value for long times regardless of the initial state, and that P_{off} is constant since we assume no trap-induced heating. The common initial value of P_{off} and P_{on} corresponds to 1 minus the initial population in the (0,1) motional state (1-0.054 = 0.946) since we read out on the OP mode.

If one only knows P_{off} and P_{on} at $\tau_{\text{spec}} > 0$ it is impossible to know whether a non-zero P_{off} stems from trap-induced heating or imperfect ground state cooling. In order to assess this, the ground state population must be measured at $\tau_{spec} = 0$ before trap-induced heating has time to move the population.

6.5 Readout efficiency

The readout efficiency is the percentage of the population in $|n_{ip}, n_{op}\rangle > 0$ which the resolved RSB shelving pulse can transfer to $|e_r\rangle$. The population could have ended up in $|n_{ip}, n_{op}\rangle > 0$ either due to the spectroscopy laser or trap-induced heating. It could also have been there before the spectroscopy pulse, due to imperfect sideband cooling to $|n_{ip}, n_{op}\rangle = 0$. How it got there does, however, not influence the readout efficiency.

6.5.1 Limitations of the π-pulse technique

The π-pulse technique applied so far is limited by the fact, that it does not transfer the population in all $|n_{ip}, n_{op}\rangle > 0$ to $|e_r\rangle$ with the same efficiency. The efficiency as a function of motional state is given by the factor

$$P_{|e_r,i_t,n_{ip},n_{op}\rangle}(\tau_r) = \sin^2\left(\Omega_{n_{ip},n_{op},s_{ip}=0,s_{op}=-1} \times \frac{\tau_r}{2}\right) \tag{6.4}$$

from Eq. 5.19, where we so far have used $\tau_r = \pi/\Omega_{n_{ip}=0,n_{op}=1,s_{ip}=0,s_{op}=-1}$ and $\omega_L = \omega_r - \omega_{op}$ corresponding to a π-pulse on the 1st RSB of the OP mode with respect to the $|n_{ip} = 0, n_{op} = 1\rangle$ state. Eq. 6.4 is thus only 1 for $|n_{ip} = 0, n_{op} = 1\rangle$. In fact, none of the population in $|n_{ip} = 0, n_{op} = 0\rangle$ is transferred, since the 1st OP RSB does not exist for these states.

For very long $\tau^{t/L}_{\text{scaled}}$ the population is spread out over many motional states far from $|n_{ip}, n_{op}\rangle = 0$. In this limit $P_{|g_r\rangle} \to 1/2$ (the average value of a $\sin^2(x)$ function). Thus when applying the π-pulse technique for shelving, the signal depth can be 1 only in the resolved PRS regime, where the motional ground state population is coherently driven to one specific excited motional state.

6.5.2 Effect of an imperfect π-pulse for shelving

If $\omega_L = \omega_r - \omega_{op}$ or $\tau_r = \pi/\Omega_{n_{ip}=0,n_{op}=1,s_{ip}=0,s_{op}=-1}$ is not fulfilled the RSB shelving pulse will not be a perfect π-pulse. Then the transfer efficiency will be decreased for the intended $|n_{ip}, n_{op}\rangle$, but the transfer efficiency could actually be better for other motional states. However since one wants to target the state giving the largest signal depth, an imperfect π-pulse will most likely be a disadvantage.

Effectively the imperfect transfer will reduce both P_{on} and P_{off}. If we denote by P_{imp} the percentage of transfer compared to the perfect π-pulse case we have

$$P'_{on} = 1 - (1 - P_{on})P_{imp} \tag{6.5}$$

$$P'_{off} = 1 - (1 - P_{off})P_{imp} \tag{6.6}$$

resulting in the reduced signal depth

$$P'_{off} - P'_{on} = (P_{off} - P_{on})P_{imp}. \tag{6.7}$$

So the signal depth is simply scaled by the new transfer efficiency. If we know the used τ_r or ω_L we can calculate P_{imp} from Eq. 5.18

6.5.3 Multiple shelving pulses

The following is specific for our $^{40}Ca^+$ readout ion, but something similar could be done using another atomic readout ion.

After sideband cooling and state initialization the $^{40}Ca^+$ ion starts out in $S_{1/2}$, $m_J = -1/2$. Specifically when performing the RSB shelving pulse on the $S_{1/2}$ to $D_{5/2}$ quadropolar transition in $^{40}Ca^+$, we do it from $m_J = -1/2$ to $m_J = -3/2$, since this is the least sensitive to magnetic field fluctuations. However all transitions of $\Delta m_J = \pm 1, \pm 2$ are allowed[1] meaning we can in principle drive to m_J = -5/2, -3/2, 1/2, and 3/2 in $D_{5/2}$ as illustrated in Fig. 6.13.

This can be exploited to target four different motional states, and not only $|n_{ip} = 0, n_{op} = 1\rangle$, by applying τ_r corresponding to a π-pulses for different motional states. If the four different pulses were simply done in succession between the same

[1]Electric quadropole transitions allow $\Delta m_J = 0, \pm 1, 2$, on certain conditions. The 729 nm laser beam (horizontal) has a 90° angle to the quantization axis defined by the magnetic field axis (vertical). Consequently $\Delta m_J = 0$ is not allowed for the specific beam geometry. Transitions with $\Delta m_J = \pm 1$ and $\Delta m_J = \pm 2$ has equal coupling strength if the light polarization has a 45° angle to the quantization axis, which is the case in the experiment.

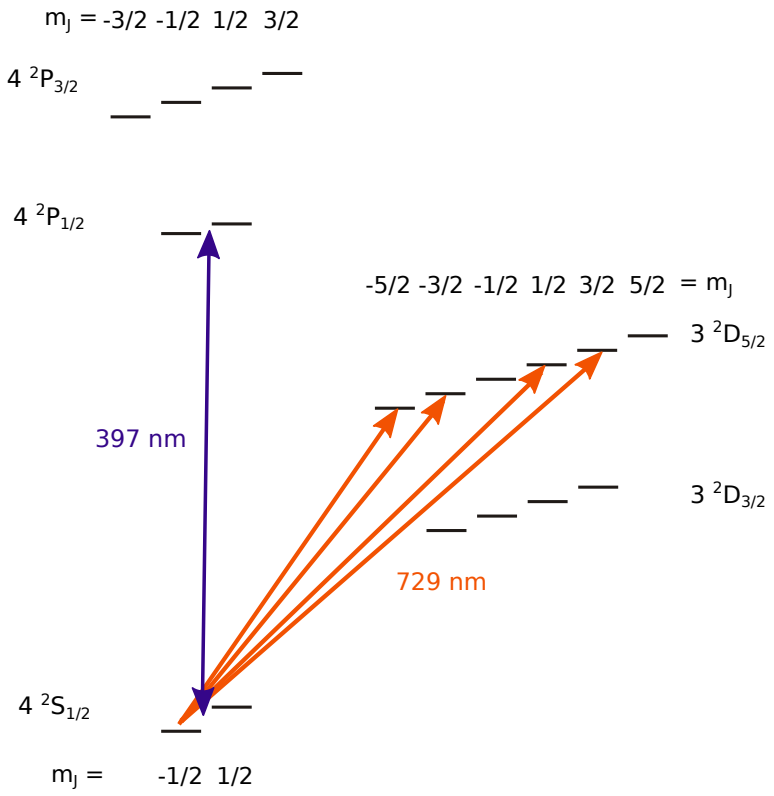

FIGURE 6.13: *The transitions in $^{40}Ca^{+}$ used for RSB shelving (729 nm) and fluorescence readout (397 nm). If the ion is moved to the $D_{5/2}$ state by the shelving pulse the 397 nm transition cannot be driven and the ion cannot fluoresce. Four different Zeeman sublevels of the 729 nm transitions can be driven with different pulse lengths corresponding to π-pulse for different $|n_{ip}, n_{op}\rangle$ states. Figure from [95].*

two m_J sub-levels, we would risk driving the population back to the electronic ground state due to the coherent nature of the transfer. Targeting more motional states increases the maximum signal depth above 1/2, since the different contributions are added to give the final signal. To find out which motional states to target one should look at the motional population spectra of Fig.s 6.3 and 6.8. From these figures it is evident why we chose to initially target $|n_{ip} = 0, n_{op} = 1\rangle$: the depth of the motional population is the largest of all motional states. This is because $\eta_{op,t} > \eta_{ip,t}$ such that the excitation by the laser is faster for the OP mode than for the IP mode, and because $R_{H,op} < R_{H,ip}$ making the excitation from trap-induced heating slower. Both these things work in favor of the $|n_{ip} = 0, n_{op} = 1\rangle$ state.

In Fig.s 6.3 the motional population depth of $|n_{ip} = 1, n_{op} = 0\rangle$ is almost as high, so this state would also be obvious to target. However in Fig. 6.8 the depth of the $|n_{ip} = 1, n_{op} = 0\rangle$ population is drastically reduced due to trap-induced heating to a point, where it would actually reduce the total signal depth to target it directly. By only driving the 1st OP RSB in this case we avoid this extra P_{off} contribution.

In Fig. 6.5 the dotted lines represent the result when applying two successive RSB π-pulses targeting first $|n_{ip} = 0, n_{op} = 1\rangle$ and then $|n_{ip} = 1, n_{op} = 0\rangle$ (the order is irrelevant). In this example the two-pulse technique drastically improves the expected signal depth to values above 1/2, which is the highest possible for a single π-pulse. However we also see that for the smallest laser intensity shown, it is not an advantage, so the technique should be used with caution.

6.5.4 Perfect shelving from all motional states

Since we are limited to doing four successive shelving pulses on the $^{40}Ca^{+}$ readout ion, it will unfortunately not be possible to transfer all the population in $|n_{ip}, n_{op}\rangle > 0$ to $|e_r\rangle$ using RSB π-pulses. If we could, the resulting fluorescence level would exactly reflect the remaining motional ground state population, like in the resolved PRS scenario.

However, other types of light pulses exist, which could maybe transfer the population via the RSB with 100% efficiency independent of motional state. Even if such a perfect 1st RSB pulse existed, one would still need to apply one for both the OP and IP mode to transfer everything. An interesting candidate is the Rapid adiabatic passage (RAP) technique [104] where the light intensity and detuning is swept during the pulse. This results in a transfer fidelity close to 100%, which is very robust towards laser and magnetic field fluctuations, i.e. changes in Rabi frequency. This robustness to different Rabi frequencies could possibly be exploited to use the RAP technique to transfer population effectively from different motional states which intrinsically have unequal Rabi frequencies [105].

For the RAP to be fast and the fidelity high, the detuning sweep much be broad. This complicates the idea of using RAP on a sideband transition, since the coupling to the carrier is much higher. One would thus risk to also transfer population on the carrier transition from $|n_{ip} = 0, n_{op} = 0\rangle$, completely ruining the basis for PRS, which relies on $\Omega_{n_{ip}=0,n_{op}=0,s_{ip}<0,s_{op}<0}$ being zero. Whether this can be avoided for the specific example systems given in this chapter would need to be investigated further.

6.6 Independence of the initial internal state of the target ion

As we have seen the motional ground state depletion by the spectroscopy laser resulting in a PRS signal can equally well happen during an absorption event or an

emission event. Therefore the following question naturally arises: is it necessary to be initially prepared in the ground state of the target transition $|g_t\rangle$, or would the PRS signal be the same if the target ion were instead prepared in the excited state $|e_t\rangle$?

Let us start by looking at the case of a perfect 2-level system, where stimulated emission dominates. Here the rates from $|e_t\rangle$ to $|g_t\rangle$ and vice versa are the same, but the rates to specific motional states through the sideband transitions $|g_t, n_{ip}, n_{op}\rangle \rightarrow \left|e_t, n'_{ip}, n'_{op}\right\rangle$ and $|e_t, n_{ip}, n_{op}\rangle \rightarrow \left|g_t, n'_{ip}, n'_{op}\right\rangle$ are also the same. This can be seen by looking at the scaling factor ξ (Eq. 3.67). It is the same for all transitions connecting the same motional states independent of the internal state of the ion, since only the absolute values of the sideband orders enter into the expression. E.g. ξ is the same for the $|g_t, 0, 0\rangle \rightarrow |e_t, 0, 1\rangle$ transition and the $|e_t, 0, 0\rangle \rightarrow |g_t, 0, 1\rangle$ transition. This means that not only are the R^L_{abs} and R^L_{stim} rates out of the motional ground state equal, they also send the population to the same excited motional states. From a PRS perspective, the signal only depends on the motional state distribution and not the initial internal state of the target ion, and hence it does not matter, whether the target ion is initially prepared in $|g_t\rangle$ or $|e_t\rangle$.

For the considered target transition in $^{24}MgH^+$ the absorption rate and stimulated emission rate are not equal due to the sub-level structure. Instead we have $R_{abs} = \frac{1}{3}R_{stim}$ in order to make the transition resemble a 2-level system.

From running some test simulations the rate out of the motional ground state was found to be dependent on R^L_{abs} and R^L_{stim} as the sum of two decay channels

$$R^{motional} \propto \frac{1}{1/R^L_{abs} + 1/R^L_{stim}}. \tag{6.8}$$

This means, that if we swap R^L_{stim} and R^L_{abs} in the rate equations, we obtain the same PRS signal. Consequently it does not matter if we start out in $|g_t\rangle$ or $|e_t\rangle$ even though R^L_{stim} and R^L_{abs} are not equal. Both these scenarios were tested using the full rate equation model, and the same results were obtained.

Conversely, for a system dominated by spontaneous emission the ground state depletion is not expected to be independent of initial state since R^t_{abs} and R^t_{spon} are not proportional. R^t_{abs} does not depend on Γ_t as seen in Eq. 5.11. From an experimental standpoint it is not so relevant to talk about preparation in $|e_t\rangle$ for strong spontaneous emission, since the lifetime of the state is very short. However, preparation in $|e_t\rangle$ for the $^{24}Mg^+$ case was tested numerically using the full rate equation model, and the motional population dynamics were found to be different as expected.

Chapter 7

Simple qualitative physical model of unresolved sideband PRS

In this chapter we will present how one can, in a simple physical picture, understand the spectroscopic signals obtained in Chapter 6. While it is essentially irrelevant whether the target ion is initially in the ground or excited state of the target transition, the initial motional state of the two-ion system is highly important, as we saw in Sec. 6.4 about imperfect ground state cooling. This is because the spectroscopic signal is in essence a measure of how much population is left in the motional ground state after the application of the spectroscopic light pulse as we saw in Sec. 6.5.4. If the RSB shelving pulse(s) on the readout ion could transfer all population in $n_{ip}, n_{op} > 0$ to $|e_r\rangle$, the resulting fluorescence level would exactly reflect the remaining motional ground state population.

From this insight, one can describe the essence of unresolved sideband PRS through a 3-level picture as depicted in Fig. 7.1. In this picture, in addition to the two target transition levels $|g_t\rangle$ and $|e_t\rangle$, one considers a third auxiliary level, $|\text{aux}\rangle$, which is a collection of all states with $n_{ip}, n_{op} > 0$ and which is populated

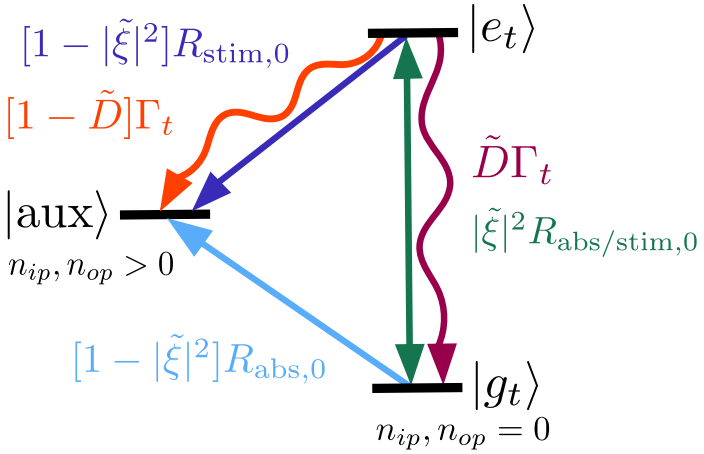

FIGURE 7.1: *Level scheme of the 3-level model of PRS including the considered transition processes and their rates.*

whenever absorption or emission leads to a change in motional state away from the ground state. During a spontaneous emission event the probability to stay within $n_{ip}, n_{op} = 0$ is $\tilde{D} = D(\eta_{ip,t}, \eta_{op,t}, 0, 0, 0, 0)$. Since

$$\sum_{s_{ip}, s_{op}} D(\eta_{ip,t}, \eta_{op,t}, n_{ip}, n_{op}, s_{ip}, s_{op}) = 1 \tag{7.1}$$

(the system has to decay to *some* state) the probability to go to $|\text{aux}\rangle$ is $1 - \tilde{D}$. Likewise, during a single absorption or stimulated emission event the probability to stay in the motional ground state is $|\tilde{\xi}|^2 = |\xi(\eta_{ip,t}, \eta_{op,t}, 0, 0, 0, 0)|^2$, and since

$$\sum_{s_{ip}, s_{op}} |\xi(\eta_{ip,t}, \eta_{op,t}, n_{ip}, n_{op}, s_{ip}, s_{op})|^2 = 1 \tag{7.2}$$

the probability to go to $|\text{aux}\rangle$ is $1 - |\tilde{\xi}|^2$. In principle the stimulated probabilities also depend on the specific sideband transition frequency through the effective energy spectral density $\rho_{\text{eff}}^{t/L}$ from Eq.s 5.9 and 5.10. However, an important feature of sideband unresolved PRS is that the carrier and the first sideband orders are simultaneously excited by almost the same energy spectral density. This is especially the case for carrier resonance conditions, since the spectral shape of the broad transition or laser will in many cases be approximately flat in the center. In the 3-level model we thus assume all sideband transition frequencies to be equal to ω_t. The rate equations for the 3-level model are thus (see Fig. 7.1)

$$\begin{aligned}
\frac{\mathrm{d}}{\mathrm{d}t} P_{|g_t\rangle} &= -R_{\text{abs},0} P_{|g_t\rangle} + (|\tilde{\xi}|^2 R_{\text{stim},0} + \tilde{D}\Gamma_t) P_{|e_t\rangle} \\
\frac{\mathrm{d}}{\mathrm{d}t} P_{|e_t\rangle} &= -(\Gamma_t + R_{\text{stim},0}) P_{|e_t\rangle} + |\tilde{\xi}|^2 R_{\text{abs},0} P_{|g_t\rangle} \\
\frac{\mathrm{d}}{\mathrm{d}t} P_{|\text{aux}\rangle} &= [(1 - \tilde{D})\Gamma_t + (1 - |\tilde{\xi}|^2) R_{\text{stim},0}] P_{|e_t\rangle} \\
&\quad + (1 - |\tilde{\xi}|^2) R_{\text{abs},0} P_{|g_t\rangle}.
\end{aligned} \tag{7.3}$$

While in our full rate equation model presented in Sec. 5.2. absorption and emission processes can also bring back population from excited motional states to the ground state, we chose to neglect it in the 3-level model for two reasons: 1) since $|\text{aux}\rangle$ is initially empty, the rates out of it will not play a role for short spectroscopy pulse times, 2) by including the rates out of $|\text{aux}\rangle$, which depend on specific motional states and sideband orders, we would soon reach the same level of complexity as for the full model, which is not desired.

Since typically $\tilde{D} \approx |\tilde{\xi}|^2$ ($\tilde{D} = 0.8608$, $|\tilde{\xi}|^2 = 0.8057$ for the $^{24}Mg^+$ case presented in Sec. 6.1 and $\tilde{D} = 0.9989$, $|\tilde{\xi}|^2 = 0.9996$ for the $^{24}MgH^+$ case presented in Sec. 6.2) PRS of systems (including the spectroscopy light field) where either spontaneous or stimulated emission dominates are not going to be fundamentally different, however the timescale of the motional ground state depletion is system dependent through Γ_t, $\rho_{\text{eff}}^{t/L}$, η_{ip}, η_{op} and if required the scaling of $R_{abs/stim}$ needed to make the transition resemble a 2-level system.

This fact can be highlighted by defining a new scaled time describing the number of motional excitations after a spectroscopy pulse time τ_{spec}, instead of the number of absorbed photons expressed by $\tau_{\text{scaled}}^{t/L}$. For each absorption event, the target ion has to decay again, and both up and down the motional state can be excited. To find the probability to leave the motional ground state during a combined absorption and emission event, we start by finding the probability for *not* doing so. From $|g_t, 0, 0\rangle$ the probability to absorb to $|e_t, 0, 0\rangle$ and then decay back to $|g_t, 0, 0\rangle$ via stimulated emission is $P_{stay} = P_{stay}^{abs} \times P_{stay}^{stim} = |\tilde{\xi}|^4$. From this, the probability to leave the motional ground state during a combined absorption and emission event must necessarily be

$$\begin{aligned} P_{leave} &= 1 - P_{stay} \\ &\approx 1 - |\tilde{\xi}|^4 \\ &= 1 - (e^{-\eta_{ip}^2/2 - \eta_{op}^2/2})^4 \\ &= 1 - e^{-2(\eta_{ip}^2 + \eta_{op}^2)} \\ &\approx 1 - (1 - 2(\eta_{ip}^2 + \eta_{op}^2)) \\ &= 2(\eta_{ip,t}^2 + \eta_{op,t}^2). \end{aligned} \tag{7.4}$$

If spontaneous emission dominates $P_{stay} = P_{stay}^{abs} \times P_{stay}^{spon} = |\tilde{\xi}|^2 \times \tilde{D}$, however we assume $\tilde{D} \approx |\tilde{\xi}|^2$. From P_{leave} we can now define the motional scaled time

$$\tau_{\text{scaled}}^{\text{motional}} \equiv \tau_{\text{scaled}}^{t/L} \times 2(\eta_{ip,t}^2 + \eta_{op,t}^2) \tag{7.5}$$

roughly corresponding to the number of excited motional quanta. Here, we naturally have to apply the relevant LDPs for the specific system. For the considered $^{24}Mg^+$ and $^{24}MgH^+$ cases we have $\eta_{ip,t}^2 + \eta_{op,t}^2 = 0.22$ and 4.4×10^{-4}, respectively.

For PRS $\tau_{\text{scaled}}^{\text{motional}}$ is the true timescale of interest, and this directly explains the large difference between the $^{24}Mg^+$ and $^{24}MgH^+$ motional populations and signal depths as a function of $\tau_{\text{scaled}}^{t/L}$. Indeed, we find that using this modified timescale

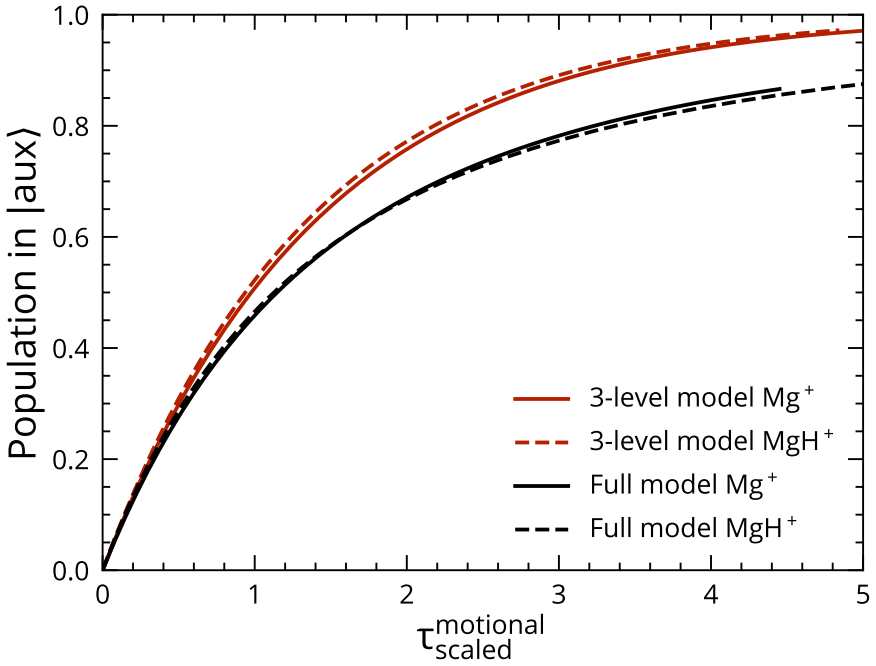

FIGURE 7.2: *Comparison between the 3-level model presented in Chapter 7 and the full rate equation sideband model presented in Sec. 5.2 for both the $^{24}Mg^{+}$ (Sec. 6.1) and $^{24}MgH^{+}$ (Sec. 6.2) example cases. The population in $|aux\rangle$, representing all states with $n_{ip}, n_{op} > 0$, is shown as a function of the motional scaled time, which approximately corresponds to the number of excited motional quanta.*

for the full model results, the evolution of the population in $|\text{aux}\rangle$, of the two cases are (trap-induced heating aside) basically identical as seen in Fig. 7.2 (black lines). For a subsequent perfect RSB shelving $P_{|aux\rangle}$ also corresponds to the resulting fluorescence level since $P_{|g_r\rangle} = 1 - P_{|aux\rangle}$. In these examples we have no trap-induced heating and therefore the results are the same for (almost) any laser energy spectral density (I_L, Γ_L) for each of the two systems when using the motional scaled time. However to be clear the used parameters are $I_L = 4.9\,\mu\text{W}\,\text{cm}^{-2}$ for $^{24}\text{Mg}^{+}$ and $I_L = 20\,\text{W}\,\text{cm}^{-2}$, $\Gamma_L/(2\pi) = 1\,\text{GHz}$ for $^{24}\text{MgH}^{+}$. The very small difference between the $^{24}\text{Mg}^{+}$ and $^{24}\text{MgH}^{+}$ systems thus only stems from the differences in the ratio of $\tilde{D}$ and $|\tilde{\xi}|^2$ for each system. Only if the laser energy spectral density is changed so much that the dominating emission process goes from spontaneous to stimulated or vice versa, will the specific size of it play a (small) role in a plot like this when $\tilde{D} \sim |\tilde{\xi}|^2$.

In Fig. 7.2 we also show the results for the 3-level model for both the $^{24}\text{Mg}^{+}$ and $^{24}\text{MgH}^{+}$ case using the same parameters (red lines). As expected, the 3-level model gives almost identical results for the two cases, even though spontaneous emission dominates for the $^{24}\text{Mg}^{+}$ case, and stimulated emission dominates for the $^{24}\text{MgH}^{+}$ case. As expected the 3-level model follows the full model for short $\tau_{\text{scaled}}^{\text{motional}}$

and overestimates the $|\text{aux}\rangle$ population for longer times. This of course stems from the missing rates back to the motional ground state. Since simulating the expected spectroscopic signal by this 3-level scheme is several orders of magnitude faster than the full model presented in Sec 5.2 (depending on the number of sideband orders one needs to take into account), it can be a very useful tool as a rough guide to optimize experimental parameters.

Chapter 8

The effect of coupling to blackbody radiation

A diatomic molecule is a molecule with one atom too many. – Arthur Schawlow [106].

In all previous chapters of this part, we considered the $^{24}MgH^+$ ion to be initially prepared in one of the two states forming the closed target transition $|v = 0, J = 1\rangle$ or $|v' = 1, J' = 0\rangle$. These states are, however, generally coupled to the rest of the rovibrational manifolds by black-body radiation (BBR) [47]. Owing to the large vibrational constant of 190 GHz [70] of the $^1\Sigma^+$ electronic ground state at room temperature ($T = 293\,\mathrm{K}$), the molecular ion is in the vibrational ground state $v = 0$ with > 99.9 % probability and one can assume that the average population of the $|v = 0, J = 1\rangle$ state is equal to the thermal equilibrium value $P_{\mathrm{J}=1} = 8.5\%$. The population distribution among the different J-states of $v = 0$ at thermal equilibrium is given in Fig. 8.1.

The fact that we expect $P_{\mathrm{J}=1} = 8.5\%$ causes the awaited signal depth for PRS to be much smaller than predicted in the previous chapters, which of course will affect the total experimental time needed to obtain a good signal to noise ratio.

To describe the effect of coupling to BBR on the PRS signal depth, we will again use the definitions of P_{off} and P_{on} for the average fluorescence signal when the molecule is always prepared in $|v = 0, J = 1\rangle$ introduced in Sec. 6.3. The probability of the $^{40}Ca^+$ ion fluorescing when the spectroscopy laser is far from resonance depends solely on trap-induced heating and imperfect ground state preparation, and is denoted P_{off} (background), whereas the probability of fluorescence close to resonance is denoted P_{on} (signal) and we always have $P_{off} \geq P_{on}$. If the target transition is driven we have $P_{off} > P_{on}$. The signal depth is given by $P_{off} - P_{on}$. P_{off} is independent of the initial state of the target transition. Hence the reduced average population in the $|v = 0, J = 1\rangle$ state due to coupling to BBR and spontaneous emission is taken into account in the PRS simulations by scaling the signal depth

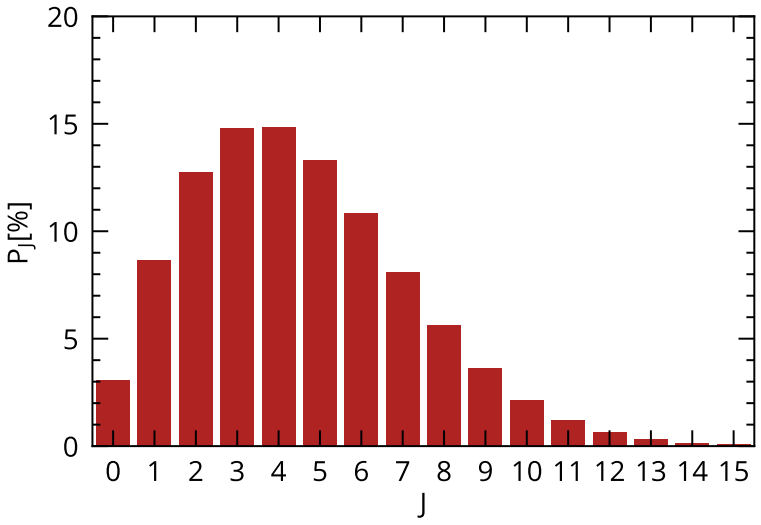

FIGURE 8.1: *The population distribution among the different J-states of the $v = 0$ vibrational ground state of the $^1\Sigma^+$ electronic ground state in $^{24}MgH^+$ at thermal equilibrium with black-body radiation at $T = 293$ K.*

$P_{off} - P_{on}$ by the probability to be in the target state, $P_{J=1}$, such that the expected signal fluorescence probability P_{on}^T becomes

$$\begin{aligned} P_{on}^T &= P_{off} - [P_{off} - P_{on}]P_{J=1} \\ &= (1 - P_{J=1})P_{off} + P_{J=1}P_{on}. \end{aligned} \tag{8.1}$$

If we put $P_{J=1} = 1$ Eq. 8.1 reduces to $P_{on}^T = P_{on}$ as it must.

In Fig. 8.2 we compare P_{on} and P_{on}^T for $I_L = 20\,\mathrm{W\,cm^{-2}}$, $\Gamma_L/(2\pi) = 1$ GHz, $\tau_{\mathrm{spec}} = 19$ ms, and $P_{J=1} = 0.085$ (i.e. at a laboratory temperature of $T = 293\,\mathrm{K}$).

P_{on}^T is the average signal we expect to obtain after many repetitions of the PRS sequence (step (i) to (iv) in Fig. **??**). For each repetition we can only either obtain a fluorescence signal of one or zero, and only after averaging over many such data points, can we get an estimate of P_{on}^T. A single repetition is denoted *an experimental cycle*, and the time it takes τ_{cycle}, which in our experiment is on the order of 100 ms (see details Sec. 12.2).

The relevant question is, how many experimental cycles we need to perform to determine P_{on}^T with a given uncertainty. Assuming Gaussian uncorrelated statistics of the parameters in Eq. 8.1 we can estimate the uncertainty as

$$\sigma_{on}^T = \sqrt{(1 - P_{J=1})^2\sigma_{off}^2 + (P_{J=1})^2\sigma_{on}^2 + (P_{on} - P_{off})^2(\sigma_{J=1})^2} \tag{8.2}$$

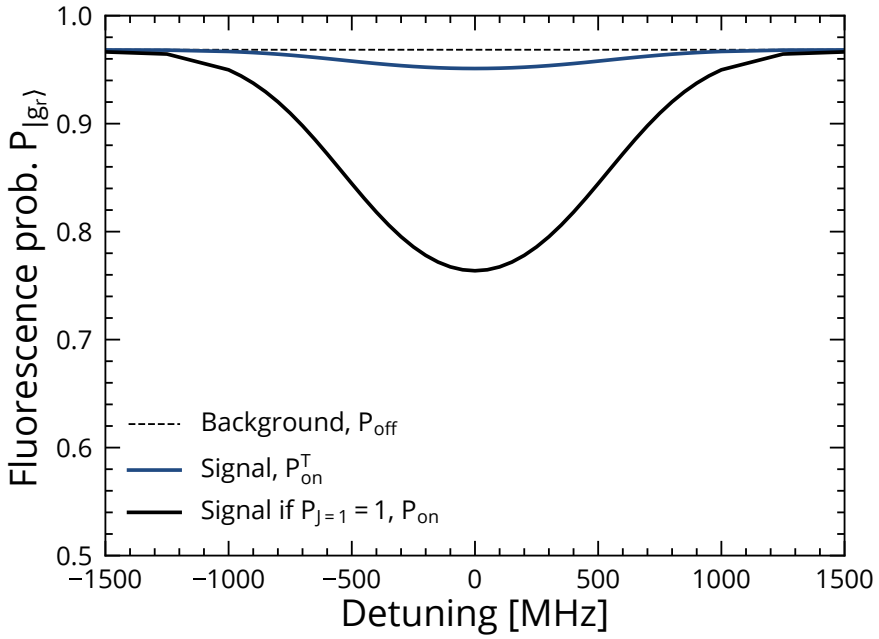

FIGURE 8.2: *Comparison between the expected signal P_{on}^{T} when the probability to find the molecule in the lower level of the target state $|v = 0, J = 1\rangle$ is $P_{J=1} = 8.5\,\%$, and the expected signal P_{on} if $P_{J=1} = 100\,\%$, along with the background from trap-induced heating P_{off} for $I_L = 20\,\mathrm{W\,cm^{-2}}$, $\Gamma_L/(2\pi) = 1$ GHz, and $\tau_{spec} = 19$ ms. Prior to the spectroscopy pulse the $^{40}Ca^{+}$-$^{24}MgH^{+}$ system was ground state cooled. The used heating rates are $R_{H,ip} = 14(1)\,\mathrm{s^{-1}}$ and $R_{H,op} = 1.7(3)\,\mathrm{s^{-1}}$. Readout was done on the 1st OP RSB only.*

where σ_{on}, σ_{off} are the uncertainties on P_{on} and P_{off}, respectively, and $\sigma_{J=1}$ is the uncertainty on $P_{J=1}$ based on our measurements. P_{on} and P_{off} are the same for every experimental cycle (for constant experimental parameters), so their values are binomially distributed and their uncertainties depend on the number of experimental cycles N as

$$\sigma_{on} = \sqrt{\frac{P_{on}(1 - P_{on})}{N}} \tag{8.3}$$

$$\sigma_{off} = \sqrt{\frac{P_{off}(1 - P_{off})}{N}} \tag{8.4}$$

Conversely, $P_{J=1}$ cannot be expected to be the same for every experimental cycle because the $J = 1$ state is coupled to the other J-states via BBR. Thus in order to find an expression for $\sigma_{J=1}$ we have to look more closely at the rovibrational state dynamics, which we will do in Sec. 8.1.

After obtaining $\sigma_{J=1}$ we will in Chapter. 9 set up a criteria for distinguishing the signal P_{on}^{T} from the background P_{off}.

8.1 Rate equation model of rovibrational dynamics in $^{24}MgH^+$

The dynamics of the population in the rovibrational states of the $^{24}MgH^+$ molecular ion in the presence of BBR can be modeled by rate equations as presented in Sec. 3.1.2, since this is exactly the case originally considered by Einstein. A program to model this[1], was set up by Anders Hansen, a former PhD student in our group, in 2012 (Sec. 4.1.4 of his thesis [71]). Since then, Steffen Meyer, also a former PhD student in the group, has rewritten the program into a more accessible form in 2015.

In his program Hansen chose to include the first 20 rotational levels of the vibrational $v = 0$, $v = 1$ and $v = 2$ states in the electronic ground state potential. As already mentioned, for $^{24}MgH^+$ only 0.1% of the molecular ensemble is vibrationally excited at room temperature and less than 5% is in states above $J = 9$ in $v = 0$. Hence the considered state space is more than sufficient to model the molecule's interaction with BBR at room temperature, which is what the program is used for in this thesis.

The Einstein A-coefficients used for the program were calculated by Anders Hansen ([71] p. 155)[2] based on potential and dipole moments calculations by Frank Jensen at the Department of Chemistry at Aarhus University in 2012 [72]. The selection rule for dipole-allowed transitions for both rotational and rovibrational transitions is $\Delta J = \pm 1$. So all coupling between states not fulfilling this condition is assumed to be zero. The B-coefficients are calculated from the A-coefficients via Eq.s 3.39 and 3.40 taking into account the degeneracy of the rotational levels of $g_J = 2J + 1$. The Einstein A-coefficients i.e. the spontaneous emission rates, and the absorption and stimulated emission rates for $v = 0$ due to interaction with radiation from a black-body at $T = 293$ K, are given in Fig.s C.4 and C.5 of Appendix C.

If the molecule is prepared in a single J-state $|\psi_J\rangle$ these rates govern the dynamics of the population as it goes towards the steady state distribution given in Fig. 8.1. When not prepared in a single J-state the molecule is in mixed state represented by the density matrix

$$\hat{\rho} = \sum_J p_J \left|\psi_J\right\rangle \left\langle\psi_J\right| , \tag{8.5}$$

[1] Hansen's script includes the simultaneous interaction with a laser light field, however in the present thesis only the interaction with BBR is considered.

[2] Hansen writes the unit as Hz but it is really s^{-1}. I.e. the A-parameters in Hansen's table should be divided by 2π to be in Hz.

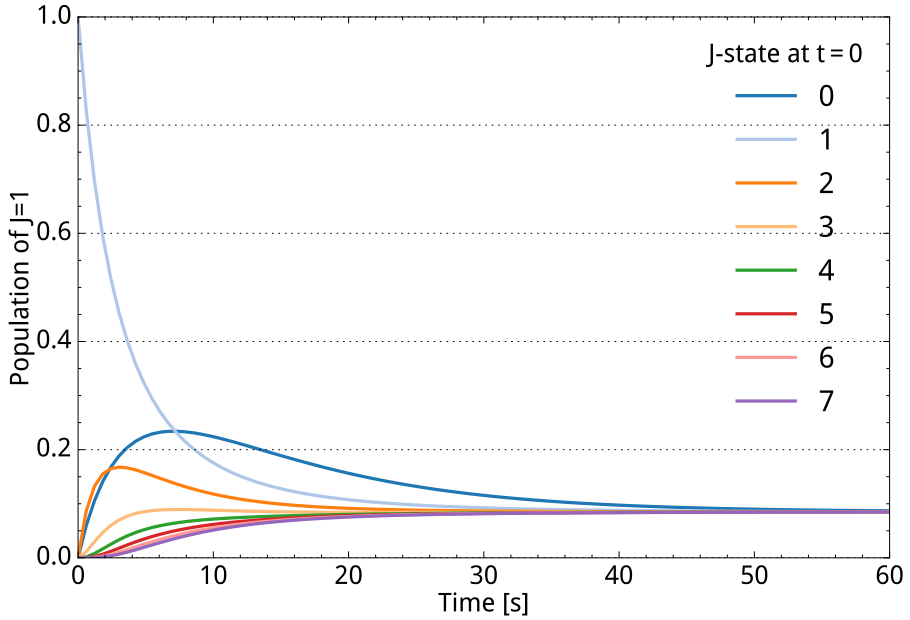

FIGURE 8.3: *The evolution of the population in the $J = 1$ state after the molecule was prepared in a single J-state when the molecule is subject to BBR at $T = 293$ K. Independent from the initial state at $t = 0$ the final population in $J = 1$ is $P_{J=1} = 8.5\%$.*

where p_J is the probability to measure it in the state $|\psi_J\rangle$ and $\sum_J p_J = 1$ at all times. At steady state the molecule is in a mixed state with $p_J = P_J$, where P_J are the thermal equilibrium probabilities. However, when a measurement of the J-state is made the mixed state must collapse into a single state. Using the rate equation program we can simulate how e.g. the $J = 1$ state is filled up after the molecule was prepared in a single J-state. This is shown in Fig. 8.3. We see that the time to reach the equilibrium value of $P_{J=1} = 8.5\%$ is on the order of 1 min. Once the molecule is projected to a specific state J, the probability to find it in the same state or a neighboring state if we measure again shortly after is increased. This means we cannot expect $p_{J=1}$ to be given by the equilibrium value $P_{J=1}$ after the first measurement unless we wait $\gtrsim 1$ min. If we do not, the probability that the molecule is in $J = 1$ depends on where it was in the former measurement. Since the cycle time in the PRS experiment is only on the order of $\tau_{\text{cycle}} = 100$ ms, and we do not want to wait 1 min between every measurement, we are in the latter scenario. Therefore the expected outcome of such repeated out-of-equilibrium measurements is treated in the next section.

8.1.1 Monte Carlo simulations of repeated rotational state measurements

The goal of this section is to simulate the outcome of repeated measurements of the J-state, where the system does not have time to reach equilibrium between the different measurements. Since it is just a simulation, we assume that we have a measurement device which can show any single J-state as the outcome. If the measurement yields J at time $t = 0$ the probability of measuring J' at time $t = \tau_{\text{cycle}}$ can be found from the rate equation model. We simply prepare the molecule in J and let the system evolve towards equilibrium for a time τ_{cycle} as in Fig. 8.3. The evolved state is a mixed state, and the population probability of each J-component $p_{J\to J'}(\tau_{\text{cycle}})$ gives the probability to find the molecule in a specific state J' at time $t = \tau_{\text{cycle}}$. Note that in Fig. 8.3 we only plot $p_{J\to J'=1}(\tau_{\text{cycle}})$.

The probability of the molecule jumping to J' at $t = \tau_{\text{cycle}}$ after being found in J at $t = 0$, $p_{J\to J'}(\tau_{\text{cycle}})$, was calculated for the first 20 J-states for $\tau_{\text{cycle}} = 100$ ms by using the rate equation program by Hansen. Note that for evolution times close to zero, the chance that the molecule stays in the same state is very large, but however never 100% due to the exponential behavior of the population evolution. In other words we cannot keep the molecule in a certain state by repeatedly measuring it there. This is only possible for coherent dynamics.

With these $p_{J\to J'}(\tau_{\text{cycle}} = 100 \text{ ms})$ jump probabilities at hand we can simulate the outcome of repeated measurements of the J-state. This was done in a Monte Carlo simulation fashion by picking an initial J-state and letting a random number between 0 and 1 determine the next J-state based on the probability of the different outcomes given by $p_{J\to J'}(\tau_{\text{cycle}} = 100 \text{ ms})$. The result of such a Monte Carlo simulation for $\tau_{\text{cycle}} = 100$ ms and $N = 1000$ measurement counts (i.e. a total experiment time of $T = N\tau_{\text{cycle}} = 100$ s) can be seen in Fig. 8.4. We see that the molecule maximally changes its J-state by 1 from one measurement to the next. We also observe long periods of time, where the outcome does not change. This means that the 100 ms between measurements is short compared to the timescale of the dynamics.

If we look at Fig. 8.4, the amount of times N_J the molecule is found in a specific state divided by the total number of measurements N must be equal to the steady state probability P_J of that state in the limit where $N \to \infty$.

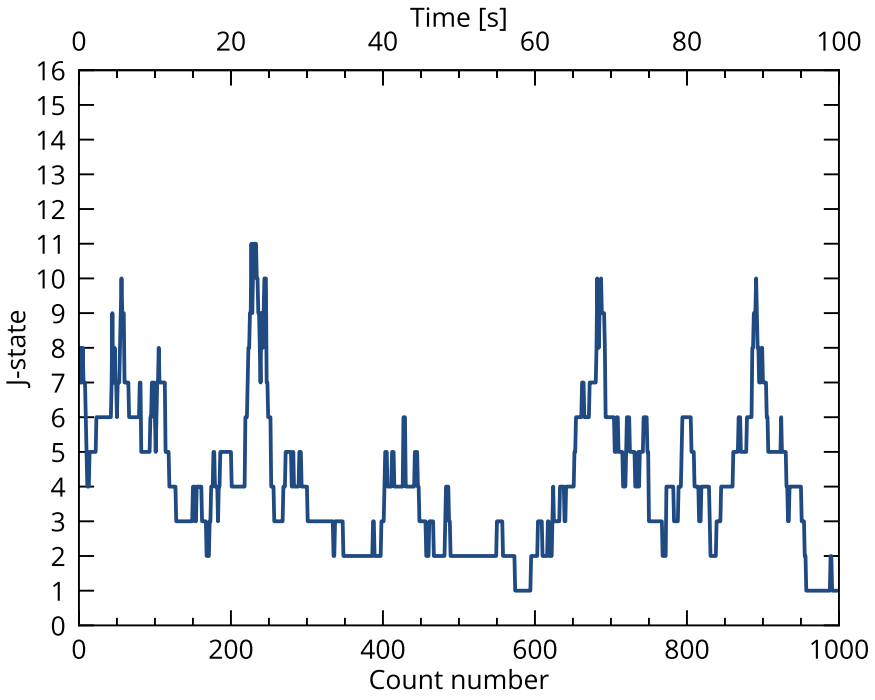

FIGURE 8.4: *Example of a molecular jumping pattern between different J-states when probing every 100 ms. How long do we need to monitor it to determine the equilibrium distribution to a good accuracy?*

8.1.1.1 J-state standard deviation

This bring us back to the question about how long we need to measure to determine the steady state population probability P_J to a given level of accuracy. To calculate σ_J as a function of total measurement time, T, the average probability to be in J was calculated for a Monte Carlo jumping pattern similar to the one shown in Fig. 8.4 for different T. To calculate the standard deviation, this was repeated 1000 times, and the standard deviation of the 1000 averages was found. The standard deviation does not depend on the number of repetitions, from which it is calculated, but to minimize random statistical fluctuations 1000 was used. The result is plotted as solid lines in Fig. 8.5. From this plot we see that σ_J is proportional to $1/\sqrt{T}$. Specifically for our state of interest $J = 1$ we write

$$\sigma_{J=1} = \frac{\alpha}{\sqrt{T}}. \tag{8.6}$$

To be sure that the time between measurements of 100 ms does not affect the result, the same simulations were performed for $\tau_{\text{cycle}} = 1$ s, 6 s and 30 s. The results for $J = 1$ are plotted together in Fig. 8.6. We see that the results for $\tau_{\text{cycle}} = 0.1$ and

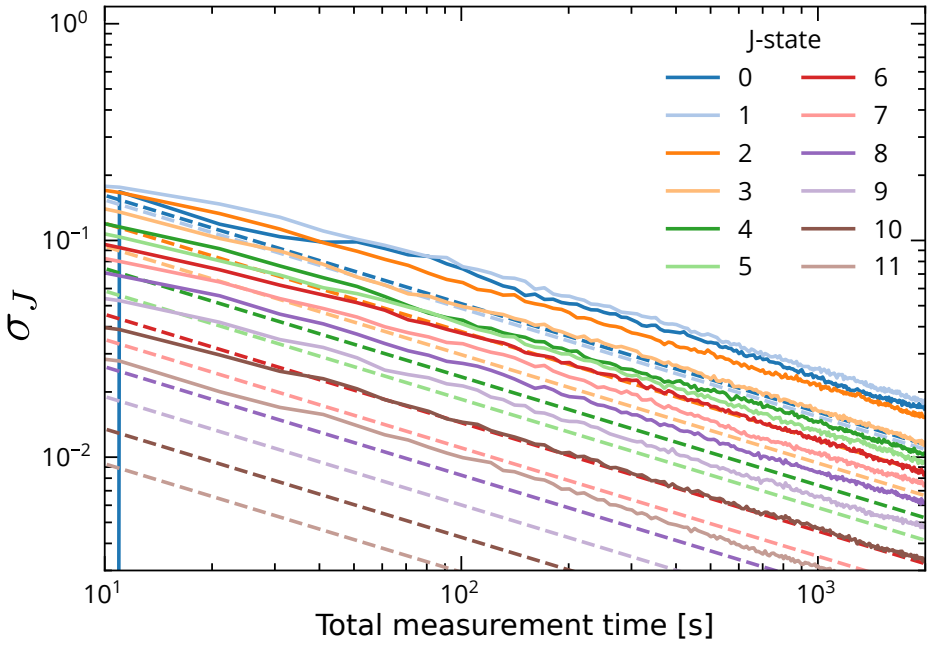

FIGURE 8.5: *The standard deviation of the different J-states, σ_J, as a function of the total measurement time when the cycle time is 100 ms. The dashed lines correspond to the theoretical Eq. 8.11, whereas the solid lines are Monte Carlo simulations. The deviation from linearity of the solid lines is due to statistical fluctuations.*

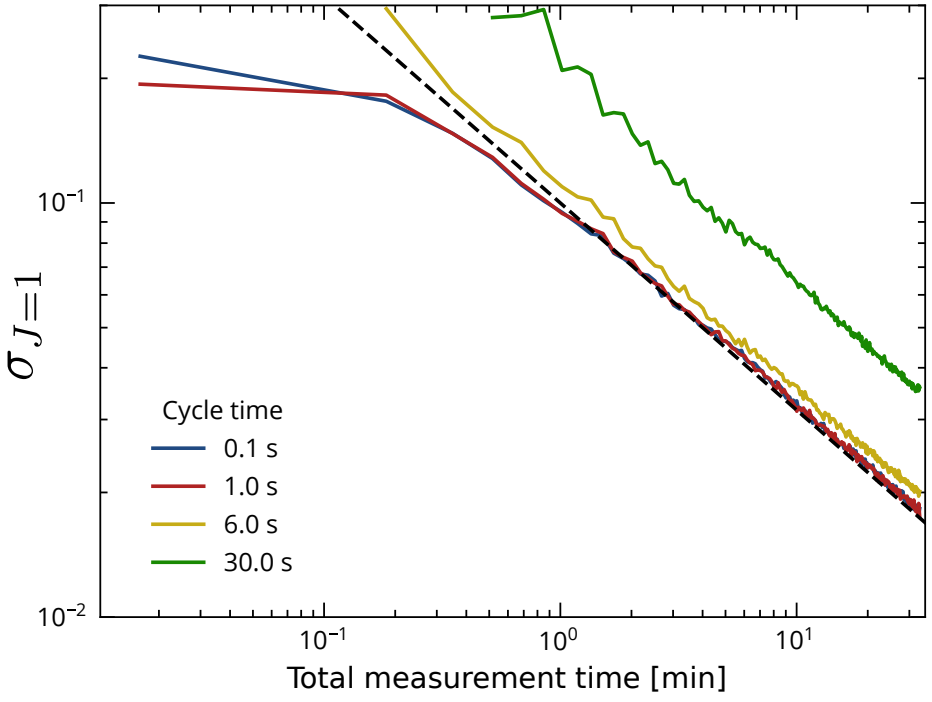

FIGURE 8.6: *The standard deviation of J=1, $\sigma_{J=1}$, as a function of the total measurement time for different cycle times, as calculated from Monte Carlo simulations. The dashed line corresponds to Eq. 8.6 with $\alpha = 0.8$. It is evident that α is a constant for cycles times below ~ 3 s, meaning that measuring faster than every 3 s will not decrease $\sigma_{J=1}$.*

1 s are almost identical, whereas the result for 6 s is a little different and the result for 30 s is very different. This proves that a probing time of both 100 ms and 1 s is enough to resolve the dynamics.

The black dashed line in Fig. 8.6 corresponds to Eq. 8.6 with $\alpha = 0.8\ \sqrt{\text{s}}$, and we see that α is the same for $\tau_{\text{cycle}} \lesssim 3$ s. In the next sub-section we will see that this corresponds to the average lifetime of the $J = 1$ state, $\bar{\tau}_{J=1}$. In effect this means that for a fixed total measurement time T, we cannot determine $P_{J=1}$ more precisely by measuring faster than every 3 s. By doing so we are simply oversampling the dynamics, as if taking a 1000 pictures per second of a movie only shot with a frame rate of 50 Hz. This means, we are not limited by our experimental cycle time of $\tau_{\text{cycle}} \sim 100$ ms.

8.1.1.2 Average time inside and outside the $J = 1$ state

The simulated jumping patterns can also be used to estimate how long the molecule stays in a specific J-state, denoted the waiting time. The result for a cycle time of 0.1 s and total number of measurements $N = 10^8$ can be seen in figure 8.7, where the relative occurrence of waiting times N_J/N for $J = 1$ and $J \neq 1$ are plotted. The

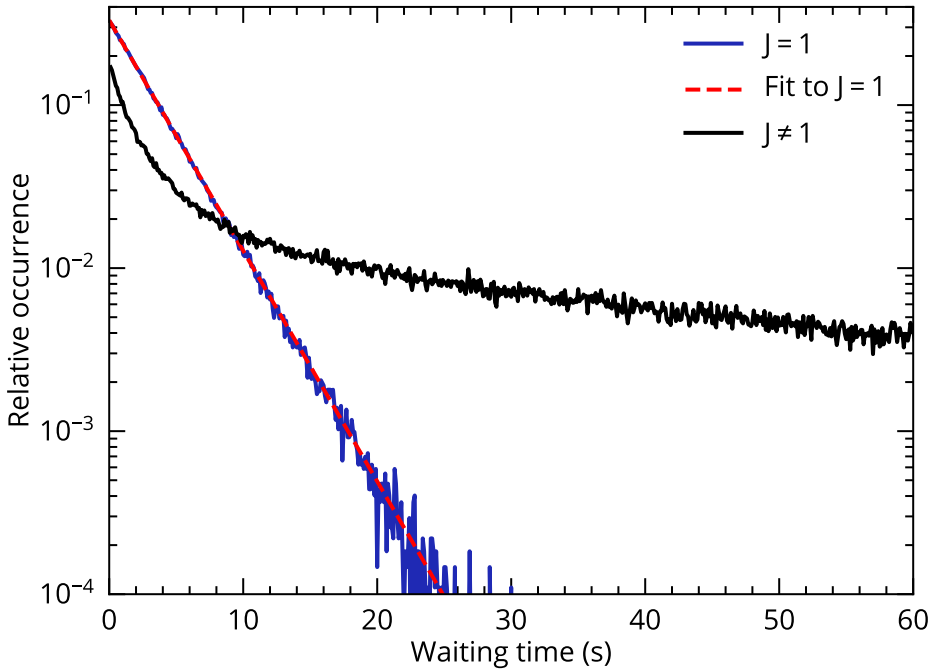

FIGURE 8.7: *The relative occurrence of waiting times in $J = 1$ (blue) and $J \neq 1$ (black) based on $N = 10^8$ simulated measurements with a cycle time of 0.1 s. The red dashed line is an exponential fit to the $J = 1$ data giving a lifetime of 3.0710(2) s.*

$J \neq 1$ waiting times correspond to how long it took before the molecule came back to $J = 1$. The waiting time distribution for $J = 1$ can be fitted to an exponential function, and the lifetime is found to be 3.0710(2) s. This means that if the molecule is in $J = 1$ we can assume it stays there during the course of the spectroscopic pulse τ_{spec} when doing PRS, which is on the order of tens of ms.

The waiting times for $J \neq 1$ do however not follow an exponential distribution. This is most easily seen when using a logarithmic y-axis as in Fig. 8.7. This is because the $J \neq 1$ waiting times do not approximately depend on the sum of outgoing rates from a single J-state as described in Eq. 8.7 of the next section. The mean value of the waiting times (black) is 33.50(9) s.

8.2 Simple qualitative model of J-state standard deviation

In this section we set up a simple qualitative model to obtain a better understanding of the physics governing the measurement uncertainty σ_J of the steady state rotational populaion P_J.

Assuming the dynamics of the population moving between the different J-states can be modeled by rate equations, the average time to stay in J can be estimated by

$$\bar{\tau}_J = \frac{1}{\sum_{J' \neq J} \Gamma_{J \to J'}}, \tag{8.7}$$

where $\Gamma_{J \to J'}$ are the total outgoing rates from J to $J' = J \pm 1$, which are the only ones of considerable size due to selection rules. This gives $\bar{\tau}_{J=1} = 3$ s matching the lifetime found by the Monte Carlo simulations above.

The average time between being in J plus the average time to stay in J is denoted $\tilde{\tau}_J$. If we measure the system on a timescale faster than $\bar{\tau}_J$ we can assume the sections where the measurement yields J to be Poisson distributed with average occurrence rate $1/\tilde{\tau}_J$. In order for the molecule to fulfill the requirement of being in J during a percentage P_J of the time we have

$$P_J \equiv \frac{\bar{\tau}_J}{\tilde{\tau}_J}. \tag{8.8}$$

This gives $\tilde{\tau}_{J=1} = 35$ s and hence that the average time between the molecule being in $J = 1$ is 32 s, similar to the average waiting time in $J \neq 1$ found by Monte Carlo simulations above.

J-state	0	1	2	3	4	5	6	7	8	9
P_J [%]	3.01	8.49	12.5	14.6	14.7	13.3	10.9	8.22	5.74	3.72
$\bar{\tau}_J$ [s]	8.9	3.0	1.3	0.71	0.44	0.30	0.21	0.16	0.13	0.10
$\bar{\sigma}_J\sqrt{T}$ [$\sqrt{s}$]	0.51	0.49	0.38	0.30	0.23	0.18	0.14	0.11	0.083	0.060

TABLE 8.1: *The steady state population of each J-state P_J, the average waiting time $\bar{\tau}_J$ in a specific J-state, and the numerator of Eq. 8.11 for the first 10 J-states of the vibrational ground state of $^{24}MgH^+$.*

For a given total observation time T we would on average observe

$$\bar{N}_J = \frac{T}{\tilde{\tau}_J}. \tag{8.9}$$

sections of measurements where the system was in J. If we define the average rate by which we observe a section where the molecule is in J during T as $\Gamma_J \equiv 1/\tilde{\tau}_J$ we also have

$$\bar{N}_J = T\Gamma_J = NP_J \tag{8.10}$$

where N is the total number of measurements and the last equality holds for $N \to \infty$. In this limit the Poisson and binomial distributions are the same and we can estimate the standard deviation of P_J as

$$\begin{aligned} \bar{\sigma}_J &= \sqrt{\frac{P_J(1-P_J)}{N}} \\ &= \sqrt{\frac{P_J^2(1-P_J)\tilde{\tau}_J}{T}} \\ &= \sqrt{\frac{P_J(1-P_J)\bar{\tau}_J}{T}} \end{aligned} \tag{8.11}$$

This expression does not depend on how long each measurement within T takes to perform, since we have assumed that we measure faster than the dynamics of the molecule. When this is the case, $\bar{\sigma}_J$ is proportional to $1/\sqrt{T}$, and the proportionality factor depends only on the steady state population probability P_J of the state in question and the average time to stay there $\bar{\tau}_J$.

Table 8.1 shows $\bar{\tau}_J$ for the first ten J-states in the $v = 0$ state of the $^1\Sigma^+$ electronic ground state of $^{24}MgH^+$ at $T = 293\,K$. We see that the molecule has a tendency to stay longer in the lower J-states once it is there, even though J-state 3 and 4 are the most populated. Hence on average the molecule will have to enter the lower states less frequently to fulfill the requirement of being in each J-state P_J of the time. The

proportionality factor $\bar{\sigma}_J\sqrt{T} = \sqrt{P_J(1-P_J)\bar{\tau}_J}$ is also shown. We see that the factor is largest for the lower J-states meaning that we have to observe these states longer to obtain the same standard deviation. We see that $J = 0$ and $J = 1$ values are very close to each other, and from the Monte Carlo simulations above, we in fact found that the proportionality factor for $J = 1$ is slightly larger than for $J = 1$ making $P_{J=1}$ the most time-consuming steady state population to measure. This is of course bad luck for us, since this is our state of interest.

The simple model given here and the Monte Carlo simulation approach can be compared for $\tau_{\text{cycle}} < \bar{\tau}_J$, which is done in Fig. 8.5 where the dashed lines represent the result of the simple model. We see that the simple model can reproduce the Monte Carlo results to within a factor of two and finds the same order for the different J-states except for $J = 0$ and $J = 1$, which is more than expected for such a crude model.

Chapter 9

Considerations regarding transition line search strategy

The best ever measurement of the target transition for spectroscopy in $^{24}MgH^+$, the $|v = 0, J = 1\rangle \leftrightarrow |v' = 1, J' = 0\rangle$ transition of the electronic ground state, was performed by W.J. Balfour in 1972 [70] yielding $f_t^B = 48619.4$ MHz. On this measurement he claimed an accuracy of ± 1.5 GHz, corresponding to a one standard deviation confidence level. Thus there is a $\sim 68\%$ chance that the transition line will lie within a $W = 3$ GHz interval centered at f_t^B.

The estimated linewidth of the transition is however only $\Gamma_t/(2\pi) = 2.5$ Hz [72], which compared to W makes the transition lineshape resemble a Dirac delta function. This means that if we tune the (assumed perfectly well-determined) central laser frequency f_L to f_t^B, we can only expect to obtain a spectroscopic signal, if the linewidth of the laser Γ_L is similar to W, and the laser spectral density is large enough, as explained below.

9.1 The time to scan a frequency interval

A different way to obtain a signal is to chose a smaller laser linewidth and cover W in several steps. This is most easily illustrated by a square spectral laser lineshape as shown in Fig. 9.1. Here we plot square spectral lineshapes (black) with widths (from left to right) of 3 GHz, 1.5 GHz and 1 GHz. The red lines represent the central laser frequency for each lineshape. We see that we have to use 1, 2, and 3 different central laser frequencies, respectively, to cover $W = 3$ GHz with the different linewidths. For the same laser intensity the narrow lineshapes have a higher energy spectral density, since this is proportional to $1/\Gamma_L$ (the area under each lineshape in Fig. 9.1 is equal). Generally the number of laser frequency steps needed to cover the range W, when

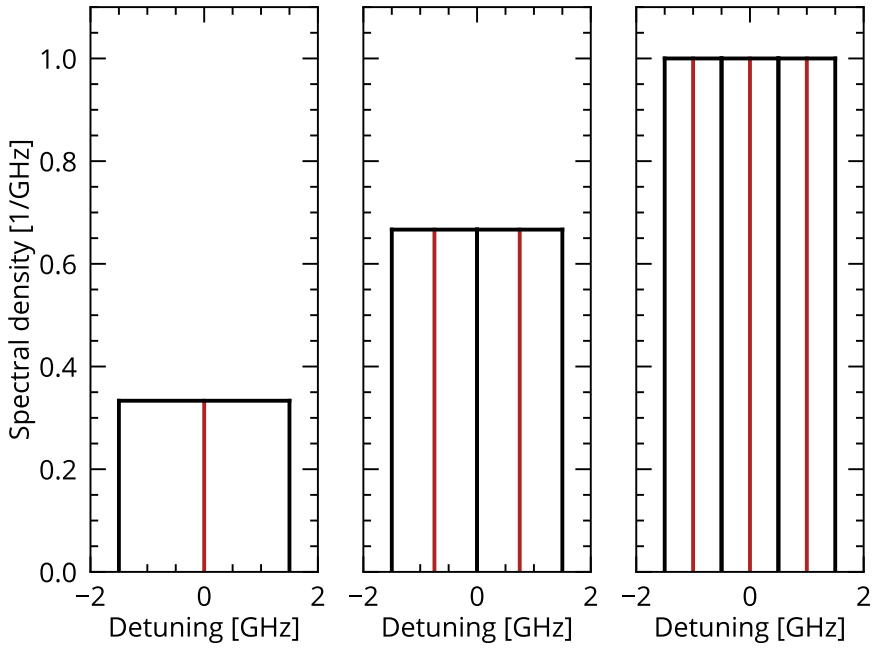

FIGURE 9.1: *Plots of quare spectral lineshapes (black) with widths (from left to right) of 3 GHz, 1.5 GHz and 1 GHz. The red lines represent the central laser frequency of each lineshape. To cover $W = 3$ GHz we have to apply 1, 2, and 3 different central laser frequencies, respectively, for the different linewidths. The area under each black curve is normalized.*

using a square laser lineshape, is

$$N_{step}(\Gamma_L) = \left\lceil \frac{W}{\Gamma_L/(2\pi)} \right\rceil \tag{9.1}$$

using the ceiling function $\lceil x \rceil = \min\{n \in \mathbb{Z} | n \geq x\}$ that rounds to the nearest larger integer. The total time to scan W is then

$$T^C_{scan}(\Gamma_L) = N_{step}(\Gamma_L) \times T^C(\Gamma_L), \tag{9.2}$$

where T^C is the minimum time to distinguish signal from background with a confidence level of C if it lies within Γ_L. The question is now, what laser linewidth we should chose to minimize T^C_{scan}, and thereby obtain a PRS signal as fast as possible.

A smaller Γ_L means a higher spectral density, which will give a faster motional depletion as shown in Fig. 6.10 and hence a smaller T^C. However, a smaller Γ_L also means a larger N_{step}. Thus for a given laser intensity there will be a Γ_L for which T^C_{scan} is minimized. Put simply, maybe it is worth it to e.g. apply two steps using a smaller Γ_L, if each step is faster than the time to get a signal by covering all of W at

once by using a larger Γ_L. In order to find the minimum T^C_{scan} we need an expression for $T^C(\Gamma_L)$, which is derived in the next section.

9.2 The time to distinguish signal from background

We now set up a criteria for distinguishing the average fluorescence signal, P^T_{on}, from the background, P_{off}, given by

$$P_{off} - P^T_{on} > C(\sigma_{off} + \sigma^T_{on}) \tag{9.3}$$

where C is the confidence level expressed in number of standard deviations, and σ_{off} and σ^T_{on} are the uncertainties on the measured values of P_{off} and P^T_{on}, respectively. P^T_{on} was defined in Eq. 8.1 , σ^T_{on} in Eq. 8.2 and σ_{off} in Eq. 8.4.

σ^T_{on} depends on the measurement uncertainty $\sigma_{J=1}$ of the steady state rotational population in $J = 1$, $P_{J=1}$, which we in Sec. 8.1.1.1 found out depends on the total measurement time T as $\alpha/\sqrt{T}$ (Eq. 8.6) with $\alpha = 0.8$ as long as the cycle time τ_{cycle} is smaller than the lifetime of the $J = 1$ state of ~ 3 s. Moreover σ^T_{on} also depends on two terms involving σ_{on} and σ_{off}. We can estimate the relative contributions of the three terms in σ^T_{on} by defining the effective contribution of each as

$$\begin{aligned} \sigma^{eff}_{on} &= P_{J=1}\sigma_{on} \\ &= P_{J=1}\sqrt{P_{on}(1-P_{on})\tau_{\text{cycle}}}T^{-1/2} \end{aligned} \tag{9.4}$$

$$\begin{aligned} \sigma^{eff}_{off} &= (1-P_{J=1})\sigma_{off} \\ &= (1-P_{J=1})\sqrt{P_{off}(1-P_{off})\tau_{\text{cycle}}}T^{-1/2} \end{aligned} \tag{9.5}$$

$$\sigma^{eff}_{J=1} = (P_{off} - P_{on})\alpha T^{-1/2} \tag{9.6}$$

where we have used $T = N\tau_{\text{cycle}}$. Using typical values of $P_{off} = 0.95$, $P_{on} = 0.60$, and $\tau_{\text{cycle}} = 0.1$ s we obtain $\sigma^{eff}_{on} \lesssim \sigma^{eff}_{off} < \sigma^{eff}_{J=1}$. Thus the term involving $\sigma_{J=1}$ is dominating. Due to the binomial nature of P_{on} and P_{off} we can always decrease σ_{off} and σ_{on} with a faster cycle time. Because we are limited by $\sigma_{J=1}$ we will not gain much from this strategy, since we are already measuring faster than the lifetime of the $J = 1$ state, which minimizes α.

Since we have expressions for all terms in Eq. 9.3 we can plug them in and solve for the total measurement time needed to distinguish the signal from the background. After a little algebra one obtains

$$T^C \equiv \tau_{cycle} C^2 \left(\frac{\sqrt{P_{off}(1-P_{off})}}{(P_{off}-P_{on})P_{J=1}} + \frac{\sqrt{(1-P_{J=1})^2 P_{off}(1-P_{off}) + P_{J=1}^2 P_{on}(1-P_{on}) + \frac{(P_{on}-P_{off})^2 \alpha}{\tau_{cycle}}}}{(P_{off}-P_{on})P_{J=1}} \right)^2 \quad (9.7)$$

which is the minimum time to distinguish between P_{off} and P_{on}^T at a confidence level C. This means, that if we tune the spectroscopy laser to a frequency where $P_{off} > P_{on}$ we will be able to distinguish the signal from the background with C standard deviations as long as we measure for a time larger than or equal to T^C. $\tau_{\text{cycle}} = \tau_{\text{spec}} + K$, where currently $K = 100$ ms in our experiment. K is the time for cooling and readout during the experimental cycle.

Since $\tau_{cycle}(\tau_{spec})$, $P_{off}(\tau_{spec})$ and $P_{on}(\tau_{spec}, \Gamma_L, I_L, \delta_t)$, the necessary measurement time for a given detuning $\delta_t = \omega_t - \omega_L$ depends on 3 independent variables: τ_{spec}, Γ_L and I_L. To minimize T^C, we want a large signal depth fast to lower τ_{spec} and thereby τ_{cycle} but also to minimize P_{off} resulting from trap-induced heating. Hence we want a large absorption rate and thus I_L should be maximized and Γ_L should be minimized.

For a given combination of I_L and Γ_L there is a τ_{spec}, which will minimize T^C. This is because the signal depth initially increases as a function of τ_{spec} (Fig. 6.10), however this trend eventually flattens out, after which it is a waste of measurement time to increase τ_{spec} further. When the trap-induced heating rate is large compared to the motional state excitation rate due to the laser, the signal depth even decreases again at large τ_{spec}. The optimal τ_{spec} does not depend on the chosen confidence level C since, as seen in Eq. 9.7, $T^C \propto C^2$, and multiplying a function with a constant will only shift it along the y-axis, and not change the x-value of the minimum.

9.3 Search optimization on resonance

In Fig. 9.2 $T^{C=1}$ is plotted as a function of τ_{spec} for $I_L = 20\,\text{W}\,\text{cm}^{-2}$ and a Gaussian laser lineshape with different FWHM Γ_L. For this and the other examples in this chapter $R_{H,ip} = 14(1)\,\text{s}^{-1}$ and $R_{H,op} = 1.7(3)\,\text{s}^{-1}$. The example is given for on-resonance conditions $\delta_t = 0$. This means that the result is very similar to that

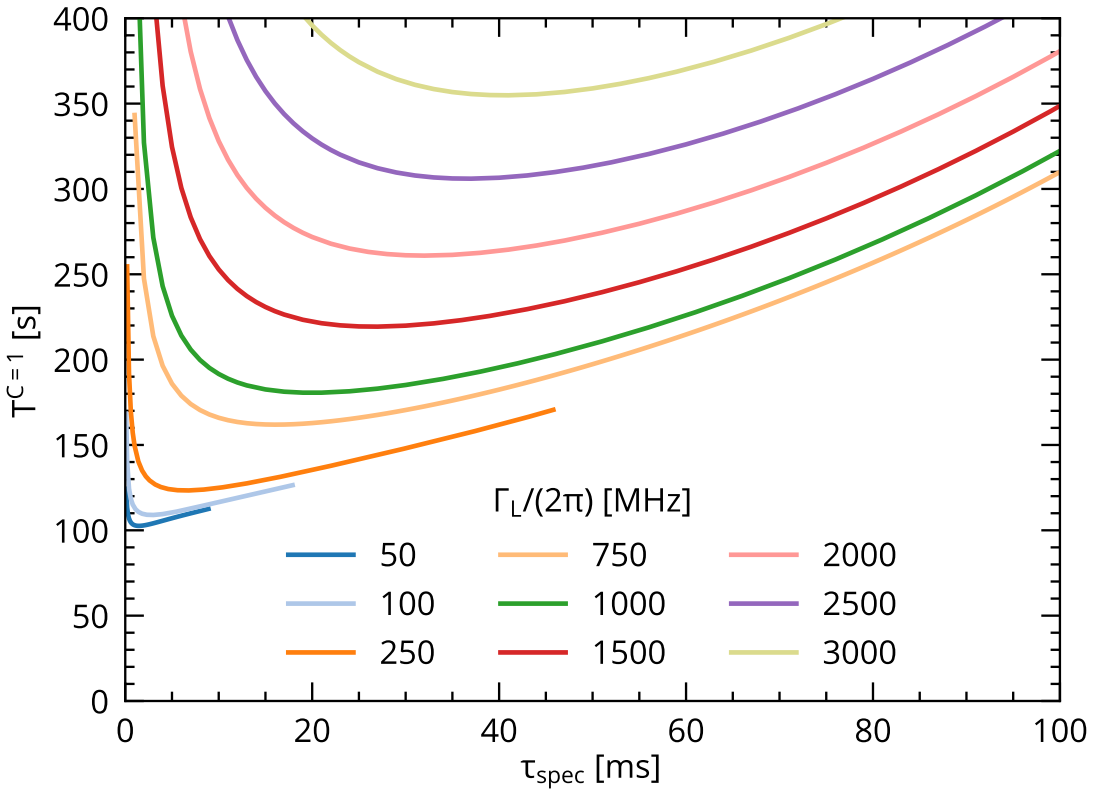

FIGURE 9.2: *The time to distinguish signal from background $T^{C=1}$ on resonance as a function of τ_{spec} for $I_L = 20\,\mathrm{W\,cm^{-2}}$ and a Gaussian laser lineshape for different laser linewidths Γ_L. Here $R_{H,ip} = 14(1)\,\mathrm{s^{-1}}$ and $R_{H,op} = 1.7(3)\,\mathrm{s^{-1}}$.*

expected for a square laser lineshape, since the maximum spectral density is $1/\Gamma_L$ in the square case and $2\sqrt{2\ln(2)}/\sqrt{2\pi}/\Gamma_L \approx 0.94/\Gamma_L$ in the Gaussian case.[1] As expected we see that T^C for the constant chosen I_L has a minimum depending on Γ_L. The minimum appears for smaller τ_{spec} for smaller Γ_L, since the spectral energy density, and thereby the motional excitation dynamics are faster for small Γ_L.

In Fig. 9.3 the total experimental time $T^{C=1}_{scan}$ is plotted for the $T^{C=1}$ curves given in Fig. 9.2 and $N_{step}(\Gamma_L)$ given by Eq. 9.1. For these conditions $\Gamma_L/(2\pi) = 2000$ MHz minimizes $T^{C=1}_{scan}$. Note that the τ_{spec} minimizing $T^{C=1}_{scan}(\Gamma_L)$ are the same which minimize $T^{C=1}(\Gamma_L)$. Also note, that the curves for $\Gamma_L/(2\pi) = 2000$, 2500, and 3000 MHz are in fact the same as in Fig. 9.2 since $N_{step} = 1$ for these cases. Consequently the best will be $\Gamma_L \to 1500$ MHz, as long as $N_{step} = 1$ is still fulfilled.

However, when we consider a Gaussian laser lineshape instead of a square one, the spectral density will not be constant over the entirety of W as illustrated in Fig.

[1]Note that the signal depth cannot be scaled by a factor $\sqrt{2\pi}/2\sqrt{2\ln(2)}$ to obtain the square lineshape result, because the effective absorption rate will also be altered by this factor. When trap-induced heating is included, it is not correct to adjust the time-scale either.

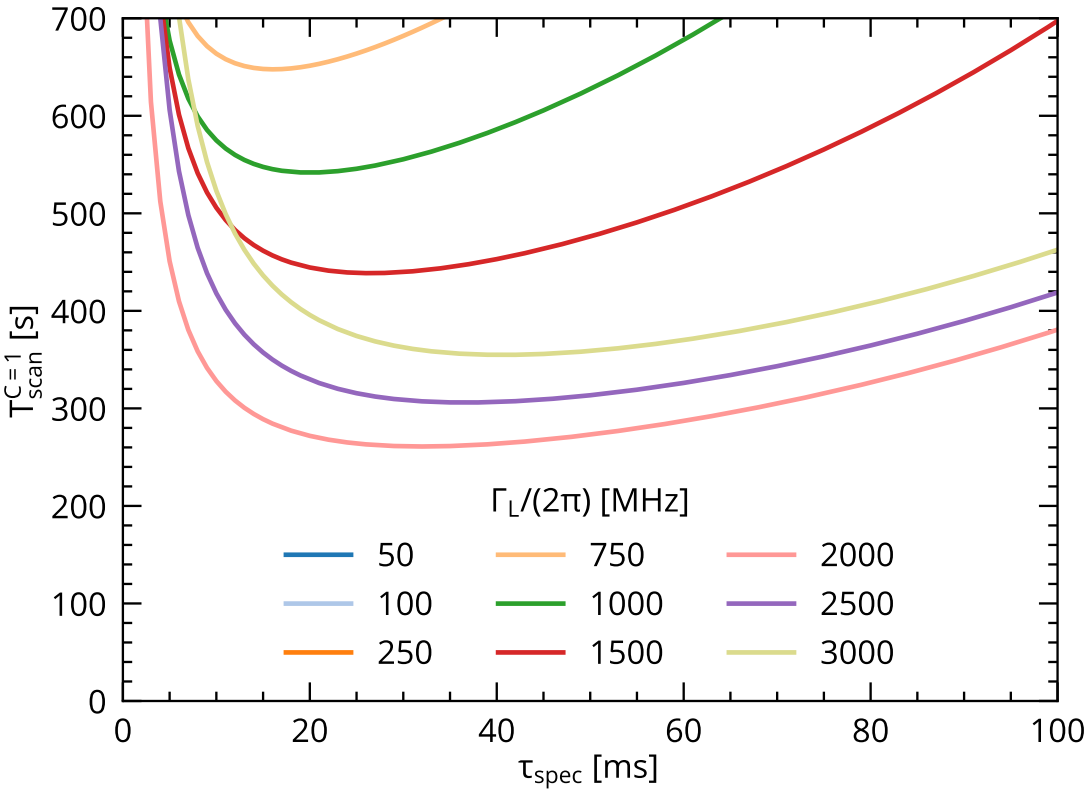

FIGURE 9.3: *The total time to scan W, $T^{C=1}_{scan}$ for the $T^{C=1}$ curves given in Fig. 9.2 and $N_{step}(\Gamma_L)$ given by Eq. 9.1. For these conditions this is minimized by $\Gamma_L/(2\pi) = 2000$ MHz at $\tau_{spec} = 30$ ms. Note that the τ_{spec} minimizing $T^{C=1}_{scan}(\Gamma_L)$ are the same that minimizing $T^{C=1}(\Gamma_L)$. Here $R_{H,ip} = 14(1)\,\mathrm{s}^{-1}$ and $R_{H,op} = 1.7(3)\,\mathrm{s}^{-1}$.*

9.4. In the left figure the used step-size is $\Gamma_L/(2\pi)$, which is the natural choice for a square lineshape as also seen in Fig. 9.1: all of W is covered, and there is no overlap. Even though all of W is also covered in the left figure of Fig. 9.4 the spectral density only comes close to that of a square lineshape at the laser center frequency. Only if the target transition frequency f_t overlaps with one of the maxima will we have a $T^{C=1}_{scan}$ corresponding to the result of Fig. 9.3. In all other cases, $T^{C=1}$ will be larger. Consequently, if we measure for a total time determined by on-resonance conditions the distinction criteria of Eq. 9.3 will not be fulfilled for all other detunings.

This is exemplified with the case of $I_L = 20\,\mathrm{W\,cm^{-2}}$ and $\Gamma_L/(2\pi) = 1$ GHz in Fig. 9.5. Here the expected signal and background is plotted for the optimum τ_{spec} of 19 ms along with the expected measurement uncertainties after measuring for a time $T^{C=1} = 180.6$ s as found from Fig. 9.2. We see that the distinction criteria is fulfilled for $P^T_{on} < P_{off}$ only for $\delta_t = 0$.

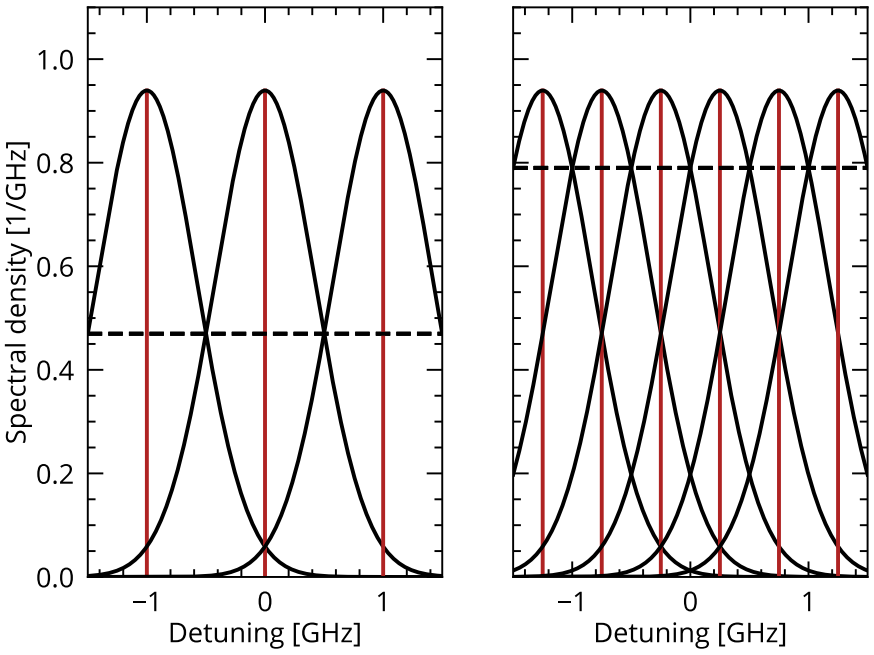

FIGURE 9.4: *Plots of Gaussian lineshapes with* $\Gamma_L/(2\pi) = 1$ *GHz where the central frequency is marked with a red line. The distance between the central frequencies is* $\Gamma_L/(2\pi)$ *(left) and* $\Gamma_L/(2\pi)/2$*. The dashed lines indicates the minimum spectral density of the combined lineshapes within* W*.*

9.4 Worst case scenario search optimization

Since the exact location of f_t is unknown *a priori*, one must consider the worst case scenario, where f_t is located at one of the minima, i.e. $\delta_t = \Gamma_L/(2\pi)/2$ in the case of Fig. 9.4 (left). The dashed line indicates the minimum spectral density within W. This plot suggests, that a step-size of $\Gamma_L/(2\pi)$ is not be the best choice for arbitrary lineshapes. E.g. in the right of Fig. 9.4 the step-size is $\Gamma_L/(2\pi)/2$ leading to a higher minimum spectral density (dashed line), but also double the amount of steps to cover W. The optimum step-size will be dependent on the specific laser lineshape.

To give a feel for how much longer the scan will take if using a Gaussian lineshape instead of a square one, a step-size of $\Gamma_L/(2\pi)/2$ is chosen for the following example. This gives $N'_{step}(\Gamma_L) = 2N_{step}(\Gamma_L)$ and a minimum spectral density at $\delta_t = \Gamma_L/(2\pi)/4$. The resulting $T^{C=1}$ (when inserting the P_{on} results for $\delta_t = \Gamma_L/(2\pi)/4$) as a function of τ_{spec} is given in Fig. 9.6. This plot is very similar to the on resonance case og Fig. 9.2, but we see that the required measurement times are longer, especially for the larger laser line widths.

Returning to our earlier example of $I_L = 20\,\text{W}\,\text{cm}^{-2}$ and $\Gamma_L/(2\pi) = 1$ GHz from Fig. 9.5, the new optimum $\tau_{\text{spec}} = 20$ ms giving $T^{C=1} = 201.6$ s corresponding

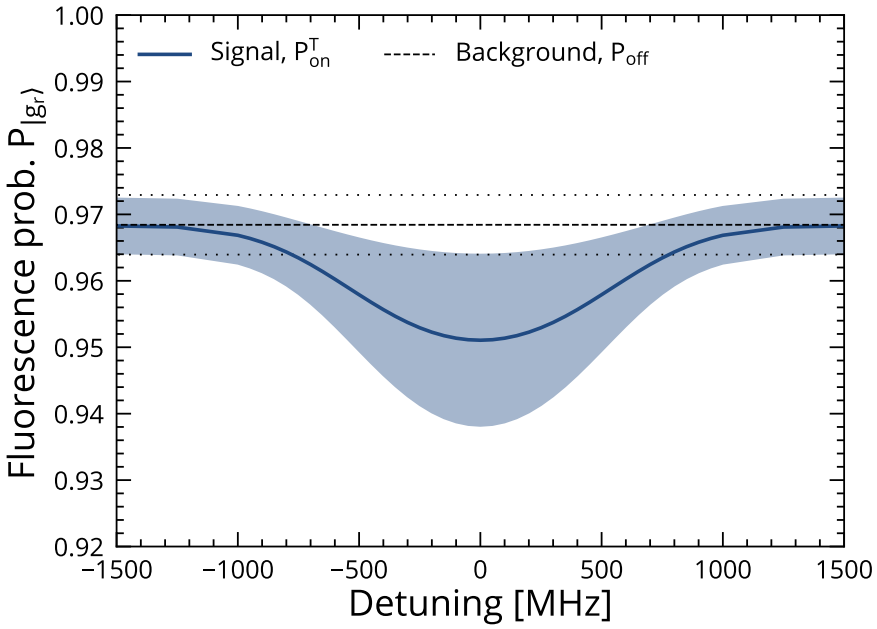

FIGURE 9.5: *The expected average PRS signal for a Guassian laser lineshape and* $I_L = 20\,\mathrm{W\,cm^{-2}}$ *and* $\Gamma_L/(2\pi) = 1$ *GHz for* τ_{spec} *of* 19 *ms. The expected measurement uncertainties after measuring for a time* $T^{C=1} = 180.6$ *s (as found from Fig. 9.2) are plotted as dotted lines for the background and a blue shaded area for the signal. We see that the distinction criteria is only fulfilled on resonance.*

to $N = 1680$ experimental cycles. The expected signal and background with the resulting measurement errors are plotted in Fig. 9.7. In this plot the error on the background and the signal does not touch at the central frequency, but first at ±250 MHz corresponding to $\pm\Gamma_L/(2\pi)/4$ as indicated by a gray line. Another PRS spectrum is plotted at a distance $\Gamma_L/(2\pi)/2$ from the first one to indicate the spectrum resulting from the laser lineshape of the neighboring scanning step.

The $T^{C=1}_{scan}$ values corresponding to the $T^{C=1}$ values of Fig. 9.6 (using $N'_{step}(\Gamma_L) = 2N_{step}(\Gamma_L)$) are plotted in Fig. 9.8 and here the difference from Fig. 9.3 is clear (notice the different y-axes). The total time to scan W has increased by more than a factor of 2, even though we only made twice the number of steps. The order of the different Γ_L results has also changed. This is due to the broadening of the PRS spectrum as a function of τ_{spec} as seen in Fig. 6.10. This effect plays a role now that we a not looking at the center frequency. For this particular example $\Gamma_L/(2\pi) = 3$ GHz minimizes $T^{C=1}_{scan}$.

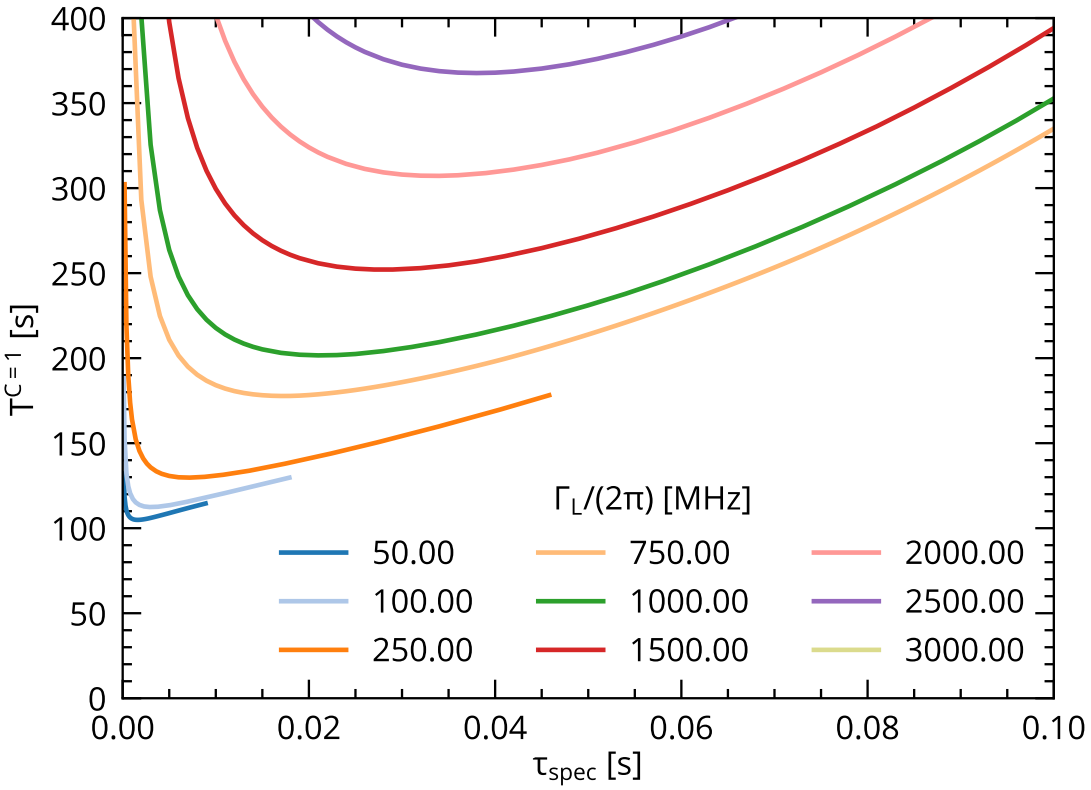

FIGURE 9.6: *The time to distinction signal from background $T^{C=1}$ for a detuning of $\delta_t = \Gamma_L/(2\pi)/4$ as a function of τ_{spec} for $I_L = 20\,\mathrm{W\,cm^{-2}}$ and a Gaussian laser lineshape for different laser linewidths Γ_L. Here $R_{H,ip} = 14(1)\,\mathrm{s^{-1}}$ and $R_{H,op} = 1.7(3)\,\mathrm{s^{-1}}$. This result is very similar to the on resonance case of Fig. 9.2, but we see that the times are longer especially for the larger widths.*

9.5 After obtaining a signal

After the initial scan of W, there is a $\sim 68\%$ chance that a signal was obtained if the confidence level of the background/signal distinction was $\sim 100\%$ i.e. $C > 2$, and we assume the experiment was working perfectly. If not, the scanning range must be increased beyond W. Depending on the laser spectral density overlap between the different scanning steps, and the location of f_t, a signal can be obtained for one or more laser frequency steps during a single scan. If W is scanned from one direction, once a signal has been obtained the next frequency step should also be measured. If this step shows none or a smaller signal, then the scan can be halted.[2]

If we consider the central step frequency f_L, that gave the largest signal, the transition has now been located to within plus/minus half the stepsize around this

[2]This procedure is similar to the binary search algorithm, but one cannot take the analogy too far.

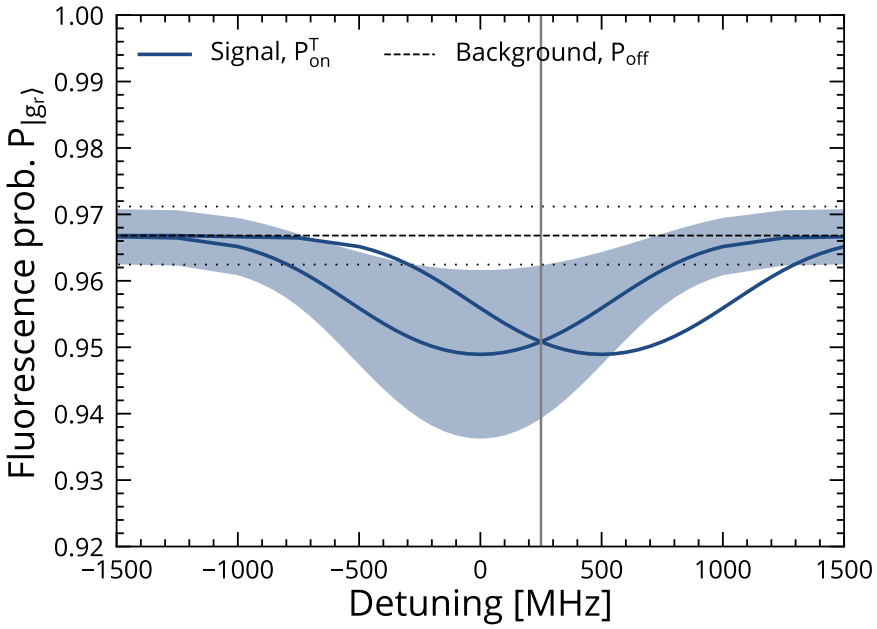

FIGURE 9.7: *The expected average PRS signal for a Guassian laser lineshape and* $I_L = 20\,\mathrm{W\,cm^{-2}}$ *and* $\Gamma_L/(2\pi) = 1$ *GHz for* τ_{spec} *of* 20 *ms. The expected measurement uncertainties after measuring for a time* $T^{C=1} = 201.6$ *s (as found from Fig. 9.6) are plotted as dotted lines for the background and a blue shaded area for the signal. We see that the distinction criteria is only fulfilled for all detunings within* $\delta_t = \pm\Gamma_L/(2\pi)/4$.

value (i.e. the frequency interval to the minimum spectral density, see Fig. 9.1 and 9.4). Again we assume that the laser frequency and its spectral shape is known perfectly. Hence if T^C_{scan} is similar for a range of Γ_L values, it is advantageous to chose a small one, since the initial spectroscopic measurement will already be more accurate.

The frequency interval, to within which f_t has been located after the initial scan, is subsequently the new search interval. Since this interval is smaller than W, the optimum laser linewidth to scan it will also be smaller, and likewise the optimum τ_{spec} (assuming a constant laser intensity).

To measure f_t as accurately as possible, the search procedure is repeated until the laser linewidth cannot be decreased further, or the search interval becomes equal to the uncertainty on the laser frequency. For the considered case of a 2.5 Hz transition linewidth, the width of the line itself is not a limitation.

9.6 Distinction time when prepared in $J = 1$

Since the experiment is limited by the timescale of the molecular dynamics, it is interesting to consider the case where the molecule is prepared in $J = 1$ before every

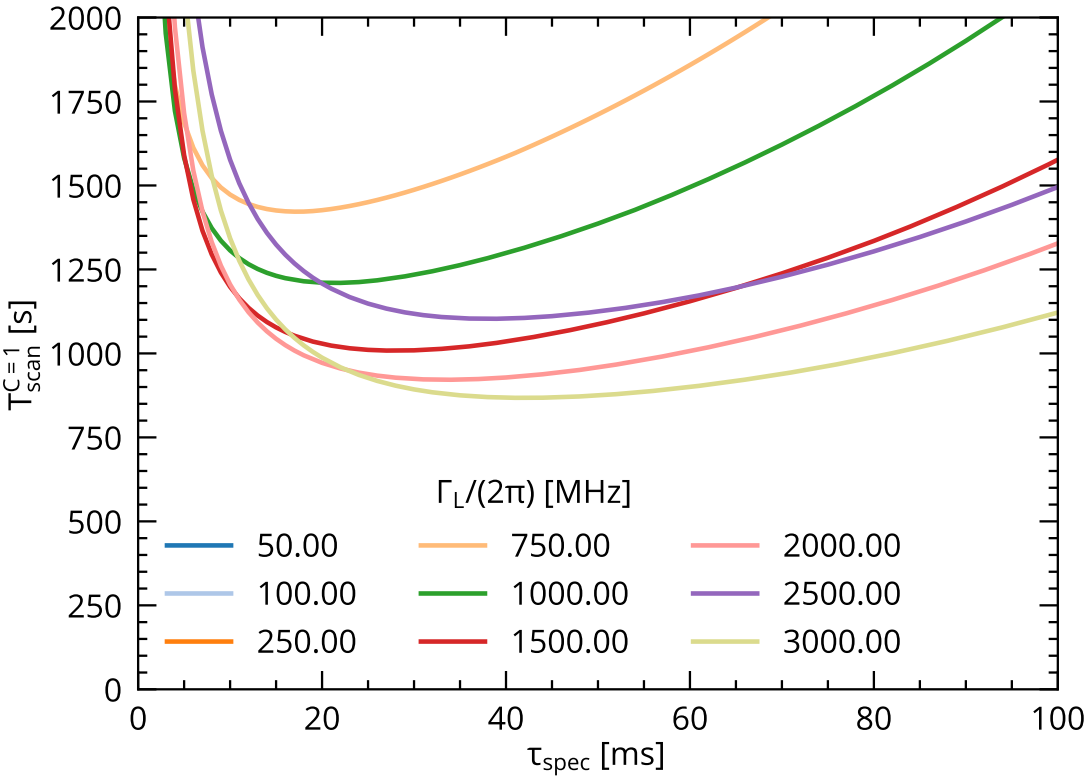

FIGURE 9.8: *The total time to scan W, $T^{C=1}_{scan}$ for the $T^{C=1}$ curves given in Fig. 9.6 when moving the laser frequency in steps of $N'_{step}(\Gamma_L) = 2N_{step}$. For these conditions this is minimized by $\Gamma_L/(2\pi) = 3000$ MHz at $\tau_{spec} = 40$ ms. Here $R_{H,ip} = 14(1)\,\mathrm{s}^{-1}$ and $R_{H,op} = 1.7(3)\,\mathrm{s}^{-1}$.*

measurement. $P_{J=1} = 1$ leads to $P^T_{on} = P_{on}$ giving the following criteria of distinction

$$P_{off} - P_{on} > C(\sigma_{off} + \sigma_{on}). \tag{9.8}$$

Without $\sigma_{J=1}$ to consider, both the background and the signal are simply binomially distributed leading to

$$T^C \equiv \tau_{cycle} \left(C \frac{\sqrt{P_{off}(1 - P_{off})} + \sqrt{P_{on}(1 - P_{on})}}{P_{off} - P_{on}} \right)^2 . \tag{9.9}$$

One quickly realizes that the minimization of K becomes very important for this scenario. Such state preparation can be performed by different means including state selective dissociation, rotational cooling or simply by cooling surroundings of the molecule down to freeze out the rotational degree of freedom. At 4 K almost 100% of the population will be in $J = 0$.

Part III

Experimental setup and procedures

Chapter 10

Ion trap setup and ion loading

10.1 Trap setup

10.1.1 Trap design

The linear Paul trap used for this thesis is called The Molecule Trap and was designed by Niels Kjærgaard around year 2000 [107]. A picture can be seen in Fig. 10.1. The dimensions and geometrical parameters of the trap were described in relation to Fig. 2.1 and given in Table 2.1. The ratio between the electrode radius r_e and diagonal distance r_0 was chosen such that the potential is nearly perfectly quadropolar close to the trap axis. With a total length of 4 cm, the trap is quite large compared to other traps of the same type. This, along with a small ratio between the length of the central electrodes $2z_0$ and the endcap electrodes z_e, was chosen to make the harmonic approximation of the DC potential in the trap center hold over mm's. This geometry was chosen with the prospects of studying large ion Coulomb crystals, however the

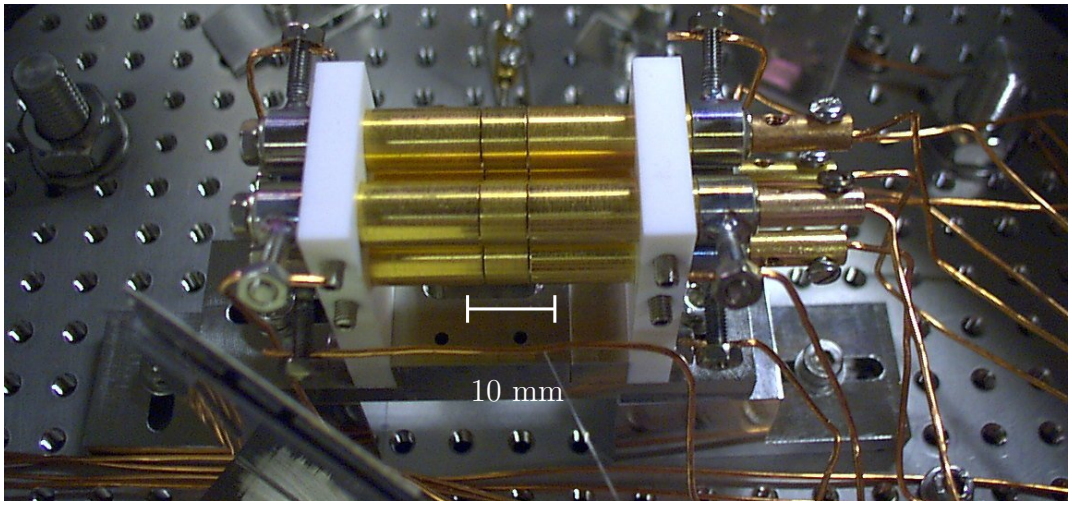

FIGURE 10.1: *A picture of the linear Paul trap used in the experiments presented in this thesis [107].*

nearly perfect potential also makes it ideal for precision experiments with single and few-ion systems.

The 12 electrodes, divided on four rods, are made of gold-coated stainless steel, and are separated by and mounted in Macor [108]. Macor is an electric insulating glass ceramic material, which experiences very little thermal expansion and outgassing, making it ideal for vacuum and low electric field noise conditions.

The electrodes are supplied by a home build mixer, which combines the DC and RF voltages. Both the RF and DC voltages on all 12 electrodes can be controlled individually facilitating very precise excess micromotion compensation. The RF voltage is supplied by a two-channel function generator[1] and further amplified[2] to achieve up to 1 kVpp. For the PRS experiments 500 Vpp was used.

The DC voltage is supplied by the homebuild etherDAC. The latest version was build by Karin Fisher around 2015. A detailed description of the trap electronics can be found in her thesis [82]. For the experiments in this thesis the DC supply has not been amplified in order to reduce noise. This gives an upper output limit of 18 V, however the PRS experiments have been performed at 5 V.

10.1.2 The vacuum chamber

A picture of the vacuum chamber containing the ion trap, can be seen in Fig. 10.2 The chamber has not been opened for more than 15 years (!) and the background pressure is usually maintained around $2 \cdot 10^{-10}$ Torr by an ion getter pump[3]. The trap must be kept in vacuum, to prevent collisions between trapped ions and rest gas atom and molecules causing heating of external as well as internal motional modes. And also to keep unwanted ions produced by photoionization of rest gas atoms and molecules to a minimum. The ovens providing the wanted Ca and Mg atoms for the experiment are located inside the chamber to the right in Fig. 10.2.

Around the chamber circumference are 6 view ports providing access to laser beams from almost all directions in the horizontal plane. An overview of how the different laser beams used for the experiments enter the trap can be seen in Fig. 10.3. The laser beams travel +10 m to the trap table through fibers or in free space depending on the wavelength.

[1] Keysight 33500B
[2] ENI 3100L
[3] Leybold IZ 270

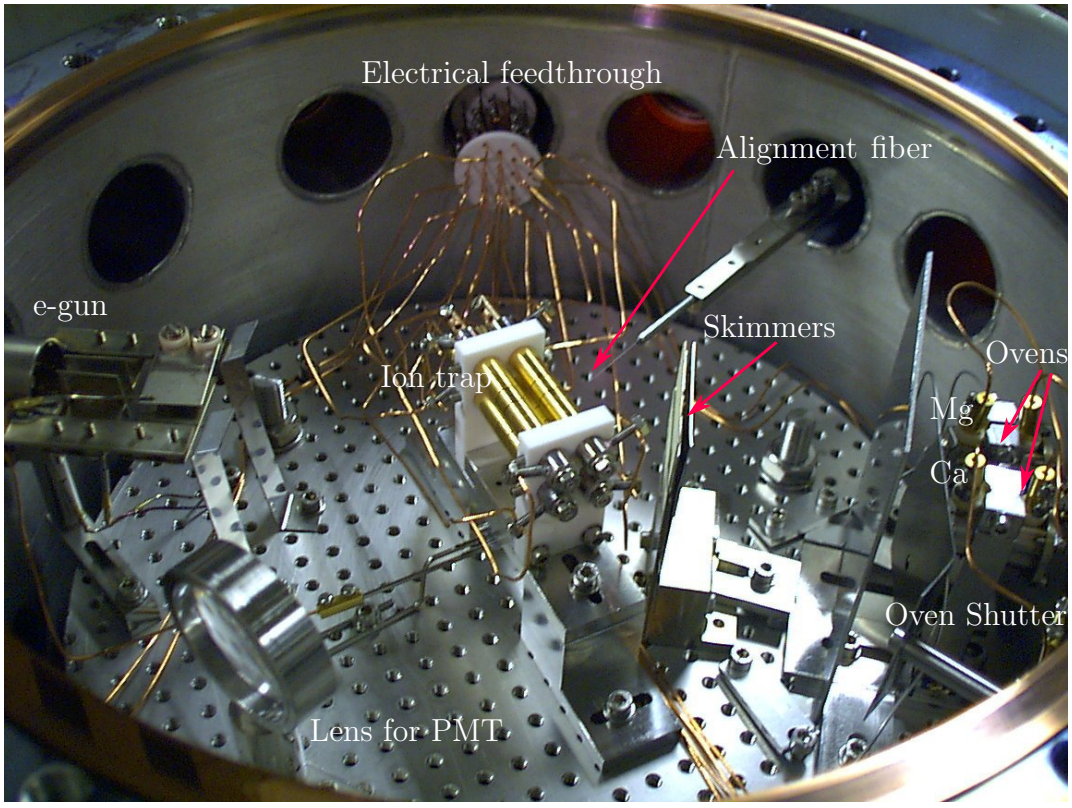

FIGURE 10.2: *Image of the vacuum chamber with the trap in the center and the two ovens with Mg and Ca, respectively, situated to the right (from Niels Kjærdgaard's thesis [107]). The oven shutter makes it possibe to block the ovens from outside. The skimmers between the ovens and the trap protects the trap electrodes from contamination by hot atoms from the ovens. The alignment fiber can be moved in and out of the center of the trap for rough alignment of the imaging system and laser beams on the trap center. The electrical feedthrough provides current to the trap electrodes. The e-gun and lens for PMT have not been used in this project.*

10.1.3 The imaging system

The CCD camera for fluorescence detection is placed above the trap and looks down on the trap through the top viewport of the vacuum chamber. Before reaching the camera the scattered light from the ions is focused by a lens with a focal length of 70 mm and a numerical aperture of 0.28. The lens sits approximately 7.5 cm above the ions and is mounted on a translation stage with micrometer screws for precision positioning. One meter above, the image is focused on an image intensifier, the output of which is focused by another lens onto the camera. The entire imaging system is mounted on a tower, the height of which can be adjusted with a motor.

The magnification of the imaging system can be calibrated by measuring the distance between two $^{40}Ca^{+}$ ions as a function of axial IP trap frequency when changing the DC potential. For two ions of equal mass $\omega_{ip} = \omega_z$ for a single ion, and one can

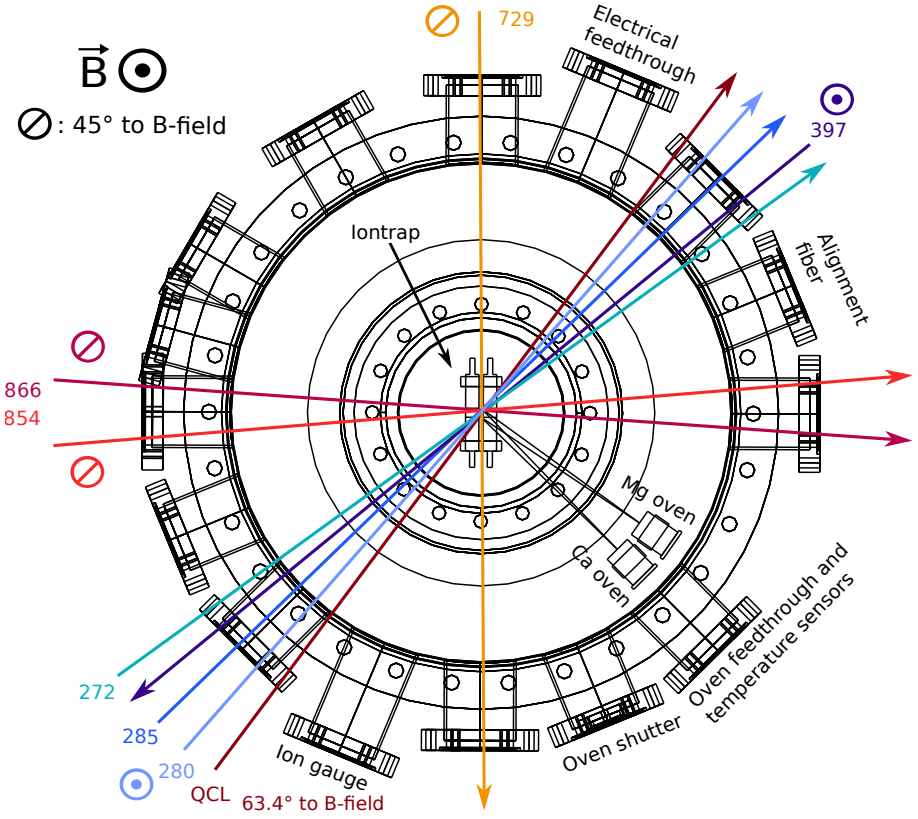

FIGURE 10.3: *Overview of the trap chamber from above with the overall direction of the different laser beampaths and their polarization directions. All the beams propagate horizontally. In reality all the laser beams go almost centrally through the viewports, and many of them are overlapped.*

calculate the expected ion distance from [109]

$$d(\omega_z) = \left(\frac{Q^2}{2\pi\epsilon_0 m\omega_z^2}\right)^{1/3}. \tag{10.1}$$

Each pixel of the CCD camera is 6.45 µm × 6.45 µm and the measured magnification is $M = 4.4$ [82].

10.1.4 Magnetic field control

The magnetic bias field at the ion position is produced by a coil sitting around the circumference of the vacuum chamber. The field produced by this coil defines a quantization axis for the ions in the vertical direction perpendicular to the trap axis. In order to make the field perfectly vertical, two smaller coils are wrapped around two view ports, such that their fields point in perpendicular horizontal directions.

The field direction is adjusted by setting the polarization of the 866 nm repump beam to vertical. In this way only $\Delta m_J = 0$ transitions can be driven if the B-field

is vertical, effectively reducing the ion fluorescence level. Thus as the current to the coils are varied, we aim for minimum fluorescence to optimize the alignment.

Additionally, the AC wall voltage of 50 Hz causes a lot of 50 Hz magnetic radiation in the lab. Therefore the experimental cycles are line-triggered, such that they always start at the same phase of the 50 Hz oscillation. This makes the experimental cycles repeatable, but does not change the fact, that the magnetic field varies. This makes it harder to compare experimental cycles of different durations. Therefore the AC magnetic field noise is compensated using an additional coil placed on top of the vacuum chamber, also producing a vertical magnetic field. This coil is fed by a phase shifted and amplitude adjusted AC line, experimentally adjusted to minimize the 50 Hz oscillation of the 4s $^2S_{1/2}$, $m_J = -1/2$ to 3p $^2D_{5/2}$, $m_J = -5/2$ shelving transition in $^{40}Ca^+$. This result in a magnetic field fluctuation during the 50 Hz cycle of amplitude 280(70) µG corresponding to a 0.8(2) kHz amplitude of the transition frequency oscillation.

During the day the magnetic field was measured to change by up to 6 mG in sudden jumps. During the night on the other hand, the fluctuations are within 400 µG [82]. Thus we try to run experiments over night when possible. For the experiments presented in this thesis the magnetic field measured on the ion was 6.523(3) G.

10.2 Ion production and verification

10.2.1 Production of atomic beams

The two atomic ovens inside the vacuum chamber are hollow graphite cylinders containing neutral Ca and Mg, respectively. By running electric current through a tungsten wire coiled around them, hot atoms effuse out of a 1 mm hole in each oven, producing an atomic beam of each element.

The Ca oven is typically heated to around 310 °C. ^{40}Ca has a high isotopic abundance of 97%, which is the main reason for using this isotope instead of another stable even-nucleon isotope. Odd nucleon numbers give rise to unwanted hyperfine structure of the internal levels.

The Mg oven is typically heated to around 270 °C. ^{24}Mg has an abundance of 79%, which is why it is chosen over the other stable even-nucleon isotope, ^{26}Mg, with an abundance of 11%.

The atomic beams have a roughly 45° angle to the trap axis, and are collimated by skimmers placed between the ovens and the trap, in order to prevent hot atoms from contaminating the electrodes. The atomic beams can also be blocked completely by

a mechanical shutter from outside the chamber. This is done as soon as the desired ions are trapped, such that the hot atoms do not disturb the experiment if they are accidentally ionized. It takes a couple of hours to heat the ovens, so they are usually kept on in case new ions need to be trapped, making the shutter necessary. In general high loading rates are not crucial for the presented experiments, since mostly we want to trap one ion of each species, which can be reused for many experiments, and not large ion crystals.

10.2.2 Ion loading by isotope selective photo-ionization

A two-photon isotope selective technique first developed in our group [110] is used to ionize Ca and Mg. As the name suggests, the advantage of this technique is that it can target specific atomic isotopes. E.g. the used transition of 285 nm in $^{24}Mg^+$ is shifted by 0.73 GHz for $^{25}Mg^+$ and 1.41 GHz for $^{26}Mg^+$, which can easily be resolved [110, 111]. Using this method, different isotopes of the same species and rest gas atom and molecules have a relatively low probability of being ionized. Another advantage is that the charge of the created ions always is one. These two features are very important, since the presented experiments rely on trapping the same very specific isotopes with charge one every time. In principle the experiments could be performed with other isotopes of Ca and Mg, but optimization of the subsequent experimental procedures is simplified if the starting system is well-defined and easily reproducible.

The electronic levels of Ca and Mg relevant for ionization are shown in Fig. 10.4. The Ca atom is resonantly excited from its ground state $4s^2\ ^1S_0$ to the $4s5p\ ^1P_1$ state

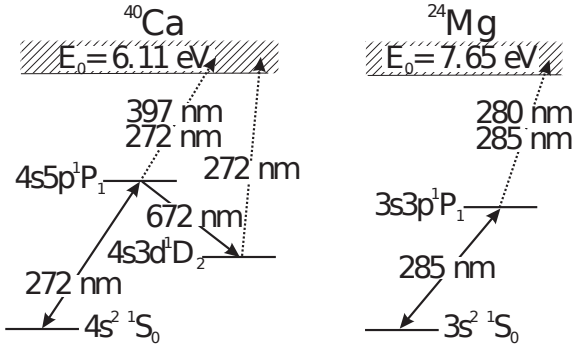

FIGURE 10.4: *Ca and Mg photoionization schemes used in our experiments [110].*

by a 272 nm photon. From here the atom can be ionized by either another 272 nm photon or a 397 nm photon, or it can decay to the $4s3d\ ^1D_2$ state from where it can also be ionized by a 272 nm photon.

Similarly, Mg is first resonantly excited from the ground state $3s^2\ ^1S_0$ to the 3s3p $^1P_1$ state by a 285 nm photon. From this state the atom can be ionized by another 285 nm photon or by a 280 nm photon. The 397 nm and 280 nm beams are present in the trap since they are used for Doppler cooling of the created Ca and Mg ions, respectively.

10.2.2.1 Ionization lasers (272 and 258 nm)

The ionization beams of 272 nm for Ca and 285 nm for Mg propagate perpendicularly to the atomic beams in order to minimize Doppler broadening, as seen in Fig. 10.3. Note that in reality many of the laser beams shown in this figure are overlapped. Both these beams travels through air to the trap due to the lack of available efficient fibers at this wavelength.

The 272 nm beam is produced by sending the 1088 nm output of a Koheras Boostik fiber laser trough two home build frequency-doubling cavities [71, 112]. The frequency is locked by sending part of the light after the first cavity at 544 nm to the optical wavemeter[4] and doing a feed-back on the laser piezo.

The 285 nm beam is produced by sending the 570 nm output of a Toptica DL pro laser through another home build frequency doubling cavity. This laser has a build in frequency doubling step. Part of the 570 nm light is send to the wavemeter for frequency stabilization.

10.2.3 Production of MgH^+ ions

A hydrogen atom is added to $^{24}Mg^+$ by leaking in H_2 gas from a valve connected to the vacuum chamber until the pressure has increased from 1×10^{-10} Torr to a steady state of 1×10^{-8} Torr. Next, the $^{24}Mg^+$ ion is excited from $3s^2S_{1/2}$ to the $3p^2\ ^2P_{3/2}$ excited state by the 280 nm laser. This is the same transition as used for PRS of $^{24}Mg^+$. From the excited state the following reactions are energetically possible by collision

$$\text{I)} \quad Mg^+ + H_2 \rightarrow MgH_2^+$$
$$\text{II)} \quad Mg^+ + H_2 \rightarrow MgH^+ + H$$

Fortunately, reaction II) is much more probable than I) [45]. The large trap depth of around 1 eV ensures that almost all molecular ions formed in this way remains

[4] Ångstrom WS-U calibrated to a stabilized HeNe laser.

trapped. Likewise, there is a probability to react the $^{40}Ca^+$ ion (from the $^2P_{1/2}$ state) with H_2 and create $^{40}CaH^+$, however this molecule can easily be dissociated by a 272 nm photon when desired [113], which is routinely done in the experiment.

10.2.3.1 Laser for driving the 3s $^2S_{1/2}$ - 3p $^2P_{3/2}$ transition in Mg^+ (280 nm)

The 280 nm laser beam for driving the 3s $^2S_{1/2}$ - 3p $^2P_{3/2}$ transition in Mg^+ has a 45° angle to the trap axis as seen in Fig. 10.3. This beam travels through air to the trap due to the lack of available efficient fibers at this wavelength. Besides from being used during the $^{24}MgH^+$ production process, the 280 nm laser is the spectroscopy laser used for PRS of the same transition in $^{24}Mg^+$.

The 280 nm beam is produced by sending the 1120 nm output of a MenloSystems 'Orange One' fiber laser trough two home build frequency-doubling cavities [71, 112]. The frequency is locked by sending part of the light after the first cavity at 560 nm to the wavemeter and doing a feed-back on the laser piezo.

10.2.4 Establishing two-ion scenarios

10.2.4.1 $^{40}Ca^+$ and $^{24}Mg^+$

To trap a single $^{40}Ca^+$ ion together with a single $^{24}Mg^+$ ion the first step is to trap a single $^{40}Ca^+$ ion by unblocking the Ca oven and shining in the 272 nm laser beam at the resonant frequency. Prior to laser cooling, the ions have temperatures given by that of the hot ovens corresponding to kinetic energies around 0.05 eV (∼300 °C), however, they can easily be confined by the ∼ 1 eV trapping potential. To only trap a single $^{40}Ca^+$ ion, the 272 nm laser pulse must be short (few ms), depending on laser power, alignment and oven temperature. If more than one gets trapped the DC potential can be switched off momentarily (tens of µs) by switching channel on the RF generator in order to try to lose the excess ions from the trap. However, due to the complex dynamics of the ion-trap system, this technique often gets rid of all the ions, and one has to start over.

To also trap a single $^{24}Mg^+$ ion the Mg oven is unblocked and the 285 nm laser beam is shined in at the resonant frequency. For this the red detuned 280 nm beam is also shined in to cool $^{24}Mg^+$ for faster crystallization. As soon as the $^{24}Mg^+$ ion crystallizes (the $^{40}Ca^+$ ion moves away from the trap center) the 280 and 285 nm beams are blocked to not trap excess $^{24}Mg^+$. If another dark ion (all other ions

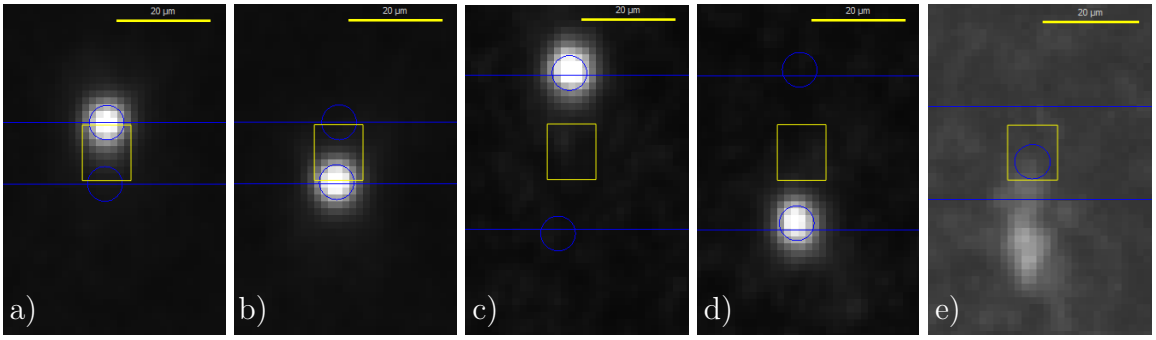

FIGURE 10.5: *Images of a single $^{40}Ca^{+}$ ion and one dark ion crystallized along the trap axis for different DC voltages creating confinement along this axis. a) and b) are taken at $U_{dc} = 18$ V, c) and d) at $U_{dc} = 1.1$ V, and e) at $U_{dc} = 5$ V. The ions swap positions on a second timescale due to collisions with rest gas atoms and molecules. In e) the 397 nm laser beam is pulsed at the ions' common axial resonance frequency (ω_{ip}) causing heating, making the $^{40}Ca^{+}$ ion much less localized. The maximum fluorescence seen in a single pixel is hence decreased. Fig. from [95].*

than $^{40}Ca^{+}$ are dark, since they do not scatter 397 nm light) gets trapped, it can be removed by going to the borders of the mass 24 u trapping potential, which can be done with a precision better than 1 u [114].

To easily confirm that the dark ion has mass 24 u we measure the mass by pulsing the 397 nm laser beam at the IP trap level frequency we expect for the $^{40}Ca^{+}$-$^{24}Mg^{+}$ system [115]. Close to resonance the motional mode will be excited, and the $^{40}Ca^{+}$ fluorescence will come from a larger area, effectively decreasing the fluorescence level from the central trap region. By scanning the pulse frequency and monitoring the fluorescence level, ω_{ip} can easily be determined to within 0.1 kHz and thereby the dark ion mass to within 1 u. This is illustrated in Fig. 10.5. In these pictures the yellow square marks the trap center, and the blue lines indicate the expected distance of two ions at the applied DC voltage. Both are useful features of the control program. Examples of mass measurements of the $^{24}Mg^{+}$ and $^{24}MgH^{+}$ ions are shown in Fig. 10.6.

To definitively confirm that the dark ion is $^{24}Mg^{+}$ the two-ion crystal can be heated by sending in a blue detuned 280 nm beam, which also results in motional excitation and hence a dip in fluorescence level.

10.2.4.2 $^{40}Ca^{+}$ and $^{24}MgH^{+}$

For $^{24}MgH^{+}$ production we load a small crystal of $^{40}Ca^{+}$ ions containing a single $^{24}Mg^{+}$ ion. Since we cannot cool $^{24}MgH^{+}$ directly as we can with $^{24}Mg^{+}$, the larger crystal helps keep the dark ion crystallized when the pressure is increased.

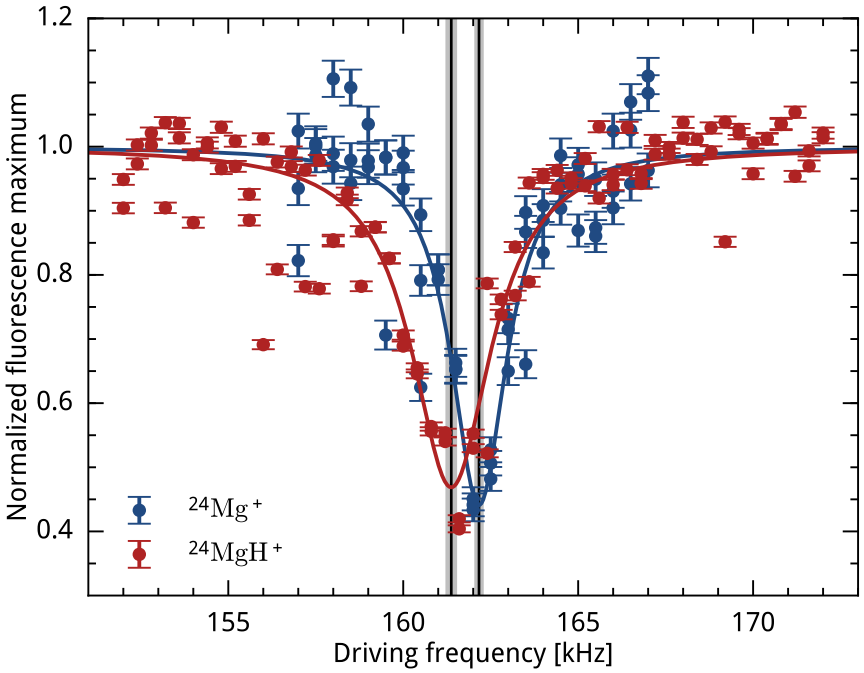

FIGURE 10.6: *Measured fluorescence level as a function of the driving frequency used for pulsing the 397 nm laser beam. Here for $^{40}Ca^+$ plus $^{24}Mg^+$ (blue) or $^{24}MgH^+$ (red). The gray shaded regions indicate double the standard deviation given by the fits to a Lorentzian function. As seen the resonance ω_{ip} frequencies, and thereby the masses, can easily be distinguished. Fig. from [95].*

After shining in the 280 nm beam for a couple of minutes many dark ions have been created. After going to normal pressure by closing the H_2 valve, te trap is cleaned by going to the mass 24 DC border and mass 25 RF border. In this way we lose $^{40}Ca^+$ but keep both $^{24}Mg^+$ and $^{24}MgH^+$ in case $^{24}MgH^+$ was not produced. Lastly we load a new single $^{40}Ca^+$ ion.

To confirm $^{24}MgH^+$ production we measure the mass as explained in the previous section. However, we cannot resolve the mass difference between $^{24}MgH^+$ and $^{25}Mg^+$ [5], meaning we can only distinguish them by probing their internal states. However, we cannot probe the $^{25}Mg^+$ ion by heating with the 280 nm laser as we can for $^{24}Mg^+$ and $^{26}Mg^+$ due to its finestructure levels.

A possible workaround would be to instead work with $^{26}MgH^+$ since ^{26}Mg is the heaviest stable Mg isotope, making the probability of trapping anything else than $^{26}MgH^+$ with mass ~ 27 u extremely small. Nevertheless, we prefer $^{24}Mg^+$ for PRS since the spectroscopic lines are known to a better accuracy (1.5 GHz) [70].

[5] Using a variation of the described technique, it is possible to obtain a mass resolution of 10^{-4} [115], which is still not enough.

Additionally we tested that a charge exchange collision from $^{26}Mg^+$ to $^{24}Mg^+$ with relative abundance of 1:8 did not take place within 30 min, so we do not expect charge exchange between $^{24}MgH^+$ and $^{25}Mg^+$ within 4 hours due to the same relative abundance of 1:8 between $^{24}Mg^+$ and $^{25}Mg^+$.

10.3 Automated experiment control

This section provides some technical details about how the ion experiments are controlled, laser pulse sequences build, and how the outcome of each experimental cycle is read out.

10.3.1 Control program

All of the ion experiments are run via a Python based control program called qControl. This program was initiated by Gregers Poulsen [52] and has been modified by all other PhD students and postdocs working on The Molecule Trap experiment since. It saves all the experimental data and configurations to the control computer and a database.

From the graphical user interface (GUI) trap voltages, camera exposure times, and laser frequencies and intensities can be changed, and different experimental sequences can be run. Each data point is typically the outcome of the same sequence, i.e. experimental cycle, repeated 100 times (more for PRS of $^{24}MgH^+$). These are build from pre-defined pieces e.g. Doppler cooling and sideband cooling and fluorescence readout as described below. From the GUI it is easy to change the different parameters of a sequence for daily optimization.

10.3.2 Sequence timing

At each data point, qControl uploads a new pulse sequence (e.g., with different pulse duration or frequency) to a programmable pulse generator (PPG), which handles the timing of the experiment using field programmable gate arrays (FPGA) to control up to 32 TTL (transistor-transistor logic) outputs. These control RF switches for the laser AOMs, camera exposure etc.

The PPG is equipped with a DDS output with its own FPGA used to control the 729 nm AOM [82]. The DDS has 8 different single frequency registers, in addition one can also program a sweep in frequency. At the output the DDS has a variable gain amplifier (VGA) for amplitude sweeps. The VGA is used to make an intensity sweep

of the 397 nm laser for the final step of Doppler cooling. Thus 1 of the 8 different single frequency registers of the DDS is dedicated to the 397 nm laser frequency during the sweep, leaving us with 7 different frequencies for the 729 nm laser in each sequence, of which we use 6 at the moment as described in Sec. 11.2. That means we have only one frequency left that could be used to improve sideband cooling or readout.

The RF drives applied to the AOMs of the 397 nm, 866 nm, and 854 nm lasers are provided by a 4-channel DDS[6] outside the PPG box. The DDS outputs are sent through RF switches, which are switched by TTL pulses provided by the PPG.

10.3.3 Fluorescence readout

Measuring whether the $^{40}Ca^{+}$ ion is in the electronic ground state 4s $^{2}S_{1/2}$, is done via so-called fluorescence readout. This is done by illuminating the ion with resonant 397 nm and 866 nm laser light on the Doppler cooling transition, with intensities far beyond the saturation limit. If this results in a high average fluorescence level as measured on the CCD camera, we know it was in the ground state and we say the ion is 'bright'.

The cutoff fluorescence level for the ion to be considered as 'bright' is determined by running a sequence where the fluorescence level is measured when both the 397 nm and 866 nm lasers are on for 12 ms, and also when only the 397 nm laser is on for 12 ms. In the latter case, the ion is pumped to $^{2}P_{3/2}$ and is dark on the camera. The cutoff is then chosen as the value right between the average of these two measurements after many cycles.

In every experimental cycle, after an attempt to shelve $^{40}Ca^{+}$ in the 3p $^{2}D_{5/2}$ state has been made by sending a 729 nm probe pulse, the 397 nm and 866 nm lasers are sent in for 12 ms where the fluorescence level is recorded (see e.g. Fig. 11.2). If it is above the predetermined cutoff value the ion is counted as 'bright' otherwise as 'dark'.

Then the 854 nm laser is also sent in for 8 ms in order to repump the ion to the ground state (if it was shelved) for the next cycle. During these 8 ms qControl checks that the ion fluoresces. If not, the ion is not crystallized and the point is discarded and retaken, since it would be a false dark count.

Then follows around 15 ms where the data is transferred from the camera to the computer and we wait for the sequence duration to be a multiple of 20 ms, such that

[6]Designed and built by Frank Mikkelsen at our electronics department.

it is synchronized with the 50 Hz wall voltage. During this time the 397 nm, 866 nm, and 854 nm beams are all on to keep the ions Doppler cooled.

When working with two ions the program additionally checks, that the $^{40}Ca^{+}$ ion was not sitting in the trap center during readout, since this would mean the spectroscopy ion was not crystallized.

Chapter 11

Ion cooling

11.1 Doppler cooling sequence

For Doppler cooling the the 397 nm, 866 nm and 854 nm laser beams are applied simultaneously to maintain a closed transition.

During ionization the 397 nm light is detuned by up to 500 MHz to cool ions created with high energy effectively. As the first step of of an experimental cycle (see e.g Fig. 11.2) the detuning is changed to the optimum for Doppler cooling $\delta_{\min} \sim -\Gamma/2$ and the intensity is reduced below the saturation limit in order to perform optimum Doppler cooling with a constant intensity for 10 ms.

During cooling the 397 nm light exerts a force on the ion, pushing it off the trap center. Consequently a sudden laser intensity cut-off will leave the ion with excess potential energy, which is why the intensity is instead ramped down to zero over 2 ms.

11.1.1 Main cooling laser (397 nm)

The 397 nm beam for Doppler cooling is produced by a Toptica DL pro diode laser, and frequency stabilized by the optical wavemeter. The beam enters the trap with a 45° angle to the trap axis as seen in Fig 10.3 and the polarization direction is along the vertical magnetic field for reasons discussed in Sec. 4.1.3. The frequency is stabilized by the optical wavemeter.

The beam is sent through a double-pass acousto-optic modulator (AOM) centered at 250 MHz, which facilitates pulse switching and frequency control during ion experiments. As an extra precaution a mechanical shutter is also installed in the beampath. The +1st order AOM output is normally used for Doppler cooling and fluorescence readout, and is therefore detuned to the optimum for Doppler cooling $\sim -\Gamma/2$. During trapping we also use the 0th order beam which is red detuned by

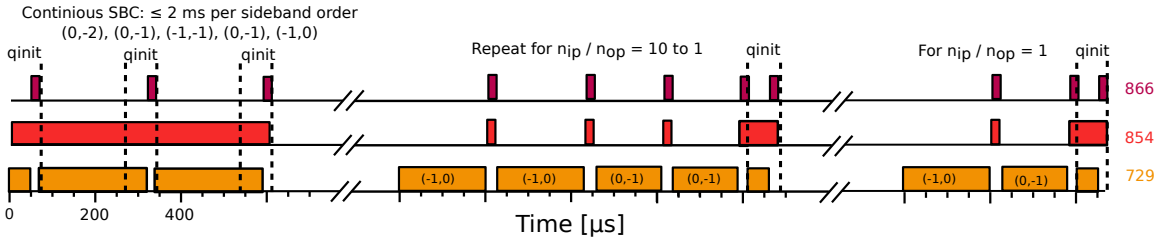

FIGURE 11.1: *Illustration of the experimental SBC sequence used for one $^{40}Ca^{+}$ ion and one $^{24}Mg^{+}$ or $^{24}MgH^{+}$ ion. It takes a total time of around 30 ms. The height of the colored bars does not correspond to light intensity.*

400-500 MHz, since this is more efficient for hot ions. Both orders are combined and coupled into a single mode polarization maintaining fiber going to the trap.

11.1.2 Repumping laser (866 nm)

The 866 nm laser for repumping during Doppler cooling is a home build external cavity diode laser (ECDL) in Littrow configuration, also frequency stabilized by the optical wavemeter. The beam enters the trap with a 90° angle to the trap axis as seen in Fig 10.3 and the polarization has a 45° angle to the vertical magnetic field for reasons discussed in Sec. 4.1.3. The beam is sent through a single-pass AOM centered at 270 MHz, which facilitates pulse switching and frequency control during ion experiments. This beam is combined with the 854 nm laser and coupled into a single mode polarization maintaining fiber going to the trap.

11.2 Sideband cooling sequence

For SBC the the 729 nm, 854 nm, and 866 nm laser beams are applied interleaved and simultaneously. The experimental SBC sequence is depicted in Fig. 11.1 and takes around 30 ms in total. After Doppler cooling, the motional population is Boltzmann distributed with average motional state $\bar{n}_{ip/op} \simeq \frac{\Gamma_{397}}{2\omega_{ip/op}}$ giving $\bar{n}_{ip} = 95$ and $\bar{n}_{op} = 52$ resulting in occupation of motional states up to ∼500 for IP and ∼300 for OP for our parameters. To avoid population trapped at high motional numbers, we start by driving the following sidebands in this order (s_{ip}, s_{op}): (0,-2), (0,-1), (-1,-1), (0,-1), (-1,0). We use (0,-1) secondly instead of (-2,0) since they have almost the same frequency compared to the Rabi frequency (∼ 100 kHz). By interleaving cooling on the two modes we aim to cool them simultaneously, such that one does not heat up the other. This is done in a continuous scheme where the 729 nm and 854 nm beams are on simultaneously. Each sideband is cooled for up to 2 ms, but less for

the higher orders according to the efficiency by which they deexcite motional quanta. The cooling is interrupted by state initialization (qinit) every 200 µs that takes 70 µs.

Next, in order to reach the SBC limit, we apply a pulsed scheme were the 729 nm laser coherently drives a RSB π-pulse for a targeted motional state. After each 729 nm pulse a 854 nm laser pulse of 20 µs repumps population out of the $^2D_{5/2}$ state. In order not to drive the carrier transition off-resonantly, the pulsed SBC is done at low intensity relative to the continuous, to do a last finetuning of the ground state preparation. Here we only drive the (-1,0) and (0,-1) sidebands since we now expect the population to be below $(n_{ip}, n_{op}) = (10, 10)$. First the (-1,0) sideband is targeted twice with a 729 nm pulse time corresponding to a π-time for the motional state $(n_{ip}, n_{op}) = (10, 0)$, then the (0,-1) sideband for $(n_{ip}, n_{op}) = (0, 10)$ is targeted twice before performing state initialization. Next the $(n_{ip}, n_{op}) = (9, 0)$ and (0,9) states are targeted twice each and so forth until $(n_{ip}, n_{op}) = (1, 0)$ and (0,1) has been targeted.

Lastly the $(n_{ip}, n_{op}) = (1, 0)$ and (0,1) states are targeted once again each before a final state initialization. The final 729 nm pulse times are on the order of 200 µs and 150 µs, respectively.

11.2.1 The S-D quadropole transition driving laser (729 nm)

The 729 nm laser used for driving the 4s $^2S_{1/2}$ to 3p $^2D_{5/2}$ transition in $^{40}Ca^+$ for sideband cooling and shelving is produced by a Toptica TA Pro diode laser. The laser enters the vacuum chamber along the trap axis as seen in Fig. 10.3, and the polarization is 45° to the vertical magnetic field, such that $\Delta m_J = \pm 1, \pm 2$ can be driven. Pulse switching and frequency control is done via a double-pass AOM centered at 200 MHz. The beam is coupled into a single mode polarization maintaining fiber going to the trap.

The wavelength of this laser is only measured by the optical wavemeter, but not locked to it, since it can only stabilize the frequency to within a few MHz. This is not enough for sideband resolution ($\Gamma_L \ll \omega_{ip}, \omega_{op}$) required for sideband cooling. The output frequency is instead linewidth narrowed and short-time stabilized by a cavity resulting in a linewidth of 1 kHz or less [52].

Since the cavity has a frequency drift of $7.6\,\mathrm{kHz\,h^{-1}}$, it cannot be used as an absolute reference. This could be compensated for with the AOM after measuring the frequency on the ion, but this is not so convenient. Instead, for long time stabilization the laser is referenced to an optical frequency comb[1]. In this way we can run hour long

[1]MenloSystems FC1500-250-WG, a resource of LASERLAB.DK

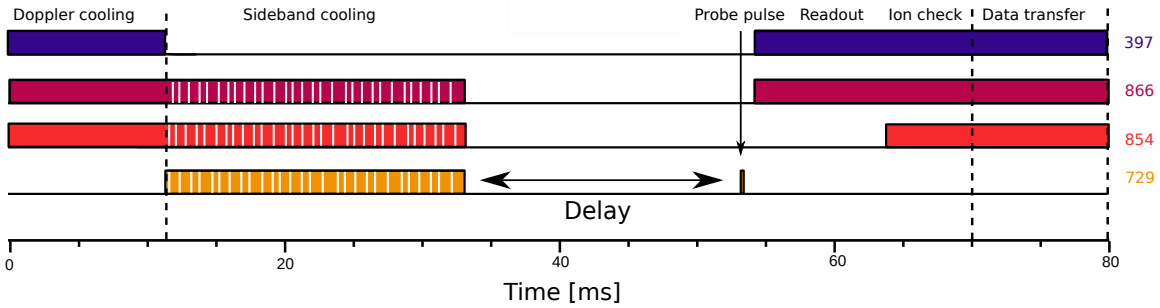

FIGURE 11.2: *A typical experimental sequence for doing SBC evaluation (zero delay) and heating rate measurements (varying delay). The average pulse times for the different lasers are indicated. The height of the boxes does not correspond to laser intensity.*

experiments without worrying about the laser frequency drift. The frequency comb is optically locked to the Stabiλaser [116], which defines the limit of its stability. The Stabiλaser is the same laser as is used to calibrate the IR wavemeter and is discussed in Sec. 12.2.1.1.

11.2.2 The D-P deshelving laser (854 nm)

The 854 nm laser for repumping during sideband cooling has the same construction and general beampath as the 866 nm laser described in Sec. 11.1.2. It also enters the trap with a 90° angle to the trap axis as seen in Fig 10.3, since the two beams share the same fiber. It also has a polarization with a 45° angle to the vertical magnetic field to drive all Δm_J transitions.

11.3 Temperature and heating rate measurements

In order to evaluate the temperature of the OP(IP) mode right after SBC, we do a shelving pulse on the 1st red OP(IP) sideband with a π-pulse corresponding to $|n_{ip}, n_{op}\rangle = |0,1\rangle(|1,0\rangle)$ before fluorescence readout. The total pulse sequence is is depicted in Fig. 11.2, where for now, the delay time is zero. In the next cycle the 1st blue OP(IP) sideband is instead addressed with the same pulse intensity and duration. For the BSB this corresponds to a π-pulse from $|n_{ip}, n_{op}\rangle = |0,0\rangle$.

The frequency is scanned such that we resolve the spectrum right around the two sidebands ($\sim$ 50 kHz span for each). The two peaks are then fitted to extract the sideband heights ρ_{rsb} and ρ_{bsb}. The average motional number can be found from Eq. 4.16.

To deduce the trap-induced heating rates of the two modes this measurement is performed for different delay duration between the end of the SBC sequence and the

shelving pulse. During this time the ion-system is not cooled and is subject to the uncontrolled heating mechanisms of the trap and lab environment. The extracted $\bar{n}_{ip}$ and $\bar{n}_{op}$ as a function of delay can then be fitted to a linear functions, where the heating rates are given by the slopes.

Chapter 12

Photon recoil spectroscopy

Once the target and readout ions have been trapped and ground state cooled, performing PRS spectroscopy is only a slight variation of the heating rate experiments presented in Sec. 11.3. With this experimental sequence in mind, doing PRS simply consists in exposing the ions to the spectroscopy laser during the delay time between the sideband cooling sequence and the resolved shelving pulse. For PRS the shelving pulse(s) must always be on a red sideband. Also, the delay time must be exactly the same length as the spectroscopy laser pulse to avoid excess trap-induced heating.

12.1 PRS of an electronic transition in $^{24}Mg^{+}$

When performing PRS of the 3s $^{2}S_{1/2}$ - 3p $^{2}P_{3/2}$ target transition in $^{24}Mg^{+}$, the laser for spectroscopy is the 280 nm laser also used for producing $^{24}MgH^{+}$ ions from $^{24}Mg^{+}$, which was presented in Sec. 10.2.3.1. For PRS the duration of laser exposure on the ions is controlled with a mechanical shutter via the PPG. The 280 nm laser frequency is controlled by changing the target locking frequency on the optical wavemeter, which is done automatically by the PPG.

The full PRS sequence for $^{24}Mg^{+}$ is shown in Fig. 12.1, where the spectroscopy pulse is shown in light blue. As depicted, the spectroscopic pulse takes up all the time between SBC and the RSB transfer pulse(s).

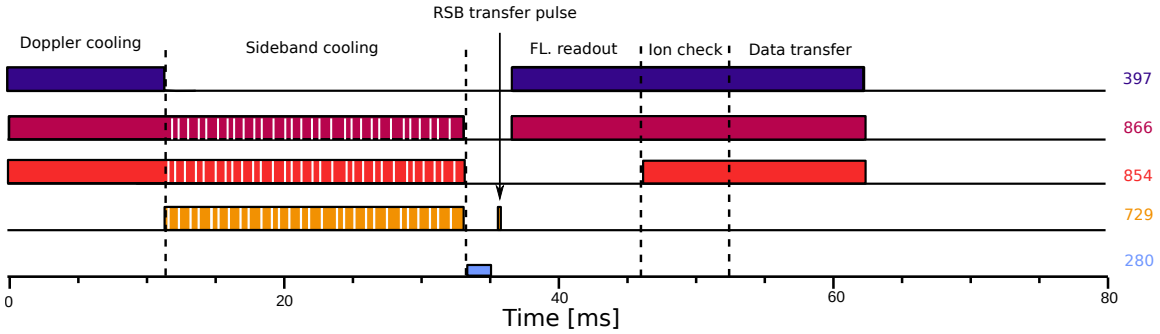

FIGURE 12.1: *A typical experimental sequence for doing PRS of the 3s $^{2}S_{1/2}$ - 3p $^{2}P_{3/2}$ transition in $^{24}Mg^{+}$. The average pulse times for the different lasers are indicated. The height of the boxes does not correspond to laser intensity.*

The goal was to verify the predictions of the simulations, in particular for short spectroscopy times where the dependence on τ_{spec} is the strongest (see Fig. 6.5). Also, simulations for larger τ^t_{scaled} are more time-consuming to calculate and the population will eventually move outside the defined state-space.

The spectroscopic time needed to be in the steep part of the mentioned curve depends on the applied laser intensity. Because the spectroscopic pulse duration was controlled by a mechanical shutter, the pulse duration could minimally be around 1 ms, effectively putting an upper bound on the laser intensity. A laser intensity giving a small τ_{scaled} for a $\tau_{\text{spec}} \sim 1$ ms was according to simulation on the $\mu\text{W/cm}^{-2}$ level.

These low laser light intensities were reached by using neutral density filters, which were changed manually. Measurements of the low light power reaching the ion were performed by measuring the power before the neutral density filter, and subsequently scaling the result by the transmittance of the filter and the vacuum chamber window. The transmittance of the density filters had first been measured at high laser intensity. The laser beam waist was measured to 0.89(5) mm.

To check if the 280 nm light pulse heated the two-ion system or not, it is checked whether the $(s_{ip}, s_{op}) = (0, -1)$ sideband transition can be driven to shelve the $^{40}\text{Ca}^+$ ion by sending a 729 nm π-pulse for the $|n_{ip} = 0, n_{op} = 1\rangle$ state. The shelving pulse is performed on the $^2\text{S}_{1/2}$, $m_J = -1/2$ to $^2\text{D}_{5/2}$, $m_J = -3/2$ transition, because it is the least sensitive to magnetic field fluctuations.

The technique of using two subsequent shelving pulses presented in Sec. 6.5.3 was also tested for $^{24}\text{Mg}^+$. Immediately after the first shelving pulse described above, another pulse was sent, instead targeting the $|n_{ip} = 1, n_{op} = 0\rangle$ state. This required driving the $(s_{ip}, s_{op}) = (-1, 0)$ sideband transition to a different $^2\text{D}_{5/2}$ sublevel in $^{40}\text{Ca}^+$ than for the first pulse. The frequency and intensity of the 729 nm laser was altered such that a perfect π-pulse was also driven for the new motional target state.

12.2 PRS of a rovibrational transition in $^{24}\text{MgH}^+$

When performing PRS of the $^1\Sigma^+$ $|v = 0, J = 1\rangle \leftrightarrow |v' = 1, J' = 0\rangle$ target transition in $^{24}\text{MgH}^+$, the laser for spectroscopy is a 6.2 µm quantum cascade laser (QCL), which is described at length in Sec. 12.2.1. The duration of laser exposure on the ions is controlled with a mechanical shutter via the PPG.

The full PRS sequence for $^{24}\text{MgH}^+$ is shown in Fig. 12.2, where the spectroscopy pulse is shown in brown. As depicted the spectroscopic pulse takes up all the time between SBC and the RSB transfer pulse(s).

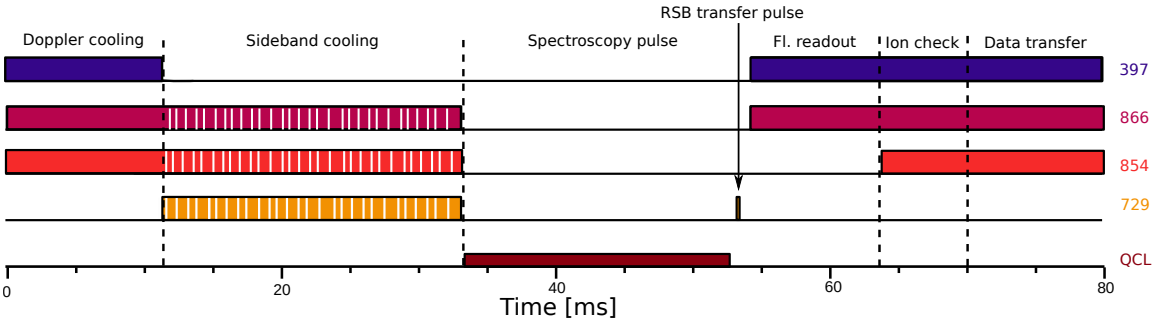

FIGURE 12.2: *A typical experimental sequence for doing PRS of the* $^1\Sigma^+$ $|v=0, J=1\rangle \leftrightarrow |v'=1, J'=0\rangle$ *target transition in* $^{24}MgH^+$. *The average pulse times for the different lasers are indicated. The height of the boxes does not correspond to laser intensity.*

The initial goal for these experiments was simply to obtain a PRS signal. The optimum experimental parameters (I_L, Γ_L and τ_{spec}) for doing so were discussed in Chapter 9. Here we found that for $I_L = 20\,\text{W cm}^{-2}$ and optimum linewidths of a few GHz the optimum pulse duration was on the order of tens of ms. Thus for intensities on this order and lower, the mechanical shutter can easily keep up.

For the $^{24}MgH^+$ PRS experiments only a single RSB shelving π-pulse on the $(s_{ip}, s_{op}) = (0, -1)$ sideband transition was used, targeting the $|n_{ip}=0, n_{op}=1\rangle$ state. This was performed on the $^2S_{1/2}$, $m_J = -1/2$ to $^2D_{5/2}$, $m_J = -3/2$ transition in $^{40}Ca^+$, since it it the least sensitive to magnetic field fluctuations.

12.2.1 Laser for driving the $^1\Sigma^+$ $|v=0, J=1\rangle \leftrightarrow |v'=1, J'=0\rangle$ transition in MgH^+ (6.2 µm)

The spectroscopy laser for driving the ro-vibrational $|v=0, J=1\rangle \leftrightarrow |v'=1, J'=0\rangle$ target transition in $^{24}MgH^+$ at 48619.4(1.5) GHz [70] is a tunable mid-IR external grating stabilized quantum cascade laser (QCL)[1] run in continuous wave mode.[2] It has a measured maximum output power of ∼60 mW at 6.2 µm, a tuning range of 5.83 - 6.31 µm and an expected linewidth < 30 MHz stated by the manufacturer. This laser was chosen in order to meet the requirements listed below.

The target transition with a linewidth of only $\Gamma_t/(2\pi) = 2.5$ Hz [72], has previously only been determined to within the in comparison very broad range of ±1.5 GHz by W.J. Balfour [70]. Hence, in order to find this very narrow line in an efficient way, the spectroscopy laser linewidth $\Gamma_L/(2\pi)$ must initially be on the order of 3

[1] The first QCL was developed by Faist et. al. in 1994 [117].
[2] Daylight Solutions 21060-MHF

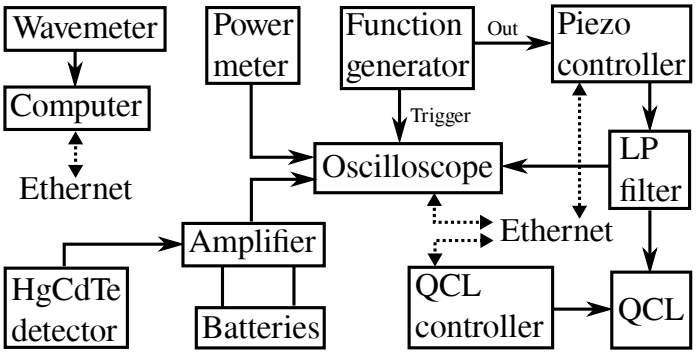

FIGURE 12.3: *Overview of the electronic instruments used in relation to the QCL [118].*

GHz, as discussed in Sec. 9. Once a signal is detected, we would, however, want to lower the laser linewidth gradually to home in on the transition.

Besides the fundamental limit of the transition linewidth itself, the final accuracy on the target line measurement is limited by the laser linewidth and the uncertainty of the laser frequency measurement, the sum of which should be below ± 1.5 GHz to exceed the accuracy of Balfour's measurement.

Additionally, in Sec. 6.2.6 we found that, for short spectroscopy pulse times, the PRS signal depth is directly proportional to the laser spectral density on resonance and that trap-induced heating puts a limit to how low the laser intensity can be for a given laser linewidth in order to separate signal from background.

This section seeks to demonstrate how the chosen laser meets the above mentioned requirements. It starts out with a presentation of the frequency determination and lock. Next, it is explained how the laser lineshape and width is altered for the line search. Finally the method used for aligning the laser beam on the ions is discussed and the obtained intensity is presented.

12.2.1.1 Frequency determination and lock

As mentioned the QCL has a wavelength tuning range of 5.83 - 6.31 µm (47.51 - 51.42 THz), which is tuned by rotating the laser's external cavity grating. This can be done in two ways. Either via the QCL controller controlling a motor for large, slow ($\sim$1 s) rough step adjustments, or via the piezo controller which controls a piezoelectric element (PZT) installed inside the laser cavity for fast and fine step adjustments. See Fig. 12.3 for an overview of the setup of electronic instruments used in relation to the QCL.

The laser frequency is measured with a Fizeau interferometer type IR wavemeter[3], with a wavelength operating range of 2 - 11 µm by sending ∼3% of the QCL power to the wavemeter through a fiber right after the output (see Fig. 12.12 top panel). The stated measurement speed is 50-100 Hz. The single shot resolution has been measured in our laboratory to ±10 MHz [119]. The accuracy depends on how the wavemeter is calibrated and how much time passed since the last calibration, as I will explain below.

During the PRS experiments the QCL is locked to the wavemeter via a simple proportional–integral–derivative (PID) control software on the computer which seeks to minimize the difference between the wavemeter reading and the chosen set point frequency for spectroscopy by changing the PZT voltage.

Calibration to the Stabiλaser In our lab the wavemeter is referenced to the Stabiλaser, an ultra-stable laser developed by NKT photonics and The Danish National Metrology Institute (DFM) [116] with a sub-kHz short-term linewidth and an upper drift limit of 1 Hz per day. This laser is internally locked to an acetylene line at 194 369 569 384(5) kHz. Due to an AOM in the lock setup, the laser output frequency is 40 MHz lower, that is 194 369 529 384(5) kHz (∼ 1.54 µm). This wavelength is according to specifications outside the range of the wavemeter, which is why we check the calibration at a wavelength closer to that used for spectroscopy (see next section). The calibration to the Stabiλaser is done by coupling it into the same fiber as when measuring the QCL. Since the fiber is not single mode for this wavelength the coupling into it influences how the Stabiλaser light enters the wavemeter. This means that the center frequency reading can vary by up to 100 MHz from one calibration to the next due to the coupling alone ([120] p. 17). Because of this, the calibration to the Stabiλaser is only accurate to within 100 MHz.

Ammonia absorption spectroscopy In order to check that the Stabiλaser calibration is also valid at the desired QCL operating frequency (∼6.2 µm) for $^{24}MgH^+$ spectroscopy the calibrated wavemeter reading can be compared to known lines in ammonia (NH_3). The used NH_3 lines are the three peaks at wavenumbers 1610.101680, 1610.302370, and 1610.409060 cm^{-1} which constitute a very distinct feature of the spectrum. Once these have been identified a peak at 1622.0880(1) cm^{-1} [121, 122][4]

[3]Prototype of the HighFinesse WS6-200 IR-III tested and characterized in our lab.

[4]Single excitation of the ν_4 vibrational mode in the electronic ground state of $^{14}NH_3$. Lines closer to the $^{24}MgH^+$ target frequency exist but this was chosen for its relatively good strength

even closer to the target frequency in $^{24}MgH^+$ at 1621.77(5) cm^{-1} can be identified and measured to check the Stabiλaser calibration.

This is done by sending the laser light through an ammonia gas cell[5] and measuring the resulting absorption spectrum with a liquid nitrogen cooled HgCdTe detector[6] [123]. This is facilitated by a special branch in the QCL optical setup, which the laser beam travels down when flip mirror 2 is flipped up as seen in Fig. 12.12. Using the QCL controller the laser frequency is set to the middle of the range defined by the three first mentioned NH_3 lines, and on top the laser frequency is continuously scanned over the lines by modulating the voltage over the PZT with a (< 100 Hz)[7] sine wave from a function generator amplified by the PZT controller. When using the HgCdTe detector to measure the power after the absorption cell, we get a signal showing a drop in power as a function of time due to the absorption lines. From here it is possible to perform spectroscopy of the peaks by measuring the absorption as a function of laser wavelength as measured by the wavemeter when scanning the PZT voltage in steps using a computer to control the PZT voltage. However, the step rate must be slow enough to average out the single shot wavemeter resolution of around ± 10 MHz ([119] p. 15). As mentioned the wavemeter can make $N = 100$ measurements per second, so an average over e.g. 1 s, which we typically do, has a resolution scaled by $1/\sqrt{N}$ i.e. ± 1 MHz. Since the HgCdTe detector is AC coupled (measures change in power), a chopper wheel is run at a rotation frequency of $\sim$ 250 Hz to create a pulsed signal at this low scanning speed. By checking the frequency difference between the peaks of the mentioned distinct three peak feature of the spectrum, we can identify it and subsequently identify all other peaks from this reference.

Then by adjusting the PZT offset voltage and decreasing the scanning amplitude the scan can be focused on the peak closest to the target transition in $^{24}MgH^+$. An example of data from such an ammonia spectrum measurement of the peak at 1622.0880(1) cm^{-1} [121, 122] is given in Fig. 12.4 (red points). It shows the detector signal as a function of detuning between the measured (by the wavemeter) QCL frequency and the expected (literature) value of the peak. The obtained signal is a convolution of the spectral shape of the laser and the lineshape of the ammonia peak. The high pressure inside the cell causes a broadening of the naturally Lorentzian

[5]The cell has an approximate pressure of 15 mbar judging from the measured ammonia peak widths, and windows made of CaF_2 and a length of 6 cm.

[6]From Judson Technologies. The detector output is amplified in order to see the signal on an oscilloscope. To avoid electrical noise the amplifier is battery driven.

[7]For increased mechanical stability and lifetime.

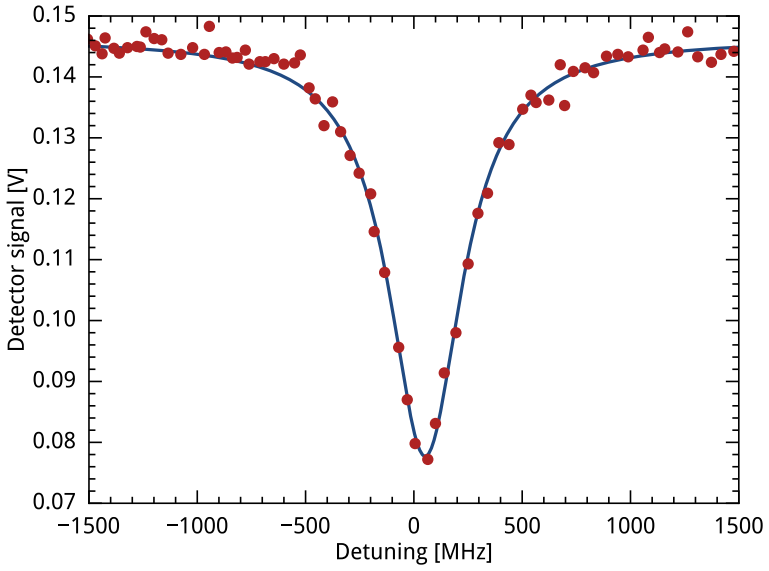

FIGURE 12.4: *Example of an absorption spectrum of the ammonia peak at 1622.0880(1) cm^{-1} [121, 122] taken without current modulating the QCL as a function of detuning between the measured (by the wavemeter) QCL frequency and the expected (literature) value of the peak. The data is fitted to a Lorentzian function with a constant added background. Fits to 6 such data sets give an average FWHM of 406(4) MHz and an average center value of 23(11) MHz. The average error on the center value for each spectrum is only 2.7(1) MHz*

ammonia peak. Since pressure broadening is a homogeneous broadening mechanism the resulting lineshape is also Lorentzian. Because the pressure broadened width of $\sim$ 400 MHz is much larger than both the natural linewidth of $\sim$ 100 Hz and the expected Gaussian QCL lineshape with a linewidth of $<$ 30 MHz, we expect the measured lineshape to be well described by a Lorentzian. Indeed, in Fig. 12.4 the data is fitted to a Lorentzian function with a constant added offset corresponding to the signal without NH_3 absorption (blue curve). Fits to 6 such data sets taken over 2 consecutive days give an average FWHM of 406(4) MHz and an average measured (by the wavemeter) offset compared to the expected (literature) value of 23(11) MHz, where the stated errors are the standard error of the mean. The measured differences on the center values from scan to scan of up to $\pm$50 MHz around zero detuning is in accordance with the previously measured day-to-day wavemeter reading fluctuations as described below. However the average error on the center values are only 2.7(1) MHz, meaning the center determination for the individual peaks, which takes around a minute to measure, is not limited by the long term fluctuations.

The accuracy of the NH_3 peak center frequency stated in the HITRAN database is $1 \times 10^{-4}\,\mathrm{cm}^{-1}$ corresponding to 3 MHz [121, 122]. This means that the total accuracy

of the wavemeter after calibration to a NH_3 peak is 4 MHz, if only the wavemeter did not fluctuate.

Stability of the wavemeter reading The stability of the wavemeter reading itself can be checked by logging its measurement of the, in comparison, completely stable Stabiλaser laser frequency. The so far longest measurement was taken over 95 hours ([119] p. 14) and showed fluctuations on the order of 50 MHz around the center value, which were found to be correlated to temperature changes in the lab. Based on this measurement it is expected that the wavemeter does not fluctuate more than 50 MHz over the course of 4 days, but in principle we cannot be sure. This means that the wavemeter fluctuations dominate the frequency reading after calibration to the ammonia line, and limits the accuracy to at least 50 MHz. However, compared to the GHz QCL linewidth we want to apply for the initial PRS experiments with $^{24}MgH^+$ a 100 MHz accuracy on the wavemeter is sufficient, meaning the calibration to the Stabiλaser alone is enough.

On the other hand once a signal has been obtained for the $^{24}MgH^+$ target transition, we want to apply smaller laser linewidths in order to determine the target line frequency with higher accuracy as described in Sec. 9. Eventually we want to apply the QCL with its natural linewidth of < 30 MHz. So in order to not be limited by the wavemeter, its accuracy has to be better than this.

In order to do a frequency measurement with an accuracy better than 50 MHz, the fluctuations of the wavemeter would have to be continuously measured and corrected for by doing a much more frequent calibration to the Stabiλaser. This could be done by using a fiber switch such that the wavemeter would alternate between measuring the QCL and the Stabiλaser. This would also mitigate the error due to alignment into the multimode fiber of the wavemeter. The switching should be done at a rate higher than the wavemeter fluctuations and preferably as fast as possible. The speed is limited by the ~ 100 Hz measurement speed of the wavemeter. Then after calibrating the wavemeter to the ammonia line, the accuracy of the QCL frequency measurement would be only limited by the 4 MHz uncertainty on the ammonia peak center, after also averaging out the single shot resolution of ± 10 MHz like already mentioned.

Prior to the PRS measurements of $^{24}MgH^+$ presented in Chapter 14 the wavemeter was calibrated to the Stabiλaser and the calibration was checked by measuring the ammonia peak. However, for these PRS measurements we can only claim the 100 MHz accuracy of the wavemeter reading stemming from the Stabiλaser calibration

alone, since the ammonia peak was not measured very frequently, because 100 MHz accuracy was sufficient at the time.

12.2.1.2 Lineshape broadening and measurement

According to the datasheet the spectral linewidth of the QCL is < 30 MHz. Other similar QCLs have been measured to have Gaussian lineshapes with widths of 1-5 MHz [124–126], which suggests a similar shape and linewidth of the QCL used for this thesis. Hence, in order to achieve the desired line widths in the few GHz range it must be broadened.

Lineshape broadening This is done by modulating the input current to the laser through applying a sinusoidal driving voltage from a function generator to a bias Tee circuit inside the laser head. The modulation voltage can have an amplitude of up to $\Delta V = 4$ Vpp centered around ground with a frequency f_{mod} between 10 kHz and 2 MHz without damaging the laser. The applied voltage will result in a change in laser current of ΔI around the center value, I_0. The expected ΔI as a function of f_{mod} for the maximum $\Delta V = 4$ Vpp can be seen in the top panel of Fig. 12.5. The blue points of Fig. 12.5 are copied from Figure 10 of the QCL manual. The measurements from the manual were made for a laser of this type, but not for the specific laser used. In a simple picture the constant voltage modulation amplitude should result in a constant current modulation amplitude ΔI, but we see that the laser acts as a high-pass filter for current modulation for $f_{mod} < 100$ kHz.

Current modulation will lead to a change of the laser frequency with amplitude Δf_L around the central laser frequency f_L. The output frequency of the laser light depends on the input current since the current affects the temperature inside the laser, effectively changing the length of the laser cavity.[8] In the bottom panel of Fig. 12.5 the expected frequency modulation Δf_L per current modulation amplitude as a function of f_{mod} is given. This decreases with modulation frequency because the thermal effect causing the wavelength change cannot keep up with the speed of the current modulation. If Δf_L is much larger than the expected non-modulated spectral linewidth of the QCL of < 30 MHz, and the frequency of the modulation f_{mod} is fast enough, the effective laser linewidth will become on the order of Δf_L. (I will come back to what 'fast' means at the end of this section.)

[8] In diode lasers a current change both leads to a temperature change and to and immediate change in the number of charge carriers causing a change in refractive index, which also changes the effective cavity length. This refractive index response, which is much faster than the thermal effect, is not present in a QCL.

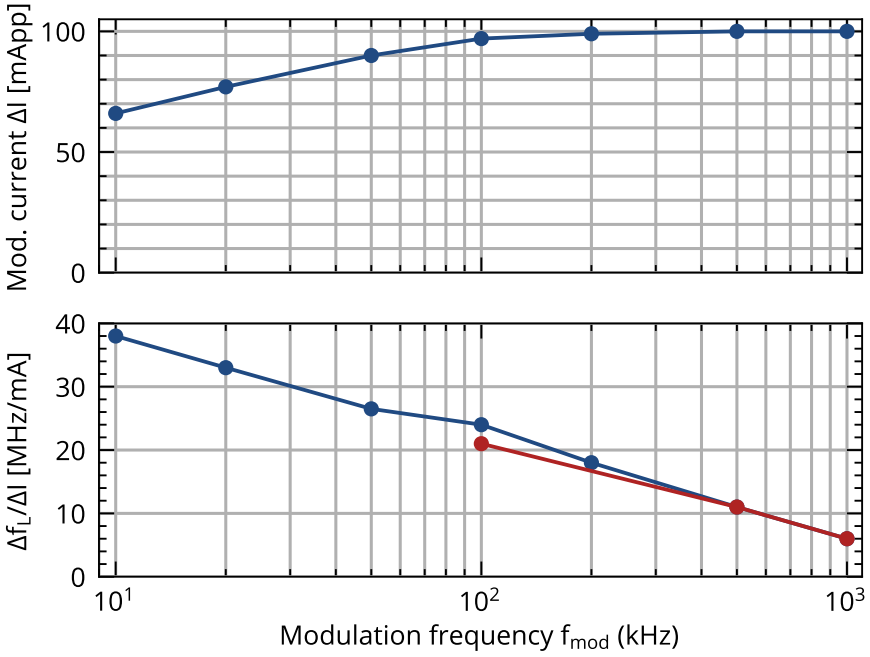

FIGURE 12.5: *Adapted from Figure 10 of the QCL manual (blue points) showing the effect of applying a sinusoidal driving voltage of* $\Delta V = 4$ *Vpp and frequency* $f_{mod} = 10 - 1000$ *kHz to a bias Tee circuit inside the laser head. This characterization was not done for the specific laser at hand, and thus only shows the rough trends of performance.* ***Top figure:*** *In a simple picture the constant voltage modulation amplitude should result in a constant current modulation amplitude* ΔI*, but we see that the laser acts as a high-pass filter for current modulation for* $f_{mod} < 100$ *kHz.* ***Bottom figure:*** *The current modulation causes a temperature change inside the laser resulting in a change of the laser frequency* Δf_L *around the central value* f_L*. We see that* Δf_L *per* ΔI *decreases for increasing modulation frequencies because the thermal effect cannot keep up. The red points are laser spectral widths extracted from fits to ammonia spectra as shown in Fig. 12.10 (yellow triangles) divided by 100 mA for comparison. The measured result agrees well with the data sheet.*

In Fig. 12.6 we see the laser frequency f_L measured with the IR wavemeter as a function of the laser current I_0 when changing it manually on the QCL controller. We see that $f_L(I_0)$ for most currents is a close to linear decreasing function, meaning that a symmetric current change around I_0 leads to a symmetric frequency change around f_L. However, we also see that large inconsistent frequency jumps on the order of 3 GHz occur. These jumps correspond to the difference between the modes of a 5 cm long laser cavity[9], which could be the length of the QCL cavity. The difference between the blue and red data points of Fig. 12.6, besides from the different dates, are the PZT and motor settings determining the cavity length and grating angle prior to the manual current scan. These settings determine for what currents the mode

[9]The free spectral range of a standing wave resonator of length L is $\Delta\nu_{FSR} \approx c/(2L)$.

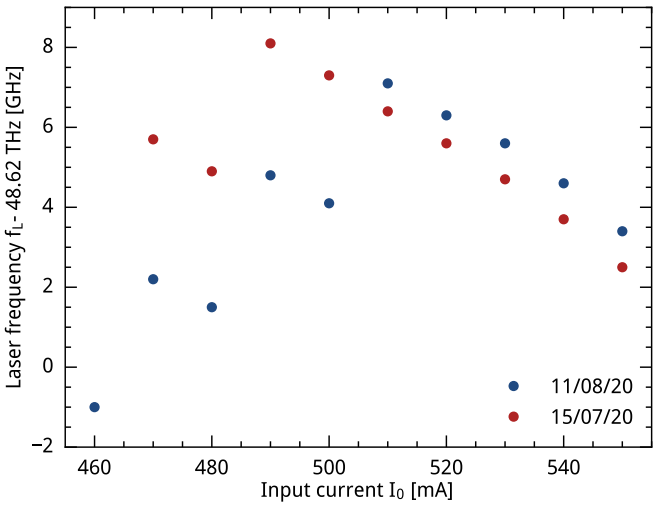

FIGURE 12.6: *QCL frequency measured with the IR wavemeter as a function of input current without modulation for two different dates and PZT and motor settings. The 3 GHz jumps on the curves corresponds most likely to mode jumps of the laser.*

jumps are located. However even if the exact same settings are chosen the mode jumps cannot be expected to appear for the same input currents due to hysteresis effects.

Scanning the laser frequency across a mode jump during the current modulation could lead to a multi-mode behavior, where only part of the spectral density is distributed around f_L. We see from the top panel of Fig. 12.5 that ΔI of above 65 mApp are expected for all f_{mod}, seemingly making it hard to find a central current in Fig. 12.6 for which the range $[I_0 - \Delta I/2; I_0 + \Delta I/2]$ would not cover a mode jump. It is, however, important to note that the data of Fig. 12.6 were taken by manually changing the current input to the laser step by step and not during a fast current scan through the bias Tee circuit. Hence we cannot expect Δf_L per ΔI to be as large as the $\sim$ 700 MHz/mA which Fig. 12.6 suggests. Indeed from Fig. 12.5 we see that the maximum expected Δf_L for $\Delta V = 4$ Vpp is 40 MHz/mA. This indicates that the risk of scanning over a mode jump during fast modulation is much smaller than what Fig. 12.6 suggests. As the IR wavemeter cannot keep up with the fast current modulation, since the measurement speed as mentioned is 50-100 Hz, it is not possible with the present setup to check directly whether the mode jumps also happen during the fast modulation.

Therefore mode jumps can have been a problem for the PRS experiments with $^{24}MgH^+$ presented in Chapter 14. Assume the laser was lasing equally on two different modes around the frequency chosen for spectroscopy and that the mode separation

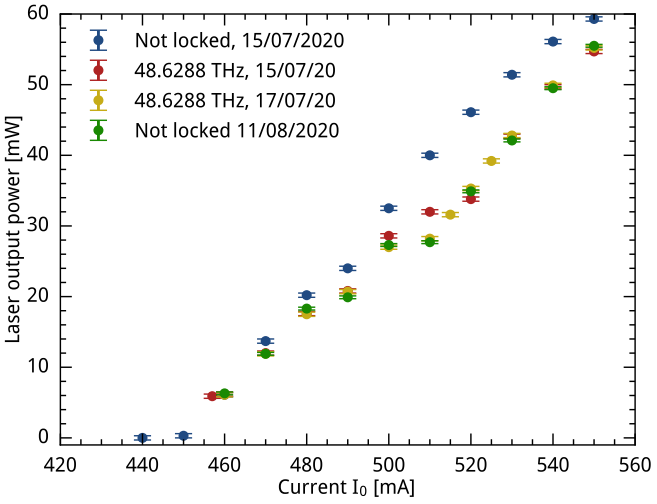

FIGURE 12.7: *Measurements of QCL output power as a function of input current. For the red and yellow data the QCL was locked to the IR wavemeter and the frequency was allowed to stabilize between each data point. For the blue and green data the frequency was not locked but allowed to change with current. For these two datasets the frequency was measured before and after the current scan (high to low) which gave 48.6288-48.6265 THz (blue) and 48.6234-48.619 THz (green). The jumps in power are due to laser cavity mode jumps and depends on the specific PZT and motor settings prior to the scan.*

is 3 GHz as expected from Fig. 12.6. If we broaden to a laser linewidth of around 1 GHz, the spectral density would be located in the intervals $[-1.5, -1]$ GHz and $[1, 1.5]$ GHz around f_L instead of in the intended interval from $[-0.5, 0.5]$ GHz. Thus if this was the case for some of the PRS data points we would not obtain a signal if the target transition was within the intended laser spectral density.

A way to minimize, but not eliminate, the risk of mode jumps, would have been to check the linearity of the f_L vs. I_0 curve in the vicinity ($\sim \pm 5$ mA) of the chosen I_0 for the specific PZT and motor settings prior to every experiment. If mode jumps are observed, the PZT and motor settings should be changed until no mode jumps are found.

The maximum current input of the QCL is 550 mA, which must not be exceeded when the current is modulated. Consequently I_0 must be below maximum when the current is modulated. E.g. for $\Delta V = 4$ Vpp the resulting current modulation ΔI is according to Fig. 12.5 100 mApp, meaning I_0 should be 50 mA below maximum corresponding to 500 mA. The laser output power is proportional to the input current as seen in Fig. 12.7. Hence, there is a trade off between width and power, and the broadening procedure effectively reduces the laser power available for spectroscopy.

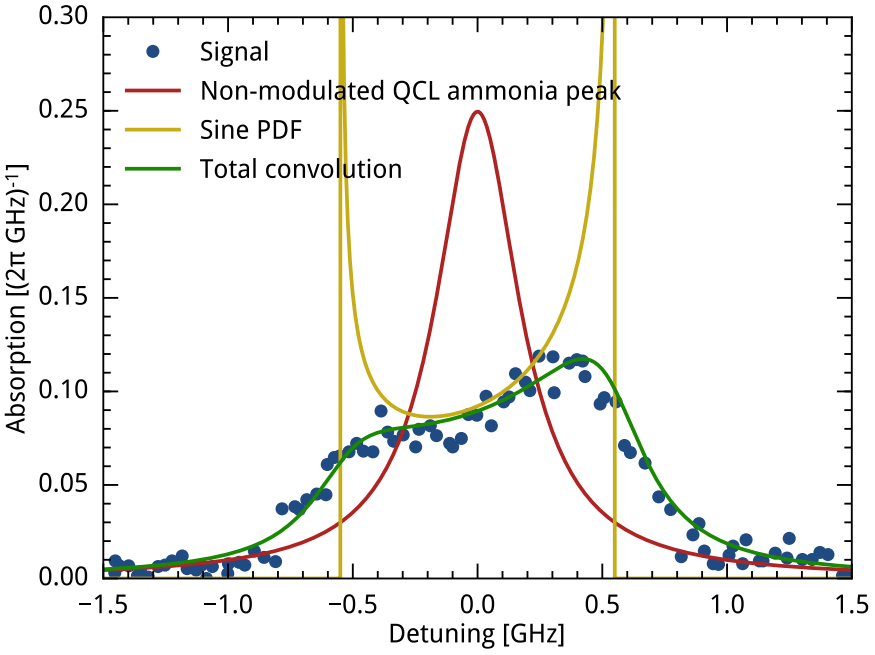

FIGURE 12.8: *The blue points are data from absorption spectroscopy of the same ammonia line at 1622.0880(1) cm^{-1} as shown in Fig. 12.4 but now with a laser current modulation of $f_{mod} = 500$ kHz and a $\Delta V = 4$ Vpp. The yellow curve represents the assumed contribution to the QCL laser linewidth stemming from current modulation for these parameters. This is given by Eq. 12.1 with $2A/(2\pi) = 1.1$ GHz and $a = 1 \times 10^{-10}$ s The red curve is a Lorentzian function of FWHM 406 MHz representing the absorption signal from the ammonia line without current modulating the laser. The green curve is the convolution between the yellow and red curves which have been overlapped with the data points by varying A and a.*

Lineshape measurement The laser lineshape resulting from current modulation can be measured using the ammonia gas cell as described in Sec. 12.2.1.1. During absorption spectroscopy the central laser frequency, f_L, is scanned with the PZT as already mentioned, and to see the broadening effect the input current to the laser is simultaneously being modulated. (The PZT cannot be used to broaden the laser linewidth, as the modulation frequency by the manual is limited to 100 Hz.[10]) Fig. 12.8 shows an example (blue points) of an absorption spectrum of the same ammonia line at 1622.0880(1) cm^{-1} as shown in Fig. 12.4 but now with a current modulation of $f_{mod} = 500$ kHz and a modulation amplitude of $\Delta V = 4$ Vpp . This spectrum, and spectra for other modulation parameters, can be fitted to extract the resulting laser

[10]Therefore a 50 Hz low-pass filter has been inserted between the external PZT controller (driving voltages between 0-100 V) and the QCL in order to protect the PZT.

lineshape by separating the contributions from the laser and the pressure broadened ammonia peak.

The laser lineshape is itself a convolution of the natural laser lineshape, which is assumed to be a Gaussian with linewidth < 30 MHz, and the probability density of the laser frequency modulation function. Since the laser frequency is approximately proportional to the input current as seen in Fig. 12.6, the frequency modulation function is also assumed to be a sine. Furthermore, the laser output power also depends linearly on the input current as seen in Fig. 12.7 adding a slope to the resulting laser lineshape. The total contribution to the lineshape from current modulation is formally written as

$$L_{\text{sine}}(\omega) = \frac{(a(\omega - \omega_L) + 1)}{\pi} \frac{1}{\sqrt{A^2 - (\omega - \omega_L)^2}}, \tag{12.1}$$

which is the normalized probability density function (PDF) of a sine around the central laser angular frequency ω_L with a width of $2A$, where the amplitude is scaled by $(a(\omega - \omega_L) + 1)$ to describe the linear dependency on current of the output power. This contribution is shown in yellow in Fig. 12.8 for $2A/(2\pi) = 1.1$ GHz and $a = 1 \times 10^{-10}$ s.

The ammonia spectrum taken without laser frequency modulation from Fig. 12.4 contributes to the modulated spectrum with a Lorentzian function of FWHM 406 MHz shown in red in Fig. 12.8. Technically the natural Gaussian laser lineshape also contributes to this ammonia spectrum, but since the linewidth is so relatively small we chose to neglect it.

The convolution of the red and yellow functions in Fig. 12.8 gives the green function which describes the measured signal very well. This was obtained by varying A and a manually until the best overlap between the data and the convolution curve was obtained. The results of such manual fits to data obtained for different modulation parameters can be seen in Fig. 12.9 giving the width of the sine PDF as a function of modulation amplitude, and in Fig. 12.10 as a function of modulation frequency (the data in each figure are the same). The errorbars are assessments from the manual fitting procedure. In Fig. 12.9 linear fits to the data give slopes of 529(8) MHz/V, 268(3) MHz/V, 139(4) MHz/V for $f_{mod} = 100$ kHz, 500 kHz and 1 MHz, respectively. In Fig. 12.10 the dotted lines are not fits but merely there to guide the eyes.

The data shows that we are able to obtain laser line widths of a few GHz as required for the molecular line search. As expected the laser line width increases for increasing modulation amplitude, however less fast for high modulation frequency.

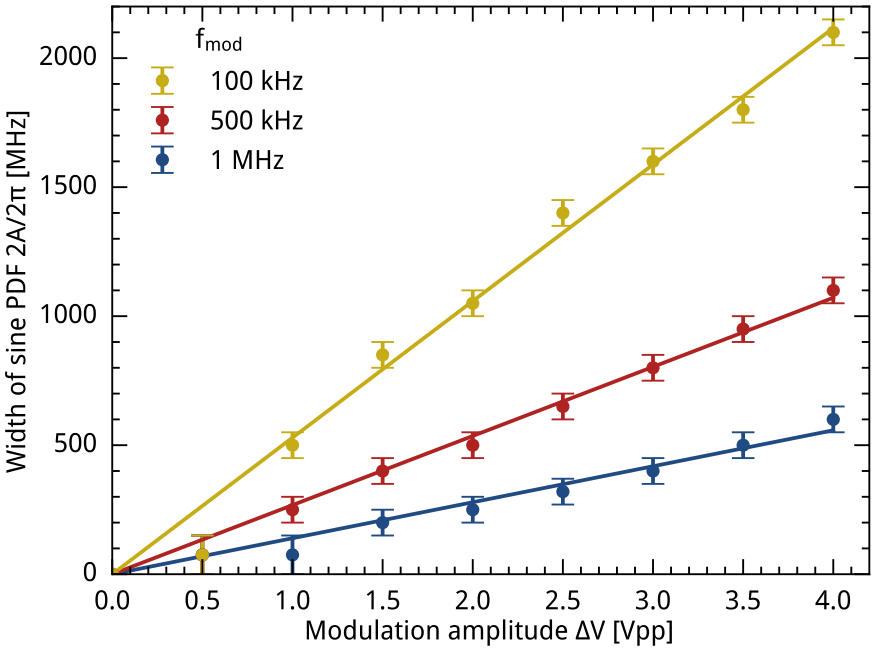

FIGURE 12.9: *Estimated width of the sine PDF ($2A/(2\pi)$) of Eq. 12.1 as a function of modulation voltage amplitude ΔV for 3 different modulation frequencies f_{mod}. Linear fits to the data give slopes of 529(8) MHz/V, 268(3) MHz/V, 139(4) MHz/V for f_{mod} = 100 kHz, 500 kHz and 1 MHz, respectively. The same data are shown in Fig. 12.10.*

The extracted laser widths for $\Delta V = 4$ Vpp shown as yellow triangles in Fig. 12.10, divided by 100 mA for comparison, corresponds to part of the curve from the QCL manual and are plotted alongside in red in Fig. 12.5. The two data sets correlate very well.

The actual lineshape of the frequency modulated laser, however, is not the sloped sine PDF alone, but a convolution between this and the natural lineshape of the laser, which was neglected earlier. Such a convolution between the yellow sine PDF curve of Fig. 12.8 and a Gaussian function of width 30 MHz representing the natural laser lineshape is shown in blue in Fig. 12.11. It is evident that the natural lineshape of the QCL is only a very small correction to the frequency modulated lineshape at this large width.

In Fig. 12.11 the frequency modulated laser spectral shape (blue) with a width of 1100 MHz is compared to a Gaussian function width the same FWHM (yellow) and a trapezoid with the same width and slope as used for the sine PDF (red). All three functions are normalized.

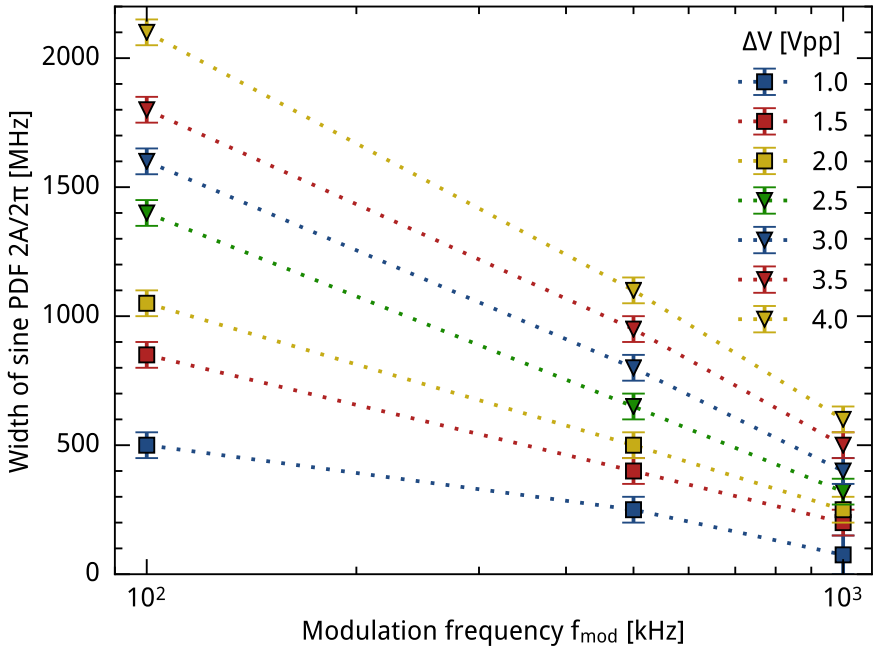

FIGURE 12.10: *Estimated width of the sine PDF ($2A/(2\pi)$) of Eq. 12.1 as a function of modulation frequency, f_{mod}, for different modulation voltage amplitudes ΔV. The data for 4 Vpp (yellow triangles) divided by 100 mA are also plotted in Fig. 12.5 to compare to the QCL manual. The same data are shown in Fig. 12.9.*

Broadening parameters chosen for PRS The blue curve of Fig. 12.11 is in fact the expected lineshape of the QCL used for the PRS experiments with $^{24}MgH^+$ presented in Chapter 14. The estimated laser FWHM is 1.10(5) GHz. The parameters used to obtain this lineshape was $f_{mod} = 500$ kHz, $I_0 = 500$ mA and $\Delta V = 4$ Vpp. This lineshape was chosen because it is the broadest achievable while maintaining a relatively high modulation frequency of 500 kHz. An almost identical width is e.g. obtained for 100 kHz and 2 Vpp as seen in Fig. 12.9. As mentioned in the beginning of the section it is important that the modulation is fast, if the modulated laser lineshape is to be interpreted as a broad spectrum. The relevant timescale is the absorption rate of the molecular target transition. If the frequency modulation is not faster than this the molecule will effectively see a laser of < 30 MHz being scanned over 1.1 GHz instead of a broad spectrum with a constant central laser frequency f_L.

When simulating the PRS spectra for $^{24}MgH^+$ in Sec. 6.2 a constant central laser frequency during the spectroscopy pulse time τ_{spec} was assumed. However, as long as the natural QCL linewidth is much larger than the trap frequencies $\omega_{ip/op}$ and the natural linewidth of the target transition Γ_t, it would still be valid to model the PRS signal obtained from scanning f_L during τ_{spec} using rate equations. In fact, as long as

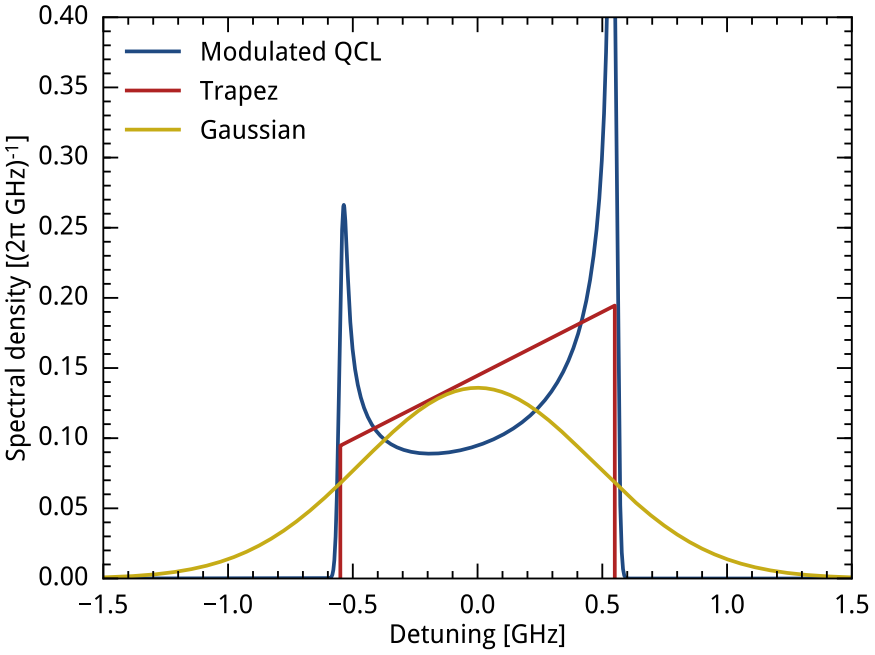

FIGURE 12.11: *The blue curve represents the expected QCL lineshape used for the PRS experiments with $^{24}MgH^+$ with a width of $2A/(2\pi) = 1.1$ MHz and slope of $a = 1 \times 10^{-10}$ s. This corresponds to the yellow curve of Fig. 12.8 convoluted with a Gaussian of FWHM 30 MHz. For comparison the spectral shape of a Gaussian with the same FWHM (yellow) and a trapezoid with the same width and the same slope are shown.*

f_{mod} is fast enough to cover the intended frequency interval within τ_{spec}, the results are expected to be very similar to the constant f_L broad spectrum result due to the linearity between the absorption rate and the laser linewidth. However, this was not checked by calculation, and further studies are needed to confirm this.

The bottom line is that for the model in Sec. 6.2 to be comparable to experiment, the used f_{mod} must be larger than the molecular absorption rate. For the experiments presented in Chapter 14 we used $f_{mod} = 500$ kHz. To calculate the absorption rate the laser intensity at the molecular ion must be known, which is treated in Sec. 12.2.1.3. We will thus come back to this matter at the end of that section.

Square lineshape As discussed in Sec. 9 the optimum spectral shape for the line search is a square function. As we have just seen, when the laser line shape is dominated by the frequency modulation, it will resemble the PDF of the current modulation function. A way to make the laser lineshape more square shaped would thus be to instead use a triangular modulation function, since it has a square PDF. However, from Fourier analysis it is well known that a triangular function is made

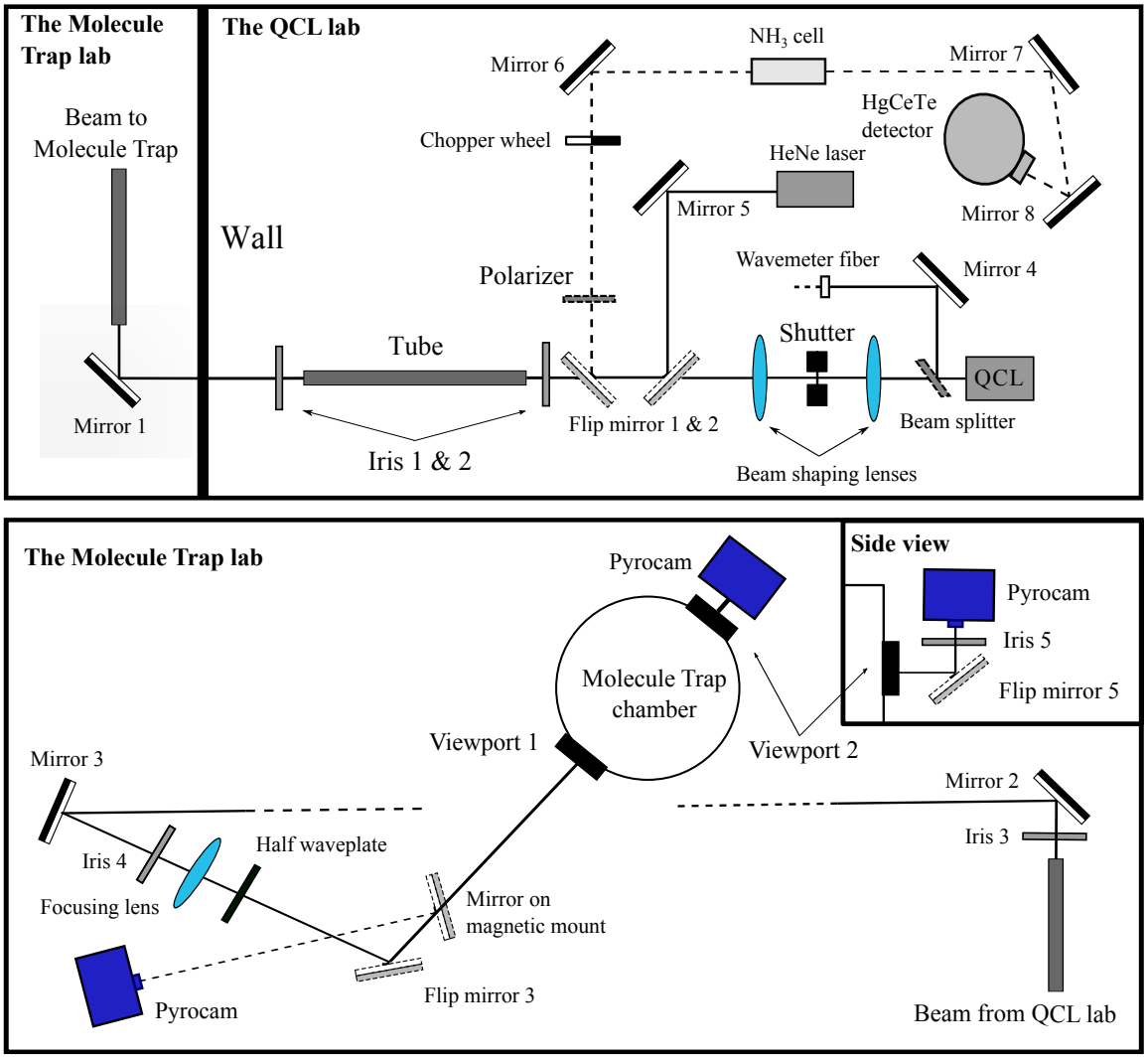

FIGURE 12.12: *Sketch of the QCL beam path with beginning in the top panel lower right corner. The sketch is an updated version of Figure 3.1 in Niklas Arent's bachelor thesis [120].*

up of many sinusoidal components, some of them with frequencies exceeding the 2 MHz limit of the laser system. Another approach would be to use spectral filters for shaping, however only a redistribution and not a reduction of the spectral energy is beneficial, since the absorption rate is proportional to power.

12.2.1.3 Laser beam alignment on the ions

From the output of the QCL to the center of the ion trap the laser light travels ∼10 m. A sketch of the beampath is shown in Fig. 12.12. Due to the very low transmission efficiency of fibers in the mid-IR region, the laser beam travels in free space. Hence, in order to diminish air pressure fluctuations resulting in pointing instability and

consequent light intensity fluctuations at the ion position, the majority of the laser beam path is surrounded by hollow plastic tubes.[11] To avoid divergence of the laser beam during the long beam path, it is collimated right after the output by a pair of lenses forming a telescope.

To aid the alignment of the invisible QCL beam to the trap, it is overlapped with a visible HeNe laser beam (632.8 nm). First the beam path of the QCL is marked by iris 1 and 2 by looking at the laser beam spot on a thermal beam profiler (Pyrocam[12]). The HeNe laser beam is then aligned through iris 1 and 2 simply by looking at the beam spot on a piece of paper after flipping up flip mirror 1. This results in a perfect overlap of the two laser beams. Subsequently the remaining mirrors in the beam path can be adjusted by looking at the visible beam, after which flip mirror 1 is flipped down to send the QCL beam to the trap.

To obtain the desired polarization axis of 63.4° to the vertical B-field as discussed in the beginning of Sec. 6.2, the initially horizontal linear polarization axis of the QCL is turned by a $\lambda/2$-waveplate just before the trap. The resulting polarization axis was checked by measuring the power transmitted through a polarizer turned to the correct angle.

Longitudinal alignment In order to increase the QCL light intensity on the ions, which are located at the common trap and vacuum chamber center, the laser beam is focused on the ions using a lens with a focal length of 300 mm positioned at approximately the same distance from the trap center. The obtained laser beam spot size at the ion position is measured by redirecting the laser beam onto the Pyrocam by placing a mirror on a magnetic mount in the beam path shortly before it enters the trap (see Fig. 12.12 bottom). The Pyrocam is then moved along the laser beam and the radius[13] at different positions is measured. Data from such a spot size measurement is given in Fig. 12.13, from which the waist is determined to be 176(10) µm from a fit to a Gaussian beam shape function. The measurement shows that the longitudinal alignment of the QCL beam could be improved, since the location of the waist does not overlap perfectly with the trap center. The waist is found to instead be located 16(5) mm after the trap center when looking in the

[11] A cumbersome but feasible alternative would be to send the beam through a N_2 filled tube to reduce the fluctuations and absorption. Or the QCL could be moved closer to the ion trap.

[12] Pyrocam III from Ophir-Spiricon Inc. operated with the software BeamGage. The Pyrocam detects changes in light power, which in the case of continuous wave lasers is facilitated by an internal chopper wheel run at 48 Hz.

[13] Defined as the radial distance from the beam axis where the intensity has dropped to $1/e^2$ percent of the maximum value.

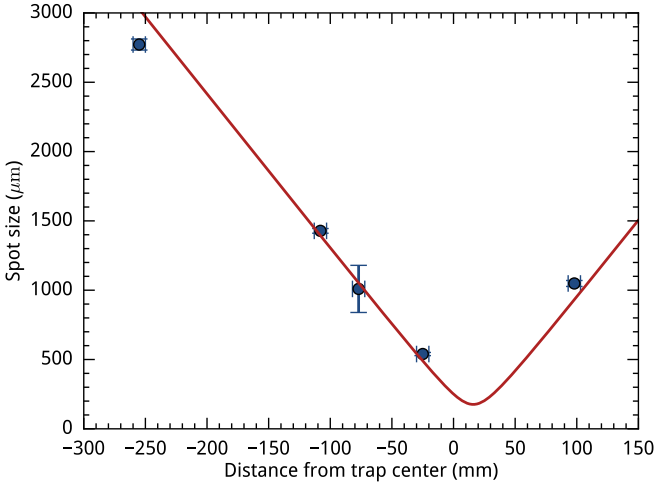

FIGURE 12.13: *Waist measurement of the QCL beam at the position of the ion from Aug. 11 2020. A fit to a Gaussian beam shape function gives a waist of* 176(10) µm. *The waist position relative to the trap center is measured to* 16(5) mm *along the propagation direction.*

propagation direction of the QCL light. The beam radius at this longitudinal position from the waist is 251(40) µm meaning the intensity is reduced to 49% of the intensity at the waist position. The vertical distance between the trap electrodes is 2.6 mm and the trap rods are 45.4 mm long. The calculated beam radius at 50 mm from the waist is 585 µm, meaning we are in no risk of hitting the trap with the horizontal beam.

Another concern might be that with two ions in the trap, the $^{24}MgH^+$ ion do not sit at the exact trap center. Instead the two ions will sit on each side of the trap center along the axis. However, the two ions' axial distance from the trap center at the working trap potential is only 10 µm. For the measured waist of about 200 µm a longitudinal displacement of this size has a completely negligible effect on the intensity.

Radial alignment The radial alignment of the QCL beam on the ions is facilitated by a glass fiber with a diameter of 125 µm, which can be moved in and out of the trap center while the trap RF potential is turned off. By placing the fiber tip exactly at the trap center, laser beams can be aligned to it either by looking at the scattered laser light from the tip or the shadow it casts in the laser beam profile.

Since the alignment of the QCL beam on the ions relies upon the fiber position being correct, we started by assessing how accurately we can align the fiber tip to the ion position. When aligning the fiber in the horizontal direction we use the CCD

camera placed above the ion trap used for fluorescence detection of $^{40}Ca^+$ ions. We trap a single $^{40}Ca^+$ ion and align the 397 nm laser beam on it by optimizing the fluorescence signal. Then we mark the ion position on the CCD image with the ROI (region of interest) box tool in the experiment control programme. Subsequently, when the RF potential is turned off and the fiber is moved in, the fiber tip is simply moved to the marked position. The fiber tip is visible on the CCD camera, since it scatters the light of the 397 nm laser beam.[14] The horizontal fiber positioning has an accuracy around 10 µm, corresponding to the ion diameter on the CCD.

To assess the vertical fiber position we use a camera (Thorcam[15]) placed after the trap to image the 397 nm laser profile. The idea is to use the 397 nm beam aligned on the ion to align the fiber after, so it is important to also know, how good this can be done.

To access the uncertainty of the vertical alignment of the 397 nm beam on the $^{40}Ca^+$ ion we start by aligning the 397 nm laser beam to the ion using the top CCD camera for maximum fluorescence before noting the centroid position on the Thorcam placed after the trap. Next, the 397 nm beam is moved up and down by adjusting the last mirror before the trap until very low and similar fluorescence levels in each direction is obtained on the CCD camera. The beam centroid positions on the Thorcam for the two outer position are also noted. The measurement was repeated 3 times to find an average distance from the central centroid position. Using this and the distance between the last mirror and the Thorcam and the distance from the last mirror to the trap center, the uncertainty on the 397 nm beam alignment on the ion was calculated to 86.3 µm. However, during a normal alignment we would never move the beam to such low fluorescence levels, so the uncertainty is estimated to maximally 10 µm.

After the 397 nm beam is aligned to the ion, we move in the alignment fiber to the ion position. Unless the diffraction pattern on the Thorcam in the 397 nm beam profile caused by the fiber is symmetric, the fiber is not at the same height as the 397 nm beam. To measure how far off the fiber is, the 397 nm beam is moved vertically until the diffraction pattern is symmetric. Then the fiber is removed, and the new position of the 397 nm beam is compared to the one before the vertical adjustment. From the difference in position on the Thorcam the difference in position at the ion can be calculated. This experiment was repeated 20 times to give a mean difference of 14(10) µm. So in total, the vertical fiber alignment uncertainty is less than 20 µm.

[14] The 397 nm laser beam waist is around 150 µm.
[15] Thorlabs DCC1545M

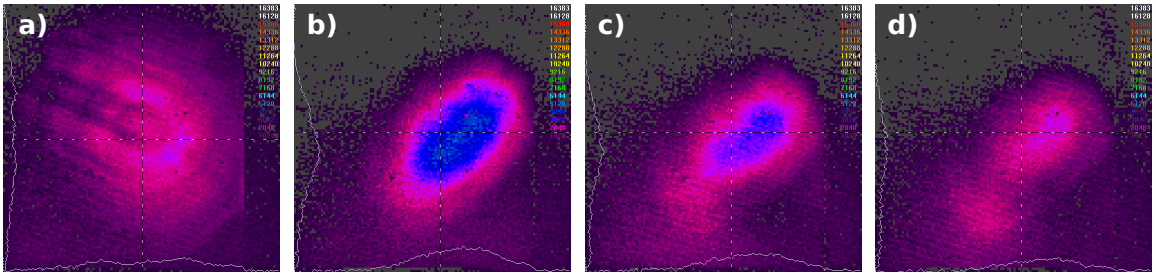

FIGURE 12.14: *Horizontal QCL beam alignment to the ion trap center using the Pyrocam placed after the trap. a) The HeNe laser beam spot with the alignment fiber clearly visible as a shadow. b) The QCL beam spot aligned to the trap center with the fiber out. c) The QCL beam spot at the same position with the fiber at the center position. d) The QCL beam spot at the same position with the fiber so far in that minimum intensity is obtained.*

Once the fiber is perfectly aligned to the trap center, we can align the QCL beam to it. When sending the HeNe laser beam through the ion trap with the fiber in the center, the fiber will show up as a shadow in the beam spot when shining it on a piece of paper after the trap. Looking at the paper the laser beam direction is adjusted until the fiber tip shadow is in the beam spot center. Since the QCL beam is overlapped with the HeNe laser beam, the QCL should now also be aligned to the trap center. However, as an extra precaution the QCL alignment on the fiber tip is checked on the Pyrocam. This is done by flipping flip mirror 5 after the trap, to send the laser beam vertically through iris 5 and onto the Pyrocam. The shadow in the HeNe laser beam can also be seen on the Pyrocam as seen in Fig. 12.14a). When shining in the QCL beam a drop in intensity is seen instead of a shadow due to the Fraunhofer diffraction pattern being much broader for the much larger wavelength of the QCL compared to the HeNe laser [127]. However the QCL beam spot center can easily be overlapped with the fiber tip by measuring the transmitted/scattered intensity. This is demonstrated in Fig. 12.14b)-d) which shows the QCL beam profile for different positions. In scenario b) the fiber is out and we measure the full intensity ($I_{\max}$) of the beam. In scenario c) the fiber is at the center of the trap, and as a consequence the QCL beam intensity is lowered. In scenario d) the fiber is moved so far in that the intensity is minimized ($I_{\min}$). When the intensity is just between the ones measured in scenario b) and d), the fiber covers half of the maximum beam spot area it can ($I = (I_{\max} - I_{\min})/2$), and the QCL beam is horizontally aligned to the fiber. In the vertical direction the intensity should simply be a minimum when the fiber covers the beam. The accuracy of the QCL beam alignment to the fiber tip is estimated to be $\pm 10\%$ of the maximum measured intensity corresponding to a positional error of $\pm 4\,\mu\text{m}$, meaning the total error on the radial QCL alignment on

the ion is dominated by the uncertainty of the fiber alignment.

The pointing instability at the waist position has earlier been measured to be below 10 µm [120], so this effect can be neglected for this large beam size.

In conclusion the 20 µm uncertainty of the radial alignment is negligible compared to the 5 mm uncertainty on the longitudinal alignment from an intensity point of view.

Laser intensity and molecular excitation rates The QCL power right before the vacuum chamber was measured on all the days where PRS data were being collected in the period from 17/08/2020 to 25/09/2020. The PRS data are presented in Chapter 14. For all the measurements the laser frequency was locked to the IR wavemeter to a value within the 2σ line search interval of 48619.4 ± 3 GHz.[16] The average of these 16 measurements gives 7.5 mW with a standard deviation of 0.4 mW. The vacuum chamber viewport the QCL beam enters through is made of CaF_2 which has a transmission at this wavelength of 95% [128]. Finally, taking the transmission into account, the intensity can be calculated from the power and spotsize at the ion position, giving $7.2(1.2)\,\mathrm{W\,cm^{-2}}$. The error is dominated by the error on the longitudinal position, however the error on the power also has an impact.

With the laser intensity at hand, we can now address the question of whether the laser frequency modulation is fast enough to assume a constant central laser frequency f_L during τ_{spec} and a broadened linewidth as described in Sec. 6.2. In order for this to hold, the absorption rate needs to be much faster than the frequency modulation rate of 500 kHz. The absorption rate in the molecule when driving the transition with an intensity of $7.2\,\mathrm{W\,cm^{-2}}$ and a $\Gamma_L/(2\pi) = 1.1$ GHz is $R^L_{abs}/(2\pi) \sim 2.5$ kHz. This number is calculated for an assumed square lineshape, so the rate is faster for the outer frequencies of the modulated QCL lineshape. Since f_{mod} is 200 times faster than $\Gamma_L/(2\pi)$, we should be safe. One could even argue that it would be safe to lower the modulation frequency in order to safely increase the laser current and thereby the intensity available for spectroscopy. However, for narrower laser linewidths the modulation frequency has to be increased. This can be seen from Fig. 12.15 where the absorption rate as a function of laser linewidth is plottet for $I_L = 7.2(1.2)\,\mathrm{W\,cm^{-2}}$.

[16] It is important to measure the power close to the working frequency since especially water molecules in the air have strong absorption lines in this frequency domain.

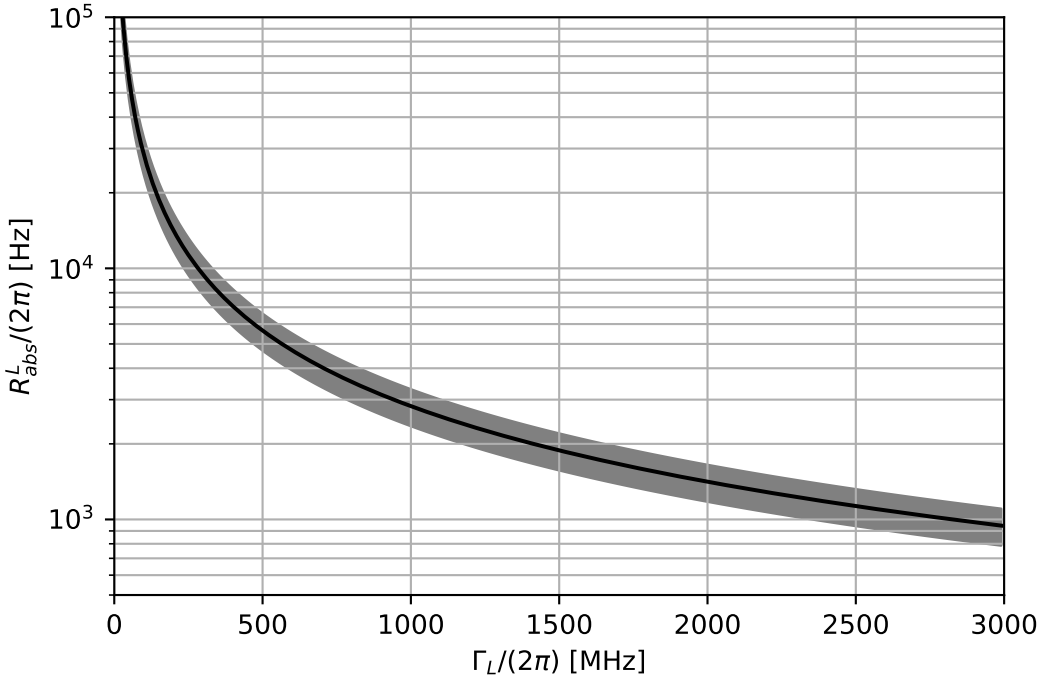

FIGURE 12.15: *The absorption rate for a square laser lineshape as a function of laser linewidth for I_L =7.2(1.2)*$\mathrm{W\,cm^{-2}}$*. The gray area indicates the error on the intensity.*

12.2.1.4 Conclusion

In this section we have presented the tunable mid-IR external grating stabilized quantum cascade laser (QCL) used for driving the ro-vibrational $|v = 0, J = 1\rangle \leftrightarrow |v' = 1, J' = 0\rangle$ target transition in $^{24}MgH^+$ at 48619.4(1.5) GHz [70] with a linewidth of only $\Gamma_t/(2\pi) = 2.5$ Hz [72]. We have also shown that it meets the requirements to obtain a PRS signal for this transition.

First of all the QCL can be tuned to the correct frequency and stably locked using an IR wavemeter. The accuracy of the wavemeter reading was found to be 100 MHz when calibrated to the ultra-stable Stabiλaser. We should hence be able to improve on the current best measurement of the target transition in $^{24}MgH^+$ since the accuracy of this is $\pm$1.5 GHz [70]. The wavemeter accuracy could be improved to 4 MHz by constant calibration to the Stabiλaser by using a fiber switch and an additional calibration to a line in ammonia using the existing setup for absorption spectroscopy. However this was not necessary for the initial search.

Secondly, the naturally Gaussian laser lineshape with FWHM $<$ 30 MHz, can be broadened to several GHz to aid the target line search, by modulating the current input to the laser head. Any laser linewidth in between this and the natural linewidth

can be obtained by varying the modulation voltage amplitude ΔV. The lineshape of the broadened laser was measured using ammonia spectroscopy, and was found to resemble a sine PDF for widths much larger than the laser natural linewidth. The blue curve of Fig. 12.11 represents the expected lineshape of the QCL used for the PRS experiments with $^{24}MgH^+$ presented in Chapter 14. The estimated laser FWHM is 1.10(5) GHz. For this a modulation frequency of $f_{mod} = 500$ kHz, a central current of $I_0 = 500$ mA and a modulation voltage amplitude of $\Delta V = 4$ Vpp was used. This rate was found to be much larger than the absorption rate of the molecule for the broadened width and intensity, such that the radiation field can be considered as broadband.

Additionally we can align the laser beam waist on the trap center with a radial uncertainty of 20 µm and a longitudinal uncertainty of 5 mm by using the alignment fiber. The laser intensity used for the PRS measurements was measured to 7.2(1.2)W cm^{-2}, which should be enough to obtain a PRS signal as we will see in Chapter 14.

Part IV

Experimental results

Chapter 13

Experimentally obtained PRS spectra of $^{24}Mg^+$

In this chapter we present experimental results of unresolved sideband PRS of the 3s $^2S_{1/2}$ - 3p $^2P_{3/2}$ transition of 280 nm in $^{24}Mg^+$ and compare them to the model presented in Sec.s 5.2 and 6.1. In this case the sidebands are unresolved due to the relatively large linewidth of the transition. Measured values of trap-induced heating rates and the motional excitation after SBC, relevant for the PRS measurement, are also presented.

13.1 Temperature and heating rate measurements

The experimental cycle for PRS is initialized by sideband cooling the $^{40}Ca^+$ -$^{24}Mg^+$ two-ion system to the ground state with respect to both the IP and OP modes. The experimental procedure is describe in Sec. 11.2.

13.1.1 Sideband spectrum

After sideband cooling, a sideband excitation spectrum can be measured by applying a shelving pulse to the 4s $^2S_{1/2}$ to 3p $^2D_{5/2}$ quadropole transition of $^{40}Ca^+$ before doing fluorescence readout. The shelving laser frequency is scanned to measure the fluoresence probability for different detunings from the carrier frequency f_r, while the shelving pulse duration and laser intensity is kept constant.

A typical sideband excitation spectrum after sideband cooling is presented in Fig. 13.1. The IP and OP mode angular frequencies are $\omega_{ip} = 2\pi \times 162.9\,\text{kHz}$ and $\omega_{op} = 2\pi \times 300.2\,\text{kHz}$, respectively, which is clearly seen from the blue sidebands in the spectrum. Each data point is an average of 100 experimental cycles.

Here the used laser intensity and pulse time corresponds to a π-pulse for the first blue IP sideband when driven from the $|n_{ip} = 1, n_{op} = 0\rangle$ motional state, which results in a close to 100% transfer efficiency at this sideband frequency. The absence

of visible RSBs indicates a high probability of occupation of the ground state for both motional modes.

The blue line is a fit to the data points using Eq. 5.18 and assuming a Boltzmann distribution for both modes. This gives mean occupation numbers of $\bar{n}_{ip} = 0.09(+0.18 - 0.09)$ and $\bar{n}_{op} = 0.14(+0.24 - 0.14)$ for the IP and OP modes, respectively.

13.1.2 Trap induced heating rate measurement

Instead of measuring the full spectrum between $f_r \pm \omega_{op}/(2\pi)$, sideband spectroscopy can be focused on the first red and blue sidebands of each motional mode in order to assess the trap-induced heating rates as described in Sec. 11.3. For each set of blue and red sideband spectra the average motional excitation can be deduced, and by adding a delay between the SBC sequence and the shelving pulse, we can find $\bar{n}_{ip}$ and $\bar{n}_{op}$ as a function of time.

The results of such trap-induced heating rate measurements for both the IP and the OP mode can be seen in Fig. 13.2. The data points for each motional mode is fitted to a linear function, and the slopes correspond to heating rates of $R_{H,ip} = 14(1)$ s^{-1} and $R_{H,op} = 1.7(3)$ s^{-1}, respectively. These are the heating rates used for the simulations in Chapter 6 and in the next Sec. 13.2. This gives a ratio $R_{H,ip}/R_{H,op} = 8.2(1.6)$. This is close to the predicted value of the white noise model presented in Sec. 4.3 but the theoretical value does not match within the uncertainty.

The intercepts with the y-axis are the average populations just after SBC. These are $\bar{n}_{ip}(t = 0) = 0.04(2)$ and $\bar{n}_{op}(t = 0) = 0.06(2)$, respectively, corresponding to $P_{|0,0\rangle} = 0.9094$, $P_{|1,0\rangle} = 0.0370$, $P_{|0,1\rangle} = 0.0536$. These results are lower, but within the uncertainties of the result from the sideband spectrum of Fig. 13.1.

The uncertainties on $\bar{n}_{ip}(t = 0)$ and $\bar{n}_{op}(t = 0)$ obtained from the heating rate measurements are also considerably lower than the ones obtained from the sideband spectrum, even though the sideband spectrum contains many more data points. The many data points, however, also result in a total measurement time of several hours. This particular dataset was taken as one long scan, where the transition frequency could have fluctuated due to magnetic field and laser instabilities. The heating rate measurements on the other hand consists of many smaller sideband spectra, during the measurement of which the 729 nm transition frequency was measured in between, to keep the SBC and readout at an optimum.

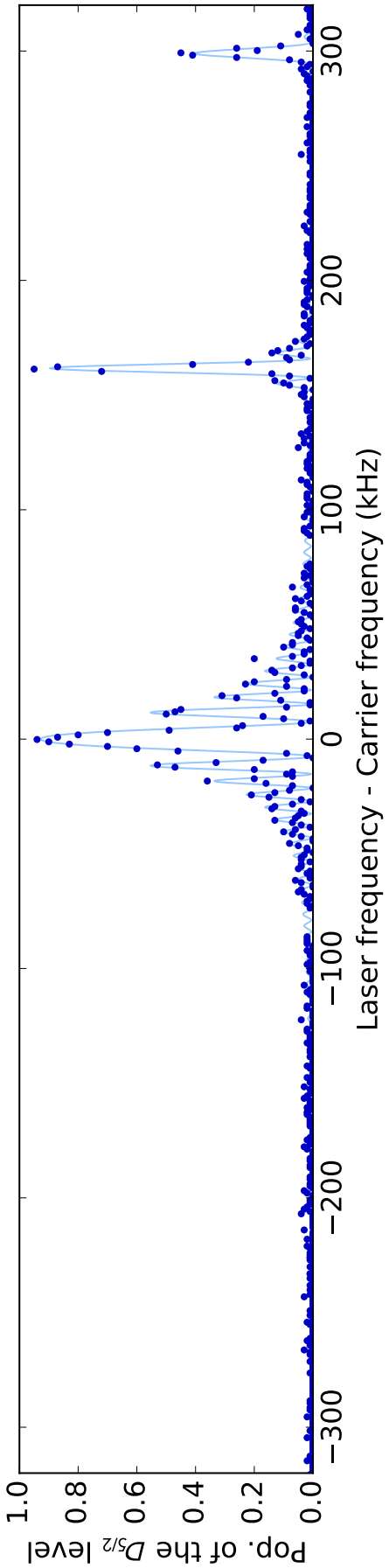

FIGURE 13.1: *Resolved sideband spectrum representing the probability of excitation of the 4s* $^2S_{1/2}$ - *3p* $^2D_{5/2}$ *quadropole transition in* $^{40}Ca^+$ *as a function of the 729 nm laser's detuning with respect to the carrier transition. This spectrum was obtained after Doppler cooling followed by sideband cooling. The absence of visible RSBs indicates a high probability of occupation of the ground state for both motional modes. The duration and intensity of the 729 nm shelving pulse were chosen to perform a* π*-pulse on the 1st BSB of the IP mode at* 162.9 kHz. *The blue line is a fit to the data points and gives mean occupation numbers of* $\bar{n_{ip}} = 0.09(+0.18 - 0.09)$ *and* $\bar{n_{op}} = 0.14(+0.24 - 0.14)$ *for the IP and OP modes, respectively.*

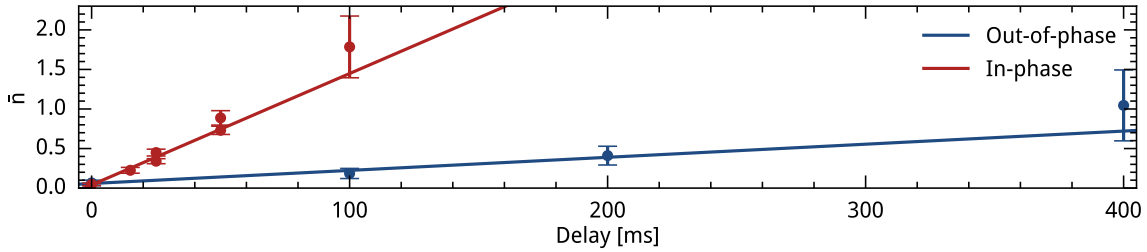

FIGURE 13.2: *Trap-induced heating rate measurements of both axial modes of the $^{40}Ca^{+}$ - $^{24}Mg^{+}$ system. The average motional states, extracted from comparison of blue and red sideband spectra, are plotted as a function of delay duration between SBC and the shelving pulse. The data are fitted to a linear function for each mode giving heating rates of $R_{H,ip} = 14(1)\ s^{-1}$ and $R_{H,op} = 1.7(3)\ s^{-1}$, respectively. The intercepts with the y-axis are the average populations just after SBC, being $\bar{n}_{ip}(t=0) = 0.04(2)$ and $\bar{n}_{op}(t=0) = 0.06(2)$.*

13.2 PRS spectra

The following experimental PRS spectra were obtained using the procedure described in Sec. 12.1. For the simulated results in this section, to which the experimental results are compared, we use the measured heating rates presented in the former Sec. 13.1.2. These values were chosen since they were measured shortly before the PRS experiments were performed, so we assume the experimental conditions were the same.

The non-perfect preparation in the motional ground state after SBC found in Sec. 13.1.2, is however not taken into account in the simulations in this section. In Fig. 6.12 the effect of imperfect ground state cooling was simulated. From this we expect almost the same signal as for perfect cooling, especially for long τ_{spec} times, but an extra constant contribution to the background, by which the signal depth is decreased.

13.2.1 Read out via out-of-phase shelving

In this section PRS spectra obtained by applying a single RSB shelving pulse on the 4s $^2S_{1/2}$, $m_J = -1/2$ to 3p $^2D_{5/2}$, $m_J = -3/2$ transition in $^{40}Ca^{+}$ are presented. Specifically the $(s_{ip}, s_{op}) = (0, -1)$ sideband transition was driven, and the pulse was a $\pi-$pulse for the $|n_{ip} = 0, n_{op} = 1\rangle$ motional state. Each spectroscopic data point is an average of 100 experimental cycles.

Examples of three experimentally obtained PRS spectra of the 3s $^2S_{1/2}$ - 3p $^2P_{3/2}$ transition of $^{24}Mg^{+}$ are presented in Fig. 13.3(a). For these experiments

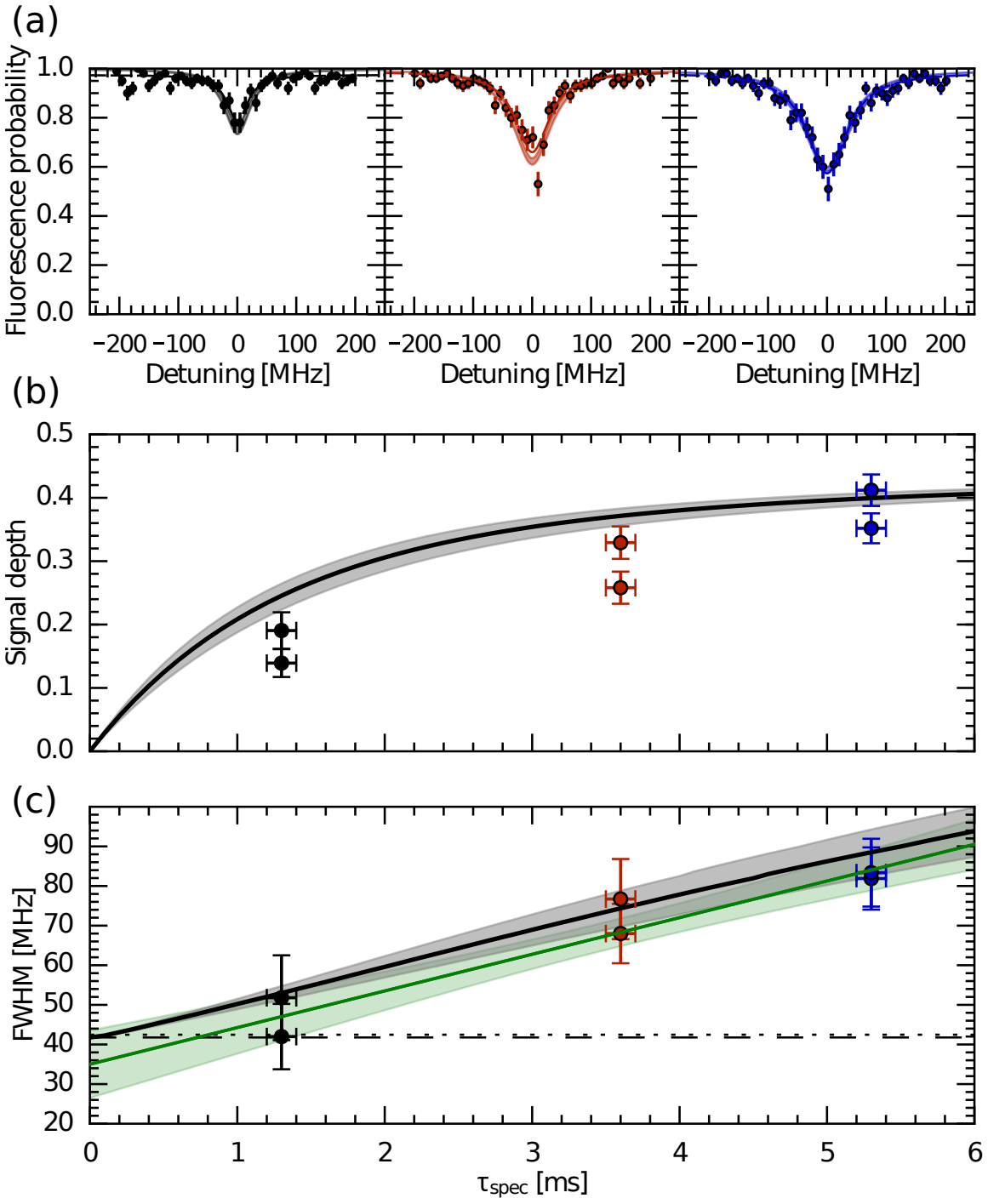

FIGURE 13.3: *Unresolved sideband PRS of the 3s* $^2S_{1/2}$ *- 3p* $^2P_{3/2}$ *transition in the* $^{24}Mg^+$ *ion with* $^{40}Ca^+$ *ion as the readout ion after readout on the OP mode (a) Typical spectra obtained for a spectroscopy laser intensity of* $I_L = 4.9(7)\,\mu\mathrm{W\,cm^{-2}} = 6.5(9) \times 10^{-6} I^t_{sat}$ *and, from left to right, spectroscopy times of* $\tau_{spec} = 1.3(1)$ *ms, 3.6(1) ms and 5.3(1) ms. The lighter colored broader lines represent the simulated results when including the* 1σ*-uncertainty on the experimental value of* I_L*. The dashed lines are Lorentzian fits to the experimental data from which the signal depths and FWHM are extracted. (b) Extracted signal depth as a function of* τ_{spec} *together with simulated values for* $I_L = 4.9\,\mu\mathrm{W\,cm^{-2}}$ *(black line) including the* 1σ*-uncertainty on* I_L *(gray shaded area). (c) Extracted FWHM as a function of* τ_{spec} *together with the simulated values (black line). A linear fit of the experimental data is shown in green together with* 1σ*-uncertainty of the fit (green shaded area). The intercept at zero spectroscopy time of 35(9) MHz matches the expected FWHM (dotted line) resulting from the natural linewidth (dashed line), the Doppler and Zeeman effects.*

$I_L = 4.9(7)\,\mu W\,cm^{-2} = 6.5(9) \times 10^{-6} I^t_{sat}$ and, from left to right, spectroscopy excitation times of $\tau_{spec} = 1.3(1)$, 3.6(1) and 5.3(1) ms ($\tau^t_{scaled} = 2.2$, 6.2, and 9.1) were applied, respectively.

All three experimental spectra have been centered at a detuning of 0 MHz, while the wavelength meter readings gave offsets of 12(4) MHz, 11(2) MHz and 18(3) MHz respectively, compared to the most precisely measured value of the transition [129]. These discrepancies are however all within the accuracy of the optical wavemeter.

The lighter colored shaded areas in Fig. 13.3(a) represent the simulated results when including the one standard deviation uncertainty on the measured value of I_L. The dashed lines are fits to a Lorentzian function with a constant added background as a free parameter, from which the signal depths and FWHM plotted in Fig.s. 13.3(b) and (c) are extracted. In the two lower plots the same colors (black, red, blue) are used for the data points to indicate which spectra they are extracted from. For each of the three applied τ_{spec} two spectra were recorded (of which only one is shown), such that there are two data points for each time.

Figs. 13.3(b) and 13.3(c) show the evolution of the measured spectral depth and FWHM as a function of spectroscopy time τ_{spec}. The simulation results are also plotted (black lines). The gray shaded areas represent the simulated results when including the one standard deviation uncertainty on the measured value of I_L. There is a fairly good agreement between experiments and simulations within the error bars. We see that the simulated signal depth is a little larger than the data points, which is expected when not taking the imperfect ground state cooling into account.

The black dashed line in Fig. 13.3(c) represents the natural FWHM of the transition ($\Gamma_t/2\pi = 41.8(4)\,MHz$) (used for the PRS simulations), whereas the black dotted line represents the effective FWHM which is slightly broader due to two effects. Firstly, the higher temperature (~ 0.75 mK) of the ions perpendicular to the z-axis leads to a Doppler broadening in the direction of the applied spectroscopic laser beam. This broadening is about $\Delta\omega_{Dopp} \sim 2\pi \times 3\,MHz$ and is common to each of the two ($m_J = \pm 1/2$) - ($m_J = \pm 1/2$) sub-level transitions. Secondly, the applied weak magnetic field (6.523(3) G) gives rise to a differential Zeeman shift of the two sub-level transitions of $\Delta\omega_{Zee} = 2\pi \times 6.1\,MHz$. By modeling the effective line profile of the transition taking both effects into account, we find an effective FWHM of about 42.5 MHz.

A linear fit (green line Fig. 13.3(c)) of the experimental data gives a FWHM at zero spectroscopy time of 35(9) MHz. The green shaded area represents the one standard deviation uncertainty on the fit. Bear in mind that we from the simulations

do not expect the spectral FWHM as a function of τ_{spec} to be perfectly linear. Although not a precision measurement, this result matches the effective FWHM of the transition well.

13.2.2 Enhanced signal via out-of-phase and in-phase shelving

In this section PRS spectra obtained by applying either one or two RSB shelving pulses on the 4s $^2S_{1/2}$ to 3p $^2D_{5/2}$ transition in $^{40}Ca^+$ are presented. Specifically, for the first pulse the $(s_{ip}, s_{op}) = (0, -1)$ sideband transition was driven, and the pulse was a $\pi-$pulse for the $|n_{ip} = 0, n_{op} = 1\rangle$ motional state. For the second pulse the $(s_{ip}, s_{op}) = (-1, 0)$ sideband transition was driven, and the pulse was a $\pi-$pulse for the $|n_{ip} = 1, n_{op} = 0\rangle$ motional state.

Note that the two pulses were driven with respect to two different upper sub-levels in 3p $^2D_{5/2}$ ($m_J = -3/2, -5/2$) to not coherently drive population back to the $^2S_{1/2}$ state after the first pulse.

In Fig. 13.4, we present experimental PRS spectra when applying only the first (red) and both the first and the second (black) RSB shelving pulses. In this particular case, one clearly sees a $\sim 50\%$ gain in signal depth by using the two π-pulse scheme, whereas the widths are similar. In the experiment, we used $I_L = 10(1)\,\mu\text{W}\,\text{cm}^{-2} = 1.3 \times 10^{-5} I^t_{sat}$ with a spectroscopy pulse time of $\tau_{\text{spec}} = 1.6(1)$ ms ($\tau^t_{\text{scaled}} = 5.6$). Note that the intensity of the spectroscopic pulse was increased by a factor two compared to the spectra in Fig. 13.3, in order to not be limited by the faster heating rate of the IP mode as compared to the OP mode.

Both experimental spectra have been centered at a detuning of 0 MHz, while the wavelength meter readings gave offsets of 16(3) MHz and 20(3) MHz, respectively. These discrepancies are once again both within the inaccuracy of the optical wavemeter.

The lighter colored shaded areas in Fig. 13.4 represent the simulated results when including the one standard deviation uncertainty on the measured value of I_L. The dashed lines are fits to a Lorentzian function with a constant added background as a free parameter. There is a fairly good agreement between the simulation and the data. The Lorentzian fits give slightly larger backgrounds than the simulations, which is expected since the imperfect ground state cooling was not taken into account in the simulations. Also bear in mind that we do not expect the PRS spectra to be perfectly Lorentzian due to the motional depletion broadening.

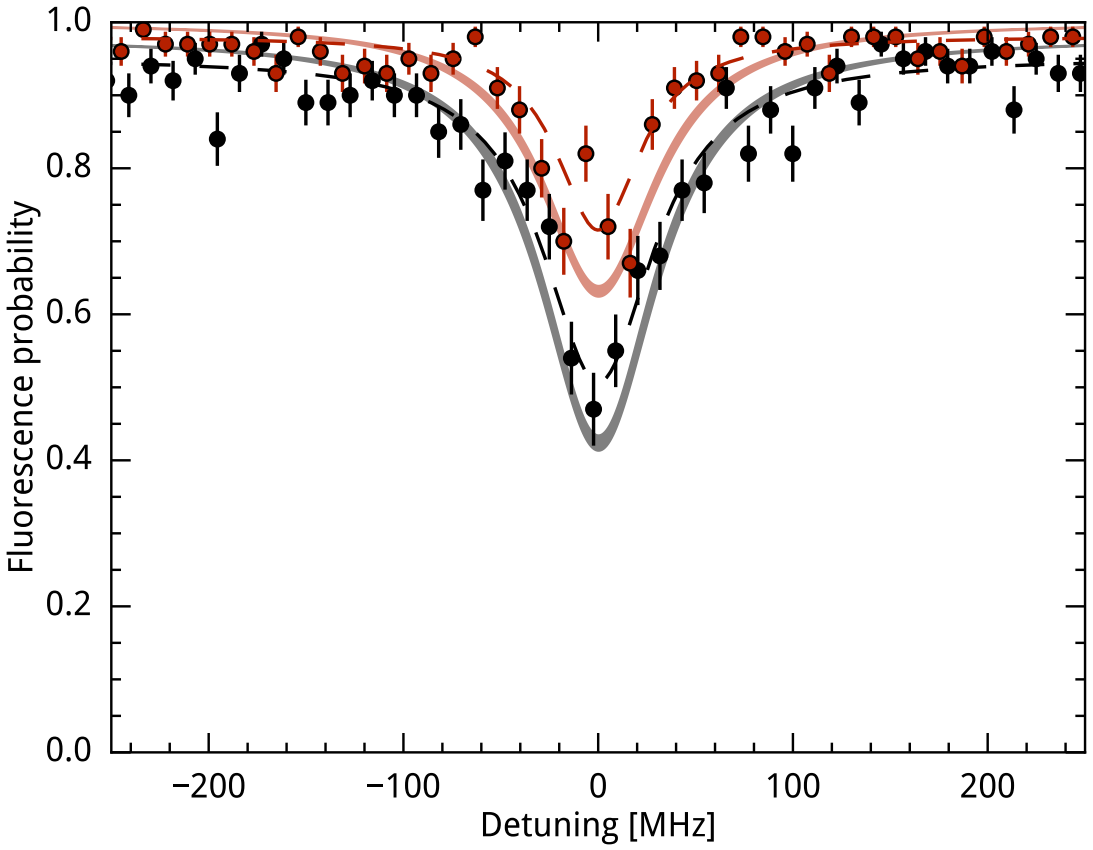

FIGURE 13.4: *Comparison of photon recoil spectra of the 3s $^2S_{1/2}$ - 3p $^2P_{3/2}$ transition in $^{24}Mg^{+}$ obtained by addressing either only the OP mode (red) or both the OP and IP mode (black) before readout. Here $I_L = 10(1)\,\mu W\,cm^{-2} = 1.3 \times 10^{-5} I^t_{sat}$ and $\tau_{spec} = 1.6(1)$ ms ($\tau^t_{scaled} = 5.6$). The lighter colored broader lines represent the simulated results when including the 1σ-uncertainty of the spectroscopy laser intensity I_L, while the dashed lines are Lorentzian fits to the experimental data. A $\sim 50\%$ increase in signal depth is clearly seen when using two shelving pulses instead of one. Note that I_L was increased by a factor two compared to the spectra in Fig. 13.3, to not be limited by the faster heating rate of the IP mode.*

13.3 Conclusion

In this chapter the experimental results of unresolved sideband PRS of the 3s $^2S_{1/2}$ - 3p $^2P_{3/2}$ transition of 280 nm in $^{24}Mg^{+}$ was presented and compared to the model set up in Sec.s 5.2 and 6.1. In this case the sidebands are unresolved due to the relatively large linewidth of the transition.

It was found that the simulations describe the general features of the data very well, and that the discrepancies due to limitations of the theoretical model are understood.

Additionally, measured values of trap-induced heating rates, implemented in the simulations, and the motional excitation after SBC were presented. Both were found to be low enough, to obtain a clear PRS signal for the considered system.

Chapter 14

Experimental search for PRS signals in $^{24}MgH^+$

Emilie: 1972 is a long time ago! – Walter Balfour

In this chapter we present the experimental attempts made to obtain unresolved sideband PRS of the $^1\Sigma^+$ $|v=0, J=1\rangle \leftrightarrow |v'=1, J'=0\rangle$ transition of 6.2 µm in $^{24}MgH^+$ and compare the data to the model set up in Sec.s 5.2 and 6.2. In this case the sidebands are unresolved due to the relatively large spectral linewidth of the spectroscopy laser. Measured values of trap-induced heating rates and the motional excitation after SBC, relevant for the PRS measurement, are also presented.

14.1 Temperature and heating rate measurements

The experimental cycle for PRS is initialized by sideband cooling the target $^{24}MgH^+$ ion and the readout/cooling $^{40}Ca^+$ ion to the ground state with respect to both the IP and OP modes. The experimental procedure is describe in Sec. 11.2.

After sideband cooling, a sideband excitation spectrum can be measured by applying a shelving pulse to the 4s $^2S_{1/2}$ to 3p $^2D_{5/2}$ quadropole transition in $^{40}Ca^+$ before doing fluorescence readout as described in Sec. 11.3. The shelving laser frequency is scanned in the near vicinity of the first blue and red sideband frequencies, while the shelving pulse duration and laser intensity are kept constant. For each set of blue and red sideband spectra the average motional excitation can be deduced. By adding a delay between the SBC sequence and the shelving pulse, we can find $\bar{n}_{ip}$ and $\bar{n}_{op}$ as a function of delay time and thereby assess the trap-induced heating rates.

The results of such trap-induced heating rate measurements for both the axial IP and OP mode can be seen in Fig. 14.1. The mode angular frequencies are $\omega_{ip} = 2\pi \times 162.0\,\text{kHz}$ and $\omega_{op} = 2\pi \times 295.7\,\text{kHz}$.

The data points for each motional mode is fitted to a linear function, and the slopes correspond to heating rates of $R_{H,ip} = 7.3(5)\ \text{s}^{-1}$ and $R_{H,op} = 0.3(1)\ \text{s}^{-1}$,

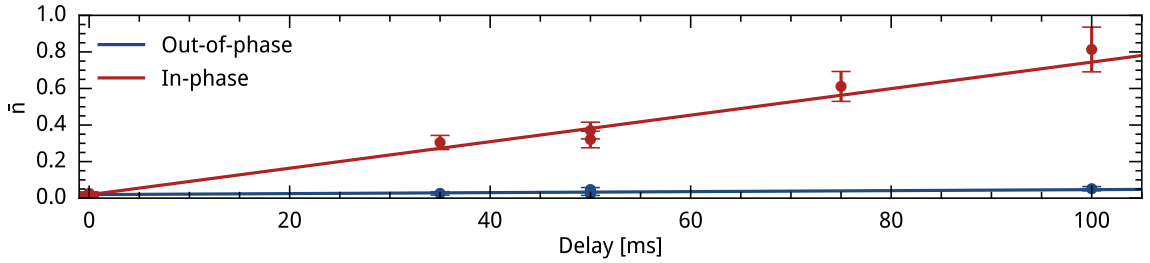

FIGURE 14.1: *Trap-induced heating rate measurements of both axial modes of the $^{40}Ca^+$ - $^{24}MgH^+$ system. The average motional states, extracted from comparison of blue and red sideband spectra, are plotted as a function of delay duration between SBC and the shelving pulse. The data are fitted to a linear function for each mode giving heating rates of $R_{H,ip} = 7.3(5)\ s^{-1}$ and $R_{H,op} = 0.3(1)\ s^{-1}$, respectively. The intercepts with the y-axis are the average populations just after SBC, being $\bar{n}_{ip}(t=0) = 0.019(5)$ and $\bar{n}_{op}(t=0) = 0.019(5)$*

respectively. These are the heating rates used for the simulations in the next Sec. 14.2. This gives a ratio $R_{H,ip}/R_{H,op} = 24(8)$, which is more than twice the predicted value of the white noise model presented in Sec. 4.3. However the large uncertainty makes it possible that the model still applies to some extent.

Compared to the trap-induced heating rate results for the $^{40}Ca^+$ and $^{24}Mg^+$ system presented in Fig. the present results are considerably better, to an extent where he different values are not within the uncertainties of one another. This is not expected from the white noise model, since the two different target ions have almost the same mass. Instead, the IP heating rates of the $^{40}Ca^+$-$^{24}Mg^+$ and $^{40}Ca^+$-$^{24}MgH^+$ systems are expected to be the same, and the OP heating rate to be only slightly smaller for $^{24}MgH^+$.

The intercepts with the y-axis in Fig. 14.1 are the average populations just after SBC. These are $\bar{n}_{ip}(t = 0) = 0.019(5)$ and $\bar{n}_{op}(t = 0) = 0.019(5)$, respectively, corresponding to $P_{|0,0\rangle} = 0.9634$, $P_{|1,0\rangle} = 0.0183$, $P_{|0,1\rangle} = 0.0183$.

The SBC results are, according to these data sets, thus also better than for the $^{40}Ca^+$-$^{24}Mg^+$ system. This makes sense, if the heating rates are truly better for $^{40}Ca^+$-$^{24}MgH^+$, since the lower limit of cooling is determined by the heating rates.

The reason for these discrepancies in heating rates and sideband cooling results are not fully understood. However, it is found more likely that the electric noise changed, than the results for $^{40}Ca^+$-$^{24}Mg^+$ and $^{40}Ca^+$-$^{24}MgH^+$ are inherently this different. In between the two measurements, electric noise reduction was attempted in relation to another project. Specifically, a 1 MHz high-pass filter was inserted at the input to the trap RF/DC mixer, with the prospect of reducing noise at the 100 kHz trap frequencies. With regards to the heating rates of a singly trapped $^{40}Ca^+$ ion

these efforts were not found to bear fruit, and hence it should not be better for the axial modes of a two-ion system either. An explanation could be that the heating of the radial modes was reduced, since these only couple to the axial modes for a two-ion system. Or maybe the excess micromotion was simply better compensated for in the later measurements. In order to check if the trapping conditions really changed, back-to-back heating-rate measurements of the $^{40}Ca^{+}$-$^{24}Mg^{+}$ and $^{40}Ca^{+}$-$^{24}MgH^{+}$ systems, with and without the filter, would have to be performed.

14.2 Preliminary PRS data

The data presented in this section were obtained by using the experimental procedure described in Sec. 12.2. For the simulated results in this section, to which the experimental data are compared, we use plus/minus one standard deviation of the measured heating rates and motional populations after SBC presented in the former Sec. 14.1. These values were chosen since they were measured shortly before the PRS experiments were performed, so we assume the experimental conditions were the same.

14.2.1 Data acquisition

From simulation, the spectroscopy pulse time was chosen to be $\tau_{\mathrm{spec}} = 35$ ms. This gave an experimental cycle time of 140 ms, since this has to be a multiple of 20 ms to be synchronized to the 50 Hz wall voltage in the lab. For each frequency step, 9000 experimental cycles were performed.

This was done in groups of 500 cycles giving a total measurement time per group of 70 s. After each 500 cycles, another 500 cycles with the laser light shut off would be run to make sure the background did not change. Ideally the cycles with the laser on the ions and the cycles with the laser off would have been interleaved after each single cycle, but this was not done due to a programming issue.

Thus for each applied central laser frequency, a total of 9000 cycles with the laser on the ions, and a total of 9000 cycles with the laser shut off was performed. This gives a total measurement time of 42 min per frequency step.

After each group of 500 cycles, the average group fluorescence count was immediately plotted in the control programme, both for the laser on and laser off groups. In this way we could continuously compare the averages and see, if there were any signs of a signal, or if the background had changed significantly. E.g. it was very clear to see, if the molecule had dissociated from one group of cycles to the next,

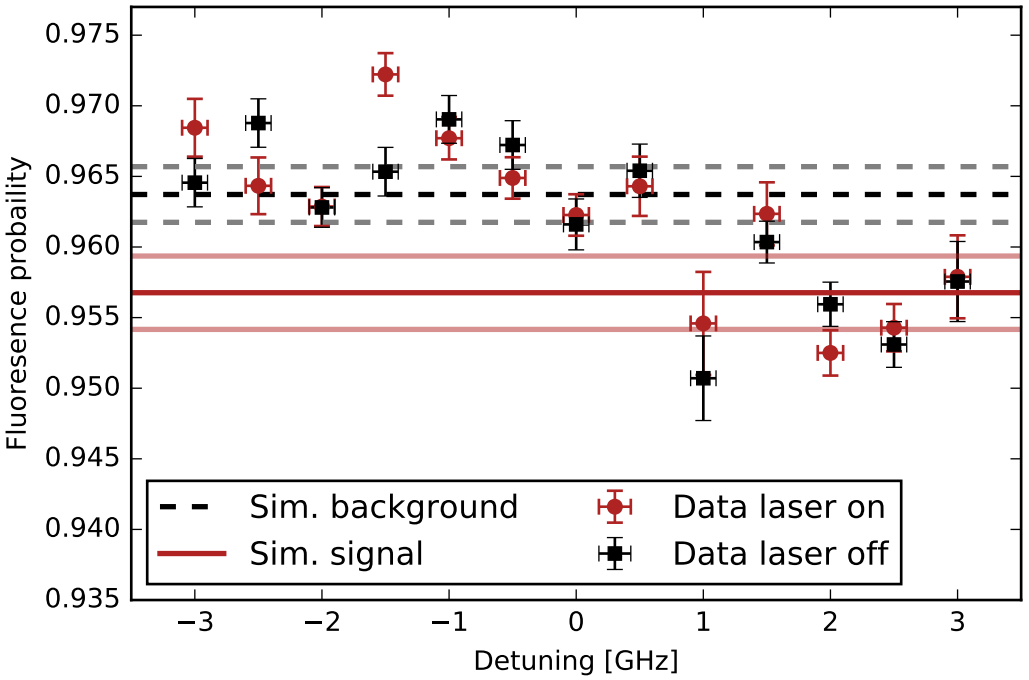

FIGURE 14.2: *Measured average fluorescence with the spectroscopy laser on the ions (red points) and for the laser shut off (black points) as a function of laser frequency detuning from the transition frequency f_t^B measured by Balfour [70]. Each data point, black and red respectively, is the average result from 9000 experimental cycles. The horizontal lines are the expected worst case fluorescence levels from simulations of the background (black dashed line) and the signal (red solid line) for the experimental parameters. The gray and light red lines represent the expected one standard deviation uncertainties on the black and red line, respectively, for the performed number of experimental cycles.*

since the background would suddenly be increased by 10 percentage points. This is a consequence of the changed mode angular frequencies when going from mass 25 u to mass 24 u, leading to poor shelving during SBC. The cooling is worse, since the 10 kHz angular Rabi frequencies used at the end of SBC, can easily resolve the 5 kHz difference in OP mode frequency for mass 24 and 25 u.

The 1st OP BSB transition frequency was measured around every 20 min to keep the SBC and RSB shelving at an optimum.

14.2.2 Obtained data

In Fig. 14.2 the total obtained dataset is presented. It consists of data for 13 different laser frequency detunings from the best former measured transition frequency f_t^B [70], starting at $f_t^B - 3$ GHz and going in steps of 500 MHz to $f_t^B + 3$ GHz. Since the applied laser lineshape was 1.1 GHz wide, this gives a good overlap between the

points. The scanned range of $f_t^B \pm 3$ GHz corresponds to the 2 standard deviation interval around f_t^B. For each detuning the average of all cycles with the laser on (red points), and the average of all cycles with the laser off (black points) are given.

It is obvious that the fluorescence probability is not constant over the whole scanning range. Especially the positive detunings have lower fluorescence levels. I will come back to why. However, it is the difference between the red and black points for each detuning that gives rise to a signal. To have a signal, the red points must be at a lower fluorescence level than the corresponding black point, and the errorbars should not overlap. As is evident from the plot, this is not fulfilled to any significant degree for any of the detunings.

The errorbars on the data points are calculated by finding the average value of each group of 500 cycles, and then calculating the average of the mean of these averages. This method was used, in order to not assume any distribution of the data. Different group sizes were also tried, but it did not have any significant effect on the errors. As a check, binomial errors were also calculated, and almost identical results were obtained. This suggests, that the individual cycle counts are not correlated in any way.

14.2.3 Comparison to simulations

14.2.3.1 Worst case scenario

The horizontal lines in Fig. 14.2 are expected worst case fluorescence levels from simulations. Using the terminology defined in Sec. 6.3 the black dashed line corresponds to P_{off} (background), and the red line to P_{on}^T (signal). This worst case result is found by applying all the experimentally measured parameters to the model, but one standard deviation in the least favorable direction. Specifically I used a higher heating rate of $R_{H,ip} = 7.8\ \mathrm{s}^{-1}$ and $R_{H,op} = 0.4\ \mathrm{s}^{-1}$, a higher initial average population after sideband cooling of $\bar{n}_{ip} = \bar{n}_{op} = 0.024$, and a lower laser intensity $I_L = 6\,\mathrm{W\,cm}^{-2}$. Additionally the laser spectral density was put to 0.085 $(2\pi\ \mathrm{GHz})^{-1}$, which is the minimum value for a QCL spectral FWHM of 1.15 GHz for the measured lineshape (ignoring the improvement from overlap between steps).

The dashed gray lines, and the light red lines in Fig. 14.2 represent the simulated one standard deviation uncertainty on the worst case P_{off} and P_{on}^T, respectively, calculated for the total measured number of cycles of 9000. The simulated fluorescence levels plus/minus their standard deviations do not overlap, meaning we should, according to simulation, still be able to resolve P_{off} and P_{on}^T to within more than one

standard deviation under the worst case conditions. However, the expected difference is not overwhelming, and there is a risk the signal could be hidden due to statistical fluctuations.

Coming back to the difference in fluoresence level for different detunings, this is belived to be a result of different SBC conditions at the specific time of acquisition, and not be related to detuning at all. Due to the long required measurement time for each detuning point, the data were taken over several weeks, during which the SBC efficiency varied due to magnetic field and laser frequency fluctuations. It is also possible that the larger background stems from trap-induced heating, which would require introduction of some new electric field noise source in the lab. Since we did not measure the ground state cooling level at zero time after SBC before all data points in Fig. 14.2 the two effects cannot be told apart. A background below the dashed lines does make the expected signal depth smaller, however the expected signal (red line) would also be at a lower fluorescence probability in this case.

14.2.3.2 Best case scenario

The best case result was also simulated, which is found by applying all the experimentally measured parameters to the model, but one standard deviation in the most favorable direction. Specifically I used a lower heating rate of $R_{H,ip} = 6.8\ \mathrm{s}^{-1}$ and $R_{H,op} = 0.2\ \mathrm{s}^{-1}$, a lower initial average population after sideband cooling of $\bar{n}_{ip} = \bar{n}_{op} = 0.014$, and a higher laser intensity $I_L = 8.4\,\mathrm{W\,cm}^{-2}$. Additionally the laser spectral density was put to 0.095 $(2\pi\ \mathrm{GHz})^{-1}$, which is the minimum value for a QCL spectral FWHM of 1.05 GHz for the measured lineshape (still ignoring the improvement from overlap between steps).

The simulated background for both the best (blue) and worst (red) case is plotted as a function of τ_{spec} in Fig. 14.3. Their values at 35 ms are indicated with gray lines. If we compare to Fig. 14.2, we see that the worst case scenario matches the background data best. This suggest that the SBC and/or the heating rates were generally worse when obtaining the PRS data, than the day the average population after SBC and the heating rates were measured.

The total measurement time needed to distinguish signal from background, to within one standard deviation, for both the best (blue) and worst (red) case scenario is seen in Fig. 14.4. The segmented structure of the lines is a consequence of taking the synchronization to the 50 Hz wall voltage into account in the simulations. The gray line indicates the used $\tau_{\mathrm{spec}} = 35$ ms. In the experiments we used $T = N\tau_{\mathrm{cycle}} = 9000 \times 0.14$ ms $= 1260$ s. We thus see that in the best case, we have measured

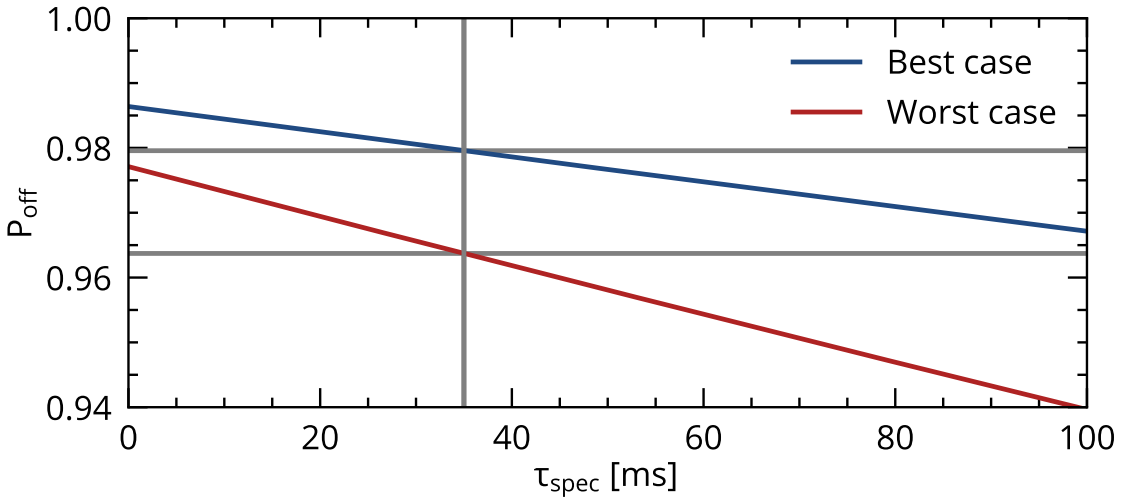

FIGURE 14.3: *The simulated background fluorescence probability P_{off} for the best (blue) and worst (red) case experimental parameters, within one standard deviation, as a function of spectroscopy pulse time τ_{spec}. The values for each case at 35 ms are indicated with gray lines.*

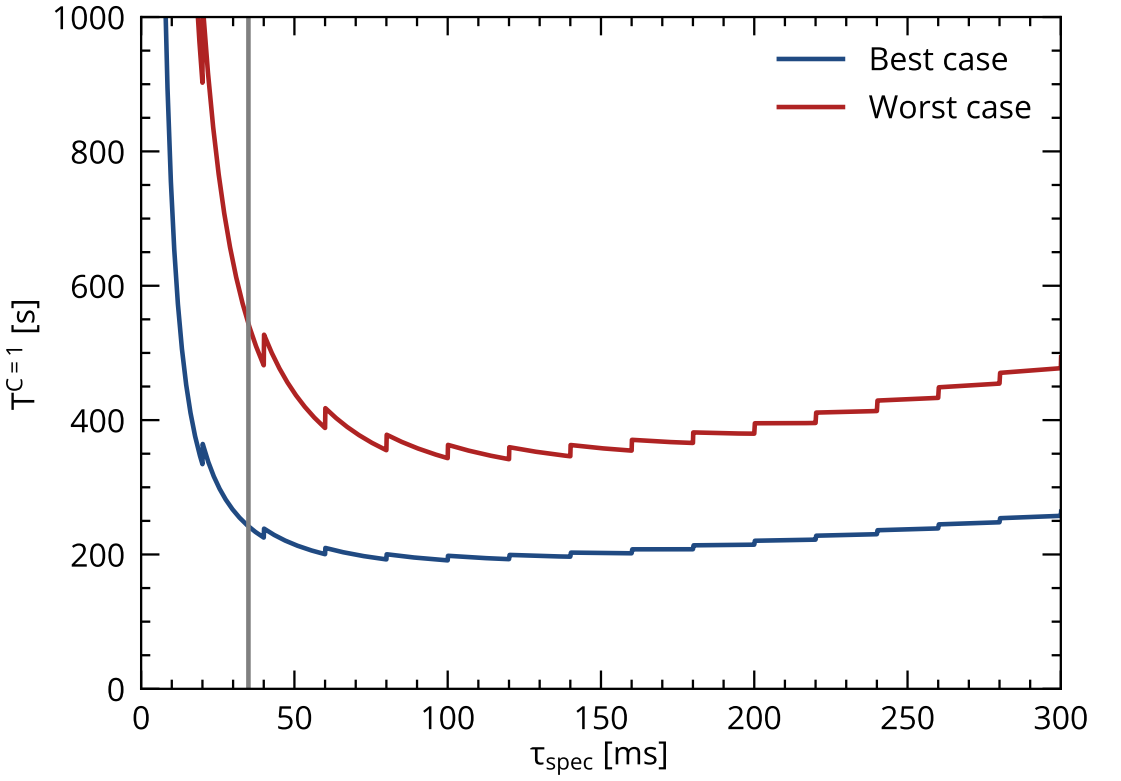

FIGURE 14.4: *The total measurement time needed to distinguish signal from background, to within one standard deviation, for both the best (blue) and worst (red) case scenario as a function of spectroscopy pulse time τ_{spec}. The segmented structure of the lines is a consequence of taking the synchronization to the 50 Hz wall voltage into account in the simulations. The gray line indicates the value of $\tau_{spec} = 35$ ms used for the experiments.*

enough points to distinguish signal from background to within 2 standard deviations since $T^C \propto C^2$. We see that in the worst case, we should also be able to distinguish to within more than one standard deviation as already shown with the lines in Fig. 14.2.

Furthermore, according to Fig. 14.4 we could have benefited from applying a longer spectroscopy pulse. The ideal would have been some value close to 100 ms. The reason why we used 35 ms, was that the intensity at the ion position was initially believed to be larger, which moves the optimum τ_{spec} to lower values as seen from Fig. 9.2.[1]

14.3 Suggestions for further work

Besides from simply taking more data points using the same experimental parameters as given above, there are several ways the experiment could be improved in order to increase the chances of obtaining a signal.

One of the experimental values, which is limiting the experiment the most, is the spectroscopy laser intensity at the ion position, which should be increased. This is most easily done by improving the alignment on the ions, where we found in Sec. 12.2.1.3 that especially the longitudinal alignment could be improved. In order to increase the intensity, the waist could also be reduced, but with the risk of not hitting the ions. The ultimate way to align the laser, would be if one could instead detect its interaction with the $^{40}Ca^+$ ion from the light shift. However, the Stark shift on the 729 nm transition for the current intensity is only expected to be around 100 µHz. The shift is porportional to intensity, so a much higher intensity is required for this to work

Another way to improve the experiment, would be to monitor the background fluctuations in real time by running one experimental cycle with the laser on the ions, and one with the laser shut off, interleaved. This was not done due to a non-trivial software issue in the control program, which should be possible to fix.

The model of molecular dynamics presented in Sec. 8.1.1 suggests that the non-fluorescing cycle counts due to the $^{24}MgH^+$ ion interacting with the laser, will not be evenly distributed in time. A search for correlations in the obtained data, which could not be explained by a binomial distribution was attempted, but no clear signs were found. However, if the laser interaction causes more dark cycle counts, this should also be possible to detect from the average fluorescence values.

[1] Since the laser energy spectral density is proportional to I_L/Γ_L for the example in this figure.

Maybe the largest limitation of the experiment, is the population distribution among the rotational states in $^{24}MgH^+$, not only decreasing the expected signal depth by 8.5% but also necessitating very long measurement times to average out the relatively slow rotational dynamics. Currently there are no very efficient ways of preparing the molecule in $J = 1$, however buffer gas cooling could be an option as long as the collision rate is low enough to allow for performing PRS in between. Because rotational cooling takes on the order of 1 min, this approach is not useful.

Another solution is to instead work in a cryogenic trap since at 4 K the molecule would be prepared almost entirely in the $J = 0$ state.

14.4 Conclusion

In this chapter the search for an unresolved sideband PRS signal of the $^1\Sigma^+$ $|v = 0, J = 1\rangle \leftrightarrow |v' = 1, J' = 0\rangle$ transition of 6.2 µm in $^{24}MgH^+$ was presented and compared to the model set up in Sec.s 5.2 and 6.2. In this case the sidebands are unresolved due to the relatively large spectral linewidth of the spectroscopy laser.

The presented preliminary data do unfortunately not show any clear sign of a signal. The simulations suggest that we should have been able to distinguish the signal from background on a confidence level corresponding to more than one standard deviation. This is however not enough to rule out that the lack of signal could be due to statistical fluctuations.

It was found that the simulations describe the background signal fairly well, but also that the variation of the background was larger, than the measured uncertainties on the average motional population and trap-induced heating rates presented in Sec. 14.1 could account for.

Lastly several possible improvements of the experiment were suggested.

Chapter 15

Conclusion and outlook

In this thesis, I have developed a model that can describe the expected spectroscopic signals when applying photon recoil spectroscopy (PRS) in the unresolved sideband limit where the linewidth of either the addressed transitions or the exciting light sources is broader than the frequencies of the involved motional modes. This model has been compared to experimental results with respect to the former case by carrying out unresolved sideband PRS on the 3s $^2S_{1/2}$ - 3p $^2P_{3/2}$ electronic transition of a single $^{24}Mg^+$ ion. Since very good agreement has been obtained between the experimental and simulation results, I strongly believe the model to be useful for other spectroscopic investigations.

The search for the closed rovibrational $^1\Sigma^+$ $|v = 0, J = 1\rangle$ - $|v' = 1, J' = 0\rangle$ transition in $^{24}MgH^+$ was also presented. The largest limitation of this experiment, was found to be the population distribution among the rotational states in $^{24}MgH^+$ due to coupling to room temeperature black-body radiation (BBR), not only decreasing the expected signal depth by 8.5% but also necessitating very long measurement times to average out the relatively slow rotational dynamics. The simulations suggest that we should have been able to distinguish the signal from background on a confidence level corresponding to more than one standard deviation. This is however not enough to rule out that the lack of signal could be due to statistical fluctuations. The chance to obtain a signal can most easily be improved by increasing the laser intensity.

An important feature of unresolved sideband PRS is that the spectroscopic signal does essentially not depend on which of the two transition states are occupied by the target ion when applying the spectroscopic light pulses. In particular, in relation to localizing a narrow transition with an associated slow spontaneous decay rate, not to have to initialize the target ion in the lowest lying state before applying the spectroscopic light source can speed up the time that is otherwise required to obtain a spectrum. Indeed, as for the $^{24}MgH^+$ case presented in Sec. 6.2, the main contribution to the spectral broadening of the intrinsically narrow line stems from

broadening of the motional state distribution due to light stimulated processes, i.e., absorption and stimulated emission. Hence the technique should be well suited to localize still vastly unknown narrow lines in various target ions, such as rovibrational transitions in molecular ions, electronic and (hyper)fine structure transitions in highly charged ions.

Additionally, it was found that the scenario of unresolved PRS, due to motional ground state depletion, gives rise to a broadening of the spectroscopic signals, that can be much larger than the natural linewidth of the transition or the spectral width of the applied light source. This broadening is highly dependent on the duration of the spectroscopic light pulse and exists even in cases where the interrogation intensities are far below the relevant saturation intensity (e.g. for the $^{24}Mg^{+}$ case of a broad transition discussed in sub-section 6.1). At a first glance this situation may seem very unfortunate and disadvantageous with respect to applying unresolved PRS for any scientific investigations. However, in situations where the aim is to localize undetermined spectroscopic lines, this technique together with rather imprecise theoretical predictions of the line positions can turn out to be a very powerful tool to search for the transitions. More precise determination of the transition frequency can be achieved eventually by shortening the spectroscopic time and/or the spectral width of the interrogation light pulses. Clearly, in the end, the width of the spectroscopic signal will be limited either by the linewidth of the transition addressed, the intrinsic width of the light source, or the measured accuracy of the laser frequency. Having initially a narrow laser source available, actively frequency broadening it during line search was found to be advantageous compared to just stepping the frequency of the narrow laser through a large frequency interval.

A near future goal of our group is to do PRS of much larger molecules in a cryogenic trap at 4 K. At this low temeperature the internal population will be distributed among much fewer states, largely improving the conditions for PRS. Therefore, the fundamental understanding of the physics governing unresolved sideband PRS and the developed model will be of great use for experiments to come.

Appendix A

The calcium ion

A.1 Ca isotopes

A	shift [MHz]	abundance in %
40	0	96.941(156)
42	967(9)	0.647(23)
43	1455(9)	0.135(10)
44	1879(14)	2.086(110)
46	2746(16)	0.004(3)
48	3528(16)	0.187(21)

FIGURE A.1: *Isotope abundance from [130] and shift for the 272 nm transition from [131]. Table from [132].*

A.2 $^{40}Ca^{+}$ structure and transitions

Transition		Wavelength [nm]	Frequency [THz]	$\Gamma/(2\pi)$
$4\,^2S_{1/2}$	$4\,^2P_{1/2}$	397	755.222 765 896(88)	21.57(15) MHz
$4\,^2S_{1/2}$	$4\,^2P_{3/2}$	393	761.905 012 599(82)	21.49(6) MHz
$3\,^2D_{3/2}$	$4\,^2P_{1/2}$	866	346.000 234 867(96)	1.481(15) MHz
$3\,^2D_{3/2}$	$4\,^2P_{3/2}$	850	352.682 481 57(15)	1.481(15) MHz
$3\,^2D_{5/2}$	$4\,^2P_{3/2}$	854	350.862 882 55(15)	1.350(6) MHz
$4\,^2S_{1/2}$	$3\,^2D_{5/2}$	729	411.042 129 776 393 2(10)	136.3(10) mHz
$3\,^2D_{3/2}$	$3\,^2D_{5/2}$	D-f ne	1 819 599 021 504(37)	
$4\,^2S_{1/2}$	$3\,^2D_{3/2}$	732	409.222 530 754 889(37)	135.3(13) mHz

FIGURE A.2: *Transition data for $^{40}Ca^{+}$. Table from [82]. Courtesy of Steffen Meyer.*

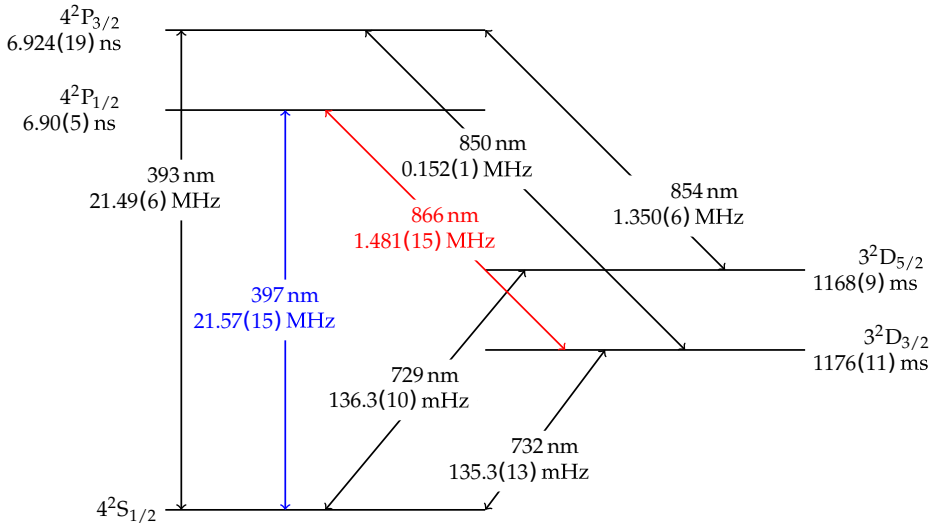

FIGURE A.3: *The level structure of* $^{40}Ca^{+}$ *. Courtesy of Hans Andersen [79].*

Appendix B

The magnesium ion

B.1 Mg isotopes

	^{24}Mg	^{25}Mg	^{26}Mg
Abundance [%]	78.99(4)	10.00(1)	11.02(3)
Nuclear Spin	0	5/2	0

FIGURE B.1: *Mg^+ isotopes abundance and nuclear spin [130].*

B.2 Mg^+ level structure

Transition	Wavelength [nm]	Frequency [THz]	Lifetime [ns]
$3\,^2S_{1/2} \rightarrow 3\,^2P_{1/2}$			
$^{24}Mg^+$	280.353	1069.338 342 56(16)	3.854(30)
$^{25}Mg^+$	280.353	1069.339 957(5)	
$^{26}Mg^+$	280.352	1069.341 427 47(16)	
$3\,^2S_{1/2} \rightarrow 3\,^2P_{3/2}$			
$^{24}Mg^+$	279.636	1072.082 934 33(16)	3.810(40)
$^{25}Mg^+$	279.635	1072.084 547(5)	3.75(15)
$^{26}Mg^+$	279.635	1072.086 021 89(16)	3.81(10)
$3\,^2S_{1/2} \rightarrow 2\,^2D_{5/2}$			
$^{25}Mg^+$	139.879	2143.223 903(7)	
$3\,^2S_{1/2} \rightarrow 4\,^2P_{3/2}$			
$^{25}Mg^+$	123.992	2417.829 196(12)	

FIGURE B.2: *Ground state transitions in Mg^+ isotopes. Wavelengths in vacuum are calculated from the given frequencies. From [132].*

Appendix C

The MgH^+ ion

C.1 Rovibrational transition

The R branch transitions have $\Delta J = 1$ and is denoted $R_v(J)$, where v and J refer to the lower state. The P branch transitions have $\Delta J = -1$ and hare denoted $P_v(J)$, where v and J refer to the lower state.

Transition	Wavenumber [cm ^{1}]	Vac. wavelength [µm]	Frequency [THz]
$R_0(0)$	12.59	794.53	0.378
$R_0(1)$	25.16	397.54	0.755
$R_0(2)$	37.82	264.43	1.135
$R_0(3)$	50.19	199.23	1.506
$R_0(4)$	62.85	159.12	1.885
$R_0(5)$	75.22	132.95	2.256
$R_0(6)$	87.66	114.07	2.630
$R_0(7)$	99.95	100.05	2.999
$R_0(8)$	112.30	89.05	3.369
$R_0(9)$	124.45	80.35	3.734

FIGURE C.1: *Transition data for the lowest- lying rotational transitions. Calculated from [70]. Table from [82]. The error on wavenumber is* $0.05\,\mathrm{cm}^{-1}$.

Transition	Wavenumber [cm ^{1}]	Vac. wavelength [µm]	Frequency [THz]
$P_1(5)$	1568.03	6377.45	47.041
$P_1(4)$	1582.06	6320.89	47.462
$P_1(3)$	1595.56	6267.41	47.867
$P_1(2)$	1608.96	6215.19	48.269
$P_1(1)$	1621.77	6166.11	48.653
$R_1(0)$	1646.70	6072.74	49.401
$R_1(1)$	1658.53	6029.44	49.756
$R_1(2)$	1670.07	5987.79	50.102
$R_1(3)$	1681.07	5948.61	50.432
$R_1(4)$	1691.86	5910.67	50.756

FIGURE C.2: *Transition data for the lowest- lying rotational transitions. Calculated from [70]. Table from [82]. The error on wavenumber is* $0.05\,\mathrm{cm}^{-1}$.

C.2 Einstein A- and B-coefficients

The Einstein A-coefficients given in Fig. C.3 and C.4 were calculated by Anders Hansen ([71] p. 155) based on potential and dipole moments calculated by Frank Jensen at the Department of Chemistry at Aarhus University in 2012 [72]. Hansen writes the unit as Hz but it is really s^{-1}. I.e. the A-parameters in Hansen's table should be divided by 2π to be in Hz. This error is corrected for the numbers given here.

The B-coefficients are calculated from the A-coefficients via Eq.s 3.39 and 3.40 taking into account the degeneracy of the rotational levels of $g_J = 2J + 1$. Using Eq. 3.31 these are multiplied by the energy spectral density $\rho(\omega_t)$ of a black-body radiation field at 293 K given by Eq. 3.30 to obtain the absorption and stimulated emission rates given in Fig. C.5.

$\|v, J\rangle_{ini}$		$\Delta v = 0$		-1		-2		-3		-4	
v	J	$\Delta J = -1$	1	-1	1	-1	1	-1	1	-1	1
	0										
	1	0.0023									
	2	0.022									
	3	0.081									
0	4	0.199									
	5	0.396									
	6	0.691									
	7	1.104									
	8	1.652									
	0				15.753						
	1	0.0020		6.139	9.701						
	2	0.020		7.955	8.059						
	3	0.070		9.195	7.079						
1	4	0.172		10.277	6.345						
	5	0.343		11.316	5.740						
	6	0.599		12.358	5.219						
	7	0.957		13.424	4.760						
	8	1.430		14.527	4.349						
	0				36.614		2.676				
	1	0.0017		14.061	22.721	0.802	1.872				
	2	0.017		18.093	19.025	0.907	1.762				
	3	0.060		20.773	16.851	0.911	1.750				
2	4	0.147		23.065	15.231	0.883	1.769				
	5	0.293		25.237	13.899	0.839	1.800				
	6	0.511		27.392	12.750	0.787	1.838				
	7	0.816		29.579	11.735	0.731	1.878				
	8	1.220		31.826	10.825	0.672	1.918				
	0				61.632		5.918		0.633		
	1	0.0015		23.391	38.480	1.741	4.172	0.202	0.431		
	2	0.014		29.927	32.422	1.947	3.953	0.236	0.396		
	3	0.050		34.167	28.899	1.934	3.949	0.247	0.385		
3	4	0.124		37.731	26.289	1.847	4.012	0.250	0.382		
	5	0.246		41.063	24.147	1.728	4.103	0.248	0.382		
	6	0.429		44.335	22.299	1.592	4.205	0.245	0.383		
	7	0.684		47.630	20.661	1.448	4.311	0.241	0.386		
	8	1.021		50.991	19.186	1.300	4.417	0.235	0.390		
	0				89.030		7.861		2.501		0.053
	1	NC		33.466	55.856	2.245	5.609	0.795	1.704	0.017	0.036
	2	NC		42.614	47.292	2.466	5.372	0.931	1.567	0.020	0.033
	3	NC		48.423	42.360	2.399	5.417	0.972	1.523	0.021	0.032
4	4	NC		53.224	38.723	2.237	5.549	0.981	1.509	0.021	0.031
	5	NC		57.656	35.742	2.035	5.715	0.975	1.510	0.021	0.031
	6	NC		61.966	33.167	1.816	5.893	0.961	1.517	0.021	0.031
	7	NC		66.268	30.879	1.589	6.073	0.942	1.529	0.021	0.031
	8	NC		70.624	28.812	1.364	6.249	0.920	1.543	0.021	0.032

FIGURE C.3: *Einstein A coefficients for low-lying rovibrational transitions in* s^{-1} *(angular frequencies). Calculations by Frank Jensen [72]. Table from [82] reproduced from [71]. In both the other versions, the unit is wrong.*

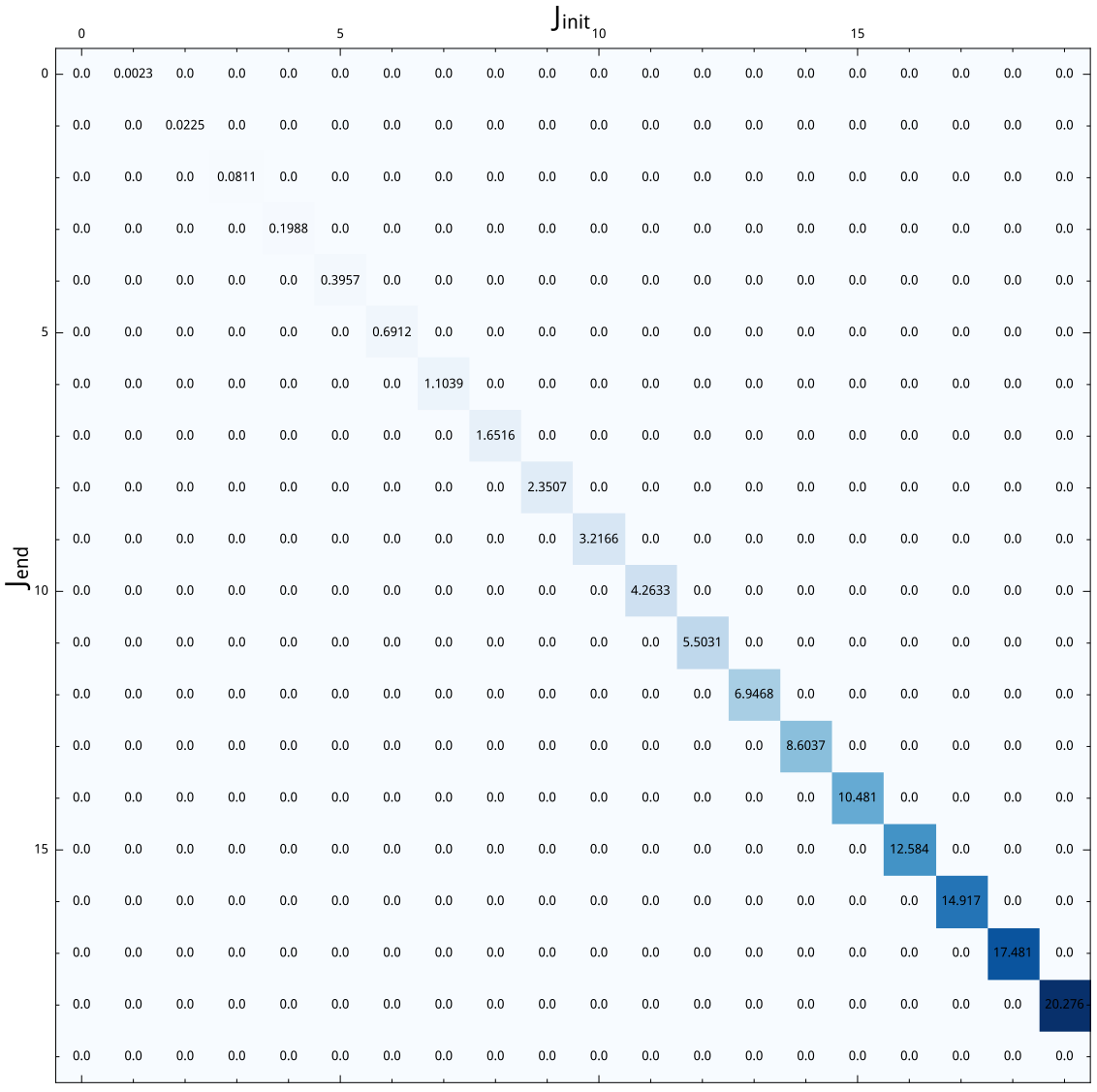

FIGURE C.4: *Einstein A coefficients in s^{-1} for rotational transitions in the electronic and vibrational ground state of $^{24}MgH^+$. Only couplings with $\Delta J = -1$ are allowed for spontaneous emission.*

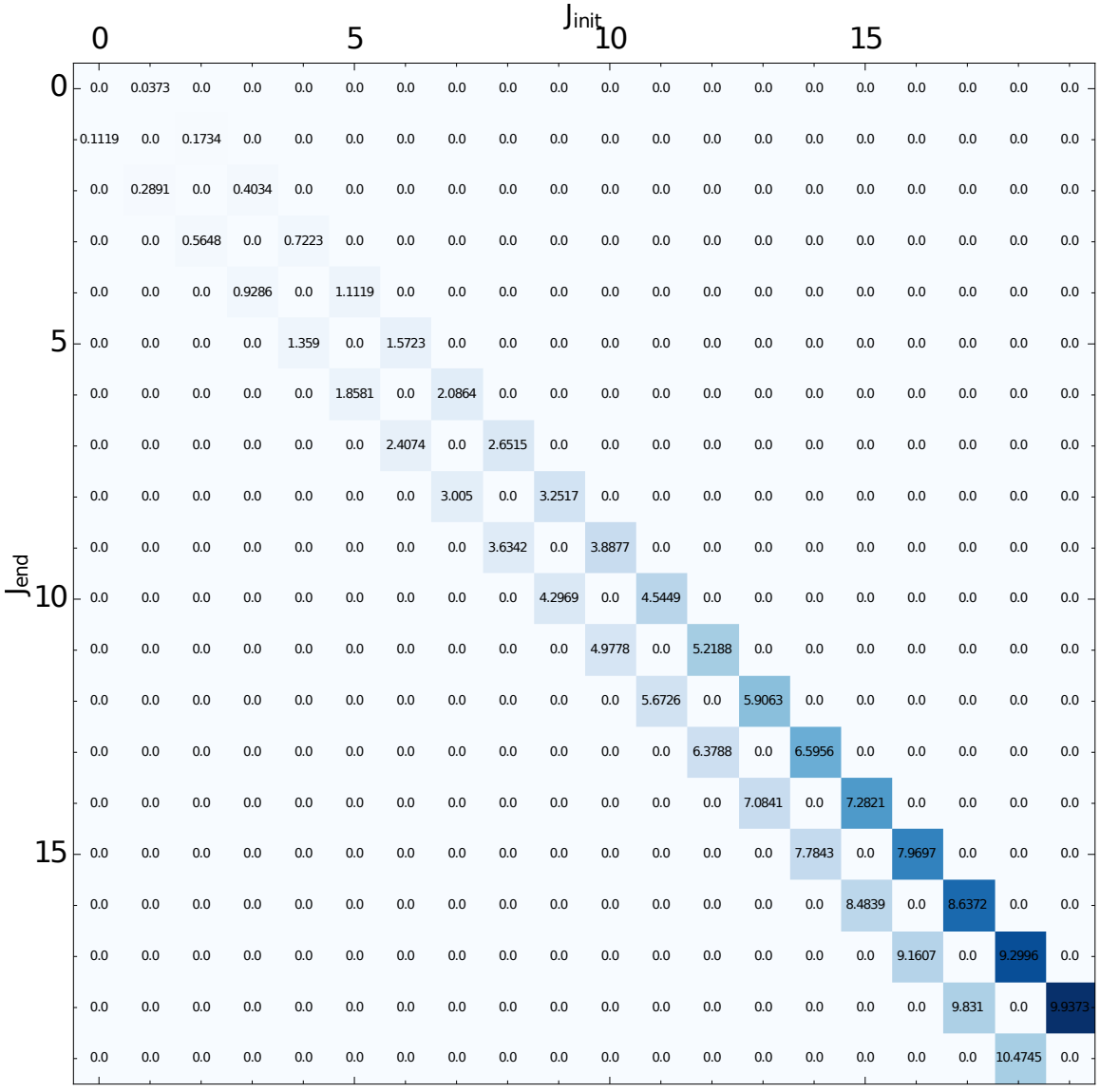

FIGURE C.5: *Stimulated emission (above diagonal) and absorption (below diagonal) rates in s^{-1} for rotational transitions in the electronic and vibrational ground state of $^{24}MgH^+$. Only couplings with $\Delta J = \pm 1$ are allowed.*

Appendix D

D and $|\xi|^2$ parameters

The probability to absorb or stimulated emit on a specific sideband from a specific motional state is given by $|\xi(\eta_{ip,t}, \eta_{op,t}, n_{ip}, n_{op}, s_{ip}, s_{op})|^2$ defined in Eq. 3.67. The sum over all sidebands is

$$|\xi_{tot}(n_{ip}, n_{op})|^2 = \sum_{s_{ip}, s_{op}} |\xi(\eta_{ip,t}, \eta_{op,t}, n_{ip}, n_{op}, s_{ip}, s_{op})|^2 \tag{D.1}$$

The probability to spontaneously emit on a specific sideband from a specific motional state is given by $D(\eta_{ip,t}, \eta_{op,t}, n_{ip}, n_{op}, s_{ip}, s_{op})$ defined in Eq. 5.17. The sum over all sidebands is

$$D_{tot}(n_{ip}, n_{ip}) = \sum_{s_{ip}, s_{op}} D(\eta_{ip,t}, \eta_{op,t}, n_{ip}, n_{op}, s_{ip}, s_{op}), \tag{D.2}$$

If all sidebands are considered we must have $|\xi_{tot}(n_{ip}, n_{op})|^2 = 1$ and $D_{tot}(n_{ip}, n_{ip}) = 1$ in accordance with Eq. 7.1 and 7.2.

This is expressed graphically in Fig. D.1 for $|\xi_{tot}(n_{ip}, n_{op})|^2$ and D.2 for the parameters used for the $^{24}Mg^+$ PRS experiments and simulations.

For all motional states in these plots, the sum is very close to 1, meaning the considered sidebands of $s_{ip} = -5 \text{ to } 5$ and $s_{op} = -6 \text{ to } 6$ considered in the model is sufficient. The asymmetry stems from the fact that $\eta_{op,t} > \eta_{ip,t}$.

The same method was used to determine the necessary number of sidebands to consider for the $^{24}MgH^+$ simulations. In this case we found that $s_{ip} = -1 \text{ to } 1$ and $s_{op} = -1 \text{ to } 1$ was sufficient.

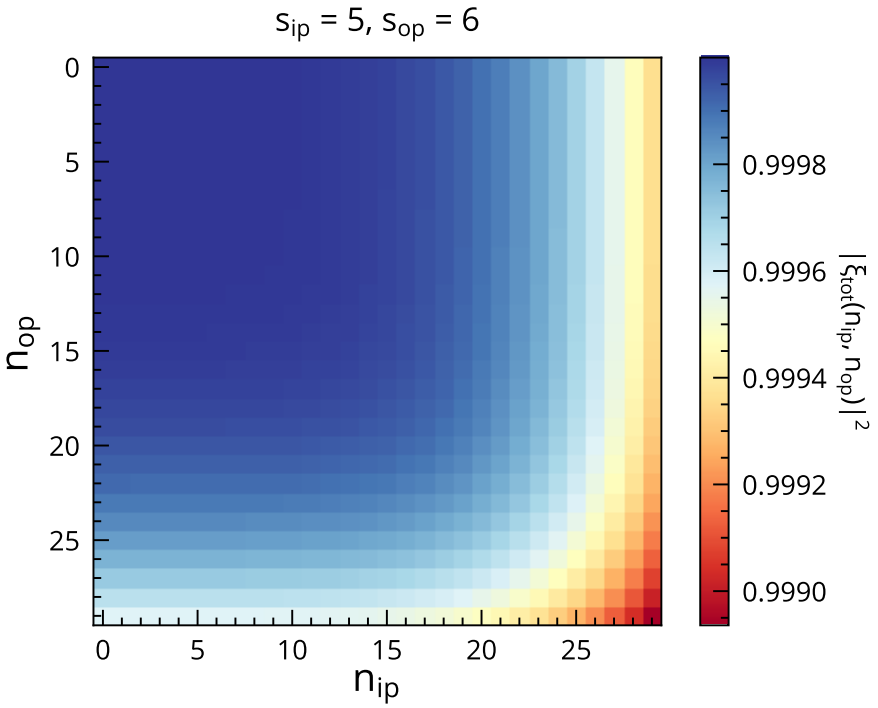

FIGURE D.1: *The color indicates the sum of the* $|\xi(\eta_{ip,t}, \eta_{op,t}, n_{ip,t}, n_{op,t}, s_{ip}, s_{op})|^2$*-parameter for all combinations of* $s_{ip} = -5\,to\,5$ *and* $s_{op} = -6\,to\,6$*, for all combinations of* $n_{ip} = 0 - 29$ *and* $n_{op} = 0 - 29$*.*

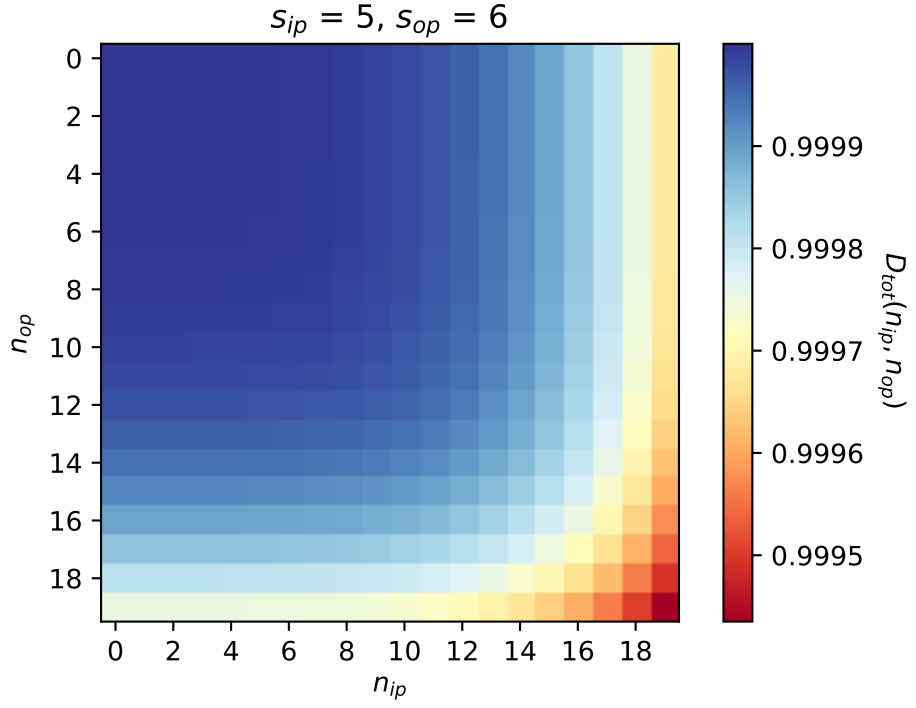

FIGURE D.2: *The color indicates the sum of the D-parameters for all combinations of* $s_{ip} = -5\,to\,5$ *and* $s_{op} = -6\,to\,6$ *for all combinations of* $n_{ip} = 0 - 19$ *and* $n_{op} = 0 - 19$*.*

Appendix E

Illustration of sideband coupling for two modes

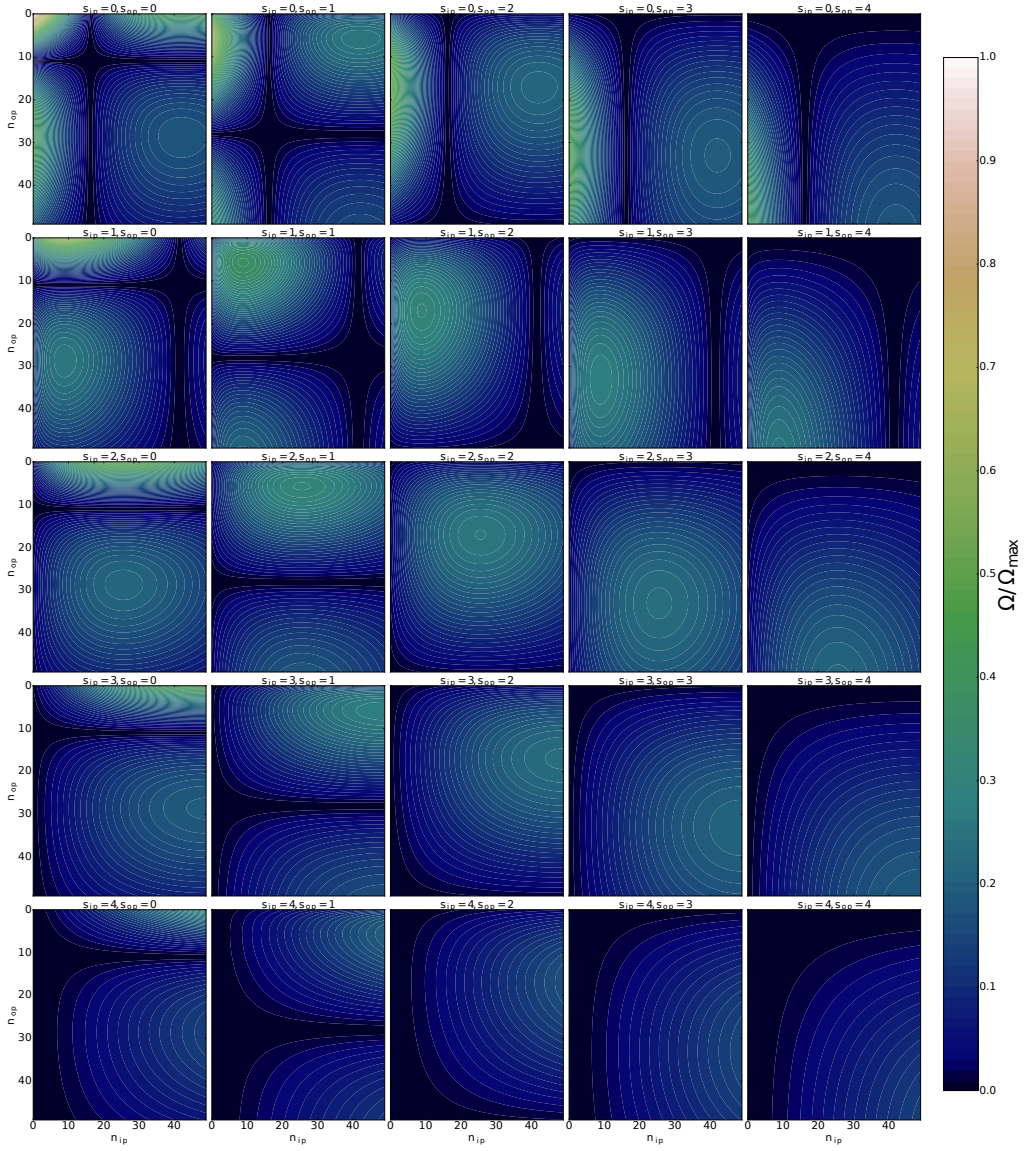

FIGURE E.1: *Plot of Rabi frequencies divided by the maximum Rabi frequency for sideband orders of 0-4 for both the IP and OP mode, as a function of the motional quantum number* n_{ip}, n_{op} *for* $\eta_{ip} = 0.29$ *and* $\eta_{op} = 0.36$ *for the trapped* $^{40}Ca^{+}$ -$^{24}Mg^{+}$ *system.*

Bibliography

[1] Wolfgang Paul and Helmut Steinwedel. Ein neues massenspektrometer ohne magnetfeld. *Z. Naturforschg.*, 84:448–450, 1953.

[2] Hans G. Dehmelt. Hans G. Dehmelt - Biographical. 1989. URL `https://www.nobelprize.org/prizes/physics/1989/dehmelt/biographical/`.

[3] D. Wineland and H. Dehmelt. Proposed 1014dnn laser fluorescence spectroscopy on tl+ mono-ion oscillator iii (sideband cooling). *Bull. Am. Phys. Soc.*, 637:20, 1975.

[4] T.W. Hänsch and A.L. Schawlow. Cooling of gases by laser radiation. *Optics Communications*, 13(1):68 – 69, 1975. ISSN 0030-4018. doi: https://doi.org/10.1016/0030-4018(75)90159-5. URL `http://www.sciencedirect.com/science/article/pii/0030401875901595`.

[5] D. J. Wineland, R. E. Drullinger, and F. L. Walls. Radiation-pressure cooling of bound resonant absorbers. *Phys. Rev. Lett.*, 40:1639–1642, Jun 1978. doi: 10.1103/PhysRevLett.40.1639. URL `https://link.aps.org/doi/10.1103/PhysRevLett.40.1639`.

[6] W. Neuhauser, M. Hohenstatt, P. E. Toschek, and H. Dehmelt. Localized visible ba^+ mono-ion oscillator. *Phys. Rev. A*, 22:1137–1140, Sep 1980. doi: 10.1103/PhysRevA.22.1137. URL `https://link.aps.org/doi/10.1103/PhysRevA.22.1137`.

[7] Warren Nagourney, Jon Sandberg, and Hans Dehmelt. Shelved optical electron amplifier: Observation of quantum jumps. *Phys. Rev. Lett.*, 56:2797–2799, Jun 1986. doi: 10.1103/PhysRevLett.56.2797. URL `https://link.aps.org/doi/10.1103/PhysRevLett.56.2797`.

[8] J. C. Bergquist, Randall G. Hulet, Wayne M. Itano, and D. J. Wineland. Observation of quantum jumps in a single atom. *Phys. Rev. Lett.*, 57:1699–1702, Oct 1986. doi: 10.1103/PhysRevLett.57.1699. URL `https://link.aps.org/doi/10.1103/PhysRevLett.57.1699`.

[9] Th Sauter, W Neuhauser, R. Blatt, and P. Toschek. Observation of quantum jumps. *Physical review letters*, 57:1696–1698, 11 1986. doi: 10.1103/PhysRevLett.57.1696.

[10] E. Schrödinger. Are there quantum jumps? part ii. *The British Journal for the Philosophy of Science*, 3(11):233–242, 1952. ISSN 00070882, 14643537. URL `http://www.jstor.org/stable/685266`.

[11] W.M. Itano, J.C. Bergquist, and D.J. Wineland. Early observations of macroscopic quantum jumps in single atoms. *International Journal of Mass Spectrometry*, 377:403–409, 2015. ISSN 1387-3806. doi: https://doi.org/10.1016/j.ijms.2014.07.005. URL `https://www.sciencedirect.com/science/article/pii/S1387380614002656`. Special Issue: MS 1960 to Now.

[12] F Diedrich, JC Bergquist, Wayne M Itano, and DJ Wineland. Laser cooling to the zero-point energy of motion. *Physical Review Letters*, 62(4):403, 1989.

[13] Andrew D Ludlow, Martin M Boyd, Jun Ye, Ekkehard Peik, and Piet O Schmidt. Optical atomic clocks. *Reviews of Modern Physics*, 87(2):637, 2015.

[14] Scott A Diddams, Th Udem, JC Bergquist, EA Curtis, RE Drullinger, L Hollberg, Wayne M Itano, WD Lee, CW Oates, KR Vogel, et al. An optical clock based on a single trapped 199hg+ ion. *Science*, 293(5531):825–828, 2001.

[15] N. Huntemann, C. Sanner, B. Lipphardt, Chr. Tamm, and E. Peik. Single-ion atomic clock with 3×10^{-18} systematic uncertainty. *Phys. Rev. Lett.*, 116:063001, Feb 2016. doi: 10.1103/PhysRevLett.116.063001. URL `https://link.aps.org/doi/10.1103/PhysRevLett.116.063001`.

[16] WF McGrew, X Zhang, RJ Fasano, SA Schäffer, K Beloy, D Nicolodi, RC Brown, N Hinkley, G Milani, M Schioppo, et al. Atomic clock performance enabling geodesy below the centimetre level. *Nature*, 564(7734):87–90, 2018.

[17] Tobias Bothwell, Dhruv Kedar, Eric Oelker, John M Robinson, Sarah L Bromley, Weston L Tew, Jun Ye, and Colin J Kennedy. Jila sri optical lattice clock with uncertainty of. *Metrologia*, 56(6):065004, 2019.

[18] TL Nicholson, SL Campbell, RB Hutson, GE Marti, BJ Bloom, RL McNally, Wei Zhang, MD Barrett, MS Safronova, GF Strouse, et al. Systematic evaluation of an atomic clock at 2× 10- 18 total uncertainty. *Nature communications*, 6(1):1–8, 2015.

[19] Samuel M Brewer, J-S Chen, Aaron M Hankin, Ethan R Clements, Chin-wen Chou, David J Wineland, David B Hume, and David R Leibrandt. Al+ 27 quantum-logic clock with a systematic uncertainty below 10- 18. *Physical review letters*, 123(3):033201, 2019.

[20] Boulder Atomic Clock Optical Network BACON Collaboration. Frequency ratio measurements at 18-digit accuracy using an optical clock network. *Nature*, 591(7851):564–569, 2021.

[21] David P DiVincenzo. The physical implementation of quantum computation. *Fortschritte der Physik: Progress of Physics*, 48(9-11):771–783, 2000.

[22] Yunseong Nam, Jwo-Sy Chen, Neal C Pisenti, Kenneth Wright, Conor Delaney, Dmitri Maslov, Kenneth R Brown, Stewart Allen, Jason M Amini, Joel Apisdorf, et al. Ground-state energy estimation of the water molecule on a trapped-ion quantum computer. *npj Quantum Information*, 6(1):1–6, 2020.

[23] JM Pino, JM Dreiling, C Figgatt, JP Gaebler, SA Moses, MS Allman, CH Baldwin, M Foss-Feig, D Hayes, K Mayer, et al. Demonstration of the trapped-ion quantum ccd computer architecture. *Nature*, 592(7853):209–213, 2021.

[24] Colin D Bruzewicz, John Chiaverini, Robert McConnell, and Jeremy M Sage. Trapped-ion quantum computing: Progress and challenges. *Applied Physics Reviews*, 6(2):021314, 2019.

[25] S Schiller and V Korobov. Tests of time independence of the electron and nuclear masses with ultracold molecules. *Physical Review A*, 71(3):032505, 2005.

[26] K Beloy, MG Kozlov, A Borschevsky, AW Hauser, VV Flambaum, and P Schwerdtfeger. Rotational spectrum of the molecular ion nh+ as a probe for α and m e/m p variation. *Physical Review A*, 83(6):062514, 2011.

[27] Soroosh Alighanbari, Michael Georg Hansen, VI Korobov, and Stephan Schiller. Rotational spectroscopy of cold and trapped molecular ions in the lamb–dicke regime. *Nature Physics*, 14(6):555–559, 2018.

[28] Fabian Wolf, Jan C. Heip, Maximilian J. Zawierucha, Chunyan Shi, Silke Ospelkaus, and Piet O. Schmidt. Prospect for precision quantum logic spectroscopy of vibrational overtone transitions in molecular oxygen ions, 2020.

[29] Sayan Patra, M. Germann, J.-Ph. Karr, M. Haidar, L. Hilico, V. I. Korobov, F. M. J. Cozijn, K. S. E. Eikema, W. Ubachs, and J. C. J. Koelemeij. Proton-electron mass ratio from laser spectroscopy of HD+ at the part-per-trillion level. *Science*, 369(6508):1238–1241, jul 2020. doi: 10.1126/science.aba0453.

[30] MS Safronova, D Budker, D DeMille, Derek F Jackson Kimball, A Derevianko, and Charles W Clark. Search for new physics with atoms and molecules. *Reviews of Modern Physics*, 90(2): 025008, 2018.

[31] Sylvio Canuto, Marcos A Castro, and K Sinha. Theoretical determination of the spectroscopic constants of cah+. *Physical Review A*, 48(3):2461, 1993.

[32] Stefan Willitsch, Martin T Bell, Alexander D Gingell, and Timothy P Softley. Chemical applications of laser-and sympathetically-cooled ions in ion traps. *Physical Chemistry Chemical Physics*, 10(48):7200–7210, 2008.

[33] Stefan Willitsch. Coulomb-crystallised molecular ions in traps: methods, applications, prospects. *International reviews in physical chemistry*, 31(2):175–199, 2012.

[34] Arne Härter and J Hecker Denschlag. Cold atom–ion experiments in hybrid traps. *Contemporary Physics*, 55(1):33–45, 2014.

[35] D Gerlich and M Smith. Laboratory astrochemistry: studying molecules under inter-and circumstellar conditions. *Physica Scripta*, 73(1):C25, 2005.

[36] MR Tarbutt. Laser cooling of molecules. *Contemporary Physics*, 2019.

[37] ES Shuman, JF Barry, DR Glenn, and D DeMille. Radiative force from optical cycling on a diatomic molecule. *Physical review letters*, 103(22):223001, 2009.

[38] Edward S Shuman, John F Barry, and David DeMille. Laser cooling of a diatomic molecule. *Nature*, 467(7317):820–823, 2010.

[39] Matthew T Hummon, Mark Yeo, Benjamin K Stuhl, Alejandra L Collopy, Yong Xia, and Jun Ye. 2d magneto-optical trapping of diatomic molecules. *Physical review letters*, 110(14): 143001, 2013.

[40] JF Barry, DJ McCarron, EB Norrgard, MH Steinecker, and D DeMille. Magneto-optical trapping of a diatomic molecule. *Nature*, 512(7514):286–289, 2014.

[41] J Lim, JR Almond, MA Trigatzis, JA Devlin, NJ Fitch, BE Sauer, MR Tarbutt, and EA Hinds. Laser cooled ybf molecules for measuring the electron's electric dipole moment. *Physical review letters*, 120(12):123201, 2018.

[42] Steven A Moses, Jacob P Covey, Matthew T Miecnikowski, Deborah S Jin, and Jun Ye. New frontiers for quantum gases of polar molecules. *Nature Physics*, 13(1):13–20, 2017.

[43] Luigi De Marco, Giacomo Valtolina, Kyle Matsuda, William G Tobias, Jacob P Covey, and Jun Ye. A degenerate fermi gas of polar molecules. *Science*, 363(6429):853–856, 2019.

[44] T. Baba and I. Waki. Cooling and mass-analysis of molecules using laser-cooled atoms. *Japanese Journal of Applied Physics*, 35(Part 2, No. 9A):L1134–L1137, sep 1996. doi: 10.1143/jjap.35.l1134. URL `https://doi.org/10.1143/jjap.35.l1134`.

[45] K. Mølhave and M. Drewsen. Formation of translationally cold MgH^+ and MgD^+ molecules in an ion trap. *Phys. Rev. A*, 62:011401, Jun 2000. doi: 10.1103/PhysRevA.62.011401. URL `https://link.aps.org/doi/10.1103/PhysRevA.62.011401`.

[46] AK Hansen, OO Versolato, SB Kristensen, A Gingell, M Schwarz, A Windberger, J Ullrich, JR Crespo López-Urrutia, M Drewsen, et al. Efficient rotational cooling of coulomb-crystallized molecular ions by a helium buffer gas. *Nature*, 508(7494):76–79, 2014.

[47] Peter Frøhlich Staanum, Klaus Højbjerre, Peter Skyt, Anders Hansen, and Michael Drewsen. Rotational laser cooling of vibrationally and translationally cold molecular ions. *Nature Physics*, 6:271–274, 03 2010. doi: 10.1038/nphys1604.

[48] IS Vogelius, LB Madsen, and M Drewsen. Probabilistic state preparation of a single molecular ion by projection measurement. *Journal of Physics B: Atomic, Molecular and Optical Physics*, 39(19):S1259, 2006.

[49] KAE Meyer, LL Pollum, LS Petralia, A Tauschinsky, CJ Rennick, TP Softley, and BR Heazlewood. Ejection of coulomb crystals from a linear paul ion trap for ion–molecule reaction studies. *The Journal of Physical Chemistry A*, 119(50):12449–12456, 2015.

[50] K Højbjerre, D Offenberg, CZ Bisgaard, H Stapelfeldt, PF Staanum, A Mortensen, and M Drewsen. Consecutive photodissociation of a single complex molecular ion. *Physical Review A*, 77(3):030702, 2008.

[51] Klaus Højbjerre, AK Hansen, PS Skyt, PF Staanum, and M Drewsen. Rotational state resolved photodissociation spectroscopy of translationally and vibrationally cold mgh+ ions: toward rotational cooling of molecular ions. *New Journal of Physics*, 11(5):055026, 2009.

[52] Gregers Poulsen. *Sideband Cooling of Atomic and Molecular Ions*. PhD thesis, Aarhus University, Denmark, 2011.

[53] Yong Wan, Florian Gebert, Fabian Wolf, and Piet O. Schmidt. Efficient sympathetic motional-ground-state cooling of a molecular ion. *Phys. Rev. A*, 91:043425, Apr 2015. doi: 10.1103/PhysRevA.91.043425. URL `https://link.aps.org/doi/10.1103/PhysRevA.91.043425`.

[54] R Rugango, J E Goeders, T H Dixon, J M Gray, N B Khanyile, G Shu, R J Clark, and K R Brown. Sympathetic cooling of molecular ion motion to the ground state. *New Journal of Physics*, 17(3):035009, mar 2015. doi: 10.1088/1367-2630/17/3/035009. URL `https://doi.org/10.1088%2F1367-2630%2F17%2F3%2F035009`.

[55] F Wolf, Y Wan, J C Heip, F Gebert, C Shi, and P O Schmidt. Non-destructive state detection for quantum logic spectroscopy of molecular ions. *Nature*, 530(457), feb 2016. doi: 10.1038/nature16513. URL `https://doi.org/10.1038/nature16513`.

[56] C Chou, C Kurz, D B Hume, P N Plessow, D R Leibrandt, and D Liebfried. Preparation and coherent manipulation of pure quantum states of a single molecular ion. *Nature*, 545(203), may 2017. doi: 10.1038/nature22338. URL `https://doi.org/10.1038/nature22338`.

[57] C. W. Chou, A. L. Collopy, C. Kurz, Y. Lin, M. E. Harding, P. N. Plessow, T. Fortier, S. Diddams, D. Leibfried, and D. R. Leibrandt. Frequency-comb spectroscopy on pure quantum states of a single molecular ion. *Science*, 367(6485):1458–1461, mar 2020. doi: 10.1126/science.aba3628.

[58] Kaveh Najafian, Ziv Meir, Mudit Sinhal, and Stefan Willitsch. Identification of molecular quantum states using phase-sensitive forces. *Nature Communications*, 11(1), sep 2020. doi: 10.1038/s41467-020-18170-9.

[59] Mudit Sinhal, Ziv Meir, Kaveh Najafian, Gregor Hegi, and Stefan Willitsch. Quantum-nondemolition state detection and spectroscopy of single trapped molecules. *Science*, 367 (6483):1213–1218, mar 2020. doi: 10.1126/science.aaz9837.

[60] Andrei Derevianko and Maxim Pospelov. Hunting for topological dark matter with atomic clocks. *Nature Physics*, 10(12):933–936, 2014.

[61] Juan M. Cornejo, Ralf Lehnert, Malte Niemann, Johannes Mielke, Teresa Meiners, Amado Bautista-Salvador, Marius Schulte, Diana Nitzschke, Matthias J. Borchert, Klemens Hammerer, Stefan Ulmer, and Christian Ospelkaus. Quantum logic inspired techniques for spacetime-symmetry tests with (anti-)protons. *arXiv preprint arXiv: 2106.06252*, 2021.

[62] Yiheng Lin, David R. Leibrandt, Dietrich Leibfried, and Chin wen Chou. Quantum entanglement between an atom and a molecule. *Nature*, 581(7808):273–277, may 2020. doi: 10.1038/s41586-020-2257-1.

[63] D. J. Wineland, J. C. Bergquist, J. J. Bollinger, R. E. Drullinger, and W. M. Itano. In P. Gill (World Scientific Singapore), editor, *Proceedings of the 6th Symposium on Frequency Standards and Metrology*, pages 361–368, 2002.

[64] P. O. Schmidt, T. Rosenband, C. Langer, W. M. Itano, J. C. Bergquist, and D. J. Wineland. Spectroscopy using quantum logic. *Science*, 309(5735):749–752, 2005. ISSN 0036-8075. doi: 10.1126/science.1114375. URL `https://science.sciencemag.org/content/309/5735/749`.

[65] Till Rosenband, DB Hume, PO Schmidt, Chin-Wen Chou, Anders Brusch, Luca Lorini, WH Oskay, Robert E Drullinger, Tara M Fortier, JE Stalnaker, et al. Frequency ratio of Al^+ and Hg^+ single-ion optical clocks; metrology at the 17th decimal place. *Science*, 319 (5871):1808–1812, 2008. doi: 10.1126/science.1154622.

[66] Yong Wan, Florian Gebert, Jannes B Wübbena, Nils Scharnhorst, Sana Amairi, Ian D Leroux, Börge Hemmerling, Niels Lörch, Klemens Hammerer, and Piet O Schmidt. Precision spectroscopy by photon-recoil signal amplification. *Nature communications*, 5:3096, 2014.

[67] Florian Gebert, Yong Wan, Fabian Wolf, Christopher N. Angstmann, Julian C. Berengut, and Piet O. Schmidt. Precision isotope shift measurements in calcium ions using quantum logic detection schemes. *Phys. Rev. Lett.*, 115:053003, Jul 2015. doi: 10.1103/PhysRevLett.115.053003. URL `https://link.aps.org/doi/10.1103/PhysRevLett.115.053003`.

[68] M. Schulte, N. Lörch, P. O. Schmidt, and K. Hammerer. Photon-recoil spectroscopy: Systematic shifts and nonclassical enhancements. *Physical Review A*, 98(6), dec 2018. doi: 10.1103/physreva.98.063808.

[69] P Micke, T Leopold, SA King, E Benkler, LJ Spieß, Lisa Schmoeger, M Schwarz, JR Crespo López-Urrutia, and PO Schmidt. Coherent laser spectroscopy of highly charged ions using quantum logic. *Nature*, 578(7793):60–65, 2020.

[70] W. J. Balfour. Rotational analysis of the A $^1\Sigma^+ \rightarrow$ X $^1\Sigma^+$ and B $^1\Pi \rightarrow$ X $^1\Sigma^+$ systems of $^{24}MgH^+$, $^{25}MgH^+$, and $^{26}MgH^+$. *Canadian Journal of Physics*, 50(11):1082–1091, 1972.

[71] A. K. Hansen. *Cold Molecular Ions: Rotational State Preparation and Single Ion Reaction Experiments*. PhD thesis, Aarhus University, Denmark, 2012.

[72] Frank Jensen. Department of Chemistry, Aarhus University. Personal communication.

[73] Emilie H Clausen, Vincent Jarlaud, Karin Fisher, Steffen Meyer, Cyrille Solaro, and Michael Drewsen. Unresolved sideband photon recoil spectroscopy of molecular ions. *arXiv preprint arXiv:2004.02959*, 2020.

[74] David J. Griffiths. *Introduction to Electrodynamics*. Pearson, 4 edition.

[75] Wolfgang Paul. Electromagnetic traps for charged and neutral particles. *Rev. Mod. Phys.*, 62:531–540, Jul 1990. doi: 10.1103/RevModPhys.62.531. URL https://link.aps.org/doi/10.1103/RevModPhys.62.531.

[76] J. D. Prestage, G. J. Dick, and L. Maleki. New ion trap for frequency standard applications. *Journal of Applied Physics*, 66:1013, 1989.

[77] D. R. Denison. Operating parameters of a quadrupole in a grounded cylindrical housing. *Journal of Vacuum Science and Technology*, 8(1):266–269, 1971. doi: 10.1116/1.1316304. URL https://doi.org/10.1116/1.1316304.

[78] P. K. Ghosh. *Ion Traps*. Clarendon Press, Oxford.

[79] Hans Harhoff Andersen. *Cooling and manipulating ions in traps with integrated optical cavities*. PhD thesis, Aarhus University, Denmark, 2015.

[80] M. Drewsen and A. Brøner. Harmonic linear paul trap: Stability diagram and effective potentials. *Phys. Rev. A*, 62:045401, Sep 2000. doi: 10.1103/PhysRevA.62.045401. URL https://link.aps.org/doi/10.1103/PhysRevA.62.045401.

[81] G Morigi and H Walther. Two-species coulomb chains for quantum information. *The European Physical Journal D-Atomic, Molecular, Optical and Plasma Physics*, 13(2):261–269, 2001.

[82] Karin Fisher. *Adiabatic Cooling for Rovibrational Spectroscopy of Molecular Ions*. PhD thesis, Aarhus University, Denmark, 2017.

[83] M. Drewsen, A. Mortensen, R. Martinussen, P. Staanum, and J. L. Sørensen. Non-destructive identification of cold and extremely localized single molecular ions. *Phys. Rev. Lett.*, 93: 243201, Dec 2004. doi: 10.1103/PhysRevLett.93.243201. URL https://link.aps.org/doi/10.1103/PhysRevLett.93.243201.

[84] Jannes B. Wübbena, Sana Amairi, Olaf Mandel, and Piet O. Schmidt. Sympathetic cooling of mixed-species two-ion crystals for precision spectroscopy. *Phys. Rev. A*, 85:043412, Apr 2012. doi: 10.1103/PhysRevA.85.043412. URL https://link.aps.org/doi/10.1103/PhysRevA.85.043412.

[85] Rodney Loudon. *The quantum theory of light*. Oxford University Press, 2nd edition, 1983.

[86] Christopher J Foot. *Atomic physics*. Oxford University Press, 2005.

[87] Wolfgang Demtröder. *Atoms, Molecules and Photons*. 2nd edition.

[88] BE King. Angular momentum coupling and rabi frequencies for simple atomic transitions. *arXiv preprint arXiv:0804.4528*, 2008.

[89] David J Wineland, C Monroe, Wayne M Itano, Dietrich Leibfried, Brian E King, and Dawn M Meekhof. Experimental issues in coherent quantum-state manipulation of trapped atomic ions. *Journal of Research of the National Institute of Standards and Technology*, 103(3):259, 1998.

[90] D. Leibfried, R. Blatt, C. Monroe, and D. Wineland. Quantum dynamics of single trapped ions. *Rev. Mod. Phys.*, 75:281–324, Mar 2003. doi: 10.1103/RevModPhys.75.281. URL https://link.aps.org/doi/10.1103/RevModPhys.75.281.

[91] Wilhelm Magnus. On the exponential solution of differential equations for a linear operator. *Communications on Pure and Applied Mathematics*, 7(4):649–673, 1954. doi: 10.1002/cpa.3160070404. URL https://onlinelibrary.wiley.com/doi/abs/10.1002/cpa.3160070404.

[92] D. J. Wineland and Wayne M. Itano. Laser cooling of atoms. *Phys. Rev. A*, 20:1521–1540, Oct 1979. doi: 10.1103/PhysRevA.20.1521. URL `https://link.aps.org/doi/10.1103/PhysRevA.20.1521`.

[93] W. Neuhauser, M. Hohenstatt, P. Toschek, and H. Dehmelt. Optical-sideband cooling of visible atom cloud confined in parabolic well. *Phys. Rev. Lett.*, 41:233–236, Jul 1978. doi: 10.1103/PhysRevLett.41.233. URL `https://link.aps.org/doi/10.1103/PhysRevLett.41.233`.

[94] Stig Stenholm. The semiclassical theory of laser cooling. *Rev. Mod. Phys.*, 58:699–739, Jul 1986. doi: 10.1103/RevModPhys.58.699. URL `https://link.aps.org/doi/10.1103/RevModPhys.58.699`.

[95] Emilie Hindbo Clausen. *Photon-recoil spectroscopy of $^{24}Mg^{+}$ sideband cooled to the motional ground state with $^{40}Ca^{+}$ in a linear Paul trap.* Master's thesis, Aarhus University, Denmark, 2018.

[96] M. Hettrich, T. Ruster, H. Kaufmann, C. F. Roos, C. T. Schmiegelow, F. Schmidt-Kaler, and U. G. Poschinger. Measurement of dipole matrix elements with a single trapped ion. *Phys. Rev. Lett.*, 115:143003, Oct 2015. doi: 10.1103/PhysRevLett.115.143003. URL `https://link.aps.org/doi/10.1103/PhysRevLett.115.143003`.

[97] Jian Jin and D. A. Church. Precision lifetimes for the ca^{+} 4p ^{2}p levels: Experiment challenges theory at the 1% level. *Phys. Rev. Lett.*, 70:3213–3216, May 1993. doi: 10.1103/PhysRevLett.70.3213. URL `https://link.aps.org/doi/10.1103/PhysRevLett.70.3213`.

[98] F. Diedrich, J. C. Bergquist, Wayne M. Itano, and D. J. Wineland. Laser cooling to the zero-point energy of motion. *Phys. Rev. Lett.*, 62:403–406, Jan 1989. doi: 10.1103/PhysRevLett.62.403. URL `https://link.aps.org/doi/10.1103/PhysRevLett.62.403`.

[99] DJ Wineland, Wayne M Itano, JC Bergquist, and Randall G Hulet. Laser-cooling limits and single-ion spectroscopy. *Physical Review A*, 36(5):2220, 1987.

[100] H. Sawamura, K. Kanda, R. Yamazaki, K. Toyoda, and S. Urabe. Optimum parameters for sideband cooling of a 40ca+ ion. *Applied Physics B*, 93(2):381–388, Nov 2008. ISSN 1432-0649. doi: 10.1007/s00340-008-3162-8. URL `https://doi.org/10.1007/s00340-008-3162-8`.

[101] D. Kielpinski, B. E. King, C. J. Myatt, C. A. Sackett, Q. A. Turchette, W. M. Itano, C. Monroe, D. J. Wineland, and W. H. Zurek. Sympathetic cooling of trapped ions for quantum logic. *Phys. Rev. A*, 61:032310, Feb 2000. doi: 10.1103/PhysRevA.61.032310. URL `https://link.aps.org/doi/10.1103/PhysRevA.61.032310`.

[102] Robert Höppner, Eugenio Roldán, and Germán J de Valcárcel. A semiclassical optics derivation of einstein's rate equations. *American Journal of Physics*, 80(10):882–890, 2012.

[103] John David Jackson. *Classical Electrodynamics, 3rd ed.* John Wiley and Sons Ltd., 1962.

[104] Nikolay V Vitanov, Thomas Halfmann, Bruce W Shore, and Klaas Bergmann. Laser-induced population transfer by adiabatic passage techniques. *Annual review of physical chemistry*, 52 (1):763–809, 2001.

[105] T Watanabe, S Nomura, K Toyoda, and S Urabe. Sideband excitation of trapped ions by rapid adiabatic passage for manipulation of motional states. *Physical Review A*, 84(3):033412, 2011.

[106] Arthur Schawlow. Physicists keep nobel prizes in the family. *New Scientist*, page 225, October 22 1981.

[107] Niels Kjærgaard. *Methods in Laser Cooling of Ions in Storage Rings and Traps*. PhD thesis, Aarhus University, Denmark, 2001.

[108] URL http://www.corning.com/worldwide/en/products/advanced-optics/product-materials/specialty-glass-and-glass-ceramics/glass-ceramics/macor.html.

[109] D.F.V. James. Quantum dynamics of cold trapped ions with application to quantum computation. *Applied Physics B*, 66(2):181–190, Feb 1998. ISSN 1432-0649. doi: 10.1007/s003400050373. URL https://doi.org/10.1007/s003400050373.

[110] N. Kjærgaard, L. Hornekaer, A.M. Thommesen, Z. Videsen, and M. Drewsen. Isotope selective loading of an ion trap using resonance-enhanced two-photon ionization. *Applied Physics B*, 71(2):207–210, Aug 2000. ISSN 1432-0649. doi: 10.1007/s003400000296. URL https://doi.org/10.1007/s003400000296.

[111] D N Madsen, S Balslev, M Drewsen, N Kjærgaard, Z Videsen, and J W Thomsen. Measurements on photo-ionization of 3s3p $^1p_1$ magnesium atoms. *Journal of Physics B: Atomic, Molecular and Optical Physics*, 33(22):4981, 2000. URL http://stacks.iop.org/0953-4075/33/i=22/a=302.

[112] P. F. Herskind. *Cavity Quantum Electrodynamics with Ion Coulomb Crystals*. PhD thesis, Aarhus University, Denmark, 2008.

[113] Hansen Anders K., Sørensen Magnus A., Staanum Peter F., and Drewsen Michael. Single ion recycling reactions. *Angewandte Chemie International Edition*, 51(32):7960–7962. doi: 10.1002/anie.201203550. URL https://onlinelibrary.wiley.com/doi/abs/10.1002/anie.201203550.

[114] Michael Drewsen and Andy Brøner. Harmonic linear paul trap: Stability diagram and effective potentials. *Physical Review A*, 62(4):045401, 2000.

[115] Michael Drewsen, Anders Mortensen, Randi Martinussen, Peter Staanum, and Jens L Sørensen. Nondestructive identification of cold and extremely localized single molecular ions. *Physical review letters*, 93(24):243201, 2004.

[116] Thomas Talvard, Philip G. Westergaard, Michael V. DePalatis, Nicolai F. Mortensen, Michael Drewsen, Bjarke Gøth, and Jan Hald. Enhancement of the performance of a fiber-based frequency comb by referencing to an acetylene-stabilized fiber laser. *Opt. Express*, 25(3):2259–2269, Feb 2017. doi: 10.1364/OE.25.002259. URL http://www.opticsexpress.org/abstract.cfm?URI=oe-25-3-2259.

[117] Jerome Faist, Federico Capasso, Deborah L. Sivco, Carlo Sirtori, Albert L. Hutchinson, and Alfred Y. Cho. Quantum cascade laser. *Science*, 264(5158):553–556, 1994. ISSN 0036-8075. doi: 10.1126/science.264.5158.553. URL https://science.sciencemag.org/content/264/5158/553.

[118] William Lund Sommer. *Characterization of a Quantum Cascade Laser and Wavelength Meter for Molecular Spectroscopy*. Bachelor thesis, Aarhus University, Denmark, 2016.

[119] Julie Harbo Arleth. *Characterization of a Quantum Cascade Laser and Wavelength Meter*. Bachelor thesis, Aarhus University, Denmark, 2017.

[120] Niklas Hedegaard Arent. *Characterization and Tuning of a Quantum Cascade Laser and Wavelength Meter for Molecular Spectroscopy*. Bachelor thesis, Aarhus University, Denmark, 2018.

[121] C Cottaz, I Kleiner, G Tarrago, LR Brown, JS Margolis, RL Poynter, HM Pickett, T Fouchet, P Drossart, and E Lellouch. Line positions and intensities in the $2\nu 2/\nu 4$ vibrational system of 14nh3 near 5–7 μm. *Journal of molecular spectroscopy*, 203(2):285–309, 2000.

[122] I Kleiner, G Tarrago, C Cottaz, L Sagui, Linda R Brown, RL Poynter, HM Pickett, P Chen, JC Pearson, Robert L Sams, et al. Nh3 and ph3 line parameters: the 2000 hitran update and new results. *Journal of Quantitative Spectroscopy and Radiative Transfer*, 82(1-4):293–312, 2003.

[123] P Norton. Hgcdte infrared detectors. *Opto-electronics Review*, 10:159–174, 01 2002.

[124] Heiko Ganser, Bertold Frech, Andreas Jentsch, Manfred Mürtz, Claire Gmachl, Federico Capasso, Deborah L Sivco, James N Baillargeon, Albert L Hutchinson, Alfred Y Cho, et al. Investigation of the spectral width of quantum cascade laser emission near 5.2 μm by a heterodyne experiment. *Optics communications*, 197(1-3):127–130, 2001.

[125] Tanya L Myers, Richard M Williams, Matthew S Taubman, Claire Gmachl, Federico Capasso, Deborah L Sivco, James N Baillargeon, and Alfred Y Cho. Free-running frequency stability of mid-infrared quantum cascade lasers. *Optics letters*, 27(3):170–172, 2002.

[126] D Weidmann, L Joly, V Parpillon, D Courtois, Yargo Bonetti, Thierry Aellen, Mattias Beck, Jérôme Faist, and Daniel Hofstetter. Free-running 9.1-μm distributed-feedback quantum cascade laser linewidth measurement by heterodyning with a c 18 o 2 laser. *Optics letters*, 28(9): 704–706, 2003.

[127] Peter W. Milonni and Joseph H. Eberly. *Laser Physics*. John Wiley & Sons, Inc., 2010.

[128] Crystran homepage. `https://www.crystran.co.uk/optical-materials/calcium-fluoride-caf2`. Accessed: 2021-07-16.

[129] M. Herrmann, V. Batteiger, S. Knünz, G. Saathoff, Th. Udem, and T. W. Hänsch. Frequency metrology on single trapped ions in the weak binding limit: The 3s $^2S_{1/2}$ - 3p $^2P_{3/2}$ transition in $^{24}Mg^+$. *Physical Review Letters*, 102(1), Jan 2009. doi: 10.1103/physrevlett.102.013006.

[130] Michael Berglund and Michael E Wieser. Isotopic compositions of the elements 2009 (iupac technical report). *Pure and applied chemistry*, 83(2):397–410, 2011.

[131] A Mortensen, JJT Lindballe, IS Jensen, P Staanum, D Voigt, and M Drewsen. Isotope shifts of the 4 s 2 s 0 1 4 s 5 p p 1 1 transition and hyperfine splitting of the 4 s 5 p p 1 1 state in calcium. *Physical Review A*, 69(4):042502, 2004.

[132] Steffen Meyer. *Frequency Comb Driven Raman Transitions in the THz Range: High Precision Isotope Shift Measurements in Ca^+*. PhD thesis, Aarhus University, Denmark, 2017.